Dynamics of elastic sheets in Stokes flow

by

Yijiang Yu

A dissertation submitted in partial fulfillment of

the requirements for the degree of

Doctor of Philosophy

(Chemical and Biological Engineering)

at the

UNIVERSITY OF WISCONSIN - MADISON

2023

Date of final oral examination: July 17, 2023

This dissertation is approved by the following members of the Final Oral Committee:

Michael D. Graham, Professor, Chemical and Biological Engineering

Daniel Klingenberg, Professor, Chemical and Biological Engineering

David Lynn, Professor, Chemical and Biological Engineering

Saverio Spagnolie, Professor, Mathematics

To my family and my loved ones.

Acknowledgements

Foremost, I dedicate this work to my parents and my grandparents. They always support me with unconditional love and I am fortunate to grow up in this great family. And to Avian, I hope blue nightshades light up every night of your life.

My sincere gratitude goes to my advisor Michael Graham as a great advisor and mentor. You have fostered my passion for research and guided me through all important aspects of my work, including giving my first conference talk and publishing my first research paper. I also acknowledge my collaborator Dr. Hugo Perrin and Professor Lorenzo Botto. I am glad that we started our conversation at the DFD conference and shared our interests to make this incredible collaboration happen.

During my time in Madison, I have crossed paths with many friends and colleagues along with cherished memories. I would like to thank all Graham Group members. To Kevin Zeng and Alec Linot, I am grateful to have you as friends since the very first day of graduate school. Kevin, you are always being supportive and have helped me get through tough periods, with many words that I don't have to say but always keep in my heart. Alec, thank you for all the talks and discussions, which keep me stay strong and brave. To RJ Hommel and Carlos Perez de Jesus, we have shared so many great memories and fun together and your kindness and support mean a lot to me. To Xiaopo Cheng and Alex Guo, your hardworking and enthusiasm to research always impress me. To Xiao Zhang, thank you for all the continuous support and help to get me through the first couple of years. To Daniel Floryan, your mentorship and knowledge are important to my success. I also want to thank

Ricardo Constante-Amores, Frank Nguyen, Manish Kumar, Andrew Fox, Charlie Young, and Dell Zimmerman for all the fun and joy we had in the group.

More thanks go to my lovely friends. Yicheng Hu and Yaqing Wu for your accompany and support at every important step of my life. Songying Li, Yaxuan Wang, and Zening Duan for our great game night and pool time. Beihang Yu and Ziyue Lu for the great Pokemon squad team and all the warmhearted talking. I want to mention my amazing friends Amy Qin, Lisa Je, Nanqi Bao, Weiqi Zhang, Huaizhe Yu, Xiangzhe Xu, and Shiwei Feng for their continuous support throughout this journey. I also want to bring my special thanks to Francesca Gambacorta. We have gone through a lot since Illinois and we all successfully defended our work.

To my dear underground friends from the University of Illinois, Timothy Chen, Yuying Wu, Kaixiang Huang, Sean Ebihara, Sean van Geldern, Will Lau, Ke Zhang, Jingyou Wang, Zijie Wu ... the list never ends. I feel grateful to meet you in my life with all happiness and joy we had together back in our college life. My sincere appreciation extends to my undergraduate advisor Prof Hyunjoon Kong for giving me the opportunity to do interesting biomaterial research and Dr. Jooyeon Park for your mentoring and insightful suggestions that convinced me to proceed to graduate school.

I also would like to thank my incredible friends since middle school, Chaowei Hu, Tunan Zhu, and Zixun Yu, for your endless support and our memories that have become an indispensable part of my life.

Finally, I express my gratitude to Professor Daniel Klingenberg, Professor David Lynn, Professor Saverio Spagnolie, and my advisor for serving on my defense committee, sharing valuable feedback and insightful suggestions for my thesis.

Abstract

Freely suspended thin sheets are ubiquitously observed in the synthesis and processing stages of thin-structured materials. Examples include the solution-based synthesis of graphene and thin polymer films, where the freely suspended thin elastic sheets are exposed to external flows and show complex stretching, folding, and wrinkling dynamics due to the deformable nature of sheets. Understanding the flow-induced deformations of sheets is crucial as they significantly influence the macroscopic properties of the flow. However, there is a lack of comprehensive knowledge in this area. Motivated by this knowledge gap, the main objective of this thesis is to develop a systematic framework for examining the dynamics of elastic sheets in fundamental flow fields. By studying the behavior of these sheets, insights can be gained that will contribute to a better understanding of their real-world applications.

Chapter 1 provides motivation for this study by exploring applications involving the flow processing of elastic sheets. This is followed by an in-depth review of existing literature on exploring elastic sheet dynamics in flow. Additionally, we extend our review to include the dynamics of related soft particles, such as flexible filaments and capsules. The insights gained from these studies can be applied to enhance the understanding of elastic sheets in flow. Furthermore, we introduce some background concepts to facilitate understanding the results.

To establish a foundation for the subsequent chapters, Chapter 2 presents a detailed formulation for a general model that considers a soft elastic sheet freely suspended in arbitrary flow conditions. We discuss detailed numerical approaches for evaluating mechanical forces

and fluid motions, and the model is validated using analytical and experimental results.

In Chapter 3, we begin the introduction of dynamics in extensional flow. Inspired by the coil-stretch transition for a long linear polymer exposed to an extensional flow, we identify a "compact-stretched transition" for a highly extensible sheet in planar and biaxial extensional flow with a flow regime showing bistable conformations; this transition is analogous to the coil-stretch transition seen for a long linear polymer exposed to an extensional flow. We give a detailed analysis of bistable regimes for elastic sheets with different rest shapes. Furthermore, we identify the origin of the bistable behavior, as in the long-chain polymer case, arising from the hydrodynamic interaction between distant elements of the sheet. Due to the nature of planar and biaxial flow fields, the steady states all remain flat.

We continue the study of bistable elastic sheets in a uniaxial extensional flow in Chapter 4, where the radially compressive stress of the flow field leads to buckling instability. We characterize the wrinkling patterns on sheets based on sheet deformability and find that buckling leads to a decrease in the stretched size due to an effect called hydrodynamic screening. Here, the compact-stretched bistability still occurs but is strongly modified by the wrinkling instability. Notably, we develop a linear stability analysis based on the flat steady states that can precisely predict and help understand the nonlinear long-term dynamics for some parameter regimes.

In Chapter 5, we are motivated by applications of shear flow processing of nanosheets and shift our focus from highly stretchable sheets in extensional flow to almost inextensible sheets in shear flow. We explore two types of rest shapes, a disk, and a rectangle, initially aligning with the flow-gradient plane. For a disk, we found two new periodic solutions: flapping and wiggling. Importantly, flapping is supported by the experimental observations from our collaborators. We also develop a linear stability analysis that yields a number of unstable modes, which helps us to understand the nonlinear evolution of dynamics. Moreover, we examined the dynamics under a free surface to help illustrate the flapping motion observed in experiments. In addition, we systematically examined the influence of aspect ratio and

characteristic evolutions for a rectangle.

In Chapter 6, we change our focus to study a thin elastic sheet freely sedimenting in a viscous fluid. Two scenarios are investigated: sedimentation in free space and near an infinite wall, where the wall can be titled. In free space, we examined the steady-state conformation and characterized the reorientation dynamics based on sheet deformability. In the near-wall case, we characterized different dynamics that are strongly modified due to the presence of the boundary. Near a vertical wall, the sheet migrates due to wall-induced asymmetric conformation with migration behaviors determined by deformability. Moreover, several additional dynamics are observed when the wall is titled: the sheet can deposit or slide along the wall with a fixed wall-normal distance.

Finally, we conclude this thesis and propose some future directions in Chapter 7. The future work includes two main topics: improvement of the current model and prospective directions. For the model development, we introduce a potential method to account for the thickness of the sheet, improvement to the bending model by applying a nonlinear formulation, and incorporate thermal fluctuations. We also explore two prospective directions for the project: sheet exfoliation and biohybrid swimming sheets, along with some preliminary tests and observations. We end the discussion of future work by presenting the results from a side project, where we are interested in developing a simple formulation for a flexible filament in shear flow.

Contents

1 General introduction **1**

1.1 Thin elastic sheets processed in fluid 2

1.1.1 Applications of thin sheets 2

1.1.2 Current studies of elastic sheets in flow 10

1.2 Dynamics of soft particles in Stokes flow 15

1.2.1 Linear flow fields 15

1.2.2 Dynamics in extensional flow 17

1.2.3 Dynamics in shear flow 19

1.2.4 Sedimentation in a viscous fluid 22

1.3 Stokes flow introduction 25

1.3.1 Properties of Stokes flow 25

1.3.2 Fundamental solutions in Stokes flow 26

1.3.3 Multipole expansion 28

1.3.4 Regularized Stokeslet 29

1.4 Outline of this work 31

2 Modeling of elastic sheets in Stokes flow **32**

2.1 Problem formulation 32

2.1.1 Mechanical forces 33

2.1.2 Dimensionless groups 35

2.2 Numerical methods 36
2.2.1 In-plane forces calculation 36
2.2.2 Out-of-plane forces calculation 40
2.3 Modeling of fluid 44
2.4 Model validation 45
2.4.1 Validation case I: a rigid disk in biaxial extensional flow 46
2.4.2 Validation case II: a flexible rectangle in simple shear flow 50
2.4.3 Validation of boundary conditions 51

3 Coil-stretch-like transition of elastic sheets in extensional flow 53
3.1 Introduction 54
3.2 Methods 57
3.3 Results 62
3.3.1 Planar extensional flow 62
3.3.2 Biaxial extensional flow 70
3.3.3 Effect of artificial hydrodynamic screening 72
3.4 Summary 74

4 Wrinkling and multiplicity in the dynamics of deformable sheets in uniaxial extensional flow 76
4.1 Introduction 77
4.2 Methods 80
4.3 Results 85
4.3.1 Dynamics of stiff sheets 85
4.3.2 Dynamics of flexible sheets in the compact (low Ca) regime 88
4.3.3 Linear stability analysis for compact sheets 92
4.3.4 Dynamics of flexible sheets in the stretched (high Ca) 101
4.4 Summary 104

5 Complex dynamics of elastic sheets in shear flow **106**

5.1 Introduction . . . 107

5.2 Methods . . . 108

5.3 Dynamics of a disk in simple shear flow . . . 113

5.3.1 Characteristic dynamics . . . 114

5.3.2 Bifurcation diagram and linear stability analysis . . . 119

5.3.3 Experimental observations . . . 122

5.4 Dynamics of a disk in shear flow under a free surface . . . 125

5.5 Dynamics of a rectangle sheet in simple shear flow . . . 130

5.5.1 Tumbling sheets . . . 130

5.5.2 Characteristic dynamics . . . 132

5.5.3 Bifurcation and phase diagram . . . 136

5.6 Summary . . . 140

6 Free-space and near-wall dynamics of a flexible sheet sedimenting in Stokes flow **142**

6.1 Introduction . . . 143

6.2 Methods . . . 146

6.2.1 Model setup . . . 146

6.2.2 Numerical methods . . . 150

6.2.3 Fluid solver . . . 150

6.3 Results . . . 155

6.3.1 Sedimentation in free space . . . 155

6.3.2 Sedimentation next to a wall . . . 159

6.4 Summary . . . 167

7 Conclusions and future work **169**

7.1 General summary . . . 169

7.2 Model development 171
7.2.1 Elastic sheet with a finite thickness 171
7.2.2 Nonlinear bending method 173
7.3 Multiple sheets interaction 174
7.4 Exfoliation 176
7.5 Biohybrid sheets 179
7.6 Flexible filaments in simple shear flow 182

8 Code **186**
8.1 Code overview 186
8.2 Code excerpt 188
8.2.1 Initialization 188
8.2.2 Iterative calculation 190

References **192**

List of Figures

1.1 (a) Examples of elastic sheets obtained from liquid-phase exfoliation. (b) Synthetic process of graphene based on a Couette flow reactor from [4]. (c) The suspension of graphene oxide shows different potential orientations in a Taylor-Couette reactor with an illustration of shear-induced flattening of sheets from [135]. 4

1.2 (a) The synthesis of graphene-incorporated carbon nanofibers via water-based electrospinning from [44]. The GO sheets mixed with polymer solutions are folded when the solution is ejected from the syringe tip through a high-voltage electric field. (b) Deformation response of a kinetoplast DNA network exposed to planar extensional flow from [57, 164]. 6

1.3 Examples of linear extensional flow: (a) Biaxial extension $\mathbf{v} = \dot{\varepsilon}(x/2, y/2, -z)$. (b) Uniaxial extension $\mathbf{v} = \dot{\varepsilon}(-x/2, -y/2, z)$. (c) Planar extension $\mathbf{v} = \dot{\varepsilon}(x, 0, -z)$. $\dot{\varepsilon}$ is the flow extension rate. (d) Decomposition of a simple shear flow $\mathbf{v} = \dot{\gamma}(-y, 0, 0)$ into a planar extension and a rigid rotation. $\dot{\gamma}$ is the flow shear rate. 16

1.4 (a) Illustration of coil-stretch transition for long-chain polymer exposed to a planar extensional flow. (b) Experimental observation of coil-stretch transition with fluorescently dyed Escherichia coli DNA molecule in planar extensional flow from [151]. 18

1.5 (a) A rigid prolate spheroid in a spherical coordinate system exposed to a simple shear flow. (b) The path of the orientation vector for a prolate spheroid undergoing Jeffery orbits with different orbit constants from Petrich *et al.* [134]. 20

1.6 (a) The center of mass trajectory of a flexible fiber sedimenting in a viscous fluid with an inset figure indicating fiber conformations from Li *et al.* [91] (b) Steady shape evolution of a sedimenting filament with increasing flexibility from Cunha *et al.* [31]. (c) A flexible sedimenting filament shows nonplanar conformation with a helical trajectory from Saggiorato *et al.* [144]. 23

1.7 Velocity profile generated due to point forces with strength **F**: Stokeslet, stresslet and rotlet. 27

1.8 Regularized Delta function $\delta_\kappa(r)$ with different choices of κ for a Gaussian regularization. 30

2.1 Description of two mechanical deformations with an example of disk: (a) In-plane deformation: the sheet is stretched without buckling. (b) Out-of-plane deformation: the sheet is wrinkled and deforms out of the lateral plane. . . . 33

2.2 Illustration of in-plane forces calculation. 40

2.3 Illustration of the four-point method to evaluate bending nodal forces between two neighboring triangular elements. 43

2.4 (a) Scenario setup: a disk radially stretched in a biaxial extensional flow and reaches equilibrium. (b) Illustration of λ in an oblate spheroidal coordinate system for an oblate spheroid and a disk. 46

2.5 The difference in perturbation velocity norm $||\mathbf{v}_p||$ between analytical and numerical solutions in the plane $y = 0$: (a) Error percentage profile (b) Absolute error profile. (c) Perturbation velocity norm $||\mathbf{v}_p||$ vs. distance r along a line away from the origin for a disc in biaxial flow: (c) The line chosen follows the vector [1,0,2] and the black dashed line is proportional to r^{-2}. (d) The line chosen follows the vector [1,1,1] and the black dashed line is proportional to r^{-4}. 49

2.6 (a) Examples of a rectangle tumbling in simple shear flow with a case below the buckling threshold where no deformation is observed and a case above the threshold where the sheet buckles. (b) Comparison with experimental results from [133]. The buckling threshold is estimated to be $\mathrm{E_V^C} \sim 1$ in both setups. 50

2.7 Average magnitude of permeation velocity, $\langle |v_{\mathrm{per}}| \rangle$, at element centers for a sheet (the taco shape in Fig. 4.2(a)) vs. mesh size $1/\sqrt{N_e}$. The filled symbol indicates the mesh of 1600 triangular elements used for the main set of results. 52

3.1 Time evolution of a deformable disk initially aligned with the $x - z$ plane in planar extensional flow ($\mathrm{Ca} = 0.2$; $\hat{K}_B = 1 \times 10^{-3}$). 62

3.2 Stable steady-state conformation of a sheet in planar extensional flow with neo-Hookean elasticity at $\mathrm{Ca} = 0.1$: (a) disk. (b) a square. (c) rectangle. The scale bar 1 dimensionless length unit. 63

3.3 Steady-state stretched length l_s vs. Ca for deformable sheets with neo-Hookean elasticity in planar extensional flow. The data points filled with light color correspond to the shapes shown in Fig 3.2. The critical Ca for each geometry are: disk ($\mathrm{Ca} = 0.34$), square ($\mathrm{Ca} = 0.214$), rectangle ($\mathrm{Ca} = 0.228$). The subplot indicates how length l is measured and the preferred stable orientation. 64

3.4 The steady-state conformation of a stretched sheet in planar extensional flow with Yeoh elasticity with $c = 5 \times 10^{-5}$: (a) a disk at Ca = 0.35. (b) a square at Ca = 0.22. (c) a rectangle at Ca = 0.24. The scale bar is 2 dimensionless length units. 65

3.5 (a) Final stretched length l_s vs. Ca for a disk with $c = 2 \times 10^{-5}$ in planar extensional flow. Blue symbols and curves represent a compact final conformation and red represent a stretched final conformation. The points filled with light color correspond to the transient evolution shown in Fig 3.5(c)-(e). The black dashed line indicates the unstable steady state. The light blue dashed line shows the critical Ca with neo-Hookean elasticity. Ca_c and Ca_s are two critical Ca marked besides the arrows. (b) Final stretched length l_s vs. Ca for a disk with $c = 1 \times 10^{-4}$ in planar extensional flow. (c)-(e): Examples of stretched length evolution of a disk from either a stretched state or a compact state with $c = 2 \times 10^{-5}$ in planar extensional flow: (c) Ca = 0.3 (d) Ca = 0.33 (e) Ca = 0.35. 66

3.6 (a) Final stretched length l_s vs. Ca for a disk in planar extensional flow with various c. All c have a similar (overlapped) compact branch. The blue dashed line refers to Ca_s with neo-Hookean elasticity. (b) Phase diagram of Ca_c and Ca_s vs. c in planar extensional flow. The gray area marks the parameter regime where hysteresis can be observed. 67

3.7 (a) Bifurcation diagram of stretched length l_s vs. Ca for a square in planar extensional flow, $c = 1 \times 10^{-4}$. (b) Phase diagram of Ca_c and Ca_s vs c for a square in planar extensional flow, with the gray area indicating the hysteresis region. 69

3.8 (a) Transient stretched length evolution of a rectangle in planar extensional flow, $c = 7 \times 10^{-5}$, Ca = 0.24. (b) Bifurcation diagram of l_s vs. Ca for a rectangle with $c = 1 \times 10^{-5}$.(c) Bifurcation diagram of l_s vs. Ca for a rectangle sheet with $c = 7 \times 10^{-5}$. The data point filled with light color corresponds to the evolution shown in Fig 3.8(a) (d) Bifurcation diagram of l_s vs. Ca for a rectangle with $c = 3 \times 10^{-4}$. (e) Phase diagram Ca_c and Ca_s vs c for a rectangle in planar extensional flow; here $\mathrm{Ca}_{s,a}$ represents the stretched critical Ca for an asymmetric conformation, and $\mathrm{Ca}_{s,s}$ represents the stretched critical Ca for a symmetric conformation. The dark gray area indicates the hysteresis region for symmetric states and the light gray area marks the hysteresis region without symmetry constraints, so the stretched state is tilted. 70

3.9 Steady-state conformation of a stable steady-state sheet with neo-Hookean elasticity in biaxial extensional flow at Ca = 0.2: (a) disk. (b) square. (c) rectangle. Scale bar is 1 dimensionless length unit. 71

3.10 Steady-state stretched length l_s vs. Ca for deformable sheets with neo-Hookean elasticity in biaxial extensional flow. The data points filled with light color correspond to the conformations shown in Fig 3.9. The critical capillary numbers are: disk: $\mathrm{Ca}_c = 0.391$, square: $\mathrm{Ca}_c = 0.309$, rectangle: $\mathrm{Ca}_c = 0.395$. The subplot indicates the length measured in each geometry. 72

3.11 Bifurcation diagrams of l_s vs. Ca for sheets of different shapes in biaxial extensional flow: (a) disk: $c = 1 \times 10^{-4}$. (b) square: $c = 1 \times 10^{-4}$, (c) rectangle: $c = 1 \times 10^{-5}$. The light blue dashed line refers to Ca_c with neo-Hookean elasticity. Phase diagram of the hysteresis regime in biaxial extensional flow: (d) disk, (e) square, (f) rectangle. 73

3.12 Bifurcation diagrams of l_s vs. Ca for a square sheet ($c = 1 \times 10^{-4}$) with increasing α: (a) planar extensional flow. (b) biaxial extensional flow. 74

4.1 (a) Steady state half-length l_s vs. Ca for a stiff disk with $c = 0$ (neo-Hookean) in uniaxial extensional flow, indicating a singularity in l_s. (b) l_s vs. Ca for a stiff disk with $c = 1 \times 10^{-5}$ in uniaxial extensional flow. Blue symbols represent a compact final conformation and red symbols represent a stretched final conformation. Ca_c and Ca_s are the two critical Ca marked beside the arrows. (c) l_s vs. Ca for a stiff disk with $c = 5 \times 10^{-5}$ in uniaxial extensional flow, with a smooth transition observed. (d) Examples of bistable sheets for $\mathrm{Ca} = 0.37$ with $c = 1 \times 10^{-5}$, corresponding to light symbols in Fig. 4.1(b). The figure shows the front view of compact and stretched states with half-length labeled l_s. (e) Examples of transient length evolution for stiff sheets with $\mathrm{Ca} = 0.36$ and $c = 1 \times 10^{-5}$, below the bistability regime. (f) Examples of transient length evolution for stiff sheets with $\mathrm{Ca} = 0.37$ and $c = 1 \times 10^{-5}$, in the bistable regime. 87

4.2 Top view ($x - y$ plane) and front view ($x - z$ plane) of shape evolutions for a deformable sheet with $\mathrm{Ca} = 0.25$ and decreasing $\hat{K}_B$: (a) Taco ($\hat{K}_B = 5 \times 10^{-3}$), (b) S shape ($\hat{K}_B = 1 \times 10^{-3}$), (c) Heart ($\hat{K}_B = 3 \times 10^{-4}$), (d) Double S ($\hat{K}_B = 1 \times 10^{-4}$). 89

4.3 Velocity norm $||\mathbf{v}||$ on a slice (plane $x = 0$) through the steady states at $\mathrm{Ca} = 0.25$: (a) A flat sheet as at t = 0 in Fig. 4.2. (b) The taco shape in Fig. 4.2(a). (c) The S shape in Fig. 4.2(b). 91

4.4 (a) Transient stretched length evolution of different conformations in Figure 4.2 with fixed $\mathrm{Ca} = 0.25$. (b) Largest eigenvalue σ_1 evolution of the cases in Figure 4.4(a). 92

4.5 Convergence of unstable modes with numbers of iterations (n). 96

4.6 Top view of examples of deformation modes (added to the flat steady state) obtained from linear stability analysis. 97

4.7 Simulation results and linear stability analysis for a disk with neo-Hookean model ($c = 0$). The symbols represent the final conformation from numerical simulation, where the initial condition is a compact and flat sheet under random perturbation, except for the sheets above Ca_c. The color of the shaded region indicates the number of unstable modes obtained from linear stability analysis. 98

4.8 Top view and front view of evolutions of modes when they become unstable, with their short-term and long-term dynamics. (a) Taco and S with $\mathrm{Ca} = 0.2$, $\hat{K}_B = 3 \times 10^{-3}$. (b) M and double S with $\mathrm{Ca} = 0.2$, $\hat{K}_B = 1 \times 10^{-3}$. 99

4.9 Dynamics of a flexible sheet for $\mathrm{Ca} > \mathrm{Ca}_c$ for the neo-Hookean model ($c = 0$): $\mathrm{Ca} = 0.4$, $\hat{K}_B = 5 \times 10^{-4}$. (a) Evolution of length. (b) Snapshots of evolution. 100

4.10 Simulation results and linear stability analysis for a disk for parameters encompassing the bistable regime for the flat sheet ($c = 1 \times 10^{-5}$). The symbols represent the final conformation from numerical simulation, where the initial condition is a stretched and flat sheet under random perturbation. The boxed region indicated where an initially stretch state reverts to a compact state upon wrinkling. The color of the shaded region indicates the number of unstable modes obtained from linear stability analysis. 101

4.11 (a)-(d): Bifurcation diagram for a flexible disk ($c = 1 \times 10^{-5}$). For reference, the light blue data indicate results for a flat stiff sheet. The hollow data points show a wrinkled sheet and the filled points represent a flat state. (a) $\hat{K}_B = 5 \times 10^{-3}$. (b) $\hat{K}_B = 2 \times 10^{-3}$. (c) $\hat{K}_B = 1 \times 10^{-3}$. (d) $\hat{K}_B = 3 \times 10^{-4}$. Labels $\mathrm{Ca}_{c,w}$ or $\mathrm{Ca}_{s,w}$ denote critical capillary numbers for the wrinkled case. (e)-(l): Conformations at the points labeled e - l on the bifurcation diagrams. 103

5.1 Rest shape of interest: (a) A disk with a radius of a. (b) Rectangle-like sheets with long edge sized $2a$ and short edge sized $2a\omega$, with examples including a slender ribbon ($\omega = 0.2$), a rectangle ($\omega = 0.5$) and a square ($\omega = 1$) with increasing ω. (c) Illustration of the initial condition for a disk and a rectangle: the sheet lies inside the shear (flow-gradient) plane. 109

5.2 The image Stokeslet to solve a force density below a free surface. The free surface locates at the plane $z = 0$. A point force with strength $\mathbf{F}$ is located below the surface at $\mathbf{X}_i$. Its image force is located at $\mathbf{X}_i^{\mathrm{I}}$ above the surface. . 111

5.3 Illustration of deformation measurement based on a local coordinate centered by the disk center. The maximum and minimum z nodal positions are marked as $z_{\max}$ and $z_{\min}$, with a deformation amplitude defined as$\Delta z = |z_{\max}| + |z_{\min}|$. 112

5.4 Deformation amplitude Δz as a function of Ca for two sheets that show flapping and wiggling, separately. The decrease in Ca leads to a decrease in deformation amplitude while the dynamics converge qualitatively. 113

5.5 (a) Snapshots of a sheet with $\mathrm{E_V} = 5$ undergoing periodic 2D rolling motion. A red marker is placed on the edge to track the dynamics. (b) Steady-state trajectory of the marker. 114

5.6 (a) Snapshots of a disk with $\mathrm{E_V} = 38$ undergoing periodic flapping motion. A red marker is placed on the edge to track the dynamics. (b) Evolution of max ($z_{\max}$) and min ($z_{\min}$) deformation amplitude relative to the sheet center. The shaded area represents the dynamics from the snapshots. (c) Lagrangian trajectory of the marker focused by the sheet center during periodic flapping. 115

5.7 (a) Snapshots of a disk with $\mathrm{E_V} = 38$ undergoing symmetric wiggling motion. A red marker is placed on the edge to track the dynamics. (b) Evolution of max ($z_{\max}$) and min ($z_{\min}$) deformation amplitude relative to the sheet center. The shaded area represents the dynamics from the snapshots. (c) Lagrangian trajectory of the marker focused by the sheet center during periodic wiggling. 116

5.8 (a) Snapshots of a disk with $E_V = 25$ undergoing asymmetric wiggling motion. A red marker is placed on the edge to track the dynamics. (b) Evolution of max (z_{max}) and min (z_{min}) deformation amplitude relative to the sheet center. The shaded area represents the dynamics from the snapshots. (c) Lagrangian trajectory of the marker focused by the sheet center during wiggling. 117

5.9 (a) Snapshots of a disk with $E_V = 96$ reaching the flow-aligned state. (b) Evolution of max (z_{max}) and min (z_{min}) deformation amplitude relative to the sheet center. 118

5.10 (a) Bifurcation diagram of deformation amplitude out of shear plane $\Delta z = z_{max} - z_{min}$ vs. E_V from simulation. Snapshots indicate the final dynamics within the observation window. (b) Examples of unstable deformation modes (M1-M3) obtained from stability analysis. Modes are plotted with a random magnitude. Modes become unstable at $E_V = 22$ for mode 1, $E_V = 38$ for mode 2, and $E_V = 48$ for mode 3, with all E_V labeled in the bifurcation diagram. . 120

5.11 (a) Illustration of Floquet analysis. The black trajectory represents the periodic solution. Red and green trajectories represent an unstable and a stable perturbation, separately. (b) Convergence of eigenvalues (λ^L) with numbers of iterations (n). 30 Arnoldi iterations are sufficient for eigenvalues to converge. 121

5.12 (a) Experiment setup: the shear cell generates quasi 2D-shear flow. The inclined laser sheet shines on the disk. The intersection of the laser sheet with the disk measures the local height of the disk with a view from the top (z vorticity direction) and out-of-shear-plane deformation can be extracted. (b) An example of curvature measurement extracted from the laser line on the sheet. 122

5.13 (a) Experiment and simulation snapshots for $E_V = 47$ show flapping. The laser line indicates the height of the sheet along the vorticity z direction and the curvature κ along the laser slice can be extracted from the curvature of the laser line. $\dot{\gamma}t = 0$ is the disk at equilibrium. Simulation snapshots for $E_V = 47$ show flapping with three views. The 3D view provides a direct view of flapping dynamics. The flow-gradient (xy) plane view shows a heat plot measuring the deformation amplitude out of the shear plane at the sheet center with an interface with an inclined plane (gray line) to mimic the laser sheet in the experiment. The gradient-vorticity (yz) plane view illustrates the sheet deformation along the slice defined by the laser line. (b) Comparison of curvature κ evolution on the sheet between experiment and simulation from (Fig 5.13(a)). The alternating sign of κ indicates the sheet flaps up and down away from the shear plane. (c) Evolution of κ_{max} vs. E_V showing flapping regime in experiment: $E_V = 24 - 59$, and in simulation: $E_V = 14 - 64$. Snapshots show flapping sheets observed in experiments. 124

5.14 Snapshots of a disk ($E_V = 4$) initially inside the shear plane at $z_0 = -0.5$ below the free surface, with colored plots indicating z position of the sheet relative to the sheet center. The grey layer represents the free surface located at $z = 0$. The disk forms a stable taco shape migrating away from the free surface. (b) Evolution of max ($z_{\max}$) and min ($z_{\min}$) deformation amplitude relative to the sheet center. The shaded area represents the dynamics from the snapshots. (c) Evolution of distance away from the free surface z. 126

5.15 (a) Snapshots of a disk ($E_V = 50$) initially inside the shear plane at $z_0 = -0.5$ below the free surface, with colored plots indicating z position of the sheet relative to the sheet center. The grey layer represents the free surface located at $z = 0$. (b) Evolution of max (z_{max}) and min (z_{min}) deformation amplitude relative to the sheet center. The shaded area represents the dynamics from the snapshots. (c) Evolution of distance away from the free surface z. 128

5.16 (a) The dominant unstable mode obtained from linear stability analysis for a flat sheet rolling at the plane $z = -1$ under a free surface at $z = 0$. (b) Comparison of curvature κ evolution on the sheet between experiment (Fig 5.13(a)) and free surface simulation for $E_V = 47$. The alternating sign of κ indicates the sheet flaps up and down away from the shear plane. 129

5.17 Phase diagram of dynamics at different height (z) below the free surface ($z = 0$). All sheets are initially located at the plane $z_0 = -0.5$. The markers represent the dynamics of the sheet at the corresponding z. 130

5.18 Snapshots of a rectangle tumbling in shear flow with increasing E_V. The long edge of the rectangle aligns with $x - y$ plane and is initially oriented 10° from the flow direction. (a) A stiff sheet shows no buckling with $E_V = 1$. (b) A flexible sheet shows C-shape buckling with $E_V = 5$. (c) A flexible sheet shows S-shape buckling with $E_V = 25$. 131

5.19 (a) Evolution of wrinkling parameter B on the sheet for three cases from Fig 5.18. A-C are snapshots of the most wrinkled states at $t = 5.5$. (b) Evolution of buckling state for sheets with different E_V. The color scales the extent of buckling $E_b^\star$ and the markers indicate the snapshots A-C. The buckling threshold is estimated to be $E_V^C \sim 1$. 132

5.20 (a) Snapshots of transient evolution of a sheet with $\omega = 0.2$ and$E_V = 13$. (b) Evolution of max (z_{max}) and min (z_{min}) deformation amplitude relative to the sheet center. (c) The transient Lagrangian trajectory of the marker. 133

5.21 (a) Snapshots of periodic flapping motion for $\omega = 0.5$ and $E_V = 8$. (b) Evolution of deformation amplitude z_{max} and z_{min} relative to the center of the sheet. The shaded area indicates the snapshot in (a). (c) The Lagrangian trajectory (based on the sheet center) of the marker after reaching the steady state. 134

5.22 (a) Snapshots of symmetric swirling motion for $\omega = 1$ and $E_V = 7$. (b) Evolution of deformation amplitude z_{max} and z_{min} relative to the center of the sheet. The shaded area indicates the snapshot in (a). (c) The Lagrangian trajectory (based on the sheet center) of the marker after reaching the steady state. 135

5.23 (a) Snapshots of asymmetric swirling motion for $\omega = 1$ and $E_V = 13$. (b) Evolution of deformation amplitude z_{max} and z_{min} relative to the center of the sheet. The shaded area indicates the snapshot in (a). (c) The Lagrangian trajectory (based on the sheet center) of the marker after reaching the steady state. 136

5.24 Phase diagram for a rectangle sheet with different ω and stiffness E_V in free space: (a) Rectangle with $\omega = 0.5$. (b) Square with $\omega = 1$. Markers represent the steady state dynamics. 137

5.25 Phase diagram for a rectangle sheet with different ω and stiffness E_V in free space. Markers represent the steady state dynamics. 138

5.26 Buckling threshold E_V^C as a function of sheet size ω for a rectangle sheet initially inside the shear plane. 139

6.1 Illustration of a square sheet sedimenting next to a tilted wall. The case shows the sheet with initial wall-normal distance $d_0 = 1.5$ is oriented $\phi = 90°$ and the titled wall angle is $\alpha = 30°$. 147

6.2 Snapshots of a square sheet sedimenting in free space with $\phi = 90°$. (a) Flat ($E_G = 1$). (b) Convex taco ($E_G = 8$). (c) Concave taco ($E_G = 40$). (d) Complex ($E_G = 198$). A-D represent the final steady conformation. Snapshots only show the conformation evolution without actual sedimenting distance. . 155

6.3 Characterization of sedimentation dynamics. A-D are steady conformations shown in Fig 6.2 representing four distinct regimes. (a) Evolution of wrinkling parameter B on the sheet vs. E_G. (b) Terminal velocity v_{sed} vs. E_G. (c) The transition of conformations between regime B and regime C is shown as the evolution of folded and relaxed edges. 156

6.4 Influence of initial orientation ϕ and E_G on the sheet reorientation dynamics: (a) Transient evolution of buckling on the sheet for $E_G = 8$ with different initial orientation ϕ. (b) Transient evolution of lateral drift distance d on the sheet for $E_G = 8$ with different initial orientation ϕ. The maximum drift distance is denoted d_{max}. (c) Maximum lateral distance d_{max} for sheets with different E_G. (d) Illustration of two types of reorientation dynamics: rotating ($E_G = 4$) and bending ($E_G = 13$) from selected cases in Fig 6.4c. The sheet is initially oriented as $\phi = 0°$ subject to small and random perturbations. . . 158

6.5 (a) Snapshots of dynamics near a vertical wall with initial orientation $\phi = 90°$ and $d_0 = 1.5$. Case A, $E_G = 8$: the sheet directly migrates away from the wall. Case B, $E_G = 28$: the sheet first migrates toward the wall and becomes trapped. Case C, $E_G = 40$: the sheet first migrates toward the wall and then reorient to escape. The transient migration distance away from the wall is denoted d. Each case has its steady free space conformation for comparison. (b) Transient evolution of migration distance d for three sheets in Fig 6.5(a). (c) Temporal evolution of migration distance d for sheets with different E_G, with labels indicating cases shown in Fig 6.5(a). 160

6.6 Comparison of wall-normal distance evolution for case A ($E_G = 8$) in Fig 6.5(a) by a fitting equation $d = (3kt + {d_0}^3)^{1/3}$ with $k = 0.085$ and $d_0 = 1.5$. We consider the dynamics for $t < 100$ to be governed by near-wall effects. . . 163

6.7 (a) Snapshots of dynamics near a tilted wall ($\alpha = 30°$) with initial orientation $\phi = 90°$: Case A. $E_G = 1$: the sheet deposits on the wall. Case B. $E_G = 40$: the sheet initially close to the wall ($d_0 = 1.5$) reaches a steady conformation and slides along the wall. Case C. $E_G = 40$: the sheet initially far from the wall ($d_0 = 3$) folds and rolls along the wall. (b) Shape evolution of steady sliding sheets with increasing E_G. (c) Transient evolution of wall-normal distance d for cases shown in Fig 6.7(a). (d) Steady wall-normal distance d_s for sheets next to a tilted wall with $\alpha = 30°$. 164

6.8 (a) Phase diagram for E_G vs. α. Symbols represent the sheet dynamics. (b)Steady wall-normal distance d_s for sliding sheets (boxed region in Fig 6.8(a)) with different E_G and α. 166

7.1 Implementation of artificial torque to account for finite thickness h: $\mathbf{n}$ is normal to the upper surface and $\mathbf{s}$ is the surface traction. Index t indicates top surface and b for the bottom. $\mathbf{t}$ is a directional vector along the traction. 172

7.2 (a) Simplified spring system with every node connected directly to the node on the other surface. (b) Improved spring system with every node connected to the corresponding node and its one-ring neighbor nodes on the other surface. (c)Example of tumbling flexible sheets with the top surface and bottom surface connected by the simple spring system in (a). 173

7.3 (a) Snapshots of two tumbling sheets with $E_V \sim 30$ (estimated) showing deformation from experiments in [133]. (b) Snapshots of two tumbling disks with $E_V = 8$. (c) Snapshots of two tumbling disks with $E_V = 4$. 176

7.4 (a) Comparison of swimming distance Δ based on actuation frequency ω. Larger ω results in faster swimming. (b) Comparison of swimming distance Δ based on sheet flexibility. More flexible sheet results in faster swimming. . 177

7.5 Examples of two sheets with van der Waals interactions: (a) Two sheets successfully exfoliate. (b) Two sheets fail to exfoliate. (c) Evolution of the averaged inter-layer distance $< d >$ for the exfoliated case in Fig 7.5(a). (d) Evolution of the averaged inter-layer distance $< d >$ for the unexfoliated case in Fig 7.5(b). 178

7.6 (a) The schematic of a self-propelled sheet with a surrounded patch. Red color is the alignment of cells. θ is the angle between node-to-node displacement and contraction force. (b) The schematic of induced moments generated by cell contraction. d is the node-to-node distance. 180

7.7 Comparison of swimming distance Δ based on alignments of cardiomyocytes: alignment along the centerline and alignment close to the edge. 181

7.8 (a) Comparison of swimming distance Δ based on actuation frequency ω. Larger ω results in faster swimming. (b) Comparison of swimming distance Δ based on sheet flexibility. More flexible sheet results in faster swimming. . 181

7.9 (a) Illustration of fiber conformation. (b) Measurement of bending stiffness K_B by bending a fiber with a fixed curvature κ. (c) Illustration of fiber orientations in shear flow. (d) Comparison of angle ϕ for a tumbling rigid fiber with analytical Jeffery orbit solutions. 183

7.10 Evolution of angle θ for a fiber with different aspect ratios and flexibility tested with various initial orientations. 185

8.1 Overview of code structure. 186

8.2 Code structure for initialization. 188

8.3 Code structure for the iterative process. 191

1

General introduction

In this thesis, our primary objective is to develop a systematic framework to understand the dynamics of elastic sheets in Stokes flow. Elastic sheets, which are thin plate-like particles with a small thickness compared to the other two lateral dimensions, exhibit intricate stretching, buckling, and wrinkling behaviors in response to stresses. In recent decades, a number of novel materials emerge with geometry and mechanical property similar to elastic sheets, such as graphene and other two-dimensional materials.

Thin-structured materials play an important role in various disciplines and their small size makes them easily processable in fluids. As a result, the suspension of sheets commonly appears in different stages of the synthesis and fabrication processes. Given the small size of the sheets in those applications, we assume the particle Reynolds number, defined as the inertia of the fluid at the length scale of the sheet size, is negligible compared to the viscous effect of the flow: $\mathrm{Re_p} = \rho\dot{\varepsilon}a^2/\eta \ll 1$, where ρ is the fluid density, $\dot{\varepsilon}$ is the flow strain rate, a is the particle size and η is the fluid viscosity. This assumption leads to the description of fluid motion as Stokes flow, where inertia is considered negligible.

Despite the growing use and fabrication of thin sheets, there remains a lack of fundamental understanding regarding the behavior of elastic sheets in Stokes flow. On the other hand, our extensive knowledge of other soft particles suggests that the dynamics of elastic sheets are likely to be rich and intricate. These facts serve as strong motivations to explore the

dynamics of elastic sheets in Stokes flow and develop a fundamental framework that can form the basis for understanding more complex flow processing applications.

In Section 1.1, we present an overview of the applications involving thin sheets that are freely suspended in flow. Specifically, we explore their role in the synthesis of 2D materials and polymer films, as well as their involvement in self-assembly processes and active swimming devices. These diverse applications serve as strong motivations to delve into the dynamics of these sheets. Moving on to Section 1.2, we conduct a comprehensive review of the existing literature focused on elastic sheets in Stokes flow. Through this review, we emphasize the persisting gap in fundamental understanding when it comes to sheet dynamics. Section 1.3 expands our examination to encompass the dynamics of other soft particles. By drawing upon the extensive studies conducted on flexible fibers and capsules, we aim to leverage this existing knowledge to gain insights into the behavior of elastic sheets. To establish a solid foundation for our subsequent findings, Section 1.4 introduces the basic concepts of Stokes flow. This understanding of fundamental principles will prove essential in comprehending the results that follow. Finally, in Section 1.5, we provide an outline of the subsequent chapters to provide an overview of the thesis structure.

1.1 Thin elastic sheets processed in fluid

1.1.1 Applications of thin sheets

Synthesis of two-dimensional materials and polymer films

Two-dimensional (2D) materials are thin elastic sheets on the sub-microscale and have gained significant attention across various disciplines. The small size of 2D materials makes them easier to process in a fluidic environment. Consequently, the suspension of 2D sheets exposed to external flow fields is frequently observed during the synthesis and processing stages [6, 58, 92, 179, 185, 197, 200]. Typical examples of 2D material are the family of graphene which include graphene and its derivatives, such as graphene oxide (GO), reduced

graphene oxide (rGO), graphite, and their composites. Besides the graphene family, another class of 2D material includes transition metal dichalcogenides (TMDs, a layer of metal atoms and two layers of chalcogen atoms, such as WS_2 and Mo_S2), and other 2D compounds like BN [25]. Those 2D materials as single monolayers, or a small number of stacked sheets, are often called nanosheets, where nano refers to the thin nature of sheets at the nanoscale. The unique structure of nanosheets with atomic thickness offers them excellent physical and chemical properties.

In general, monolayers of graphene are hard to obtain because they naturally exist in the form of layered materials, which are defined as stacks of sheets with strong in-plane chemical bonds and are sustained by weak out-of-plane van der Waals interactions [100, 125]. The layered materials, like graphite, can be sheared to yield monolayer graphene and this process is called exfoliation. Actually, when graphene was first introduced by Geim and Novosolov, they applied an adhesive tape to exfoliate graphite to obtain an atomically thin monolayer of graphene [127]. The synthetic approaches of nanosheets can be summarized in two main routes: vapor-based and solution-based. The vapor-based approach applies a carrier gas to transport the nanoparticles in the vapor phase from a heated solution to a substrate downstream where nanosheets can be collected [33, 72, 86]. This approach fosters the sheets to grow on the substrate and is not the interest of this work. In contrast, the solution-based approach gives a high yield of nanosheets and can achieve large-scale production which benefits industrial processing.

Typically, liquid-phase exfoliation is a solution-based technique to obtain monolayer sheets from layered materials. The layered materials initially dispersed in solutions are exfoliated by weakening interlayer forces, such that layers are separated from each other to create a suspension of freely suspended nanosheets [25, 125]. There are three main categories of liquid-phase exfoliation. The ion intercalation approach and ion exchange approach both weaken the inter-layer van der Waals interaction by inserting ions or replacing ions with different charges for materials with ions between layers, followed by mechanical agitation such

as shear and ultrasonication to result in a suspension of exfoliated sheets. The sonication-assisted approach directly applies strong mechanical agitation and exfoliation depends on the type of solvents. In good solvents, exfoliated sheets are stabilized without reaggregation while in poor solvents monolayers reaggregate. In all approaches, the sheets experience high local shear to be exfoliated by the flow and involve complex fluid-structure interactions that are not fully understood. AlAmer *et al.* improved the bulk-scale production of exfoliation

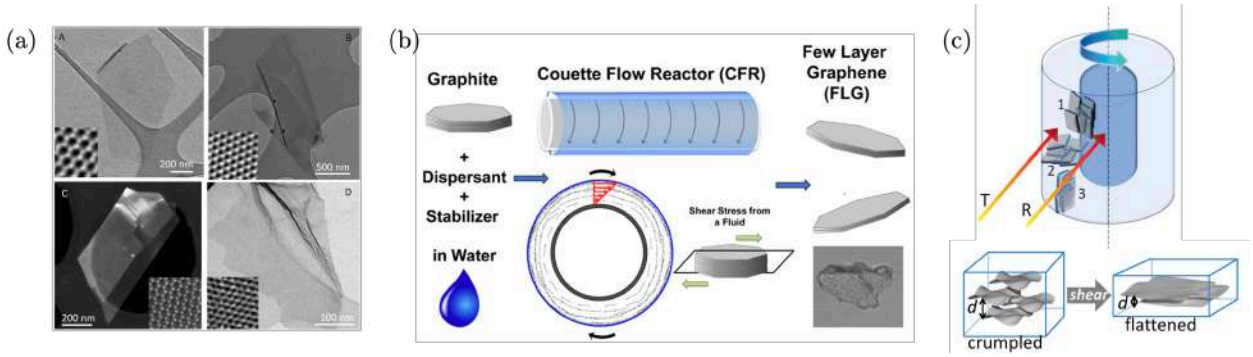


Figure 1.1: (a) Examples of elastic sheets obtained from liquid-phase exfoliation. (b) Synthetic process of graphene based on a Couette flow reactor from [4]. (c) The suspension of graphene oxide shows different potential orientations in a Taylor-Couette reactor with an illustration of shear-induced flattening of sheets from [135].

by applying a continuous flow reactor, where they use a Taylor-Couette reactor (TCR) to generate a high shear environment to obtain a mixture of expandable graphite and few-layer graphene [3, 4]. The reactor consists of two coaxial cylinders. Some applications make the inner cylinder rotate and the outer cylinder still, which can generate toroidal vortices that can improve the mixing of solutions [167]. Here, they make the inner cylinder still while the outer cylinder is still to alleviate vortex formation due to the decrease in centrifugal forces acting on the mixture. They showed that a still inner cylinder can maintain continuous and laminar Couette flow and results in a structurally uniform product with a larger lateral dimension.

The liquid-phase exfoliation usually results in a suspension of layered sheets, making it important to understand the rheology of sheet suspension. Graphene oxide (GO), as the precursor of graphene-based materials, has a very large Young's modulus but is super flexible.

Poulin *et al.* studied the orientation of GO in suspension with a combination of synchrotron X-ray diffraction at small angles and in situ rheology (rheo-SAXS) in a Taylor–Couette shear cell [135]. They found the suspension of GO shows shear-thinning behavior, and the alignment of GO sheets varies with the shear rate. At a higher shear rate, GO sheets align with the flow direction as the shear-induced flattening, and the spacing between GO sheets decreases because strong shear stress suppresses undulations due to thermal fluctuations.

The processing of 2D materials often incorporates complex flow fields. Recently, graphene sheets are found to be a useful tool to help fuse silicon nanoparticles into carbon nanofiber. The silicon/graphene nanocomposites are prepared by wrapping and folding graphene sheets and the incorporation of nanocomposites helps improve the conductivity and mechanical stability of the fiber [66, 74, 75, 77, 193]. Among many techniques to process the composites, solution-based electrospinning has many advantages to processing the silicon/graphene nanocomposites as it is easy to control product quality, environmentally friendly, and high yield for large-scale production [44, 74, 188]. The synthesis is achieved by ejecting a jet of charged polymer solutions via a high-voltage electric field where the jet is stretched and elongated to generate fiber, which dries in the air and is collected on a substrate [189]. Fei *et al.* demonstrated a robust electrospinning setup [44]: graphene or its precursor GO and silicon nanoparticles are dispersed in a polymer solution and pass a small syringe tube under an electric field. The high voltage field stretches the corner of the graphene sheet and incorporates the micro-sized sheet into the fiber structure. The fiber is then thermally treated and graphene composites are nicely folded and wrapped on the fiber surface.

Besides graphene and transition metal films, other important thin structured materials including 2D polymer networks and clays also show many scenarios where sheets are processed in suspension under external flows. The synthesis of polymer sheets often involves the polymerization of monomers in solution, where 2D macromolecules can grow either by step-growth or chain-growth mechanism, resulting in a suspension of clustered materials [131]. Efforts are made to control and restrict the polymerization to remain in 2D without gen-

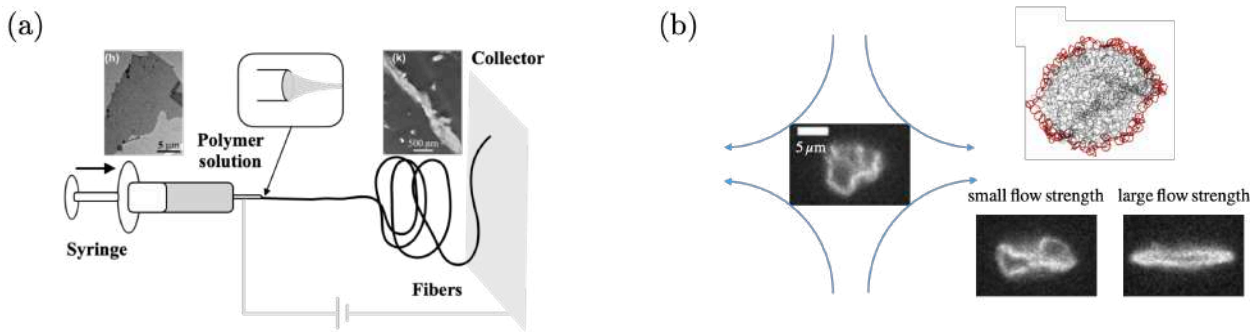


Figure 1.2: (a) The synthesis of graphene-incorporated carbon nanofibers via water-based electrospinning from [44]. The GO sheets mixed with polymer solutions are folded when the solution is ejected from the syringe tip through a high-voltage electric field. (b) Deformation response of a kinetoplast DNA network exposed to planar extensional flow from [57, 164].

erating a 3D random network. One common approach is to construct a pre-organized 2D confined space like an interface [36, 131]. Some early works have explored the potential to synthesize polymer sheets in a confined space created by the liquid-liquid or liquid-gas interfaces [34, 95, 105, 139, 145]. Apart from the interfacial assembly, several works have highlighted the potential to obtain 2D polymer sheets simply in solutions. For example, Baek and coworkers developed a solution-based synthetic technique that can obtain free-standing, single-monomer-thick 2D polymer without relying on any solid substrate or interface [7]. They leveraged the lateral cross-linking of rigid and disk-shaped monomers that have multiple in-plane reactive sites that can engender the predominant lateral growth of the polymer. Later, Kory *et al.* demonstrated the feasibility of photochemically converting certain single crystals of monomers into chiral 2D crystals, and resulting 2D polymer crystals can be exfoliated in solution to get sheets with nanometer thickness [78].

In addition, recently a novel two-dimensional DNA network has gained considerable attention. A Kinetoplast naturally exists in the mitochondria of parasites and is made of thousands of DNA loops that interconnect together to form a 2D catenated network [57, 101, 153]. Klotza *et al.* studied the deformation response of a complex DNA structure called a kinetoplast in extensional flow. They probed the physics of this 2D polymer at equilibrium [76]. Soh and Doyle examined the deformation response of a single kinetoplast sheet under a

planar extensional flow and showed a stagewise transition in conformation determined by strains [164].

Self-assembly and active sheets

It has been a long interest to assemble 3D shapes from 2D planar precursors, such as thin polymeric sheets. The advantages of this strategy include the fact that 2D polymer sheets can achieve high-throughput production at a relatively low cost and the planar nature of sheets ease storage and transport. Liu *et al.* categorizes the shaping of 2D sheets based on different strategies applied [99]. One strategy is conventional fabrication that applies additive or subtractive to create topology on the 2D substrate. This strategy is widely used in lithography in the production of electronics by exposing polymer film to UV light, X-ray, or photosynthesis to directly change surface patterns [22, 113, 183], which is not the focus of this work. The rest of the strategies all leverage the chemical or mechanical nature of the sheets, such as generating wrinkling or buckling patterns in response to internal stresses or external stimuli, applying creases and hinges to achieve out-of-plane folding, and so on.

The flexibility of 2D materials allows a new strategy to obtain novel materials by the self-assembly of 2D sheets. Nanoscroll is a special 1D structure that is formed by rolling 2D sheets [61, 83, 171]. The rolling up of sheets can be triggered simply via sonication in flow [174], organic solvent-assisted lyophilization where the dispersed sheets absorb the organic solvent and the imbalanced surface tension from two sides of the sheet drives the sheet to roll up [61], a nanowire-templated assisted assembly where a fast formation of nanowire guides the rolling of sheets [191], and so on. The assembly allows the scroll to inherit most of the unique properties of 2D sheets while exhibiting new characteristics arising from 1D morphology. For example, a 1D graphene scroll shows similar mechanical properties and conductivity compared to its precursor as a 2D graphene sheet [176]. On the other hand, polymer networks like hydrogel can be engineered in response to external stimuli to develop a 3D structure. Py *et al.* [137] induced the folding of a triangular elastic polydimethylsiloxane (PDMS) sheet with a liquid droplet. The surface tension drives the sheet to wrap the droplet

and forms a pyramid as a result of the interaction between elastic and capillary forces. Wu and coworkers developed a programmable hydrogel sheet with periodic stripes of different materials. The sheet can reversibly form a ribbon-like structure by switching the environment in sodium chloride solution and deionized water [182].

The art of origami has inspired plenty of designs and structures which involve intriguing folding dynamics of a sheet. The idea of generating a well-developed shape from a planar sheet-like precursor has been applied in the fabrication of microsized origami-inspired devices. Many origami-inspired structures are assembled from a planar sheet, with the presence of creases and hinge to guide the folding. Due to the small manufacturing size, they are assembled in a fluid. So *et al.* [162] developed a sequential and reversible self-folding box based on gel hinges made of different polymers. The hinges swell in the ionic liquid at different temperatures to achieve reversible and sequential folding. When it comes to a more complicated structure, Leong *et al.* [90] assembled a microstructure container, which can fold in different directions controlled by the internal stress generated from a thermally sensitive hinge made of metallic alloy in solution.

Many recent studies and advances in soft materials have revealed the possibility to fabricate an active swimming device for applications in drug delivery, disease diagnosis, and non-invasive surgical operations. Those applications are inspired by the locomotion of microorganisms with a small scale in micrometers, where the inertia and Reynolds numbers are negligible [84]. Bacteria such as Escherichia coli and Salmonella typhimurium, leverage flagellum propelled by the cell body to achieve locomotion [165]. Here, locomotion is driven by coordinated movements of cellular motors, which are integrated to produce a macroscopic contractile force for propulsion [140]. For a larger swimmer like a stingray fish, it swims with its paired pectoral fins near the sea bed like a giant swimming sheet, where the bending of bones and muscles generates propagative waves to sustain the locomotion. It is worth noting that larger organisms like some fish and birds are swimming under high Reynolds numbers. Their swimming strategies are ineffective under Stokes flow conditions due to large viscous

damping [84].

Inspired by those biological systems, there emerge many studies of active devices, and some of those are based on prototypes of swimming sheets. There are some examples where the motion of sheets is purely sustained and guided by external magnetic or electric fields without biological power sources. For example, Zhang *et al.* manufactured a thin micro helical ribbon with a squared head. The head is made of metal alloy stacked thin film and can be controlled wirelessly by the rotating magnetic field [198]. They found a linear relationship between the magnetic field frequency and the swimming velocity. In contrast, another group of swimming sheets harnesses the power as well as the actuation from biological tissues, as biohybrid swimmers. The biohybrid swimmer is a combination of engineered artificial substrates and living bio-systems: the synthesized polymer substrate or metallic film, is combined with biological tissues to generate a biohybrid device that can self-propel to swim in complex domains [140, 181]. Common biological actuation includes the cells that show consistent contraction. The cardiac muscle cell, or cardiomyocyte, is a commonly used bio-actuator. A single cardiomyocyte generates forces in response to the mechanical deformation in the environment and the beating frequency can be trained and tuned [126]. Multiple cells in the same environment will communicate and synchronize, making it possible to generate a stable and tunable contractile force. One example is an active filament developed by Williams *et al.* that combines cardiomyocytes with a polydimethylsiloxane (PDMS) filament [181]. The cell generates periodic contractions, which causes the filament to form a bending wave that propagates and produces net propulsion to sustain the swimming. When it comes to a sheet-like swimmer, Feinberg *et al.* [45] engineered two triangular muscular thin films with different distributions of cardiomyocytes. The anisotropic sheet has the axial alignment of cells and the isotropic sheet has an even distribution. Under stimulation from the electric field, the anisotropic sheet swims five times faster than the isotropic case as the isotropic sheet fails to generate net propulsion. Nawroth *et al.* [118] designed a sheet with cultured muscle tissues synchronized by an electrical field to study the stroke swimming of a jellyfish.

Park *et al.* [130] developed an artificial swimmer by multilayer assembly of elastomer and metallic films to study the locomotion of a ray. The swimmer powered by cardiomyocytes achieves coordinated undulatory swimming under optical stimulation.

1.1.2 Current studies of elastic sheets in flow

Though we lack knowledge of the dynamics of elastic sheets in fluids, there has been increased attention to freely suspended sheets in recent years. Here, we provide an in-depth review of the recent works related to elastic sheets in Stokes flow. Apart from the zero Re regime, there exists a number of works to investigate a flapping flag in a laminar or turbulent flow. Those interesting studies are important to understand many applications such as fish swimming. However, they are not the interest of this work as we focus on sheets in zero Re flow.

Due to booming applications in 2D material, most of the recent studies address the sheets in shear flow, from a single to a pair of sheets [150] and suspensions [107, 108]. The dynamics of a freely suspended flexible sheet were first tackled by Leong [89]. The author studied a graphene nanosheet rotating in simple shear flow modeled with molecular dynamics simulation and reported characteristic bending modes during tumbling. Later, Xu and Green examined the shear-induced deformation of nanosheets using a bead-rod model with thermal fluctuation formulation, where Brownian particles are connected with four neighbors to form a 2D lattice network [186]. They characterized a cyclic crumple-stretch-crumple motion for a flexible sheet and found the flow exhibits weak shear thinning behavior.

Later, inspired by the idea of flow-induced assembly and the art of origami, Dutta and Graham studied piecewise rigid creased non-Brownian sheets in shear flow [39]. The creases act like hinges to tessellate the sheet into an array of parallelograms known as Miura-pattern, where the folded state can be described by a single-fold angle. They modeled a single unit in simple shear flow and ignore hydrodynamic interactions between sheet pieces. Depending on initial conditions, the rigid Sheets either approached a steady, periodic, or quasi-periodic state. Recently, Silmore and coworkers studied a semiflexible hexagon sheet in simple shear

flow. The sheet is modeled based on a bead-spring model with a strong stiffness constant that highly constrains in-plane deformations and the fluid motion is solved by Rotne–Prager–Yamakawa (RPY) method. They probed both a non-Brownian sheet [156] and a Brownian sheet [157] with different initial conditions. For non-Brownian sheets, they identified the transition from a quasi-Jeffery-like tumbling to continuous chaotic tumbling with increasing bending stiffness, with a global attractor for semiflexible sheets to arrive at a flow-aligned state in the flow-vorticity plane. They also predicted the transient buckling dynamics for a tumbling sheet with a simple 1D elasticity model where the results match well with their 3D simulations. The transient buckling of a tumbling elastic sheet is also examined by Salussolia *et al.* with a 2D line-integral approach. They identified a buckling threshold that is within an order of magnitude compared to Silmore *et al.* [150]. For Brownian sheets, Silmore *et al.* found that thermal fluctuation expands the dynamics by overcoming the flow-aligned state in the non-Brownian sheet. They characterized a dynamical transition for increasing flexibility from stochastic flipping to crumpling and continuous tumbling. Furthermore, they examined the effect of dynamics on the macroscopic rheological properties, where the dilute suspension of Brownian sheets shows shear-thinning behavior, similar to what has been observed in graphene oxide suspension [135]. However, they noticed the solution becomes shear-thickening when the sheet is very flexible and undergoes dynamical crumpling. In a recent experimental study, Perrin and coworkers investigated the critical shear rate required to generate wrinkling for a rectangle sheet in shear flow [133]. They also developed a 2D sheet model with dynamics resolved by the regularized Stokes method. Their numerical results show good agreement in the buckling threshold obtained from experiments.

When considering nanosheets like graphene immersed in a fluid, the interfacial effects are complicated due to the atomically smooth nature of the sheet surface. For example, a relatively large particle immersed in fluid satisfies the classic no-slip boundary condition, where the fluid moves along the material point on the sheet at the same location. However, for a nanosheet, the fluid molecule may slip on the solid sheet surface, with a slip length

termed by the distance within the solid that fluid velocity is extrapolated to zero. Kamal *et al.* probed into this phenomenon with molecular dynamic simulation and a continuum model to simulate a rigid nanoplatelet freely suspended in shear [67]. They found the effect of hydrodynamic slip allows the rigid platelet to attain a stable steady orientation with a fixed angle with respect to flow. In a subsequent study, they found strong thermal fluctuation can break the alignment of the rigid sheet due to hydrodynamic slip [69]. In addition, they extended the study of hydrodynamic slip to a flexible and non-Brownian sheet in shear flow [68]. The flexible sheet is modeled in 2D and is based on a coupled Euler-Bernoulli beam theory and boundary integral formulation to solve for hydrodynamic traction acting on the sheet surface. They showed that slip-induced alignment occurs even for flexible sheets and gave a detailed analysis of the edge effects.

Beyond a single sheet in shear flow, the synthesis and processing of nanosheets often yield a suspension of sheets-like particles. The lacking of knowledge in sheet suspension motivates works related to particle-particle interactions and the rheology of sheet suspension. Salussolia *et al.* extended their 2D sheet model to study pairs of interacting sheets and observed hydrodynamic-induced parallel sliding or bending depending on sheet flexibility [150]. Moreover, they found that sufficiently flexible pairs of sheets under strong shear flow may reattach after separation. In a recent study, Perrin *et al.* applied theory and experiments to probe into the buckling of multiple sheets in shear flow [133]. They observed the presence of a second parallel sheets can largely decrease the critical shear rate required to trigger buckling compared to a single sheet. This effect is due to the hydrodynamic forces caused by the perturbation flow field from the neighboring sheet. Meng and Higdon explored the suspension of non-Brownian [107] and Brownian [108] plate-like particles in a linear shear flow where the plates with different aspect ratios are modeled as planar assemblages of spheres and hydrodynamics are resolved based on the Stokesian dynamics. In a non-Brownian suspension, the plates show a high degree of alignment with the flow direction at a low volume fraction. At a high volume fraction, increased hydrodynamic interactions due to dense sus-

pension make plates align in the flow-vorticity plane, along with transient stacking of plates. In a Brownian suspension, the stacking of plates is disrupted with increasing thermal fluctuation, which yields random particle orientations. They found the suspension exhibits both shear thinning and shear thickening determined by the interplay between thermal effects and particle alignment.

As reviewed in the previous section, liquid-phase exfoliation is a powerful technique that uses a shear flow to produce few-layer nanosheets from layered materials. Several recent studies have explored the controlling of exfoliation at microscale and nanoscale [14, 51, 88, 149]. Lee and Carignano tackled the exfoliation by performing molecular dynamic simulations to explore the propylene carbonate as an electrolyte to induce the exfoliation of graphite [88]. The electrolyte intercalates graphene sheets and facilitates the separation of layered materials. Salussolia *et al.* proposed a 2D hydrodynamic peeling model to describe the microscopic flow-induced exfoliation process, where layers of sheets are removed in a layer-by-layer manner from the freely suspended substrate in shear flow [149]. Gravelle *et al.* performed a non-equilibrium molecular dynamics simulation of a freely suspended graphite particle in a wall-bounded shear flow [51]. The graphite particle is modeled as a stack of graphene layers. They tested different solvents and extracted a critical shear rate above which the exfoliation can occur. Additionally, Venkatesh and coworkers [173] recently explored the peeling dynamics of two Hookean sheets in a non-Newtonian fluid.

While the aforementioned works all focus on the shear flow, little attention has been paid to investigating the sheet dynamics in the extensional flow. Park and coworkers investigated the rheological behaviors of the suspension of three layered silicate composites under uniaxial extensional flow. With two-dimensional, small-angle X-ray scattering and transmission electron microscopy, they found the layered materials own a preferred orientation as aligning with the flow direction. Xu and Green utilized the previous model in shear flow [186] to investigate the sheet morphology in biaxial extensional flow [187]. They found the sheets with large bending stiffness stayed flat while sheets with small stiffness crumpled as a re-

sult of Brownian fluctuations. Dutta and Graham presented the teaser in their shear flow work [39] to adapt their hinged sheet model to simulate a waterbomb-based origami sheet in uniaxial extensional flow. Their preliminary results showed the compressive stress from the extensional flow folds the sheet with complex dynamics based on initial conditions.

Finally, some recent efforts have been made to explore the swimming of an active sheet. The early analysis of a swimming sheet was done by Taylor back in 1951, who studied an infinite 2D sheet immersed in a viscous fluid and propelled by the transversal displacement from a traveling wave [168]. Recently, several works have explored the potential swimming strategy by inducing traveling waves on a sheet-like particle with finite size. Montenegro-Johnson and coworkers developed a model to simulate elastic ribbons with a boundary element method coupled with regularized Stokes [111]. They investigated the swimming of a microscale "magic carpet" as a ribbon sheet with prescribed waves to propel swimming. They found an increase in the sheet width decreases the swimming speed. Though the increase in width leads to a larger surface area that brings more propulsive forces. However, the increase in drag due to the larger surface area is much faster than the propulsive forces such that the sheet swims slower. Corsi *et al.* modeled a neutrally buoyant and pre-stressed circular shell subject to traveling waves and rotating in a viscous fluid [26]. They applied a geometrically nonlinear finite-element model to account for large deformation due to the traveling wave, which generates counter-rotating vortices that propel the rotation of the shell. Recently, they extended the study to numerically simulate a 3D homogeneous magnetoelastic sheet at low Reynolds numbers with the lattice Boltzmann approach [16]. Using a magnetic field to generate a rotational wave, they break the morphological symmetry of a hexagon sheet and achieve nonreciprocal motions.

1.2 Dynamics of soft particles in Stokes flow

In the previous section, we introduce many applications related to the processing of thin elastic sheets in various flow conditions. Though little is known about elastic sheets in fluid, other soft particles such as fiber, capsules, and vesicles, have been extensively explored in the past decades, which help us gain insights into elastic sheets. The high similarities between soft elastic sheets and other soft particles imply the dynamics of sheets will be rich in flow. Typically, fibers like deformable sheets, show buckling instabilities under compressive stresses along with complex motions in flows.

Here, we begin with an introduction to different linear flow fields. We then review the dynamics of soft particles in Stokes flow, with a primary focus on fibers and filaments. In extensional flow, we focus on a phenomenon of coil-stretch transition observed in long-chain polymers. In shear flow, we introduce a theoretical prediction of rigid particle dynamics in Stokes flow, with examples of fibers and capsules to show the influence of particle deformability on the dynamics. Finally, we visit the sedimentation dynamics of flexible filaments in free space.

1.2.1 Linear flow fields

In this study, we mainly focus on the dynamics of soft particles in linear flow fields. A linear flow field has a constant velocity gradient $\nabla \mathbf{v}$ and is independent of positions $\mathbf{x}$. More specifically, the velocity at any position $\mathbf{x}$ can be represented by a tensor:

$$\mathbf{v}(\mathbf{x}) = \nabla \mathbf{v}^T \mathbf{x}, \tag{1.1}$$

The velocity gradient tensor can be decomposed into the symmetric rate of strain tensor $\mathbf{E}$ and antisymmetric rotation or vorticity tensor $\mathbf{W}$:

$$\nabla \mathbf{v} = \mathbf{E} + \mathbf{W}, \tag{1.2}$$

where we can represent $\mathbf{E}$ and $\mathbf{W}$ using $\nabla\mathbf{v}$:

$$\mathbf{E} = \frac{1}{2}(\nabla\mathbf{v} + \nabla\mathbf{v}^T) \quad \text{and} \quad \mathbf{W} = \frac{1}{2}(\nabla\mathbf{v} - \nabla\mathbf{v}^T). \tag{1.3}$$

Typically, the flow field with $\mathbf{E} = 0$ becomes a purely rotational flow where any material

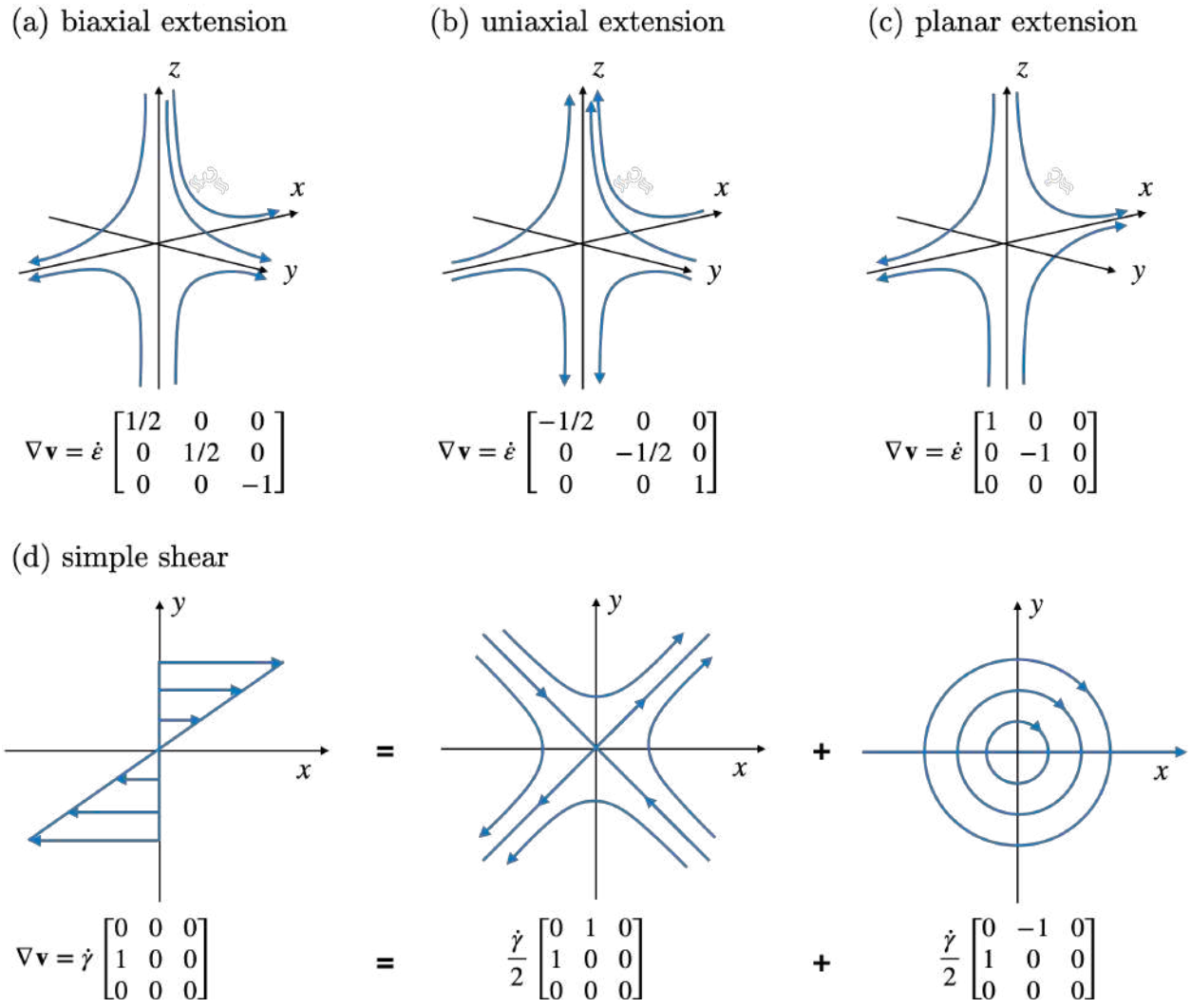


Figure 1.3: Examples of linear extensional flow: (a) Biaxial extension $\mathbf{v} = \dot{\varepsilon}(x/2, y/2, -z)$. (b) Uniaxial extension $\mathbf{v} = \dot{\varepsilon}(-x/2, -y/2, z)$. (c) Planar extension $\mathbf{v} = \dot{\varepsilon}(x, 0, -z)$. $\dot{\varepsilon}$ is the flow extension rate. (d) Decomposition of a simple shear flow $\mathbf{v} = \dot{\gamma}(-y, 0, 0)$ into a planar extension and a rigid rotation. $\dot{\gamma}$ is the flow shear rate.

point of fluids undergoes rigid body rotation. If $\mathbf{W} = 0$, the flow field becomes purely extensional without rotation. Fig 1.3(a)-(c) show three extensional flow fields with a symmetric

velocity gradient. In those flow fields, the deformation of a material point will grow or decay exponentially with time. On the other hand, Fig 1.3(d) presents another important flow field as simple shear flow. The simple shear flow can be decomposed into a planar extensional flow ($\mathbf{E} \neq 0$) and a pure rotational flow ($\mathbf{W} \neq 0$) with equal strength. Typically, the planar extension acts as a straining component of shear flow with a major compressive axis and a major extension axis.

1.2.2 Dynamics in extensional flow

Long-chain linear polymer dissolved in fluid subject to extensional flow exhibits an interesting phenomenon called a "coil-stretch" transition. The transition, first predicted by De Genne in 1974, refers to an abrupt change in polymer conformation from a coiled state to a stretched state within a slight increase in flow operating conditions [35].

In the absence of external forces, a long-chain polymer often adopts a coiled and entangled structure due to thermal effects. In an extensional flow, the flow stretches and deforms the polymer, while the polymer has a restoring force against flow deformation. The competition is measured by a dimensionless Deborah number ($\mathrm{De} = \tau\dot{\varepsilon}$) measures the ratio between two intrinsic time scales: a polymer relaxation τ (how quickly the polymer recovers from the deformation) and an extensional strain rate $\dot{\varepsilon}$ (how fast the flow deforms the polymer). Larger De indicates the viscous effect from flow dominates and the polymer is easier to be deformed by the flow. De Genne predicted an S shape transition with a critical flow strength (De), beyond which the conformation of polymer changes abruptly from a coiled to a fully stretched state [35]. The discontinuity in conformation evolution implies the coexistence of both coiled and stretched states in a range of flow strengths as the hysteresis, as an S-shape transition. The idea is illustrated in Fig 1.4(a): under a small flow strain rate, the polymer is coiled and inner monomers are hydrodynamically shielded. The S-shape transition was also brought up by Tanner [166] and Hinch [60] around the same period.

Interestingly, there was a debate between researchers for decades to argue the validity of

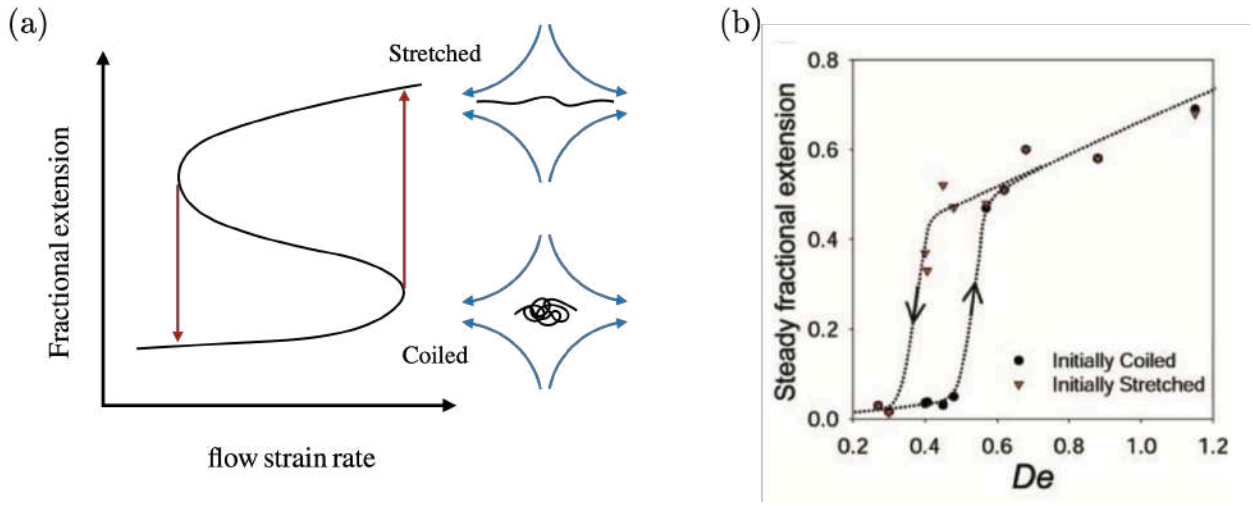


Figure 1.4: (a) Illustration of coil-stretch transition for long-chain polymer exposed to a planar extensional flow. (b) Experimental observation of coil-stretch transition with fluorescently dyed Escherichia coli DNA molecule in planar extensional flow from [151].

the S transition. Some argued that the existence of hysteresis was a result of the insufficiency in De Genne's mathematical model. The simulations from a bead-spring chain model [180], nonlinear elastic dumbbells [41], and Brownian dynamics simulation of a freely jointed bead-rod model [96] demonstrated a smooth transition from the coiled state to the stretched state without conformational hysteresis. In contrast, a number of subsequent simulations based on a dumbbell model with conformation-dependent drag result in hysteresis [47]. For a polymer with N Kuhn segments, the hydrodynamic drag acting on a coiled polymer roughly scales with the radius of gyration, as $N^{0.5}$, whereas the stretched polymer like a slender filament that has the drag scales as N. Fuller and Leal applied a bead-spring dumbbell with conformation-dependent drag on the beads and found coil-stretch hysteresis [47].

The above controversy has finally been resolved when the experimental observation from Schroeder *et al.* verified the existence of coil-stretch hysteresis with a dilute long-chain DNA solution in a planar extensional flow [151]. They trapped the fluorescently dyed Escherichia coli DNA molecule at the stagnation point where the strains can accumulate in response to the flow generated via a cross-slot device. They performed two sets of experiments: an initially coiled polymer with increased strain rate, and an initially stretched polymer with

decreased strain rate. At each strain rate, the polymer was monitored for enough time for strains to accumulate. The results in Fig 1.4(b) demonstrated the existence of conformational hysteresis. They also probe into the transition with a Brownian dynamics simulation of a bead-spring model and incorporate the hydrodynamic interaction between beads through Rotne-Prager-Yamakawa (RPY) method.

The coil-stretch transition has been observed beyond the dilute solution limit. Industrial processing often involves a dense suspension or concentrated melts, where polymers or fibers are highly entangled. Mohammad *et al.* recently reported the existence of coil-stretch transition for atomistic entangled polyethylene melts in planar extension with molecular dynamics simulation [115]. The conformation hysteresis was observed with a larger critical strain rate (De ~ 1.5) compared to that in a dilute solution.

1.2.3 Dynamics in shear flow

Dynamics of rigid and deformable particles in simple shear flow are fundamental aspects of fluid mechanics. Jeffery proposed a model to describe the periodic motions of a neutrally buoyant, rigid, and axisymmetric ellipsoid in simple shear flow [64]. For a rigid prolate spheroid with an aspect ratio AR (defined as the major axis length a/minor axis length b), the angular dynamics of the spheroid follow:

$$\begin{aligned} \tan\theta &= \frac{CAR}{\sqrt{AR^2\cos^2\phi + \sin^2\phi}} \\ \tan\phi &= AR\tan\left(\frac{2\pi t}{T}\right) \end{aligned} \tag{1.4}$$

where θ is the angle between the major axis and the vorticity z direction and ϕ is the angle between the projection of the major axis inside the flow-gradient plane and the gradient y axis. C is called an orbit constant that determines the initial orientation (defined by θ_0 and

ϕ_0) of the spheroid and T is the orbit period.

$$C = \tan\theta_0 \sqrt{\cos^2\phi_0 + \frac{1}{AR^2}\sin^2\phi_0}$$
$$T = \frac{2\pi}{\dot{\gamma}}\left(AR + \frac{1}{AR}\right) \tag{1.5}$$

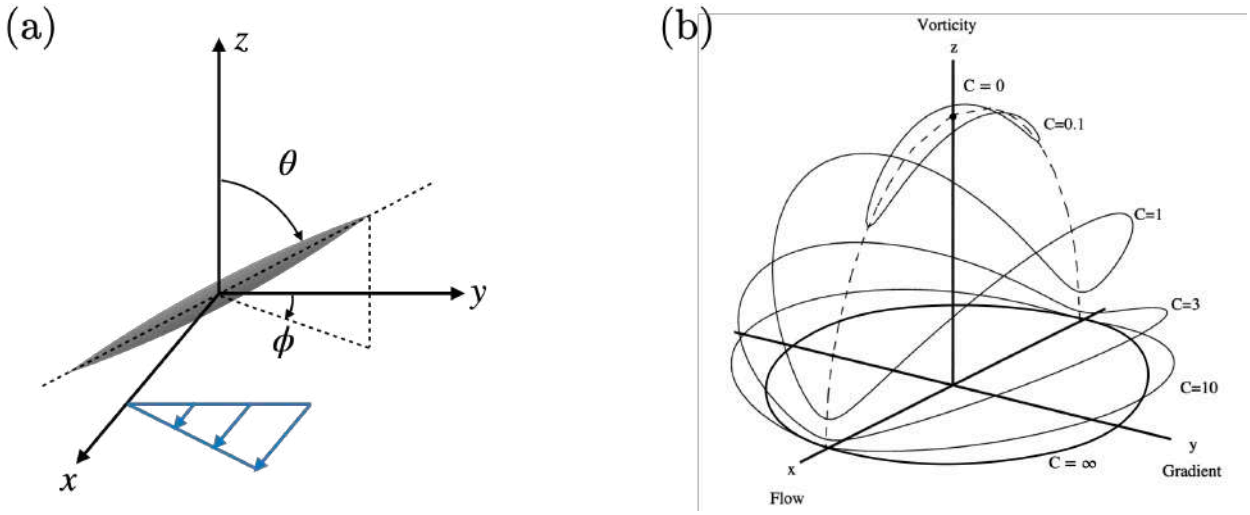


Figure 1.5: (a) A rigid prolate spheroid in a spherical coordinate system exposed to a simple shear flow. (b) The path of the orientation vector for a prolate spheroid undergoing Jeffery orbits with different orbit constants from Petrich *et al.* [134].

The initial condition is characterized by an orbit constant C. The solution to Jeffery's equation is called Jeffery orbit, which contains an infinite number of closed periodic orbits where the steady state only relates to the initial configuration of the particle or the orbit constant C. Jeffery orbits are closed trajectories due to the reversibility of Stokes flow. The dynamics can be summarized as:

- When $C = 0$, the particle rolls with the axis of revolution aligned in the vorticity direction.
- Intermediate C leads to a motion called kayaking, where the trajectories follow a path like kayaking paddles.
- When $C \to \infty$, the particle undergoes a tumbling motion with the axis of revolution

tracing out a circle in the shear plane.

Jeffery's theory is a foundation to understand other rigid particles in shear flow. Though the theory was proposed for ellipsoids, Bretherton *et al.* [15] proved that the Jeffery orbits can describe any axisymmetric rigid particles with fore-aft symmetry, with a conversion to an effective aspect ratio. Therefore, Jeffery orbits are applicable to other non-spherical particles such as rigid rods, which also show closed periodic motions like rolling, tumbling, and kayaking without migration in the flow.

However, if the rigid particle is not axisymmetric such as a slightly curved rigid fiber, the dynamics still follow Stokes reversibility but show complex dynamics different from Jeffery's prediction. Wang *et al.* modeled a rigid and slightly curved nonchiral fiber using linked rigid rods [177]. For some initial conditions, the curved fiber can drift steadily along the gradient direction due to the combined effect of rotational and translational effects in shear, along with non-Jeffery-like flipping, scooping, and spinning motions. Based on Wang *et al.*'s numerical observation in [177], Crowdy developed analytical equations for the motion of a curved rigid 2D fiber in shear [30].

Shear flow is a combination of planar extension and rigid rotation. For rigid particles that strongly resist straining deformation, dynamics are governed by the rotation component in the shear. In contrast, deformability allows particles to deform under straining flow and when particles restore from deformation due to elasticity, they no longer follow Stokes reversibility. As a result, deformable particles respond to the compressive stress that leads to complex wrinkling dynamics. For example, a flexible fiber in shear flow experiencing compressive stresses leads to buckling instability that introduces complex morphology. In an early experiment, Forgacs and Mason observed the buckling in the shear flow of a thread-like rayon filament immersed in corn syrup [46]. For a short and relatively stiff filament with small deformability, they observed the classic springy motion as the filament show a slight C shape during tumbling. For a long and flexible filament, they observed U-shape snaking and even a coiled structure when the filament becomes too flexible. Those dynamics have been

observed by a number of experiments later and new dynamics such as S-shape snaking, tank-treading, helical, and other complex behaviors were reported [56, 85, 98, 152]. Typically, for filaments under microscale, such as experiments involving actin filament [56, 98] and DNA molecules [85, 152], thermal fluctuation strongly affects the dynamics.

Capsules are small liquid droplets enclosed by a layer of thin elastic membrane and are widely used as an agent for encapsulation and transportation in the applications of the food industry, drug delivery, and cosmetics. Red blood cell (RBC) is a special type of capsule that holds a significant role within the biological system. A healthy RBC has a biconcave discoidal shape with an elastic lipid bilayer membrane. The fact that RBC has no nucleus and cytoskeleton allows it to be mechanically treated as a deformable fluid-filled capsule [136]. Researchers have shown great interest in understanding the dynamics of individual RBCs due to their close association with the buck rheological properties and multiphase behaviors in RBC suspension. Numerous experimental and computational studies have probed the dynamics of a single RBC in simple shear flow. Experiments have shown that at a low shear rate, the RBC behaves like a rigid particle and tumbles, while a high shear rate allows the RBC to reach a fixed orientation with the membrane rotating about its interior as a tank-treading motion [49].

1.2.4 Sedimentation in a viscous fluid

When a flexible particle in a viscous fluid is subjected to external forces such as gravity, the competition between gravity and particle elasticity may introduce complex sedimenting dynamics and gravity-induced deformation, which further influence the particle's macroscopic transport [37]. A rigid filament settles with a steady shape and orientation in free space [55]. For a flexible filament, the deformability and inhomogeneous distribution of hydrodynamic drag along the filament leads to rotation [81, 184]. The competition between gravity and filament bending elasticity is measured by an elasto-gravitational number $\beta = F_g L^2/E$, where F_g is the gravitational force, L is the length scale and E is bending rigidity.

Xu and Nadim [184] first tackled this problem by deriving analytical solutions for a sedimenting filament with small deformation, where the filament is modeled based on the slender body theory and the Euler-Bernoulli beam. Their results predicted the reorientation of the deformed filament where the deformation-induced hydrodynamic torque drives the filament to orient perpendicularly against gravity. The orientation dynamics have been captured in a number of later studies with either slender body theory [91] or a bead-spring model [81] for a filament with finite deformations.

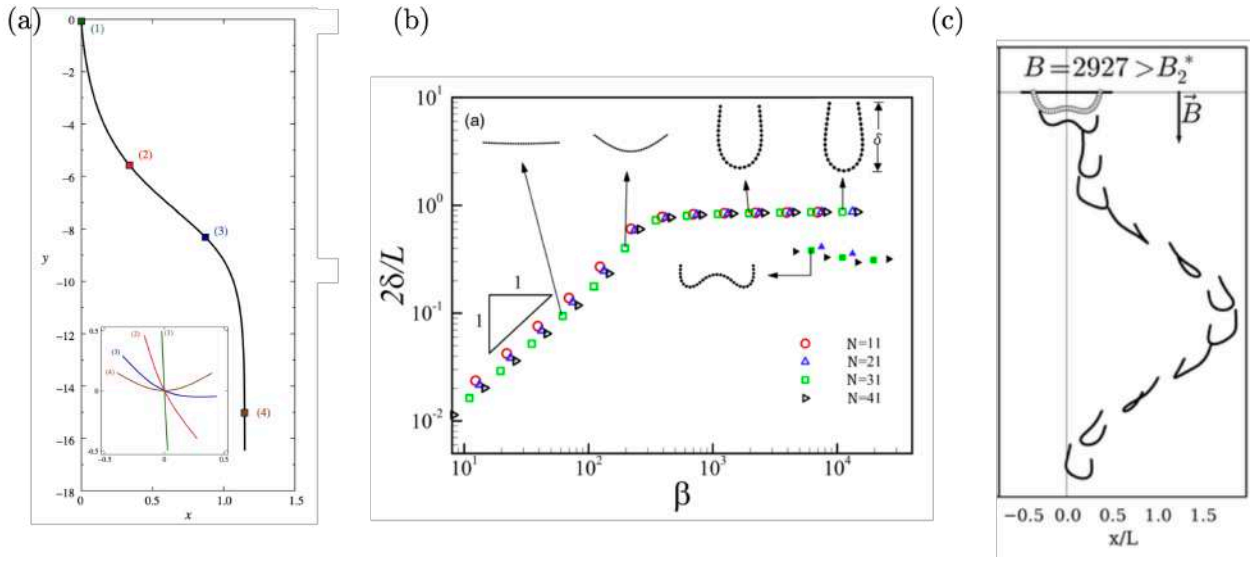


Figure 1.6: (a) The center of mass trajectory of a flexible fiber sedimenting in a viscous fluid with an inset figure indicating fiber conformations from Li *et al.* [91] (b) Steady shape evolution of a sedimenting filament with increasing flexibility from Cunha *et al.* [31]. (c) A flexible sedimenting filament shows nonplanar conformation with a helical trajectory from Saggiorato *et al.* [144].

Li *et al.* applied theoretical and numerical methods to study the trajectory of flexible filaments sedimenting with different initial conditions. As indicated in Fig 1.6(a), the reorientation leads to the drift in the lateral direction, and the trajectories of the filament are restricted to a cloud where the shape is determined by filament flexibility [91].

Flexible filaments reorient to gain a stable orientation and the elasto-gravitational number β determines the steady shape of filaments at equilibrium. Many studies have characterized the equilibrium shape evolution with increasing β [31, 81, 103]. For small β, the dominance of

bending elasticity over gravity leads to negligible deformation along the filament, such that the filament becomes almost straight while sedimenting perpendicularly to gravity. The filament shows a V-like shape and a linear relationship has been found between deformation (height of the filament) and β. With increasing β, a transition to a U-like and even a horseshoe-like shape was observed. The ends of the filament due to the dominance of gravity get closer to each other to generate a more compact shape. For more flexible filaments, some numerical studies observed a W-like shape. The shape is a metastable solution and any small perturbation induces the transition back to the horseshoe-like shape [31, 81, 144]. This shape has not been reported in experiments as it is sensitive to perturbation.

For very flexible filaments, nonplanar conformations have been observed in both computational and experimental studies [103, 144, 154]. Saggiorato *et al.* numerically studied the conformation of semiflexible filaments subject to gravity and identified helical trajectories during sedimentation due to the nonplanar conformation of filaments [144]. Shashank *et al.* performed the experiments of very flexible ball chains settling in viscous silicon oil and observed non-symmetric deformations that significantly deformed out of a plane. In addition, Li *et al.* also probed the case when the extremely flexible filament initially aligns with gravity. The non-uniform tension along the filament causes the buckling mainly on focuses on the leading part and the filament sediments like a J shape.

1.3 Stokes flow introduction

This section aims to deliver the necessary information required to understand the results of this thesis. We briefly review some key concepts in Stokes flow and present a systematic introduce a special scenario called Stokes flow, which owns many interesting properties that are different from our intuition. In the following, we briefly introduce some key properties in Stokes flow and systematically introduce how we calculate induced velocity due to perturbation forces exerted in the flow. The contents of this section are mainly referred to the book Microhydrodynamics, Brownian motion, and Complex fluids [50].

1.3.1 Properties of Stokes flow

For an incompressible Newtonian fluid, the conservation of mass and momentum is represented by the Navier-Stokes equation:

$$\begin{aligned} \rho\left(\tfrac{\partial \mathbf{v}}{\partial t} + \mathbf{v}\cdot\nabla\mathbf{v}\right) &= -\nabla p + \eta\nabla^2\mathbf{v}, \\ \nabla\cdot\mathbf{v} &= 0. \end{aligned} \tag{1.6}$$

where ρ is the fluid density, p is the pressure, and η is the fluid viscosity. This equation contains nonlinear terms and there is no analytical solution. However, if we consider the case where the Reynolds number $\mathrm{Re} = \rho U a/\eta$, defined as the ratio between the time scale for the diffusion of momentum $\rho a^2/U$ over the translation of flow a/U, is negligible. This can happen when the viscosity is large or the flow at the microscale. The acceleration and nonlinear convection terms become negligible and the resulting equation becomes the Stokes equation and the inertialess flow is called Stokes flow:

$$\begin{aligned} -\nabla p + \eta\nabla^2\mathbf{v} &= 0, \\ \nabla\cdot\mathbf{v} &= 0. \end{aligned} \tag{1.7}$$

The equation is time-independent, indicating that the momentum can be diffused instantaneously and the flow condition does not rely on the knowledge from the previous time.

Stokes flow has two important properties: linearity and kinematic reversibility. The linearity comes from the linear Stokes equation, which allows us to obtain analytical solutions that will be discussed later. More importantly, this implies the solutions can be linearly superimposed and enables us to analyze complex scenarios like suspension by simply summing the contribution of each individual particle. The reversibility also arises from the linearity: if the perturbation forces and boundary conditions are reversed, the induced flow field is also reversed. This property is useful to interpret the motions of particles in Stokes flow. For example, a rigid particle next to a rigid wall shows no migration due to the symmetry of the flow. Another important observation is the locomotion of rigid particles in Stokes flow. Due to the reversibility, if a particle undergoes cyclic motions that are identical after a time-reversal transformation, it generates no net motions [84]. However, the aforementioned statements may fail once the particle is deformable because the relaxation of flow-induced deformation due to particle elasticity breaks the reversibility.

1.3.2 Fundamental solutions in Stokes flow

The linearity of Stokes flow allows us to treat complex problems as a combination of simple subproblems. For example, a suspension involves complicated particle-particle and particle-fluid interactions, with the presence of particles perturbing the surrounding flow field thereby changing local rheological properties. In Stokes regime, we can resolve the system by considering the influence of each individual particle and summing them up, the perturbation due to each particle to the surrounding fluid can be linearly superposed.

We introduce the solution to Stokes equation with a simple scenario: a particle freely sediments in an unbounded domain. The particle exerts a force on the surrounding fluid. If we are far away from the particle, the particle size is negligible and the force can be treated as a point force. Numerically, we can localize a force $\mathbf{F}$ with a delta function $\delta(\mathbf{x})$, whose value is zero everywhere except for the origin and the integral of $\delta(\mathbf{x})$ over the space sum up to 1. Therefore, we obtain a singular force density $\mathbf{f} = \mathbf{F}\delta(\mathbf{x})$. The point force has the unit

of force per unit volume.

In the following, we show how to obtain the solution (velocity) due to the presence of a point force. In an unbounded domain, assume a force $\mathbf{F}\delta(\mathbf{x})$ perturb a stationary fluid at the position $\mathbf{x}_0$. The generated velocity field satisfies:

$$\begin{aligned} -\nabla p + \eta \nabla^2 \mathbf{v} + \mathbf{F}\delta(\mathbf{x} - \mathbf{x}_0) = 0, \\ \nabla \cdot \mathbf{v} = 0. \end{aligned} \tag{1.8}$$

By solving the Stokes equation, we can obtain the velocity at any position $\mathbf{x}$:

$$\mathbf{v}(\mathbf{x}) = \mathbf{G}(\mathbf{x} - \mathbf{x}_0) \cdot \mathbf{F}, \tag{1.9}$$

where

$$\mathbf{G}(\mathbf{x} - \mathbf{x}_0) = \frac{1}{8\pi\eta|\mathbf{x} - \mathbf{x}_0|}\left(\mathbf{I} + \frac{(\mathbf{x} - \mathbf{x}_0)(\mathbf{x} - \mathbf{x}_0)}{|\mathbf{x} - \mathbf{x}_0|^2}\right) \tag{1.10}$$

is the free-space Green's function for the Stokes equation, which is often called Stokeslet or Oseen-Burgers tensor. The velocity generated due to a Stokeslet as shown below, is axisymmetric with respect to the forcing direction.

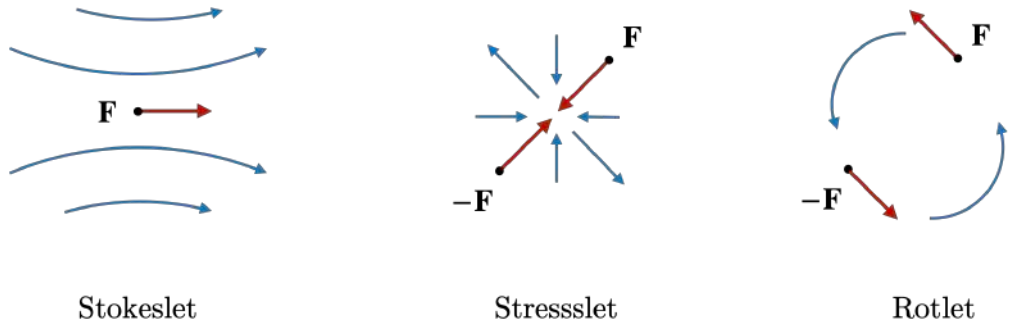


Figure 1.7: Velocity profile generated due to point forces with strength $\mathbf{F}$: Stokeslet, stresslet and rotlet.

One important observation is that the Stokeslet velocity flow field is nonlocal. The velocity shows a very slow decay rate as the Stokeslet is scaled with 1 over distance: $\mathbf{G}(\mathbf{x} - \mathbf{x}_0) \sim |\mathbf{x} - \mathbf{x}_0|^{-1}$. As illustrated in the later chapters, the slow decay rate leads to many

important observations arising from nonlocal hydrodynamic interactions.

Besides the perturbation of a singular force, we introduce another fundamental scenario called force dipole solution, corresponding to the gradient of Stokeslet. When two equal force densities with opposite directions act on the fluid, they construct force dipole tensor $\mathbf{D}$ as the dyad between forces $\mathbf{F}$ and directional vector $\mathbf{u}$. The flow field generated due to a force dipole is called Stokes doublet:

$$\mathbf{v}(\mathbf{x}) = \nabla \mathbf{G}(\mathbf{x} - \mathbf{x}_0)\mathbf{D}. \tag{1.11}$$

The flow field can be further decomposed based on symmetry. The symmetric part is called stresslet, arising from symmetric point forces densities that deform the fluid. The asymmetric part is called rotlet, which generates pure rotation. The effect of two flow fields are illustrated in Fig 1.7.

1.3.3 Multipole expansion

When we consider a particle freely suspended in an unbounded domain, the perturbation velocity $\mathbf{v}_p$ is generated due to the force exerted by the particle on the fluid (Stokeslets). The velocity at random position ($\mathbf{x}$) can be evaluated as an integral of the Stokeslets over particle surface S:

$$\mathbf{v}_p(\mathbf{x}) = -\int_S \mathbf{G}(\mathbf{x} - \mathbf{x}')(\hat{\mathbf{n}} \cdot \sigma(\mathbf{x}'))dS, \tag{1.12}$$

where $\mathbf{x}'$ are material points on the particle, $\mathbf{G}$ is the Stokeslet, $\hat{\mathbf{n}}$ is a normal vector pointing outward of particle, σ is the stress tensor. Therefore, $(\hat{\mathbf{n}} \cdot \sigma(\mathbf{x}'))dS$ represents the differential force exerted on the area element $dS(\mathbf{x}')$ by the fluid. If position ($\mathbf{x}$) is far away from the particle ($||\mathbf{x}|| \ll 1$), we can Taylor expand the Green's function $\mathbf{G}(\mathbf{x} - \mathbf{x}')$. The resultant expression is called the multipole expansion of the velocity field:

$$\mathbf{v}_p(\mathbf{x}) = -\mathbf{G}(\mathbf{x}) \int_S (\hat{\mathbf{n}} \cdot \sigma(\mathbf{x}'))dS + \nabla \mathbf{G}(\mathbf{x}) \int_S \mathbf{x}'(\hat{\mathbf{n}} \cdot \sigma(\mathbf{x}'))dS + O(||\mathbf{x}||^{-3}) \tag{1.13}$$

The integral in the first term corresponds to the stress exerted by the fluid on the particle, which is the drag force:

$$\mathbf{F}_{\text{drag}} = \int_S (\hat{\mathbf{n}} \cdot \sigma(\mathbf{x}'))dS. \tag{1.14}$$

The second term, as the gradient of the Stokeslet, is called Stokes doublet $\mathbf{D}$ and is related to the stress and torque exerted on the fluid:

$$\mathbf{D} = \int_S \mathbf{x}(\hat{\mathbf{n}} \cdot \sigma(\mathbf{x}'))dS. \tag{1.15}$$

Therefore, the multipole expansion can be rewritten in the form of the Stokeslet and doublet.

$$\mathbf{v}_p(\mathbf{x}) = -\mathbf{G}(\mathbf{x}) \cdot \mathbf{F}_{\text{drag}} + \nabla\mathbf{G}(\mathbf{x})\mathbf{D} + O(||\mathbf{x}||^{-3}) \tag{1.16}$$

For a particle sedimenting in free space, the drag forces term dominates. The velocity field is governed by the Stokeslet which decays very slowly as $\mathbf{G} \sim 1/r$. If the particle is neutrally buoyant, the drag force term vanishes, and the perturbation velocity is dominated by the following term as the doublet with a faster decay rate $\nabla\mathbf{G} \sim 1/r^2$.

1.3.4 Regularized Stokeslet

In the previous section, we introduced the Stokeslet as a fundamental solution to a concentrated external force acting on the fluid. As the Stokeslet is singular, it becomes unrealistic to evaluate the induced velocity where the force is exerted as the delta function blows up. One approach to dealing with the singularity is to regularize the Stokeslet by introducing a small cutoff function. The method of regularized Stokeslet is a numerical method originally introduced by Cortez [27] that smooths the forces and removes the singularity. The method is commonly used to model biological systems such as cilia and bacterial flagellar [28, 29, 120, 121]. Another approach is to replace the singular Stokeslet with an approximated flow field as the Rotne-Prager-Yamakawa (RPY) method, which is useful in modeling the hydrodynamic

interactions between small spherical particles in a colloidal suspension [142, 190]. In the following, we elaborate on the implementation of the regularized Stokeslet. For a regularized

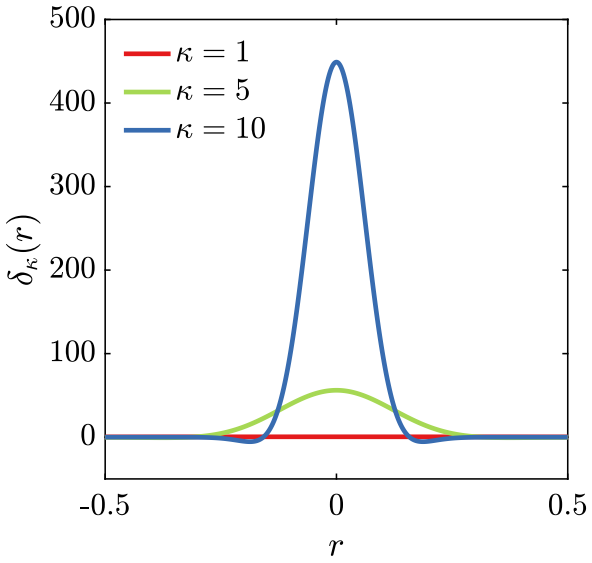


Figure 1.8: Regularized Delta function $\delta_\kappa(r)$ with different choices of κ for a Gaussian regularization.

Stokeslet, the delta function $\delta(\mathbf{x})$ is replaced by a regularized function $\delta_\kappa(\mathbf{x})$, such that the singular force density is spread within a small range: $\mathbf{f} = \mathbf{F}\delta_\kappa(\mathbf{x})$. Consequently, the velocity can be resolved via the regularized Stokelet $\mathbf{G}_\kappa$ everywhere including the origin $\mathbf{x} = \mathbf{x}_0$.

$$\mathbf{v}(\mathbf{x}) = \mathbf{G}_\kappa(\mathbf{x} - \mathbf{x}_0) \cdot \mathbf{F}. \tag{1.17}$$

Here, we list some examples of commonly used cutoff functions for regularization, where $r = ||\mathbf{x} - \mathbf{x}_0||$ and κr scales regularization distance. In Fig 1.8, we show the influence of κ by plotting the Gaussian regularization method from Table 1.1, where the difference between the regularization function and the Delta function decays exponentially. The regularization parameter κ is inversely proportional to the regularization distance. Therefore, as $\kappa \to \infty$, the function becomes a singular Delta function.

Type	Regularization function $\delta_\kappa(r)$
Algebraic	$\delta_\kappa(r) = \frac{15}{8\pi\kappa^4(r^2+\kappa^{-2})^{7/2}}$
Exponential	$\delta_\kappa(r) = \frac{5\kappa^2+5\kappa^3 r-\kappa^4 r^2}{64\pi}\exp(-\kappa r)$
Gaussian	$\delta_\kappa(r) = \frac{\kappa^3}{\sqrt{\pi}^3}\exp(-\kappa^2 r^2)\left[\frac{5}{2}-\kappa^2 r^2\right]$

Table 1.1: Examples of regularization functions from Cortez *et al.* [29].

1.4 Outline of this work

This thesis aims to develop a fundamental understanding of thin elastic sheets processed under different types of flow conditions and apply the knowledge gained as a base to probe into real-world applications. The rest of this thesis is split into five chapters. In Chapter 2, we give a detailed theoretical and numerical formulation to model a thin elastic sheet under different flow fields. We show two validation cases for the model by comparing numerical results with analytical solutions and experiments. In Chapter 3, we demonstrated the existence of a coil-stretch-like transition for highly stretchable sheets within two extensional flows: planar and biaxial. The coil-stretch transition is a phenomenon originally observed in dilute linear long-chain polymer solution exposed to extensional flow and we observe a similar effect on 2D elastic sheets. In Chapter 4, we extend the observation of a coil-stretch-like transition in elastic sheets to a uniaxial extensional flow, where elastic sheets can buckle. We probed into the relationship between sheet deformability on buckling instability and investigate the influence of buckling on the coil-stretch-like transition. In Chapter 5, we switch from extensional flow to shear flow. We systematically explore the influence of deformability on the dynamics of a highly inextensible sheet with different rest shapes. Certain dynamics are identified by our experimental collaborator with a quantitative comparison.

In Chapter 6, we change the focus from freely suspended sheets to sedimentation. We tackle the sedimentation dynamics in free space and near an infinite wall, where the dynamics are comparable with sedimentation of flexible filaments. Finally, we summarize the thesis in Chapter 7 and provide insights for future directions.

2

Modeling of elastic sheets in Stokes flow

In this chapter, we formulate the problem and present the numerical methods to show the modeling of elastic sheets. The model is considered to be general, with more specific details fitting each scenario to be discussed in each Chapter.

2.1 Problem formulation

We consider an elastic thin sheet in an arbitrary rest shape with a characteristic length scale a and thickness h such that $h \ll a$. The sheet is incompressible and is freely suspended in an unbounded flow field determined by the flow strain tensor. The fluid is Newtonian with viscosity η and density ρ.

In this work, we have explored various rest shapes such as disks, squares, and rectangles. The sheet follows two boundary conditions: no-slip surface and free edge. The no-slip surfaces indicate that material points on the surface move with the same velocity as the local fluid. In addition, it also implies the sheet is impermeable (no-penetration surface) – if the sheet moves with the local fluid velocity, then no fluid is passing through the sheet. The free edge condition is due to the fact that $h \ll a$, such that negligible thickness ensures a traction-free

edge, along which fluid exerts no forces.

Benefiting from the no-slip condition, we evaluate the dynamics of the sheet based on the fluid velocity. In this work, we consider a small, thin sheet and assume that the particle Reynolds number $\mathrm{Re_p} = \rho\dot{\epsilon}a^2/\eta$ is negligible. This assumption ensures the fluid inertia is negligible at the scale of sheet size and the governing equations for fluid motion are the Stokes equation and the continuity equation for an incompressible fluid:

$$\begin{aligned} -\nabla p + \eta\nabla^2\mathbf{v} + \mathbf{f} &= \mathbf{0} \\ \nabla\cdot\mathbf{v} &= 0. \end{aligned} \tag{2.1}$$

2.1.1 Mechanical forces

We focus on two specific types of mechanical responses: in-plane stretching and out-of-plane bending, with examples to illustrate each type of deformation in Fig.

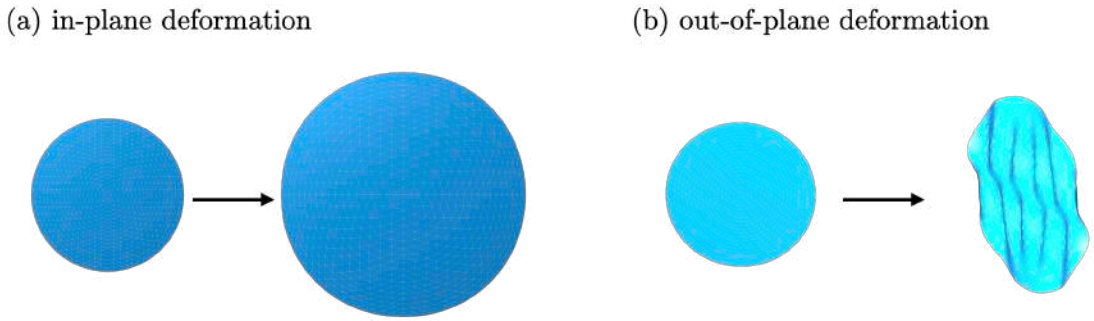


Figure 2.1: Description of two mechanical deformations with an example of disk: (a) In-plane deformation: the sheet is stretched without buckling. (b) Out-of-plane deformation: the sheet is wrinkled and deforms out of the lateral plane.

Therefore, the total strain energy of the elastic sheet can be written as the sum of in-plane strain energy E_s and out-of-plane bending energy E_b:

$$E = E_s + E_b. \tag{2.2}$$

Here, the in-plane strain energy is evaluated by integrating the strain energy density W

over the sheet surface Γ:

$$E_s = \int_\Gamma W dS. \tag{2.3}$$

The choices of W depend on the specific types of materials interested. We list some common strain energy densities with their nonlinear response to strain. In Table 2.1, we show three examples of potential strain energy densities. Neo-Hookean is a hyperelastic model for rubber-like materials [73]. It is similar to Hookean model under small stains and the stress-strain relation becomes nonlinear at moderate strains. However, it cannot accurately predict large deformation. Yeoh model is an extension of neo-Hookean mode by adding additional higher-order terms [192] and controlled by a constant c. Therefore, Yeoh model can account for strain-hardening behavior for cross-linked polymer networks and capture large deformation. The last example is Skalak model. Similar to Yeoh model, it includes higher-order terms controlled by a constant C_a that yields the strain-hardening property of the material and resits local area change. The model was originally proposed by Skalak to simulate red blood cells [160]. For models listed above, the two-dimensional shear modulus G scales with

Models	Formulation
Neo-Hookean (NH) [73]	$W_{\mathrm{NH}} = \frac{G}{2}(I_1 - 3)$
Yeoh (YH) [192]	$W_{\mathrm{YH}} = \frac{G}{2}(I_1 - 3) + cG(I_1 - 3)^3$
Skalak (SK) [160]	$W_{\mathrm{SK}} = \frac{G}{2}(I_1 - 3) + C_a I_2^2$

Table 2.1: Examples of strain energy densities.

the equilibrium thickness h. The term I_1 and I_2 are invariants of the right Cauchy-Green deformation tensor, which depend on the local principal stretch ratios λ_i along the tangential direction of the sheet surface:

$$I_1 = \lambda_1^2 + \lambda_2^2 + \frac{1}{\lambda_1^2\lambda_2^2}, \quad I_2 = \lambda_1^2\lambda_2^2 - \frac{1}{\lambda_1^2\lambda_2^2}. \tag{2.4}$$

The last term denotes λ_3, as the stretch ratio along the thickness direction, is obtained by

incompressibility of the material ($\lambda_1\lambda_2\lambda_3 = 1$). The constant c and C_a control the energy penalty for significant change in strain and are determined by material property.

The bending energy E_b is estimated from curvatures integrated over the sheet surface. The classic Canham-Helfrich energy follows:

$$E_b = \int_\Gamma \left(\frac{K_B}{2}(2\kappa_H - c_0)^2 + \overline{K}_B \kappa_G \right) dS, \tag{2.5}$$

where K_B is the bending modulus, and $\overline{K}_B$ is the Gaussian bending rigidity. κ_H and κ_G are the local mean and Gaussian curvature, separately. c_0 is the spontaneous curvature measured at equilibrium. In this study, we assume the rest shape of the sheet to be flat thereby $c_0 = 0$ everywhere.

2.1.2 Dimensionless groups

We now introduce nondimensional parameters to describe the aforementioned mechanical properties. Here, we use the symbol $\dot{\varepsilon}$ to represent the flow strain rate, which depends on the specific flow type (extensional or shear). For the in-plane deformation, the capillary number Ca compares the viscous stresses exerted by the fluid on the sheet to the in-plane elastic response of the sheet, where larger Ca indicates that the sheet is more deformable/stretchable:

$$\mathrm{Ca} = \frac{\eta \dot{\varepsilon} a}{G}. \tag{2.6}$$

In this thesis, we define two different parameters for bending. The relative size of the bending and in-plane stresses is measured by a dimensionless bending stiffness $\hat{K}_B$:

$$\hat{K}_B = \frac{K_B}{a^2 G}. \tag{2.7}$$

Smaller $\hat{K}_B$ indicates that the sheet is more flexible. On the other hand, the parameter comparing the bending with flow is the elastoviscous number $\mathrm{E_V} = \mathrm{Ca}/\hat{K}_B$, where larger $\mathrm{E_V}$

indicates that the sheet is more flexible:

$$\mathrm{E_V} = \frac{\eta \dot{\varepsilon} a^3}{K_B}. \tag{2.8}$$

We apply the dimensionless bending stiffness $\hat{K}_B$ in the study of highly extensible sheets in the study of extensional flow in Chapter 3 and Chapter 4, where the dynamics are determined by both Ca and $\hat{K}_B$. When it comes to almost inextensible sheets in Chapter 5 and Chapter 6, we mainly focus on the effect of bending where the elastoviscous number $\mathrm{E_V}$ is used. We will address the dimensionless groups for different scenarios for subsequent Chapters.

2.2 Numerical methods

In this section, we systematically introduce how to numerically solve the two types of mechanical responses: in-plane stretching and out-of-plane bending. We evaluate the local deformation on the sheet surface by tracking the material points anchored on the sheet. Based on material points, or nodes, the sheet is discretized into triangular elements, with the deformation resolved at the element scale. On a specific node i, we obtained the summed nodal elastic forces $\mathbf{F}_{e,i}$ from the stretching ($\mathbf{F}_{s,i}$) and bending ($\mathbf{F}_{b,i}$) from the first variation of the total energy with respect to the nodal displacement:

$$\mathbf{F}_{e,i} = \mathbf{F}_{s,i} + \mathbf{F}_{b,i}. \tag{2.9}$$

The elastic nodal force $\mathbf{F}_{e,i}$ is the total force that fluids exerted on the sheet leading to deformation.

2.2.1 In-plane forces calculation

The method to evaluate in-plane deformation is based on a finite-element formulation adapted from Charrier *et al.* [21]. The key idea for the method is to simplify the calculation by solving

the 3D deformation with a 2D planar transformation via a coordinate transformation.

Characterization of deformation in 1D element

Before considering the deformation of a triangular element, we introduce the planar deformation of a material point in a plane defined by 2D Cartesian axes (x, y). A random material point whose initial position $\mathbf{x} = (x, y)$ undergoes deformation and becomes $\mathbf{X} = (X, Y)$. The displacement components along the x and y direction are denoted as u and v, respectively, such that:

$$X = x + u, \quad Y = y + v. \tag{2.10}$$

Therefore, the deformation of a vector defined by two random material points, as a line element, can be represented as $d\mathbf{x} = (dx, dy)$ (undeformed) and $d\mathbf{X} = (dx, dy)$ (deformed). The relation is:

$$\begin{bmatrix} dX \\ dY \end{bmatrix} = \begin{bmatrix} 1 + \partial u/\partial x & \partial u/\partial y \\ \partial v/\partial x & 1 + \partial v/\partial y \end{bmatrix} \begin{bmatrix} dx \\ dy \end{bmatrix}, \tag{2.11}$$

or in the matrix form:

$$d\mathbf{X} = \mathbf{F} d\mathbf{x}, \tag{2.12}$$

where $\mathbf{F}$ is the deformation gradient tensor. On the other hand, we can represent the magnitude ds of this vector by:

$$ds^2 = d\mathbf{X}^T d\mathbf{X} = \mathbf{x}^T \mathbf{F}^T \mathbf{F} d\mathbf{x} = d\mathbf{x}^T \mathbf{G} d\mathbf{x}, \tag{2.13}$$

where $\mathbf{G} = \mathbf{F}^T \mathbf{F}$ is the right Cauchy tensor that is symmetric and positive definite:

$$\begin{aligned} G_{11} &= \left(1 + \frac{\partial u}{\partial x}\right)^2 + \left(\frac{\partial v}{\partial x}\right)^2, \\ G_{12} = G_{21} &= \left(1 + \frac{\partial u}{\partial x}\right)\left(\frac{\partial u}{\partial y}\right) + \left(1 + \frac{\partial v}{\partial x}\right)\left(\frac{\partial v}{\partial y}\right), \\ G_{22} &= \left(\frac{\partial u}{\partial y}\right)^2 + \left(1 + \frac{\partial v}{\partial y}\right)^2. \end{aligned} \tag{2.14}$$

The eigenvalues of $\mathbf{G}$ (λ_i) are the principal stretch ratios for the in-plane deformation, along two locally orthogonal principal directions.

$$\lambda_1 = \sqrt{\frac{G_{11} + G_{22} + \sqrt{(G_{11} - G_{22})^2 + 4G_{12}^2}}{2}},$$
$$\lambda_2 = \sqrt{\frac{G_{11} + G_{22} - \sqrt{(G_{11} - G_{22})^2 + 4G_{12}^2}}{2}}. \tag{2.15}$$

The principal stretch ratios are key components in the strain energy density functions listed in SEC.

Calculation of nodal forces in 2D elements

Now let us move from a 1D line element to a 2D triangular element, which is the structure to be resolved for the sheet. We consider the deformation at the scale of a single triangular element. The size of the element is assumed to be small such that the edges remain straight. This assumption implies that the deformation is homogenous and the displacement for the material points on the element is linear. Therefore, we track the deformation of the element simply by the displacement of three nodes (i, j, k) at the corners. The local coordinate for three nodes is in 2D. For example, the nodal position for node i is (x_i, y_i).

Here, the nodal displacement of three nodes $u = [u_i, u_j, u_k]^T$ and $v = [v_i, v_j, v_k]^T$ (u and v are not vectors) are represented by a set of functions N_i, called shape functions. For instance, $N_i = 1$ at node i and $N_i = 0$ at nodes j and k. For any point (x, y) inside the element, N_i has the form:

$$N_i = (a_i x + b_i y + c_i)/L_i, \tag{2.16}$$

where,

$$a_i = y_j - y_k, \quad b_i = x_k - x_j, \quad c_i = x_j y_k - x_k y_j, \quad L_i = a_i x_i + b_i y_i + c_i, \tag{2.17}$$

are parameters calculated based on nodal positions. Similarly, we can derive expressions for

N_j and N_k by applying a cyclic change of index $i \to j \to k \to i$. With those basis functions, we can represent the deformation at any point inside the element, and calculate the linear variation of the deformation (u, v) based on local coordinates (x, y):

$$\begin{aligned} \partial u/\partial x = u^T A, \quad \partial u/\partial y = u^T B, \\ \partial v/\partial x = v^T A, \quad \partial v/\partial y = v^T B, \end{aligned} \tag{2.18}$$

where $A = [\partial N_i/\partial x, \partial N_j/\partial x, \partial N_k/\partial x]^T$ and $B = [\partial N_i/\partial y, \partial N_j/\partial y, \partial N_k/\partial y]^T$ are derivatives of shape functions based on coordinates. With the information above, we can construct the deformation gradient tensor $\mathbf{G}$ and calculate the principal stretch ratios λ_i of the element based on Eq 2.14 and 2.15.

By the principle of virtual work, we write the change in total strain energy W_{total} due to a small nodal displacement δu and δv for three nodes, where the change in total strain energy can also be written in the product of the change in strain energy density and local area at equilibrium A_e:

$$\delta W_{\text{total}} = A_e \delta W = \delta u^T F_x + \delta v^T F_y \tag{2.19}$$

where F_x and F_y, similar to the nodal displacement, represent the force component of three nodes along x and y directions. On the other hand, the variation in strain energy density can be considered as the change in the in-plane stretch ratios λ_1 and λ_2.

$$\begin{aligned} \delta W &= \delta u^T \frac{\partial W}{\partial u} + \delta v^T \frac{\partial W}{\partial v} \\ &= \delta u^T \left(\frac{\partial W}{\partial \lambda_1}\frac{\partial \lambda_1}{\partial u} + \frac{\partial W}{\partial \lambda_2}\frac{\partial \lambda_2}{\partial u} \right) + \delta v^T \left(\frac{\partial W}{\partial \lambda_1}\frac{\partial \lambda_1}{\partial v} + \frac{\partial W}{\partial \lambda_2}\frac{\partial \lambda_2}{\partial v} \right) \end{aligned} \tag{2.20}$$

Therefore, the 2D nodal forces can be derived as:

$$\mathbf{F}^{\text{2D}} = \begin{bmatrix} F_x \\ F_y \end{bmatrix} = A_e \begin{bmatrix} \frac{\partial W}{\partial \lambda_1}\frac{\partial \lambda_1}{\partial u} + \frac{\partial W}{\partial \lambda_2}\frac{\partial \lambda_2}{\partial u} \\ \frac{\partial W}{\partial \lambda_1}\frac{\partial \lambda_1}{\partial v} + \frac{\partial W}{\partial \lambda_2}\frac{\partial \lambda_2}{\partial v} \end{bmatrix} \tag{2.21}$$

One important reminder is that $\mathbf{F}^{2D}$ are forces applied to maintain the current deformation. Therefore, the elastic resistance force from the sheet follows the opposite direction.

Resolution to 3D deformation

The idea to resolve the nodal force is simple. We introduce two different coordinate systems: a global 3D coordinate based on the Lagrangian position (x, y, z) of a triangular element in 3D Euclidean space, and a local 2D coordinate (x, y) of a triangular element in 2D Euclidean space. Two coordinates can be transformed via a rigid body rotation. We

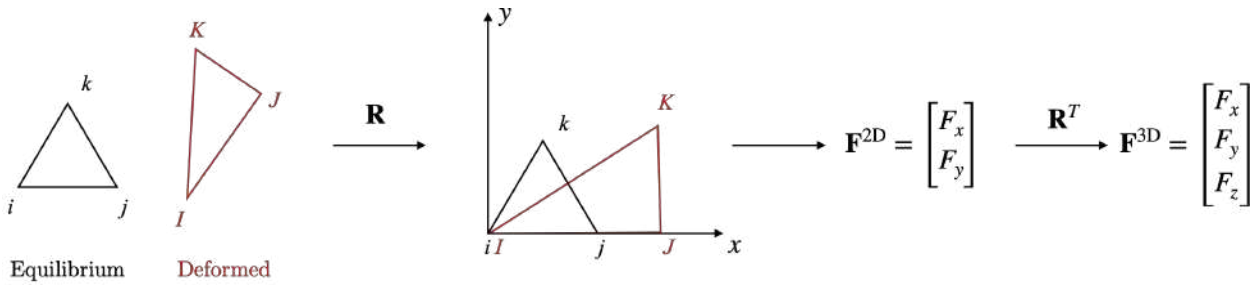


Figure 2.2: Illustration of in-plane forces calculation.

first transform a deformed 3D triangular element into a local 2D coordinate using rotation matrix $\mathbf{R}$, where we calculate the nodal force by comparing the deformed element with the corresponding equilibrium element. The obtained nodal forces $\mathbf{F}^{2D}$ are then transformed back to the 3D coordinate via the rotation matrix $\mathbf{R}^T$ and forces are assigned to the corresponding nodes.

2.2.2 Out-of-plane forces calculation

The numerical formulation for bending is based on a discretization of the Helfich energy mentioned previously. The discretized bending energy is evaluated at the element scale and assigns a penalty for the deflection between neighboring elements. The method is easy to implement and is widely used in the modeling of membranes [42, 43, 156, 157, 196]. However, the method is linear and it is only capable of predicting bending dynamics in the linear regime. Therefore, a more realistic nonlinear bending model is required in the future

to capture nonlinear bending dynamics. We show a more detailed discussion of the potential bending methods in Chapter 7.

This simple linear bending energy is the sum of penalty energy caused by the deflection angle θ between each pair of neighboring triangular elements α and β:

$$E_b = \sum_{\text{adj } \alpha,\beta} k_b \left(1 - \cos(\theta_{\alpha\beta} - \theta_0)\right), \tag{2.22}$$

where k_b is a bending constant. The angle θ_0 is the deflection angle at equilibrium. In this work, we assume a flat equilibrium state thus θ_0 remains zero. The bending constant $k_b = \alpha K_B$ relates to the continuum bending rigidity K_B. The specific value of α still requires discussion. In the extensional flow results (Chapter 3 and Chapter 4), we consider $\alpha = 3\sqrt{3}/2$ to account for the bending in sheets simply based on the scaling relation from [42] and the incompressibility of the sheet by taking $\nu = 0.5$. For the shear flow and sedimentation results (Chapter 5 and Chapter 6), we updated α with the following setup.

The prefactor in [42] is based on a sphere approximation, which does not include the presence of a free edge. To test the bending constant k_b and the actual α, we enforce a part of a sheet to match a cylinder profile with known curvature κ. Here, we can simplify the Canham-Helfrich energy in Eq 2.5 as the spontaneous curvature c_0 vanishes. For a cylinder, one of its principal curvature κ_2 has to vanish, which makes the Gaussian curvature $\kappa_G = 0$ all over the surface, and the mean curvature $\kappa_H = -\kappa_1/2$, where $\kappa_1 = \kappa$ as the curvature of the circle we enforced. Therefore, the Helfrich energy becomes:

$$E_b = \frac{K_B A}{2}\kappa^2. \tag{2.23}$$

We assume negligible area change to prevent in-plane deformation by enforcing a small curvature κ, and in test cases, the area changes less than 1%. By comparing the simplified

energy with discretized energy in Eq 2.5, we obtain the prefactor α:

$$\alpha = \frac{K_B A\kappa^2/2}{K_B \sum_{\text{adj } \alpha,\beta} [1 - \cos(\theta_{\alpha\beta} - \theta_0)]} = \frac{A\kappa^2}{2 \sum_{\text{adj } \alpha,\beta} [1 - \cos(\theta_{\alpha\beta})]}. \tag{2.24}$$

We examined sheets with a rectangle and a disk rest shape and bent the sheet with different κ. The results below show that results converge with decreasing κ, which eliminates the influence of in-plane deformation.

	Rectangle			Disk		
Curvature κ	0.1	0.01	0.0001	0.1	0.01	0.0001
Prefactor α	1.0307	1.0322	1.0323	1.0939	1.0945	1.0945

Table 2.2: Convergence of prefactor with decreasing curvature in bending formulation.

The method to resolve the nodal bending force is based on the "four-point interaction" in [42]. In Fig 2.3, we take a pair of neighboring elements α and β with unit normal vectors $\mathbf{n}_i$ as well as element area A_i. The angle $\theta_{\alpha\beta}$ measures the angle between two normal vectors. The four nodes are represented by position vectors $\mathbf{p}_i$ and the edge vectors are calculated by $\mathbf{a}_{ij} = \mathbf{p}_i - \mathbf{p}_j$.

To evaluate the bending forces, we take the derivative of the discretized bending energy with respect to nodal position $\mathbf{X}_i$:

$$\mathbf{F}_{b,i} = -\frac{\partial E_b}{\partial \mathbf{X}_i} = -k_b \sin(\theta_{\alpha\beta} - \theta_0) \frac{\partial \theta}{\partial \mathbf{X}_i}, \tag{2.25}$$

where the term $\partial\theta/\partial\mathbf{X}_i$ can be approximated as (CITE FEDOSOV):

$$\frac{\partial \theta}{\partial \mathbf{X}_i} = \frac{\partial \arccos(\mathbf{n}_1 \cdot \mathbf{n}_2)}{\partial \mathbf{X}_i} = -\frac{1}{\sqrt{1 - \cos^2\theta_{\alpha\beta}}} \frac{\partial \mathbf{n}_1 \cdot \mathbf{n}_2}{\partial \mathbf{X}_i}, \tag{2.26}$$

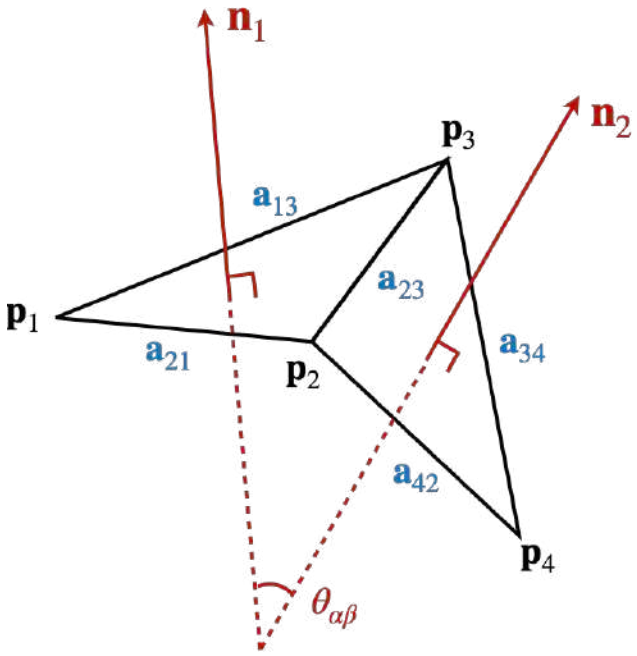


Figure 2.3: Illustration of the four-point method to evaluate bending nodal forces between two neighboring triangular elements.

To conclude, the resolved nodal bending forces on $\mathbf{p}_i$ follows:

$$\begin{aligned}
\mathbf{F}_{\mathbf{p}_1} &= b_{11}\left(\mathbf{a}_{21}\times\mathbf{a}_{31}\times\mathbf{a}_{32}\right)+b_{12}\left(\mathbf{a}_{34}\times\mathbf{a}_{24}\times\mathbf{a}_{32}\right)\\
\mathbf{F}_{\mathbf{p}_2} &= b_{11}\left(\mathbf{a}_{21}\times\mathbf{a}_{31}\times\mathbf{a}_{13}\right)+b_{12}\left(\mathbf{a}_{21}\times\mathbf{a}_{31}\times\mathbf{a}_{34}+\mathbf{a}_{34}\times\mathbf{a}_{24}\times\mathbf{a}_{13}\right)+b_{22}\left(\mathbf{a}_{34}\times\mathbf{a}_{24}\times\mathbf{a}_{34}\right)\\
\mathbf{F}_{\mathbf{p}_3} &= b_{11}\left(\mathbf{a}_{21}\times\mathbf{a}_{31}\times\mathbf{a}_{21}\right)+b_{12}\left(\mathbf{a}_{21}\times\mathbf{a}_{31}\times\mathbf{a}_{42}+\mathbf{a}_{34}\times\mathbf{a}_{24}\times\mathbf{a}_{21}\right)+b_{22}\left(\mathbf{a}_{34}\times\mathbf{a}_{24}\times\mathbf{a}_{42}\right)\\
\mathbf{F}_{\mathbf{p}_4} &= b_{12}\left(\mathbf{a}_{21}\times\mathbf{a}_{31}\times\mathbf{a}_{23}\right)+b_{22}\left(\mathbf{a}_{34}\times\mathbf{a}_{24}\times\mathbf{a}_{23}\right),
\end{aligned} \tag{2.27}$$

where

$$\begin{aligned}
b_{11} &= -\frac{k_b(\sin\theta_{\alpha\beta}\cos\theta_0-\cos\theta_{\alpha\beta}\sin\theta_0)\cos\theta_{\alpha\beta}}{\sqrt{1-\cos^2\theta_{\alpha\beta}}||\mathbf{a}_{21}\times\mathbf{a}_{31}||^2}\\
b_{12} &= \frac{k_b(\sin\theta_{\alpha\beta}\cos\theta_0-\cos\theta_{\alpha\beta}\sin\theta_0)}{\sqrt{1-\cos^2\theta_{\alpha\beta}}||\mathbf{a}_{21}\times\mathbf{a}_{31}||||\mathbf{a}_{34}\times\mathbf{a}_{24}||}\\
b_{22} &= -\frac{k_b(\sin\theta_{\alpha\beta}\cos\theta_0-\cos\theta_{\alpha\beta}\sin\theta_0)\cos\theta_{\alpha\beta}}{\sqrt{1-\cos^2\theta_{\alpha\beta}}||\mathbf{a}_{34}\times\mathbf{a}_{24}||^2}
\end{aligned} \tag{2.28}$$

.

The detailed calculation and formulation can be found in SEC. The total bending forces $\mathbf{F}_{b,i}$ acting on the node i due to the bending deformation of each surrounding element j shared by the node: $\mathbf{F}_{b,i} = \sum_j (\mathbf{F}_{b,i})_j$, where the sum is over all the elements meeting at the node.

2.3 Modeling of fluid

In this work, we assume the particle Reynolds number is negligible, which means the inertia of the fluid at the scale of the particle size vanishes. Consequently, the sum of all the forces in Stokes flow is zero everywhere:

$$\sum_i \mathbf{F}_i = \mathbf{0}. \tag{2.29}$$

More specifically, for any material point on the sheet surface (or discretized node in the current case) $\mathbf{X}_i$, the elastic nodal forces $\mathbf{F}_{e,i}$ as the forces exerted by the sheet on the surrounding fluid, is balanced with the hydrodynamic forces $\mathbf{F}_{h,i}$ acting on the sheet:

$$\mathbf{F}_{e,i} + \mathbf{F}_{h,i} = \mathbf{0}. \tag{2.30}$$

To evaluate the dynamics of the sheet, we make full use of the no-slip boundary condition, where the velocity of any material point on the sheet matches the fluid velocity at the same position. To calculate the fluid velocity, we need to consider the perturbation due to the forces exerted on the fluid, or simply the elastic force of the sheet $\mathbf{F}_e$. As introduced in the previous SEC, we solve the velocity field based on the method of regularized Stokeslet. In Stokes flow, the fluid motion is governed by the linear Stokes equation and the continuity equation:

$$\begin{gathered} -\nabla p + \eta \nabla^2 \mathbf{v} + \textstyle\sum_i \mathbf{F}_i \delta_\kappa(\mathbf{x} - \mathbf{X}_i) = \mathbf{0} \\ \nabla \cdot \mathbf{v} = 0. \end{gathered} \tag{2.31}$$

The perturbation velocity field at any location $\mathbf{x}$ generated due to a regularized point force

$\mathbf{f} = \mathbf{F}\delta_\kappa(\mathbf{x} - \mathbf{X}_i)$ at $\mathbf{X}_i$ can be represented using a regularized Stokeslet $\mathbf{G}_\kappa$:

$$\mathbf{v}_p(\mathbf{x}) = \mathbf{G}_\kappa(\mathbf{x} - \mathbf{X}_i) \cdot \mathbf{F}. \tag{2.32}$$

Here, we choose a regularization function with a Gaussian distribution, where the difference between the regularized solution and the singular solution decays exponentially:

$$\delta_\kappa(r) = \frac{\kappa^3}{\sqrt{\pi}^3} \exp(-\kappa^2 r^2) \left[\frac{5}{2} - \kappa^2 r^2\right], \tag{2.33}$$

where $r = ||\mathbf{x} - \mathbf{X}_i||$ and κr scales regularization distance. As $\kappa r \to \infty$, $\mathbf{G}_\kappa$ reduces to Stokeslet solution $\mathbf{G}(\mathbf{x} - \mathbf{X}_i) = 1/8\pi\eta r(\mathbf{I} + (\mathbf{x} - \mathbf{X}_i)(\mathbf{x} - \mathbf{X}_i)/r^2)$. Therefore, the velocity of sheets at nodal position $\mathbf{X}$ is a combination of free flow flow $\mathbf{v}_\infty$ and perturbation velocity $\mathbf{v}_p$:

$$\mathbf{v}(\mathbf{x}) = \mathbf{v}_\infty(\mathbf{x}) + \mathbf{v}_p(\mathbf{x}). \tag{2.34}$$

Here, the free flow field depends on the specific problem we are interested in. Through no-slip condition, the dynamics of material points $\mathbf{X}_i$ on the sheet are approximated from the fluid velocity at the same location:

$$\frac{d\mathbf{X}_i}{dt} = \mathbf{v}(\mathbf{X}_i). \tag{2.35}$$

2.4 Model validation

In this section, we aim to validate our model with two validation cases. The first validation case examined the perturbation velocity field due to the presence of a rigid disk freely suspended in biaxial extensional flow, where we can derive an analytical solution for comparison. In the second case, we compare the buckling threshold for a rectangle tumbling in shear flow with an experimental study. In addition, we also show several cases for the

validation of boundary conditions in the model.

2.4.1 Validation case I: a rigid disk in biaxial extensional flow

We proposed a validation case for the current model by considering a rigid disk freely suspended in biaxial extensional flow $\mathbf{v} = \dot{\epsilon}(x/2, y/2, -z)$. At equilibrium, the disk stays flat and perturbs the surrounding fluid. We derive an analytical solution based on a rigid disk perturbing biaxial extensional flow and compare the perturbation velocity around the disk with our numerical solutions. Several comments can be made:

- The case only validates the in-plane stretching part of the model. There has not been any analytical approach to validate the bending formulation, but we will show a comparison with an experimental study later.
- The analytical solution we derived can be applied to sheets beyond the rigid limit since the solution is only determined by the equilibrium shape. Thus, it is also applicable to a disk that has limited deformability (very small Ca).

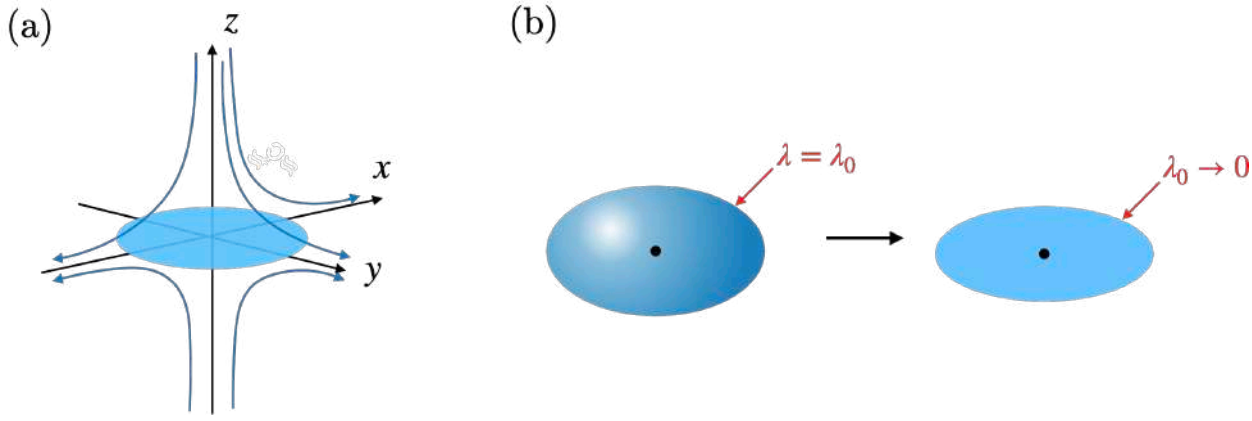


Figure 2.4: (a) Scenario setup: a disk radially stretched in a biaxial extensional flow and reaches equilibrium. (b) Illustration of λ in an oblate spheroidal coordinate system for an oblate spheroid and a disk.

To derive the analytical solution, we assume the rigid disk with an equilibrium radius m, and we solve the stream function in a combined cylindrical (r, θ, z) and oblate spheroidal

(ξ, η, ϕ) coordinate. Typically, we define a coordinate surface parameter $\lambda = \sinh \xi$ $(0 < \lambda < \infty)$ as a nonnegative real number that defines a family of confocal oblate spheroids. That is, on the surface of the spheroid, $\lambda = \lambda_0$ remains a constant. We also define an angle parameter $\zeta = \cos \eta$ $(-1 < \zeta < 1)$.

In this case, we solve the Stokes equation in a biaxial extensional flow $\mathbf{v}_\infty = \dot{\epsilon}(x/2, y/2, -z)$ in the stream function form: $\psi_\infty = -r^2 z\dot{\epsilon}/2$:

$$E^2(E^2\psi) = 0, \text{ where } E^2 = \frac{1}{m^2(\lambda^2+\zeta^2)}[(\lambda^2+1)\frac{\partial^2}{\partial\lambda^2} + (1-\zeta^2)\frac{\partial^2}{\partial\zeta^2}]. \tag{2.36}$$

Here, the operator E^2 is in a modified oblate spheroidal coordinate. We derive an analytical solution that describes the stream function of the velocity field around the disk. A detailed derivation for a similar system of oblate spheroid can be found in [55]. The analytical solution for the stream function is:

$$\psi = -\frac{1}{2}r^2 z\dot{\epsilon}\left[1 - \frac{2}{\pi}\left(\cot^{-1}\lambda - \frac{\lambda}{\lambda^2+1}\right)\right]. \tag{2.37}$$

The solution consists of two parts. In the bracket, the first unit constant recovers the free biaxial extensional flow as ψ_∞, and the second complicated term describes the perturbation due to the presence of a disk. The solution satisfies three boundary conditions:

1. The streamline assembles free space when far away from the disk (as $\lambda \to \infty$, $\psi(\lambda) \to \psi_\infty$).

2. The velocity vanishes on the sheet surface (no-slip surface: $\frac{\partial\psi}{\partial\lambda}(\lambda \to 0) = 0$).

3. No fluid passes through the sheet surface (no-penetration surface: $\frac{\partial\psi}{\partial\mathbf{n}}(\lambda \to 0) = \psi(\lambda \to 0) = 0$).

We have verified the above boundary conditions and the details of derivation and boundary conditions validation can be found in Appendix. In cylindrical coordinates (r, θ, z), the

velocity along r and z direction can be estimated from stream function ψ:

$$v_r = -\frac{1}{r}\frac{\partial \psi}{\partial z}, \quad v_z = \frac{1}{r}\frac{\partial \psi}{\partial r}, \quad ||\mathbf{v}|| = \sqrt{v_r^2 + v_z^2}. \tag{2.38}$$

The full expression of analytical velocity magnitude $||\mathbf{v}_{\text{analytical}}||$ around the disk is:

$$||\mathbf{v}_{\text{analytical}}|| = \left(\frac{r^2}{4}\left[1 - \frac{2}{\pi}\left(\cot^{-1}\lambda - \frac{\lambda}{\lambda^2+1}\right) + \frac{2z^2}{m^2\lambda\pi(\lambda^2+1)^2}\left(1 + \frac{r^2+z^2+m^2}{\sqrt{(r^2+z^2-m^2)^2+4m^2z^2}}\right)\right]^2 \right.$$
$$\left. + z^2\left[1 - \frac{2}{\pi}\left(\cot^{-1}\lambda - \frac{\lambda}{\lambda^2+1}\right) + \frac{r^2}{m^2\lambda\pi(\lambda^2+1)^2}\left(1 + \frac{r^2+z^2-m^2}{\sqrt{(r^2+z^2-m^2)^2+4m^2z^2}}\right)\right]^2 \right)^{1/2}. \tag{2.39}$$

The numerical solution of velocity magnitude $||\mathbf{v}_{\text{numerical}}||$ is obtained by performing simulations of an almost rigid disk exposed to a biaxial extensional flow at equilibrium. We enforce small in-plane deformability with a small capillary number $\text{Ca} = 0.01$, which shows a negligible deformation (less than 0.01% change in the disk area). At equilibrium, the disk will be slightly stretched with a final radius m, which will be used for the analytical solution.

The velocity $\mathbf{v}$ around the disk in both analytical and numerical solutions has two contributions: a free velocity $\mathbf{v}_f$ as the background biaxial extensional flow and a perturbation velocity $\mathbf{v}_p$ due to the presence of the disk:

$$\mathbf{v} = \mathbf{v}_f + \mathbf{v}_p. \tag{2.40}$$

We mainly compare the perturbation velocity norm $||\mathbf{v}_p||$ between analytical and numerical solutions. In Fig 2.5(a)-(b), we choose a slice ($x - z$ plane, where the disk is shown as a line at the origin) around the disk and show the difference in $||\mathbf{v}_p||$ between two solutions. Overall, the model shows good agreement with the analytical solution. Though some parts in Fig 2.5(a) shows a relatively large error percentage, the actual difference in magnitude remains small.

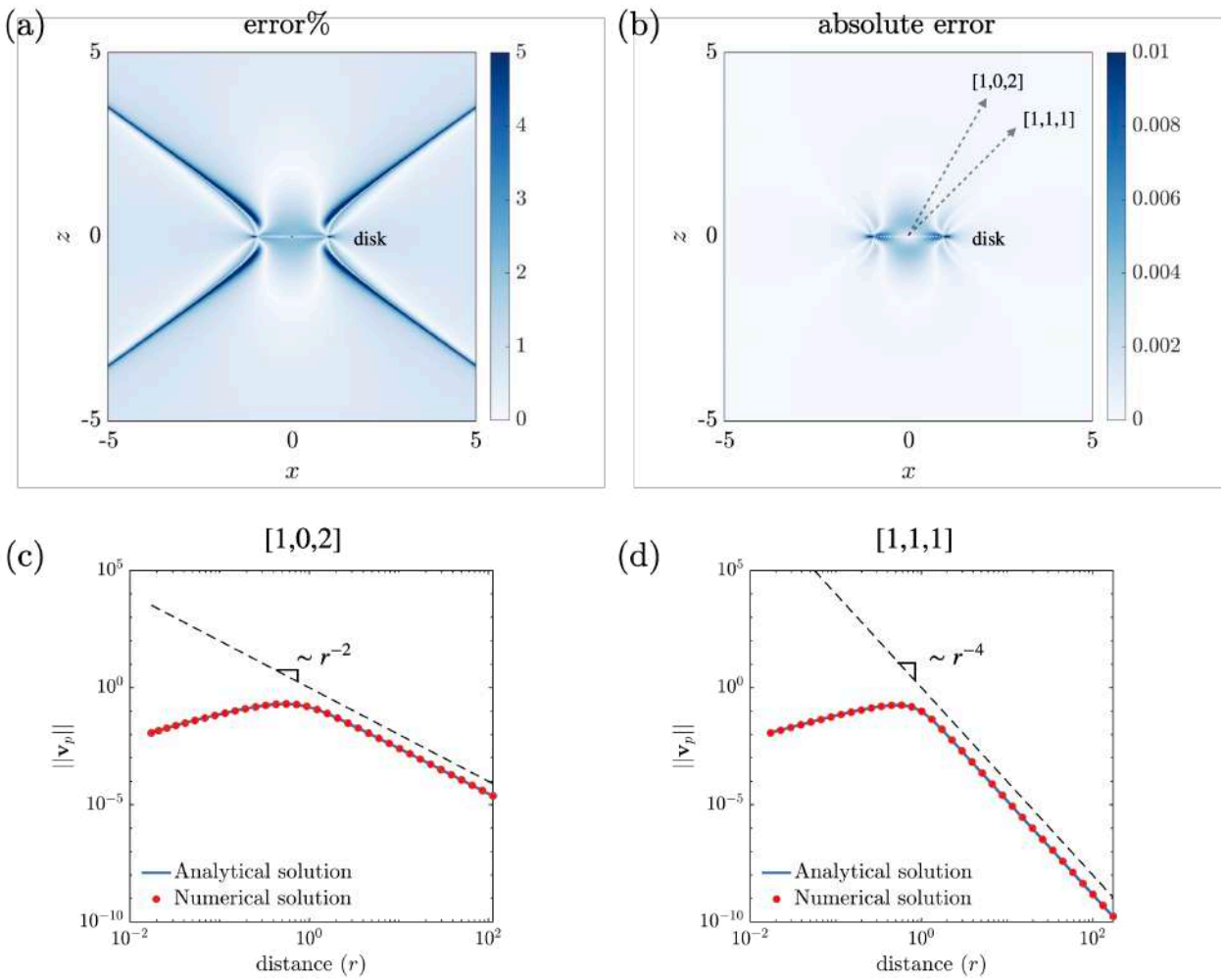


Figure 2.5: The difference in perturbation velocity norm $||\mathbf{v}_p||$ between analytical and numerical solutions in the plane $y = 0$: (a) Error percentage profile (b) Absolute error profile. (c) Perturbation velocity norm $||\mathbf{v}_p||$ vs. distance r along a line away from the origin for a disc in biaxial flow: (c) The line chosen follows the vector [1,0,2] and the black dashed line is proportional to r^{-2}. (d) The line chosen follows the vector [1,1,1] and the black dashed line is proportional to r^{-4}.

For a more detailed comparison, we choose two arbitrary paths away from the disk center in Fig 2.5(c)-(d). The results also show excellent agreement with the analytical solution. Interestingly, along most of the random paths tested, the perturbation velocity norm decays as r^{-2} (Fig 2.5(c)), while some specific paths lead to a faster decay rate as r^{-4}(Fig 2.5(d)). As introduced in the previous section, a neutrally-buoyant particle has zero net force in Stokes flow. Therefore, the major contribution of perturbation velocity comes from the dipole which decays as r^{-2}. The presence of a faster decay rate along certain directions indicates the force

dipole vanishes and the dominant term is the quadrupole.

2.4.2 Validation case II: a flexible rectangle in simple shear flow

Though there is no analytical approach to verify bending formulation, we compare our model with a recent experiment by Perrin and coworkers [133]. We investigated the buckling dynamics of a rectangle polymer film (with the longer edge $2a$) tumbling in shear flow.

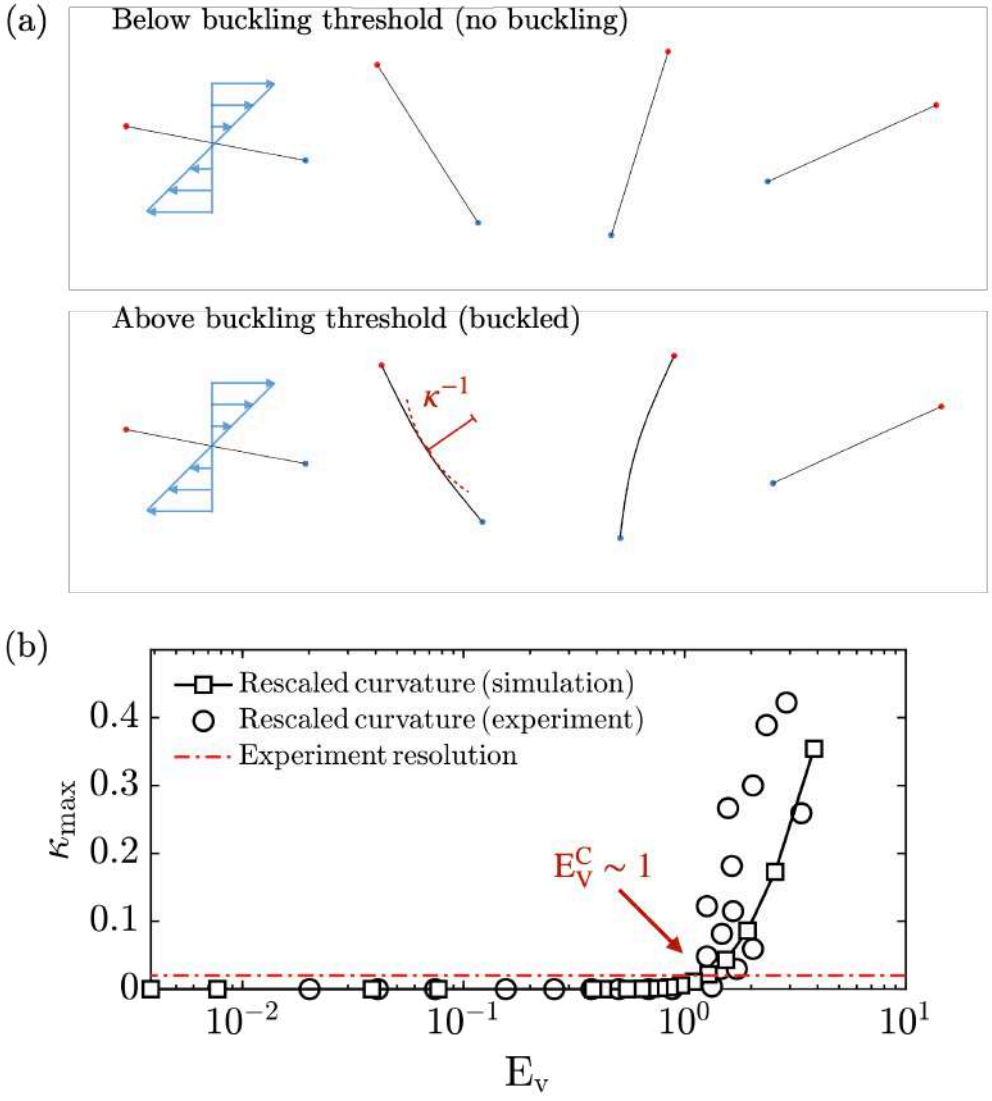


Figure 2.6: (a) Examples of a rectangle tumbling in simple shear flow with a case below the buckling threshold where no deformation is observed and a case above the threshold where the sheet buckles. (b) Comparison with experimental results from [133]. The buckling threshold is estimated to be $E_V^C \sim 1$ in both setups.

For a rigid and stiff film in simple shear flow with the normal of the sheet lives in the flow-gradient plane, the sheet will tumble due to the rotation component of the shear. When the sheet is sufficiently flexible, the compressive stresses from the shear flow trigger the buckling instability. The ratio between flow strength to deform the sheet and sheet elasticity that resists deformation is described by an elasto-viscous number $\mathrm{E_V}$ described in Sec 2.1.2. Examples of sheets showing buckling instability are indicated in Fig 2.6(a). Following the method in experiments, we measured the curvature at the sheet center and recorded the largest curvature $\kappa_{\max}$ during the tumbling. After sweeping the parameter space of dimensionless bending stiffness $\mathrm{E_V}$, we determined a critical buckling threshold $\mathrm{E_V^C} \sim 1$ based on the resolution of curvature measurement $\kappa = 0.02a$ used in [133]. Surprisingly, the buckling threshold shows good agreement with experimental observation. Additionally, the results also agree well with the 2D simulation performed in [133], showing the robustness of our bending formulation.

2.4.3 Validation of boundary conditions

The freely suspended sheet in fluid satisfies no-slip boundary condition. That is, the velocity of a material point matches the fluid velocity at the same position. This also implies a no-penetration surface where no fluid passes through the sheet. We carefully check the accuracy of boundary conditions as they are all indirectly implemented in the model.

Although we satisfy the no-slip and no-penetration conditions to high accuracy on the nodal points $\mathbf{X}_i$, with a finite discretization these conditions cannot be exactly satisfied at every point on the sheet. In particular, with a finite-resolution mesh, the sheet may be slightly permeable, so we address here the effect of resolution on the velocity normal to the sheet surface relative to the velocity of the sheet itself. At the center of each triangular element, we can define two velocities: $\mathbf{v}_{\mathrm{int}}$ is the velocity estimated by linear interpolation from the velocities on the nodes, and $\mathbf{v}_{\mathrm{num}}$ is the velocity obtained from the regularized Stokeslet expression evaluated at that point. At that point the permeation velocity v_{per},

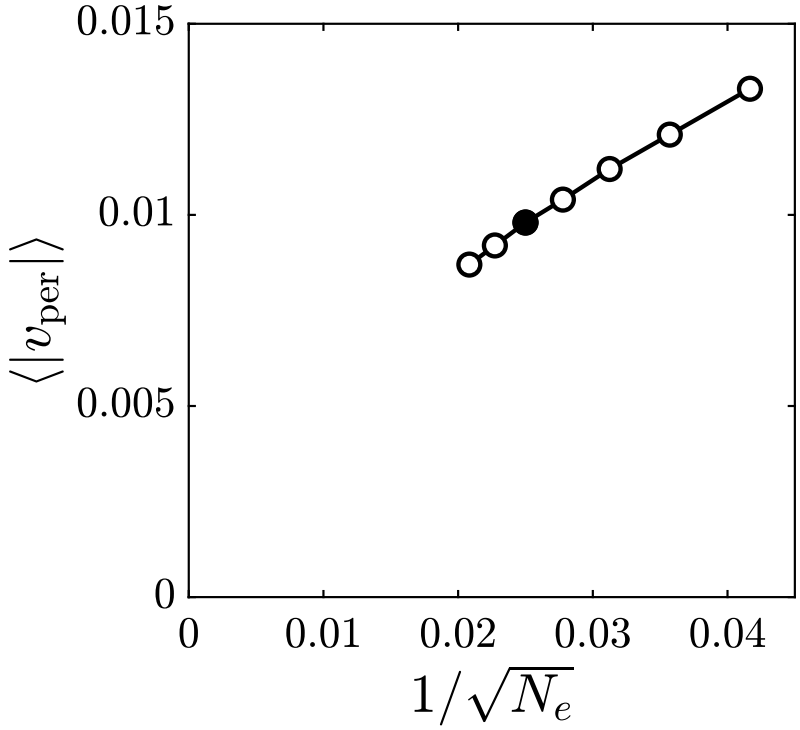


Figure 2.7: Average magnitude of permeation velocity, $\langle|v_{\rm per}|\rangle$, at element centers for a sheet (the taco shape in Fig. 4.2(a)) vs. mesh size $1/\sqrt{N_e}$. The filled symbol indicates the mesh of 1600 triangular elements used for the main set of results.

i.e. the error in the no-penetration condition, is given by

$$v_{\rm per} = \mathbf{n} \cdot (\mathbf{v}_{\rm int} - \mathbf{v}_{\rm num}), \tag{2.41}$$

where $\mathbf{n}$ is the unit normal of the element. To evaluate $v_{\rm per}$, we use as an example the steady state sheet conformation shown below in Fig. 4.2(a), and note that the linear size of each element in a mesh with N_e elements scales as $1/\sqrt{N_e}$. Figure 2.7 shows the averaged magnitude of perturbation velocity $\langle|v_{\rm per}|\rangle$ vs. $1/\sqrt{N_e}$ for this case. The result indicates that the error is small and tends roughly linearly toward zero as the mesh gets finer. The choice of mesh size (filled symbol on the plot) used for the main results gives about 1% error for points at the element centers, and as noted above, we perfectly satisfy no-slip and no-penetration conditions on the nodal positions $\mathbf{X}_i$.

3

Coil-stretch-like transition of elastic sheets in extensional flow

[1] The conformation of a long linear polymer dissolved in fluid and exposed to an extensional flow is well-known to exhibit a “coil-stretch" transition, which for sufficiently long chains can lead to bistability. The present work reports computations indicating that an analogous “compact-stretched" transition arises in the dynamics of a thin elastic sheet. Sheets of nominally circular, square or rectangular shape are simulated in planar and biaxial flows using a finite element method for the sheet conformations and a regularized Stokeslet method for the fluid flow. If a neo-Hookean constitutive model is used for the sheet elasticity, the sheets will stretch without bound once a critical extension rate, as characterized nondimensionally by a capillary number, is exceeded. Nonlinear elasticity, represented with the Yeoh model, arrests the stretching, leading to a highly-stretched steady state once the critical capillary number is exceeded. For all shapes and in both planar and biaxial extension, a parameter regime exists in which both weakly stretched (compact) and strongly stretched states can be found, depending on initial conditions. I.e. this parameter regime displays bistability. As in the long-chain polymer case, the bistable behavior arises from the hydrodynamic interac-

[1]The text of this chapter is adapted from the publication by Y. Yu and M. D. Graham *Soft Matter*, 2021,17, 543-553

tion between distant elements of the sheet, and vanishes if these interactions are artificially screened by use of a Brinkman model for the fluid motion. While the sheets can transiently display wrinkled shapes, all final shapes in planar and biaxial extension are planar.

3.1 Introduction

In recent years, thin-structured materials have gained considerable attention in many fields. For example, freely suspended sheets immersed in a fluid environment arise the synthesis and processing of polymer networks [87, 123]. Polymer sheets are often used as planar substrates in soft origami-inspired devices, which further assemble into complicated structures [62, 63, 114, 163]. Thin polymer films are also used as the basis of self-propelled swimming devices, with living cells deposited on the sheet to drive the motion [45]. Highly extensible polymer films, hydrogels structures and their composites have shown great potential in biomedical and electronic applications [23, 48, 94, 106, 202]. Many of above examples involve complicated fluid-structure interactions, but little is known about the dynamics of soft sheet-like particles in fluid. The present work aims to shed light on some aspects of these dynamics through simulations of soft elastic sheets in two canonical flow fields that arise in many applications such as coating operations: planar and biaxial extensional flows.

While soft elastic sheets have not been studied in these flows, long-chain polymer molecules have been. An important phenomenon in this situation is the coil-stretch transition [35, 47, 151]: polymers show an abrupt change in conformation from a coiled state to a strongly stretched state when reaching a critical flow strength in planar extension. The discontinuity in the stretched length marks a bistable regime that corresponds to the existence of multiple stable (or more precisely, metastable) conformations. This behavior was first predicted by De Gennes in 1974 [35], based on the idea that, compared to a fully stretched state, in the coiled state the inner monomers are hydrodynamically screened and therefore less exposed to the strong stretching flow. Fuller and Leal modeled this effect using a bead-spring dumbbell with

conformation-dependent drag on the beads, showing that this simple approach could yield coil-stretch hysteresis [47]. Schroeder *et al.* experimentally confirmed this prediction, visualizing the hysteresis behavior with fluorescent dyed Escherichia coli DNA molecules in dilute solution under planar extension [151]. They also probed the hysteresis phenomenon with a Brownian dynamics simulation of a bead-spring polymer model and found a double-welled effective potential of polymer conformational energy around the transition flow strength that leads to hysteresis in conformation. The coil-stretch transition and hysteresis are also observed in simulations beyond the dilute limit. Mohammad *et al.* applied molecular dynamics simulation to study atomistic entangled polyethylene melts in planar extension [115]. They found that the bistable region in the polymer melts is wider than in dilute solution, with a higher transition flow strength.

Similar conformational transitions have been observed in systems other than polymers as well. Kantsler *et al.* performed experiments to study the stretching of a single tubular vesicle suspended in planar extensional flow [70]. They found a transition in conformation from a tubular to a dumbbell shape when reaching a critical extension rate. With further increasing flow strength, the shape evolves to a pearling state due to unstable higher order shape modes. This behavior is also found in a computational study by Narsimhan *et al.* [117], who also considered other extensional flows. Kumar *et al.* recently developed a microfluidic Stokes trap to make a vesicle remain at the stagnation point and extended the work of Kantsler *et al.* by giving a more detailed analysis of the vesicle shape transition in the parameter space of reduced volume and bending modulus [80].

In contrast to the substantial literature on polymers or vesicles, there is only a small amount of work on the dynamics of deformable freely suspended sheets in flow and no prior study has probed the possibility of hysteretic conformational transitions of extensible sheets in extensional flow. (Though there exist many studies on flapping sheets with a clamped edge in flow (flapping flags) [5, 155], this is not our interest here.) Motivated by applications of relatively inextensible sheetlike materials such as graphene and boron

nitride, Green and Xu investigated the dynamics of freely suspended nanosheets in both extensional and shear flow [186, 187]. They modeled a nominally square sheet with a bead-rod network inspired by coarse-grained models of polymers in solution, simulating the model with a Brownian dynamics method. Because of the inextensibility of the rods, the model they consider is highly resistant to stretching deformations, so much of the dynamics in this system are determined by the relative importance of flow, bending resistance and Brownian motion. In biaxial extensional flow, a sheet with large bending stiffness tends to stay at a flat conformation. With small bending stiffness, Brownian motion leads to crumpling [187]. In shear flow at low bending stiffness, they found that sheets undergo a cyclic crumple-stretch-crumple motion [186]. Botto and co-workers performed molecular dynamic simulations to study the liquid phase exfoliation of graphite sheets in shear. They studied the critical shear rate for exfoliation to occur in different solvent and developed a theoretical model that can predict the critical shear rate in simulation [51]. They also applied molecular dynamics simulations to explore the effects of hydrodynamic slip on the dynamics of a sheet in shear [67]. Interestingly, in the presence of slip, they found that a rigid nanosheet can take on a stable steady orientation with a finite orientation angle with respect to the flow direction. Finally, Dutta and Graham investigated the dynamics of a piecewise rigid creased sheet – a model of an origami figure known as a Miura pattern [39]. Depending on geometry and initial conditions, this sheet can show steady, periodic or quasiperiodic orientational and conformational dynamics in shear.

The present work describes the behavior of sheetlike particles in a parameter regime that has not been explored in the studies above. We consider soft (highly extensible) elastic sheets, taking Brownian forces to be negligible compared to hydrodynamic and elastic ones, and focus on planar and biaxial extensional flows. We consider three different rest shapes: disk, square, and rectangle. The rest of the paper is organized as follows: Section 3.2 summarizes the model we use and the discretization and solution methods. Section 3.3 shows detailed results for the sheet dynamics, illustrating a bistability phenomenon analogous to

the coil-stretch transition. Concluding remarks are presented in Section 3.4.

3.2 Methods

We briefly illustrate the modeling of a freely suspended soft sheet in extensional flow. We consider a very thin, neutrally buoyant, elastic sheet suspended in an unbounded, incompressible Newtonian fluid with viscosity η and density ρ, and subjected to planar and biaxial extensional flow fields. Expressed in Cartesian coordinates, the fluid velocity $\mathbf{v}_\infty$ in the absence of the particle is given in planar extension by $\mathbf{v}_\infty = \dot{\epsilon}\,[x, 0, -z]^T$ and in biaxial extension by $\mathbf{v}_\infty = \dot{\epsilon}\,[x/2, y/2, -z]^T$, with $\dot{\epsilon}$ the strain rate.

The sheet is modeled as an elastic continuum. Fluid cannot pass through the sheet, and each point on the sheet is taken to move with the local velocity of the fluid. That is, the usual no-penetration and no-slip boundary conditions are applied for the fluid velocity at the sheet surfaces. In this case, no specification of the details of fluid-solid interfacial forces is necessary. As noted above, for atomically smooth surfaces, the no-slip boundary condition may not apply, in which case interesting dynamics have been seen to arise in simulations of rigid sheets in shear flow [67]. That case is not considered here.

In this work, we focus on sheets with three rest shapes: a disk with radius a, a square with edge $2a$, and a rectangle with short edge a and long edge $2a$. The rest thickness h is much less than a such that the fluid exerts no traction along their edges.

The mechanical response of a very thin sheet is split into two parts: in-plane shearing elasticity, with strain energy E_s, and out-of-plane bending elasticity, with strain energy E_b. The total strain energy is thus

$$E = E_s + E_b. \tag{3.1}$$

The in-plane shearing energy E_s on the sheet surface Γ can be written as

$$E_s = \int_\Gamma W \, dS, \tag{3.2}$$

where W is the areal shear strain energy density that is defined pointwise on the sheet surface. We consider the sheet as isotropic and incompressible and describe the in-plane energy with the Yeoh model, a model used to simulate rubber-like materials [192]. Its strain elastic energy W is given by:

$$W = \frac{G}{2}(I-3) + cG(I-3)^3 . \tag{3.3}$$

Here, $I = \lambda_1^2 + \lambda_2^2 + \lambda_3^2$ is the first invariant of the right Cauchy-Green deformation tensor, which is a function of principal stretch ratios λ_i, and G is a two-dimensional shear elasticity modulus given by $G_{3D}h$, where G_{3D} is the usual 3D shear modulus. The quantities λ_1 and λ_2 are the local principal stretch ratios along the (local) tangential directions of the sheet surface, while the normal stretch ratio λ_3 is determined by incompressibility of the sheet material: $\lambda_1\lambda_2\lambda_3 = 1$. The parameter c determines the weight of the cubic terms in the energy formulation and determines whether the material is strain-softening or strain-hardening. When $c = 0$, the Yeoh model reduces to the strain-softening neo-Hookean (NH) model.

For bending energy, we apply a simple linear bending model that penalizes deflection between neighboring discretized elements [42, 43]. Details of the discretization will be covered in later paragraphs. This energy has the form

$$E_b = \sum_{adjacent\ \alpha,\beta} k_b\left[1 - \cos(\theta_{\alpha\beta} - \theta_0)\right], \tag{3.4}$$

where k_b is a bending constant, $\theta_{\alpha\beta}$ is the angle between two neighboring elements and θ_0 is the angle at equilibrium. In this study, we assume the sheet is flat at rest, so $\theta_0 = 0$ for all adjacent element pairs. The bending constant $k_b = \sqrt{3}(2K_B + \overline{K_B})$ denotes an averaged bending modulus, which is derived from the Helfrich bending energy of a spherical shell with a zero spontaneous curvature [43]. Here K_B is the bending modulus and is related to the Gaussian curvature modulus $\overline{K_B}$ by $\overline{K_B}/K_B = \nu - 1$, where the Poisson ratio $\nu = 1/2$ for

an incompressible sheet [169]. A nondimensional bending stiffness can be defined: $\hat{K}_B = K_B/a^2G$.

The simulations performed and the results presented are in nondimensional form. Lengths are scaled with a and time with the inverse extension rate $1/\dot{\epsilon}$. Forces are nondimensionalized by viscous drag force $\eta\dot{\epsilon}a^2$. With these choices, two nondimensional parameters arise that characterize the deformability of the sheet by the flow: the in-plane deformability is determined by the capillary number $\mathrm{Ca} = \eta\dot{\epsilon}a/G$, with the competition between flow and bending deformations characterized by $\mathrm{Ca}/\hat{K}_B$. It is worth pointing out here that in all cases studied here, the sheet becomes flat at long times, in which case the bending energy becomes irrelevant. It does, however, have an effect on dynamics at short times, determining the transient wrinkling behavior that the sheet exhibits while orienting with the flow.

Our results below indicate that complex behavior in extensional flow occurs once $\mathrm{Ca} \gtrsim 0.1$. We present here some estimates to illustrate how these results will be relevant to microscale sheets of specific materials. Materials like polymer hydrogels usually have shear modulus $G_{3D} \approx 1\mathrm{kPa})$ [48, 94, 106]. If a disc-shaped polyethylene glycol (PEG) hydrogel sheet with radius of 100 μm and thickness of 100 nm is suspended in water ($\eta \sim 10^{-3}$ Pa $\cdot$ s), a modest extension rate of about $10^2\mathrm{s}^{-1}$ will yield $\mathrm{Ca} = 0.1$.

Other interesting two-dimensional materials, such as graphene flakes, have much too large a shear modulus ($G_{3D} \approx 300$ GPa[97]) to yield a capillary number in the range where they will be strongly stretched by flow, except in extreme conditions.

In addition, the thermal fluctuation for polymer sheets at room temperature is considered negligible compared to strain energy. If we still consider the above PEG hydrogel, its estimated shear strain energy ($\sim 10^9 k_BT$) and bending energy ($\sim 3 \times 10^5 k_BT$) are much larger than thermal energy. Therefore, thermal fluctuations will have a negligible influence on the dynamics.

The numerical method for the elasticity problem is adapted from Charrier *et al.* [21, 128]. We simulate the sheet by keeping track of material points as nodes on the sheet surface. The

sheet surface is discretized into triangular elements with a node at each corner. From the above two energies, we obtain the elastic force $\mathbf{F}_e$ exerted on each node from the first variation of the total energy with respect to the nodal displacements. Each discretized element of the sheet is assumed to have homogenous deformation, so the element edges always remain linear. The deformed element is compared to its equilibrium shape under a local coordinate transformation via a rigid body rotation and the displacement for any point inside the element is obtained by linear interpolation from nodes. The detailed implementation can be found in Chapter 2. The total nodal force $\mathbf{F}_e$ is evaluated by summing the elastic force $\mathbf{F}_{e,i}$ due to deformation of each surrounding element shared by the node: $\mathbf{F}_e = \sum_i \mathbf{F}_{e,i}$, where the sum is over all elements meeting at the node. For the results shown, we discretize the disk with 1600 elements and 841 nodes, the square with 2048 elements and 1089 nodes, and the rectangle with 1024 elements and 561 nodes. We have verified that changes in mesh resolution lead to only small quantitative changes in the results and no qualitative changes.

We consider the case of very small sheets, such that the particle Reynolds number $Re = \rho\dot{\epsilon}a^2/\eta$ is much less than unity and the fluid motion is governed by the Stokes equation. Neglecting the inertia of the sheet, the total elastic force $\mathbf{F}_e$ exerted on each node by the surrounding solid is balanced by the force $\mathbf{F}_h$ exerted by the fluid on the node:

$$\mathbf{F}_e + \mathbf{F}_h = \mathbf{0}. \tag{3.5}$$

Thus, the sheet exerts a force on the fluid at each nodal position. To account for the fact that the forces are not completely localized to the nodal positions, we use the method of regularized Stokeslets [28]: the force $\mathbf{F}_i$ exerted by node i on the fluid corresponds to a regularized force density $\mathbf{f}^\kappa = \mathbf{F}\delta_\kappa(\mathbf{x} - \mathbf{x}_i)$, where $\delta_\kappa(\mathbf{x})$ is a regularized delta function with regularization parameter κ. Thus, the governing equations are the Stokes equation with regularized nodal forces and the continuity equation:

$$\begin{aligned} -\nabla p + \eta \nabla^2 \mathbf{v} + \textstyle\sum_i \mathbf{F}_i \delta_\kappa(\mathbf{x}) = \mathbf{0} \\ \nabla \cdot \mathbf{v} = 0. \end{aligned} \tag{3.6}$$

Here the sum is over the nodal positions. The velocity field generated due to a regularized point force $\mathbf{f} = \mathbf{F}\delta_\kappa(\mathbf{x})$ can be represented using a regularized Stokeslet $\mathbf{G}_\kappa$:

$$\mathbf{v}_\kappa(\mathbf{x}) = \mathbf{G}_\kappa(\mathbf{x}) \cdot \mathbf{F}. \tag{3.7}$$

As $1/\kappa \to 0$, $\mathbf{G}_\kappa$ reduces to the usual Stokeslet operator $\mathbf{G}(\mathbf{x}) = 1/8\pi\eta r(\mathbf{I} + \mathbf{xx}/r^2)$, where $r = |\mathbf{x}|$. There are many ways to regularize a delta function $\delta_\kappa(\mathbf{x})$; we choose a regularization function for which the deviation between $\mathbf{G}$ and $\mathbf{G}_\kappa$ decays exponentially as $\kappa r \to \infty$ [50, 59]:

$$\delta_\kappa(\mathbf{x}) = \frac{\kappa^3}{\sqrt{\pi}^3} \exp(-\kappa^2 r^2) \left[\frac{5}{2} - \kappa^2 r^2\right]. \tag{3.8}$$

With this choice,

$$\mathbf{G}_\kappa(\mathbf{x}) = \frac{\operatorname{erf}(\kappa r)}{8\pi\eta r}\left(\mathbf{I} + \frac{\mathbf{xx}}{r^2}\right) + \frac{\kappa e^{-\kappa^2 r^2}}{4\pi^{3/2}\eta}\left(\mathbf{I} - \frac{\mathbf{xx}}{r^2}\right). \tag{3.9}$$

In the simulations, κ must be chosen to scale with the minimum node-to-node distance $l_{\min}$. We take $\kappa l_{\min} = 2.1842$, which is obtained using a validation case discussed below. Due to the no-slip and the no-penetration boundary conditions, the velocity of each node on the sheet surface equals the fluid velocity at the nodal position. This velocity is the sum of the free velocity $\mathbf{v}_\infty$ in the absence of the sheet and the perturbation velocity $\mathbf{v}_p$ generated by the nodal forces:

$$\mathbf{v}(\mathbf{x}) = \mathbf{v}_\infty(\mathbf{x}) + \mathbf{v}_p(\mathbf{x}) = \mathbf{v}_\infty(\mathbf{x}) + \sum_i \mathbf{G}_\kappa(\mathbf{x} - \mathbf{x}_i) \cdot \mathbf{F}_i. \tag{3.10}$$

The position of each node is determined by integrating the velocity with a fourth-order Runge-Kutta method. The time step applied in simulation follows $\Delta t = 0.1\mathrm{Ca} l_{\min}$, with an

upper limit of 5×10^{-4} strain unit.

3.3 Results

3.3.1 Planar extensional flow

We begin the discussion of sheets in planar extensional flow with an important general observation. Consider an initial condition where the sheet is flat, with arbitrary orientation. We find that this initial condition will almost always evolve at long time to a flat shape aligned with the $x - y$ plane, where the x- and y-axes are the extensional and neutral directions for the flow, respectively. The only exception is the case where the sheet is initially oriented perfectly in the $x - z$ plane. By symmetry, this sheet's orientation will remain in this plane for all time. However, this situation seems to be unstable for a sheet of any shape with any finite deformability, as exemplified in Fig 3.1 for a disk. In all cases studied, the transient dynamics, and in particular the degree of transient wrinkling as the sheet is compressed along the z-direction, depend on Ca and $\hat{K}_B$, but eventually a flat state aligned with the $x - y$ plane is reached. Accordingly, all subsequent results consider sheets with this orientation and with $\hat{K}_B = 1 \times 10^{-3}$. Only the in-plane deformability (Ca) is varied in the rest of the paper, as $\hat{K}_B$ has no influence on the final conformation.

Another stability issue arises for sheets whose initial shapes are not circular. Fig 3.2 shows steady states for the three shapes we consider here, for low Ca and the neo-Hookean constitutive model (Eq.3.3 with $c = 0$). For a disk, the steady state is roughly ellipsoidal, as

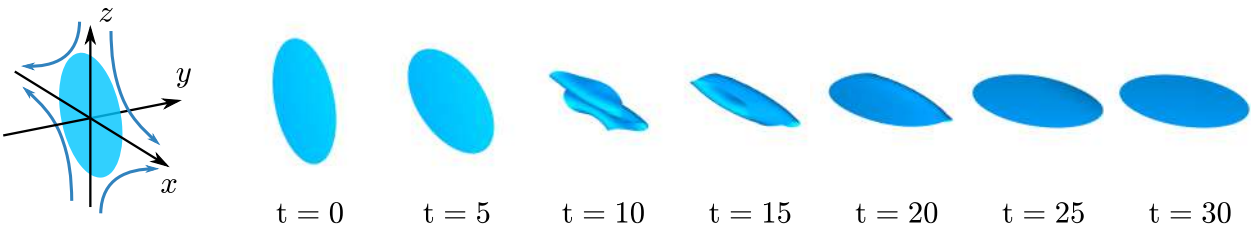


Figure 3.1: Time evolution of a deformable disk initially aligned with the $x - z$ plane in planar extensional flow (Ca $= 0.2$; $\hat{K}_B = 1 \times 10^{-3}$).

shown in Fig 3.2(a). For a non-radially symmetric geometry like a square, we also need to consider its stable orientation. Even at very small Ca, an initial condition where the sides of the square are aligned with the x and y coordinate axes will eventually rotate until the diagonal aligns with the flow direction, reaching a steady state as indicated in Fig 3.2(b). (At Ca = 0, where the sheet is perfectly rigid, Stokes flow reversibility would prevent this reorientation.) By contrast, the rectangular shape we study here remains symmetric at low Ca, as illustrated in Fig 3.2(c)).

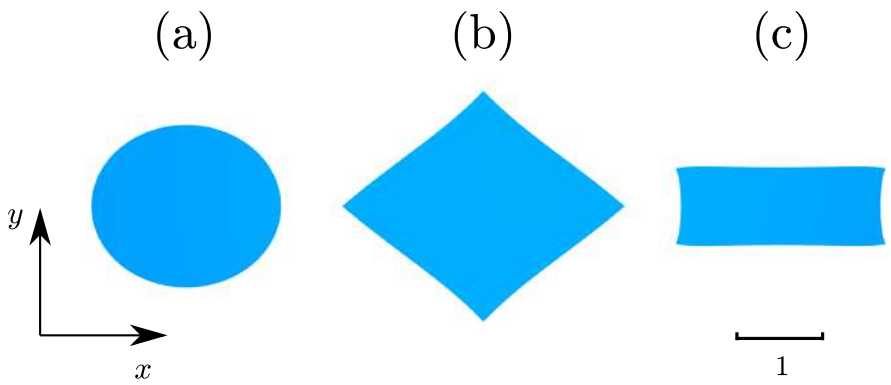


Figure 3.2: Stable steady-state conformation of a sheet in planar extensional flow with neo-Hookean elasticity at Ca = 0.1: (a) disk. (b) a square. (c) rectangle. The scale bar 1 dimensionless length unit.

Continuing with the neo-Hookean model, Fig 3.3 shows the steady-state extension l_s as a function of Ca for the three shapes. In each case, there is a critical value of Ca beyond which the sheet will stretch without bound, not reaching a steady state shape. The appearance of the singularity is caused by the strain-softening property of the neo-Hookean model – the increasing flow strength overcomes the elastic response of the sheet – and is analogous to the behavior found in a bead-spring dumbbell model of a polymer molecule when the spring force obeys Hooke's law [50] and the Weissenberg number exceeds a critical value. In the case of the dumbbell model, if the Hookean spring model is replaced by a finitely extensible spring, the singularity vanishes and the chain reaches a steady state where the chain is highly stretched. This is the simplest version of the "coil-stretch" transition of flexible polymers. In the sheet case, we will refer to conformations at Ca values below the transition as "compact".

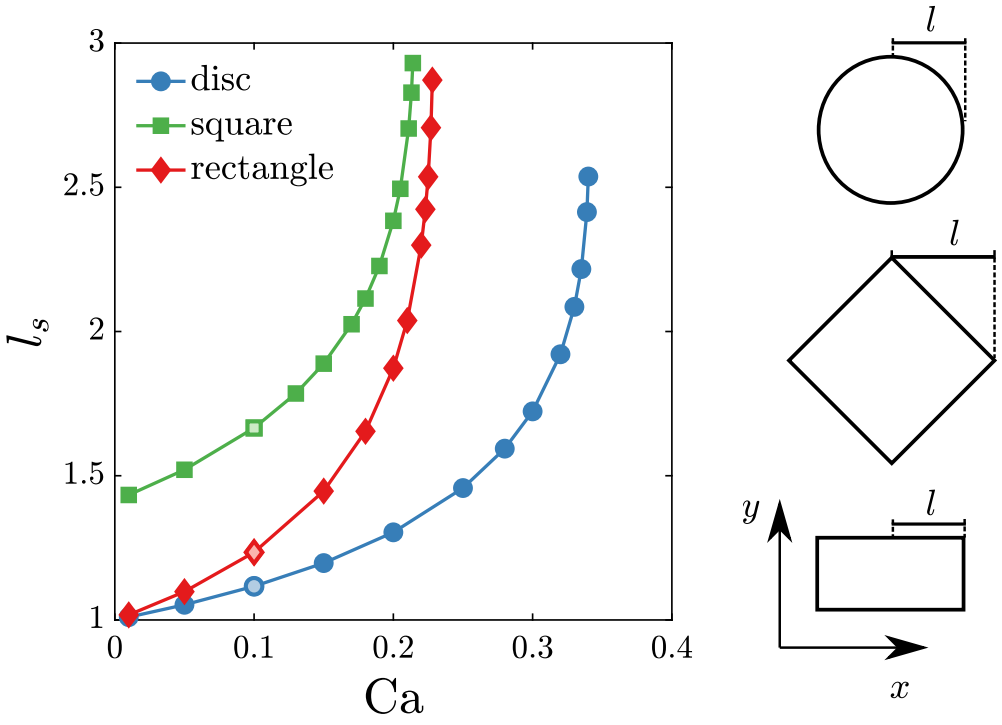


Figure 3.3: Steady-state stretched length l_s vs. Ca for deformable sheets with neo-Hookean elasticity in planar extensional flow. The data points filled with light color correspond to the shapes shown in Fig 3.2. The critical Ca for each geometry are: disk (Ca = 0.34), square (Ca = 0.214), rectangle (Ca = 0.228). The subplot indicates how length l is measured and the preferred stable orientation.

To further explore the compact-stretched transition, we turn to the strain-hardening Yeoh model. At low Ca, a finite, small value of c leads to negligible change in conformation. However, once the critical capillary number is exceeded, the the behavior is very different: the singularity is replaced by a sudden jump in the stretched length within a small Ca interval around the critical Ca. Fig 3.4 shows steady states for our three rest shapes with $c = 5 \times 10^{-5}$ at values of Ca just above the singularity in the neo-Hookean case, i.e., Ca = 0.35, 0.22 and 0.24 for disk, square, and rectangle, respectively. All cases take on strongly stretched conformations, and in addition, the rectangle takes on an asymmetric shape: reflection symmetry across the extensional axis is broken. The following paragraphs describe the parameter dependence in further detail.

Figure 3.5(a) shows steady state stretching length of a disk vs. Ca for $c = 2 \times 10^{-5}$.

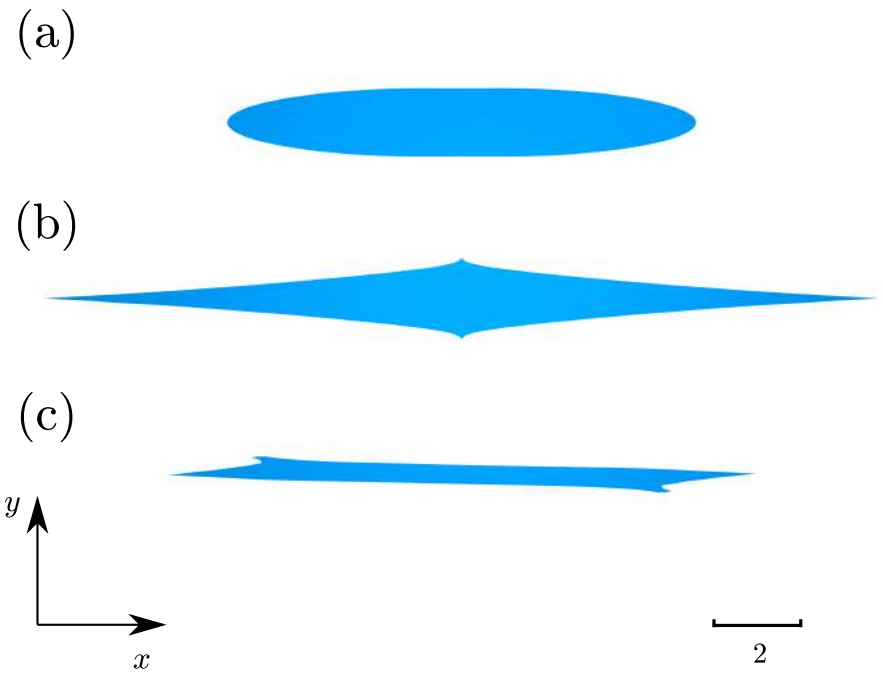


Figure 3.4: The steady-state conformation of a stretched sheet in planar extensional flow with Yeoh elasticity with $c = 5 \times 10^{-5}$: (a) a disk at Ca = 0.35. (b) a square at Ca = 0.22. (c) a rectangle at Ca = 0.24. The scale bar is 2 dimensionless length units.

At sufficiently low Ca the only steady state is compact (blue). Once Ca exceeds a critical value Ca_c, the compact steady state branch loses existence and the length evolves to a stretched state (red), as indicated by the upward black arrow. This type of transition is known as a saddle-node bifurcation. The critical value Ca_c splits the result into two branches in the parameter space: a compact branch and the stretched branch. Meanwhile, the diskontinuity in the stretched length suggests the existence of a bistable region that corresponds to hysteresis as Ca is increased or decreased quasistatically. Indeed this is the case – if we use an initial condition corresponding to a stretched state, then as long as Ca is greater than some lower limit, denoted Ca_s, then the final state will be highly stretched. For $\mathrm{Ca} < \mathrm{Ca}_s$, the stretched steady state branch loses existence, and an initially stretched sheet will relax to a compact steady state, as indicated by the downward black arrow. In general, this type of bistable behavior implies the existence of a branch of unstable steady states intermediate between the upper and lower ones. This branch is indicated schematically by the black dashed lines – we have not explicitly computed it. Fig 3.5(c)-(e) show the evolution

of either an initially compact or an initially stretched state for $\mathrm{Ca} < \mathrm{Ca}_s$, $\mathrm{Ca}_s < \mathrm{Ca} < \mathrm{Ca}_c$, and $\mathrm{Ca} > \mathrm{Ca}_c$, respectively.

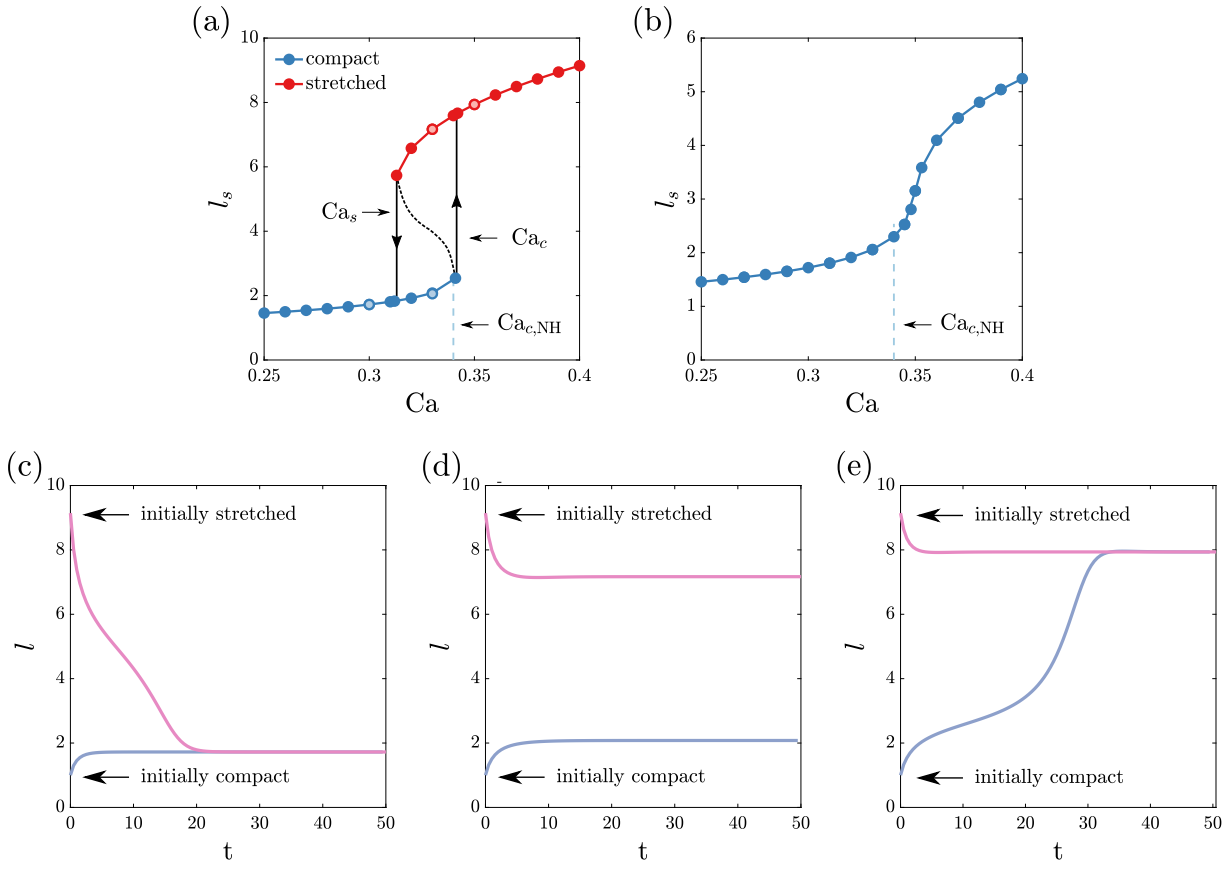


Figure 3.5: (a) Final stretched length l_s vs. Ca for a disk with $c = 2 \times 10^{-5}$ in planar extensional flow. Blue symbols and curves represent a compact final conformation and red represent a stretched final conformation. The points filled with light color correspond to the transient evolution shown in Fig 3.5(c)-(e). The black dashed line indicates the unstable steady state. The light blue dashed line shows the critical Ca with neo-Hookean elasticity. Ca_c and Ca_s are two critical Ca marked besides the arrows. (b) Final stretched length l_s vs. Ca for a disk with $c = 1 \times 10^{-4}$ in planar extensional flow. (c)-(e): Examples of stretched length evolution of a disk from either a stretched state or a compact state with $c = 2 \times 10^{-5}$ in planar extensional flow: (c) $\mathrm{Ca} = 0.3$ (d) $\mathrm{Ca} = 0.33$ (e) $\mathrm{Ca} = 0.35$.

In polymer dynamics, the origin of coil-stretch hysteresis is understood to be the conformation-dependent hydrodynamic interactions. The situation here is somewhat analogous. When the sheet remains at a compact state, the strain is relatively small and there is not a substantial change in surface area for the fluid to exert stresses on. In the stretched state, however, the surface area is substantially larger, leading to larger forces on the sheet from the flow, pre-

venting relaxation back to a compact state. Consequently, the sheet maintains a deformed state that is larger in size than the compact state under the same Ca. In Section **??**, we verify this picture by examination of an artificial model in which hydrodynamic interactions are artificially screened out.

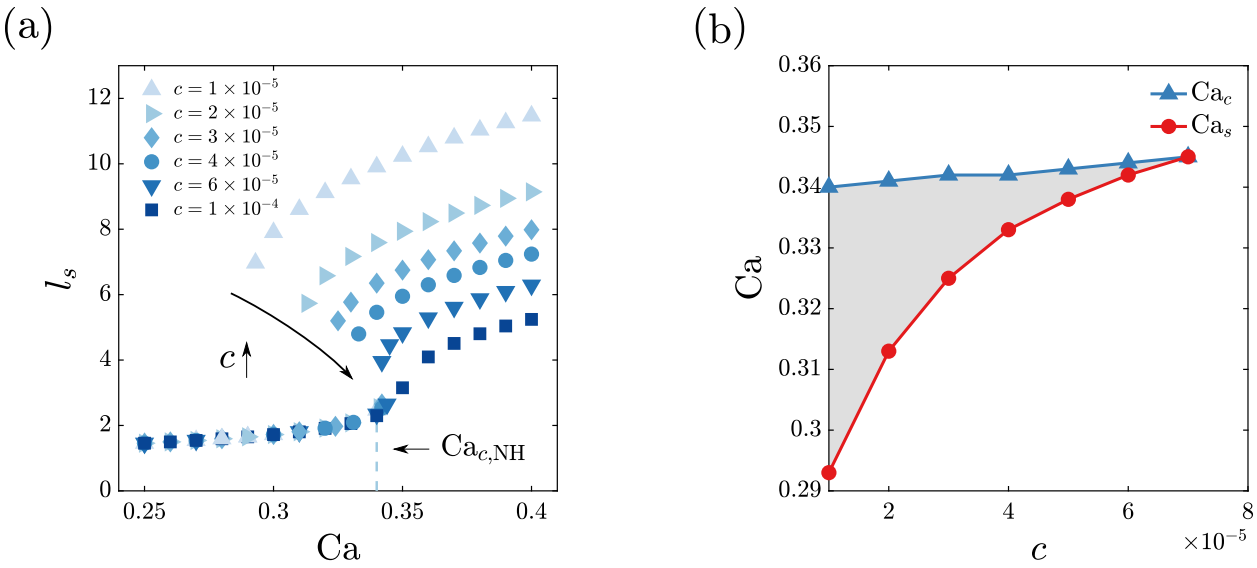


Figure 3.6: (a) Final stretched length l_s vs. Ca for a disk in planar extensional flow with various c. All c have a similar (overlapped) compact branch. The blue dashed line refers to Ca_s with neo-Hookean elasticity. (b) Phase diagram of Ca_c and Ca_s vs. c in planar extensional flow. The gray area marks the parameter regime where hysteresis can be observed.

This bistability phenomenon only exists for small c. The steady-state stretch for $c = 1 \times 10^{-4}$ is shown in Fig 3.5(b); while there is a sharp increase in l_s as Ca increases, there no longer exists a discontinuous transition or a multiplicity region. Fig 3.6(a) shows the steady states over a range of c. All choices of c share a similar compact branch, as the cubic energy term does not play a role when the strain is small. The discontinuity between the compact and the stretched branch becomes more evident with decreasing c, where hysteresis arises. In the linear polymer case, bistable behavior in extension is only observed for very long chain – highly extensible – polymers, where the equilibrium coil size and the contour length differ by orders of magnitude. In the present case, the extensibility is represented by the nonlinearity parameter c in the strain energy. Thinking of the sheet as a crosslinked polymer network, small c roughly corresponds to a material with a large number of polymer

segments between crosslinks: $c = 0$ is the neo-Hookean limit where the material can stretch without limit. As c increases, large deformations are increasingly penalized, as in the case of a linear chain with finite extensibility. Consistent with the linear polymer case, for the sheets, bistability vanishes as extensibility decreases (c increases).

Figure 3.6(b) summarizes the values of Ca_c and Ca_s as a function of c. Hysteresis exists in the gray region between the two curves. Note that Ca_c increases only slightly with c, as the nonlinear elastic behavior only has a small influence on a compact state. The Ca_s branch increases faster with c as a result of the increasing energy penalty for a stretched state as c increases. Based on the chosen mesh resolution, we note that Ca_c and Ca_s are not sensitive to further increase in resolution; increasing the number of elements by 10% shifts Ca_s and Ca_c in the third decimal place.

Since we found compact-stretched transition and hysteresis behavior for a disk sheet in planar extensional flow, we expect a similar transition to be found for a different sheet geometries. We now briefly present the behavior of a square in planar extensional flow. As previously mentioned, the square shape preferentially orients with diagonally opposed corners in the extension direction (Fig 3.2(b) and Fig 3.4(b)) for both the compact and the stretched state. We provide an example of compact-stretched transition and hysteresis behavior for a square in Fig 3.7a, for $c = 1 \times 10^{-4}$. Fig 3.7(b) shows the region in $\mathrm{Ca} - c$ space where hysteresis can be found.

In contrast, the rectangle is less symmetric than the disk or the square. From the previous steady-state analysis, we have already noted the existence of an asymmetric stretched steady state. This result indicates that there exists a symmetry-breaking bifurcation that interacts with the bifurcation behavior shown above. Fig 3.8(a) illustrates the length evolution for a rectangle initially in its rest state and oriented with the extension direction. This sheet is initially stretched by the flow symmetrically relative to the $x - z$ plane until it reaches a symmetric stretched state. The sheet stays at this unstable symmetric state for some time, but then evolves to a tilted asymmetric stable conformation. This observation suggests that

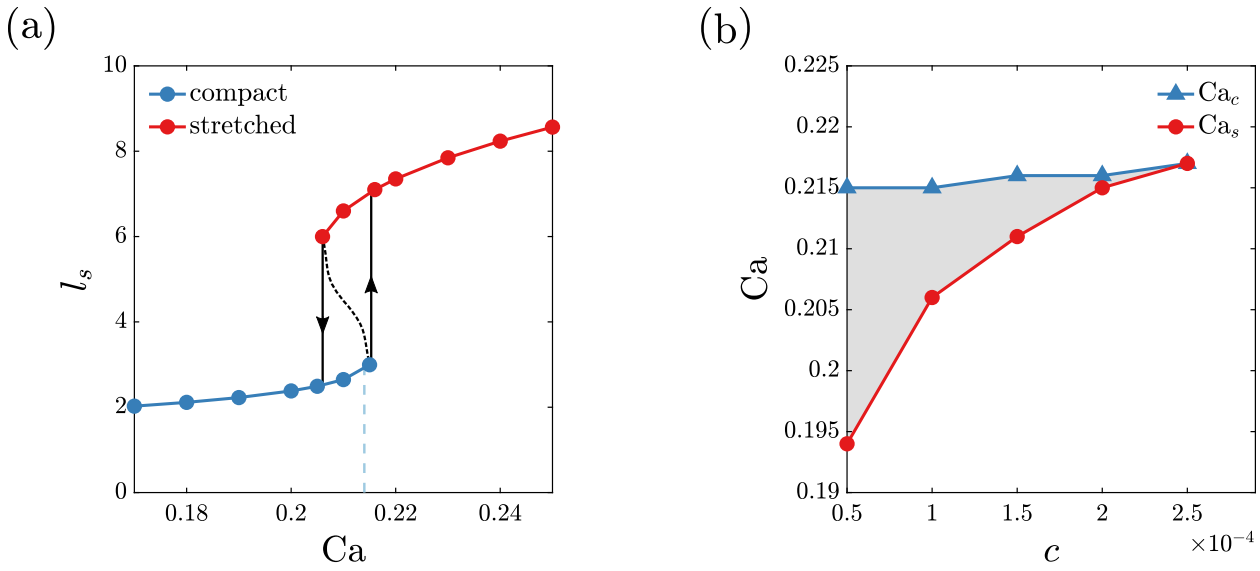


Figure 3.7: (a) Bifurcation diagram of stretched length l_s vs. Ca for a square in planar extensional flow, $c = 1 \times 10^{-4}$. (b) Phase diagram of Ca$_c$ and Ca$_s$ vs c for a square in planar extensional flow, with the gray area indicating the hysteresis region.

there is a stretched symmetric state that is unstable with respect to symmetry-breaking perturbations, leading the final steady state to be asymmetric.

Figures 3.8(b) and (c) shows bifurcation diagrams for $c = 1 \times 10^{-5}$ and 7×10^{-5}, respectively. (We can compute symmetric steady states that unstable in the full space by enforcing reflection symmetry.) In Fig 3.8b, multiplicity behavior exists for both the symmetric and the (unstable) symmetric stretched steady states. The bifurcation diagram indicates two saddle node bifurcations on the symmetric branch and a hypothesized subcritical symmetry-breaking (pitchfork) bifurcation that also undergoes a saddle-node bifurcation, yielding the stable stretched asymmetric state. This is the simplest bifurcation scenario consistent with the computational results – the orange dashed curve has not been computed but is consistent with this scenario. For the larger value of c considered in Fig 3.8(c), there is no bistability of symmetric solutions, but the asymmetric branch still bifurcates subcritically and turns around to yield a stable asymmetric stretched state. If we further increase c, bistability will vanish for the asymmetric solution and we obtain a supercritical bifurcation. We present a case in Fig 3.8(d) to show the existence of supercritical bifurcation.

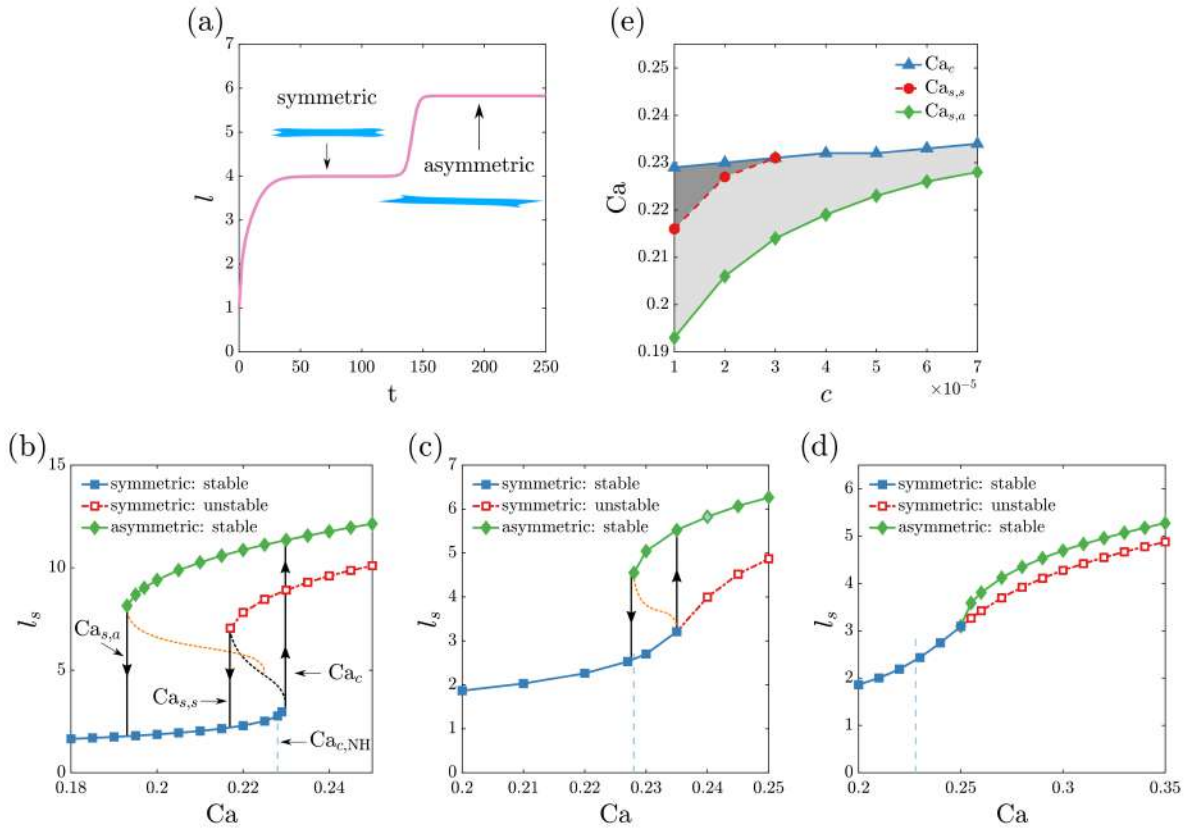


Figure 3.8: (a) Transient stretched length evolution of a rectangle in planar extensional flow, $c = 7 \times 10^{-5}$, Ca $= 0.24$. (b) Bifurcation diagram of l_s vs. Ca for a rectangle with $c = 1 \times 10^{-5}$.(c) Bifurcation diagram of l_s vs. Ca for a rectangle sheet with $c = 7 \times 10^{-5}$. The data point filled with light color corresponds to the evolution shown in Fig 3.8(a) (d) Bifurcation diagram of l_s vs. Ca for a rectangle with $c = 3 \times 10^{-4}$. (e) Phase diagram Ca_c and Ca_s vs c for a rectangle in planar extensional flow; here $\text{Ca}_{s,a}$ represents the stretched critical Ca for an asymmetric conformation, and $\text{Ca}_{s,s}$ represents the stretched critical Ca for a symmetric conformation. The dark gray area indicates the hysteresis region for symmetric states and the light gray area marks the hysteresis region without symmetry constraints, so the stretched state is tilted.

Figure 3.8(e) summarizes the behavior, showing the parameter space where hysteresis arises for both the asymmetric and the symmetric stretched states. The conformational hysteresis disappears faster as c increases for symmetric conformations than tilted ones.

3.3.2 Biaxial extensional flow

This section briefly turns to the case of biaxial extension, in which we shall see many of the features described above in planar extension. To begin with, similar to planar extension,

the strong compressive flow inward along the z direction suppresses any out-of-plane deformations, so at long times the deformations only occur in the $x-y$ plane. Different from the planar extension case, due to the radial symmetry of the biaxial flow in the $x-y$ plane, there is no issue of a preferred orientation for a square and a rectangle. Examples of stable steady states are illustrated in Fig 3.9.

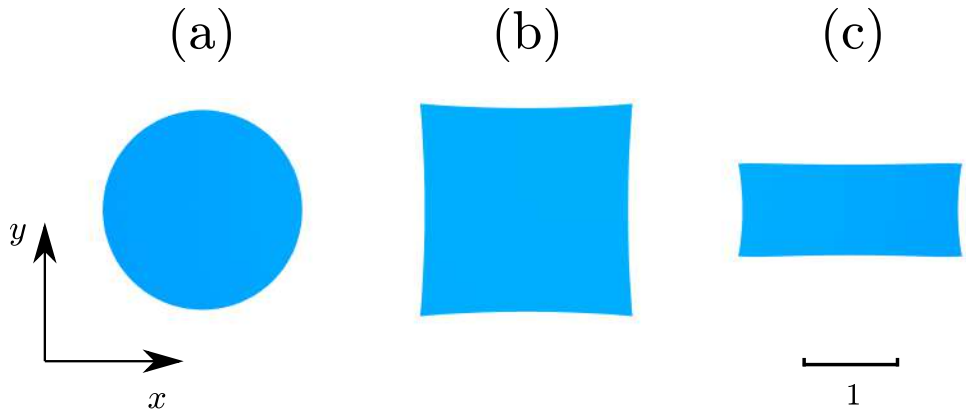


Figure 3.9: Steady-state conformation of a stable steady-state sheet with neo-Hookean elasticity in biaxial extensional flow at Ca = 0.2: (a) disk. (b) square. (c) rectangle. Scale bar is 1 dimensionless length unit.

As in planar extension, if neo-Hookean elasticity is used, there is again a singularity in stretching as Ca increases, as shown in Fig 3.10. In general, Ca_c is larger compared to planar extension. With the Yeoh model, bistability behavior similar to that found above is again observed. In biaxial extension, all three shapes have a stretched state similar to its compact state, just more stretched. No symmetry-breaking has been observed. Fig 3.11(a)-(c) show bifurcation diagrams for the disk, square and rectangle cases, respectively.

Figure 3.11(d)-(f) give the corresponding phase diagrams, showing where where hysteresis occurs. Compared with planar extensional flow results, the disk and rectangle in biaxial flow have larger effective hysteresis regimes. Interestingly, the rectangle has a substantially smaller hysteresis regime in c. This may arise from the smaller extent of the rectangle in one of the two characteristic stretching directions of biaxial extension.

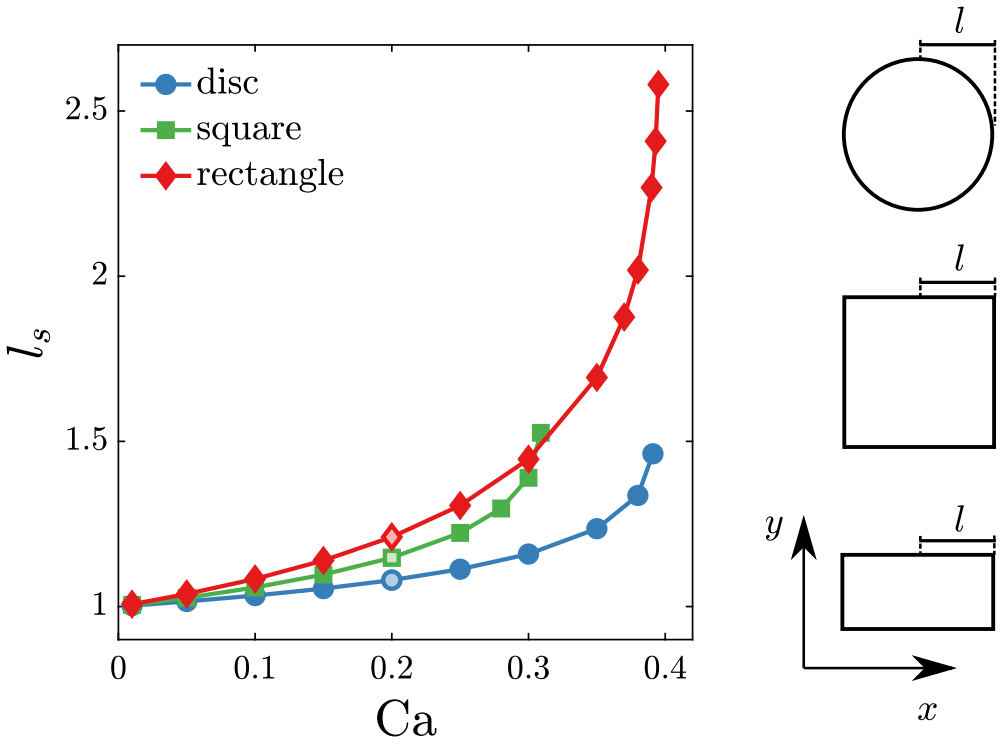


Figure 3.10: Steady-state stretched length l_s vs. Ca for deformable sheets with neo-Hookean elasticity in biaxial extensional flow. The data points filled with light color correspond to the conformations shown in Fig 3.9. The critical capillary numbers are: disk: $\mathrm{Ca}_c = 0.391$, square: $\mathrm{Ca}_c = 0.309$, rectangle: $\mathrm{Ca}_c = 0.395$. The subplot indicates the length measured in each geometry.

3.3.3 Effect of artificial hydrodynamic screening

Recall that the presence of hysteresis in the coil-stretch transition is due to the different hydrodynamic drag forces by the polymer in its coiled and stretched states[35, 151]. To assess the role of hydrodynamic forces on bistability in the present case, we now consider an artificial model that weakens the hydrodynamic interaction between different parts of the sheet. In this model, we take the medium in which the sheet is moving to be a Brinkman porous medium rather than a simple viscous fluid. In a porous medium, hydrodynamic interactions decay quickly with distance, because the obstacles in the medium absorb momentum [**?**]. With this model, the velocity field generated by point force **F** is determined not by the Stokeslet, but by the so-called Brinkmanlet:

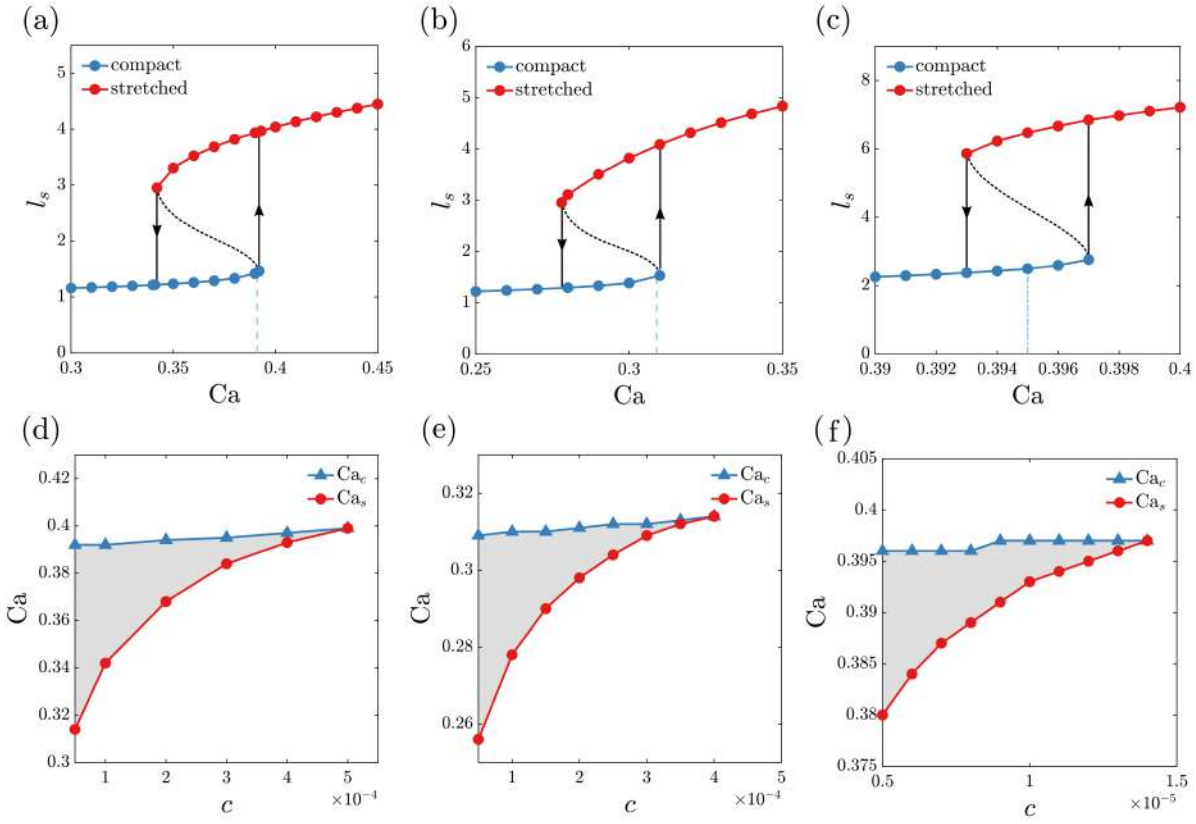


Figure 3.11: Bifurcation diagrams of l_s vs. Ca for sheets of different shapes in biaxial extensional flow: (a) disk: $c = 1 \times 10^{-4}$. (b) square: $c = 1 \times 10^{-4}$, (c) rectangle: $c = 1 \times 10^{-5}$. The light blue dashed line refers to Ca_c with neo-Hookean elasticity. Phase diagram of the hysteresis regime in biaxial extensional flow: (d) disk, (e) square, (f) rectangle.

$$\mathbf{B}(\mathbf{x}) = \frac{2}{8\pi\eta\alpha^2 r^3}\left[2\left(1-(1+\alpha r)e^{-\alpha r}\right)\frac{\mathbf{xx}}{r^2} + \left(\left(1+\alpha r+\alpha^2 r^2\right)e^{-\alpha r}-1\right)\left(\mathbf{I}-\frac{\mathbf{xx}}{r^2}\right)\right]. \tag{3.11}$$

Here a new length scale α^{-1}, the Brinkman screening length, arises. When $\alpha r \ll 1$, the Brinkmanlet reduces to the Stokeslet. When $\alpha r \gg 1$, the velocity decays as r^{-3}, as in a Darcy's law porous medium [50]. In our model, we apply the Brinkmanlet, rather than the regularized Stokeslet, to the interactions between different nodes, and examine the effect of α. In dimensionless form, α is scaled with sheet size a, so once $\alpha > 1$, hydrodynamic will be

important only between nearby positions on the sheet.

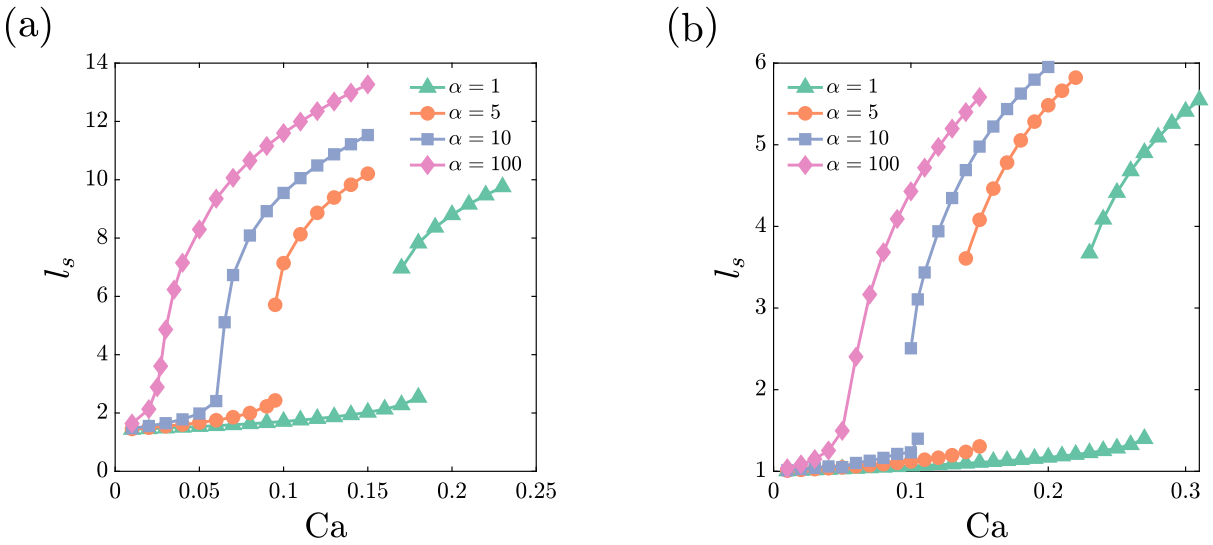


Figure 3.12: Bifurcation diagrams of l_s vs. Ca for a square sheet ($c = 1 \times 10^{-4}$) with increasing α: (a) planar extensional flow. (b) biaxial extensional flow.

We take a square ($c = 1 \times 10^{-4}$) in both planar and biaxial extension as an example to illustrate how the HI influences the hysteresis behavior. Fig 3.12 shows the steady state stretching length vs. Ca for multiple choices of α. Compared with the case $\alpha = 0$ (Fig 3.7a for planar extension and Fig 3.11(b) for biaxial extension at $c = 1 \times 10^{-4}$), the bistable region becomes narrower and shifts towards smaller Ca as α increases. When $\alpha = 100$, the hysteresis region vanishes and we obtain a smooth monostable curve. We conclude that, as with linear polymers, bistable behaviors arise from the hydrodynamic interactions between different parts of the sheet surface.

3.4 Summary

In this study, we systematically explored the dynamics of freely suspended elastic sheets with three different rest shapes in planar and biaxial extensional flows. In both flow fields, the sheet always takes on a flat steady conformation in the stretching plane. If neo-Hookean elasticity is applied, we observed a weakly stretched “compact" sheet conformation at low

Ca, while above a critical Ca_c the degree of stretching diverges. With a nonlinear Yeoh elasticity model, this singularity vanishes, but for sufficiently small nonlinearity parameter c, we observe a “compact-stretched" transition, where the sheet suddenly becomes highly stretched once a critical capillary number is exceeded. The discontinuity in stretched length marks a bistable or hysteretic regime, where the sheet has either a compact or a stretched conformation based on its deformation history. This behavior occurs for all three rest shapes considered. The origin of such bistable behavior is a result of hydrodynamic interaction between different parts of the sheet. The dynamics become monostable if hydrodynamic interactions are artificially screened out. The highly nonlinear behavior predicted here may play a substantial role in the behavior and performance of flow processes involving soft sheet-like particles.

4

Wrinkling and multiplicity in the dynamics of deformable sheets in uniaxial extensional flow

[1] The processing of thin-structured materials in a fluidic environment, from nearly inextensible but flexible graphene sheets to highly extensible polymer films, arises in many applications. So far, little is known about the dynamics of such thin sheets freely suspended in fluid. In this work, we study the dynamics of freely suspended soft sheets in uniaxial extensional flow. Elastic sheets are modeled with a continuum model that accounts for in-plane deformation and out-of-plane bending, and the fluid motion is computed using the method of regularized Stokeslets. We explore two types of sheets: “stiff" sheets that strongly resist bending deformations and always stay flat, and “flexible" sheets with both in-plane and out-of plane deformability that can wrinkle. For stiff sheets, we observe a coil-stretch-like transition, similar to what has been observed for long-chain linear polymers under extension as well as elastic sheets under planar extension: in a certain range of capillary number (flow strength relative to in-plane deformability), the sheets exhibit either a compact or a

[1]The text of this chapter is adapted from the publication by Y. Yu and M. D. Graham *Physical Review Fluids*, 2022,7, 023601

highly stretched conformation, depending on deformation history. For flexible sheets, sheets with sufficiently small bending stiffness wrinkle to form various conformations. Here, the compact-stretched bistability still occurs, but is strongly modified by the wrinkling instability: a highly-stretched planar state can become unstable and wrinkle, after which it may dramatically shrink in length due to hydrodynamic screening associated with wrinkling. Therefore, wrinkling renders a shift in the bistability regime. In addition, we can predict and understand the nonlinear long-term dynamics for some parameter regimes with linear stability analysis of the flat steady states.

4.1 Introduction

Two-dimensional materials, such as graphene, boron nitride and thin polymeric films, have received great attention in recent years. Thin graphene flakes and graphene composites, due to their superior mechanical and electronic properties, are widely used in the energy storage field [3, 4, 44, 197, 199]. Electronic nanomaterials, such as MoS_2, GeSe and graphene, are used in nanoscale thin films for semiconductor nanomembranes in high-performance electronic devices [141, 194]. Thin polymer sheets and films are important in the development of cell-based biohybrid machines [99].

These examples all involve stages of synthesis or processing where thin sheet-like structures are freely suspended in a fluidic environment, potentially showing complicated dynamics under external flow fields. For instance, Fei and coworkers improved the performance of carbon nanofibers in battery anodes by adding graphene oxide (GO) nanosheets to the fibers, which were produced by water-based electrospinning [44]. Once the mixture of nanosheets and polymer solutions was injected into the air, the uniaxial extensional flow near the needle tip stretched the nanosheet and helped it to wrap around the fiber surface. Park *et al.* investigated behavior and orientation of layered silicate nanocomposites in uniaxial extensional flow, finding that exfoliated nanosheets tended to align with the extensional direction [129].

Recently, Ng *et al.* performed capillary breakup extensional rheometry (CaBER) with dilute GO solutions, demonstrating that a very small amount of GO nanosheets can influence extensional rheology [119]. Yoon *et al.* synthesized GaAs nanomembranes in suspension with a combination of dispersion and sonication that generated complicated flow fields [194]. Liu *et al.* reviewed the fabrication of thin and ultra-thin polymer films, some of which involved an exfoliation process to dissolve the substrate where the films were suspended in solution [99].

The understanding of these nontrivial scenarios requires a comprehensive knowledge of the dynamics of suspended deformable sheet-like structures in flow, an area that has barely been explored. The above examples involve uniaxial extensional flow, which is, therefore, the focus of the present work. To our knowledge, this is the first study of flexible sheets in uniaxial extension.

Though little is known about deformable sheet dynamics in extensional flow, other soft objects such as flexible polymers have been well-studied. De Gennes suggested the possibility of a discontinuous, hysteretic coil-stretch transition for sufficiently long chain polymers under extensional flow, because of the conformation-dependence of the hydrodynamic interactions between chain segments [35]. Fuller and Leal modeled this situation in planar extensional flow with a bead-spring dumbbell model with conformation-dependent drag on the beads, observing the discontinuous transition and conformational bistability and hysteresis hypothesized by De Gennes [47]. Bistability was experimentally observed by Schroeder and coworkers with dilute solutions of fluorescently labeled E. coli DNA under planar extension [151]. They also performed Brownian dynamics simulations of a bead-spring polymer model with hydrodynamic interactions, finding conformational hysteresis consistent with what they observed in experiments. Recent computational work has also suggested the transition not only happens in a dilute polymer solution but also for polyethylene melts under planar extension [116].

Coil-stretch-like transitions have been shown to exist beyond linear polymers. Kantsler

et al. reported experimental observation of a tubular-dumbbell transition for vesicles in planar elongational flow when a critical strain rate is reached [70]. They did not observe bistability. Zhao *et al.* found a similar transition computationally for a vesicle in uniaxial extensional flow [201]: when reaching a critical flow strength, the vesicle became unstable and deformed into an extended asymmetric dumbbell shape with two unequally sized ends. The simulation results are consistent with experimental observations from Kantsler *et al.* in planar extension and vesicles did not show bistability. Soh and Doyle studied the deformation response for 2D kinetoplast DNA sheets, which are networks of linked ring structures that appear in mitochondria, in planar elongational flow [164]. The DNA sheets underwent a relatively smooth transition from an undeformed state to a deformed stretched state, with no evidence of a hysteretic coil-stretch transition. A recent computational study from Yu and Graham demonstrated that a sufficiently deformable elastic sheet in planar or biaxial extension can display a compact-stretched transition with hysteresis that is closely analogous to the coil-stretch transition in long polymer chains in solution [195]. As in the polymer case, the bistability was shown to arise from the hydrodynamic interaction between different parts of the sheet surface, and vanished if the hydrodynamic interactions were turned off. Due to the nature of biaxial and planar extension, the long-time conformations of the sheets were always flat. However, as we shall see, a flexible sheet in uniaxial extension experiences radial compressive stress and may wrinkle, influencing the shape evolution and bistability.

While the above discussion focused on extensional flows, a number of recent studies consider the dynamics of inextensible sheets in shear flow in order to understand synthesis processes of sheets such as graphene, which usually involve a liquid-phase exfoliation in a shear-dominated flow where complicated folding dynamics may occur. Xu and Green studied a Brownian bead-spring model for a square sheet in simple shear flow [186], where they characterized a cyclic crumple-stretch-crumple motion for a flexible sheet. In addition, they also applied the same model to investigate the dynamics in biaxial extension [187], where sheets with large bending stiffness stayed flat while sheets with small stiffness crumpled as a result

of Brownian fluctuations. Silmore and coworkers studied semiflexible non-Brownian sheets in shear [156]. They found that, depending on initial conditions and bending stiffness, the sheets can either undergo a continuous chaotic tumbling or follow a Jeffery-like orbit then reach a flat state in the flow-vorticity plane. They also predicted some transient buckling dynamics with a simple 1D elasticity model. Dutta and Graham studied piecewise rigid creased sheets in shear flow [40]. Sheets either approached a steady, periodic or quasiperiodic state depending on initial conditions. Botto and coworkers examined liquid-phase exfoliation of multiple graphene sheets via molecular dynamic simulation and characterized the parameter regime where exfoliation can occur [51]. They also applied molecular dynamic simulation to study thin nanoplatelets in shear [67]. They found the effect of hydrodynamic slip influenced the dynamics, allowing the platelet to attain a stable steady orientation with a fixed angle with respect to flow.

In the present work, we investigate the dynamics of soft, non-Brownian elastic sheets in uniaxial extensional flow. We examine cases that range from relatively stiff sheets like graphene to highly deformable polymeric sheets. We are interested in the wrinkling instability and its influence on compact-stretched bistability – i.e. the analogue of the coil-stretch transition in linear polymers. The rest of the paper is presented as follows: Section 4.2 presents the model and numerical methods. Section 4.3 presents the results in three parts: dynamics of stiff sheets (sheets with large stiffness that prevents out-of-plane deformation); wrinkling transitions at low extension rates where sheets are not highly stretched; dynamics of stretched sheets and the interaction between wrinkling and the compact-stretched transition. We conclude in Section 4.4.

4.2 Methods

Model setup

We consider an elastic thin sheet that is freely suspended in an unbounded uniaxial

extensional flow ($\mathbf{v}_\infty = \dot{\varepsilon}\,[-x/2, -y/2, z]^T$, with $\dot{\varepsilon}$ as the flow strain rate). The fluid is Newtonian with viscosity η and density ρ. We model the sheet as a continuum with a no-slip surface, so material points on the surface move with the same velocity as the local fluid. The no-slip boundary condition also implies that the sheet is impermeable – if the sheet moves with the local fluid velocity, then no fluid is passing through the sheet. The sheet surface is discretized into triangular elements with a node at each corner. The detailed numerical methods will be introduced in the following section. In the present study, we focus on a sheet whose equilibrium shape is a disk with radius a and thickness h such that $h \ll a$. Thus, the sheet has a traction-free edge, along which fluid exerts no forces.

The total strain energy of the elastic sheet can be written as the sum of in-plane strain energy E_s and out-of plane bending energy E_b:

$$E = E_s + E_b. \tag{4.1}$$

Here, the in-plane strain energy is evaluated by integrating the strain energy density W over the sheet surface. We choose a nonlinear Yeoh model (YH), as it is often used to model rubber-like polymer structures [192], with the form:

$$W_{\mathrm{YH}} = \frac{G}{2}\,(I_1 - 3) + cG\,(I_1 - 3)^3\,. \tag{4.2}$$

The two-dimensional shear modulus G scales with the equilibrium thickness h. The term I_1 is the first invariant of the right Cauchy-Green deformation tensor, and depends on the local principal stretch ratios λ_i along the tangential direction of the sheet surface:

$$I_1 = \lambda_1^2 + \lambda_2^2 + \frac{1}{\lambda_1^2\lambda_2^2}. \tag{4.3}$$

The last term denotes λ_3, as the stretch ratio along the thickness direction, is obtained by incompressibility of the material ($\lambda_1\lambda_2\lambda_3 = 1$). The parameter c weights the cubic term in the energy density, and can be physically related to the properties of the material. For

example, for a polymeric sheet, c is inversely related to the distance between cross-linked points inside the sheet, thus small c indicates higher extensibility. Consequently, large c makes the material strain-hardening, due to the penalty from the cubic energy term under large strain. If $c = 0$, the model recovers the strain-softening neo-Hookean (NH) model.

For the bending energy E_b, we apply a simple bending model that sums the energy due to dihedral angles $\theta_{\alpha\beta}$ between neighboring elements [42, 43]:

$$E_b = \sum_{\text{adj } \alpha,\beta} k_b \left(1 - \cos(\theta_{\alpha\beta} - \theta_0)\right) \tag{4.4}$$

where k_b is the bending constant calculated from bending stiffness K_B ($k_b = \frac{3\sqrt{3}}{2} K_B$). The angle θ_0 is zero as we assume a flat equilibrium state.

In addition, we also add a truncated Lennard-Jones(LJ) repulsive potential to prevent the sheet from self-intersecting. Numerically, the potential acts between all the nodes, except for the nodes that are located within 3-ring neighbors of the targeted node at the equilibrium state. The potential has the form:

$$E_{LJ} = \begin{cases} 4\varphi_0 \left[\left(\frac{\sigma}{r}\right)^{12} - \left(\frac{\sigma}{r}\right)^{6} \right], & \text{if } r < \sigma \\ 0, & \text{otherwise} \end{cases} \tag{4.5}$$

where r is the distance between nonadjacent nodes at equilibrium state, σ is the range of the potential, and φ_0 measures is the strength of the potential. Here, we choose $\sigma = 0.06a$ and $\varphi_0 = 4 \times 10^{-6}$ such that the potential has no influence on the dynamics for sheets without intersection. We find that the only case where the repulsive force is active is when the sheet edge would otherwise cut through the surface, which only occurs for sheets with very small bending stiffness.

We introduce two nondimensional parameters to describe the aforementioned mechanical properties. The capillary number $\text{Ca} = \eta\dot{\varepsilon}a/G$ compares the viscous stresses exerted by the fluid on the sheet to the in-plane elastic response of the sheet. Larger Ca indicates that the

sheet is more deformable. The relative size of the bending and in-plane stresses is measured by $\hat{K}_B = K_B/a^2G$: the parameter comparing the bending with flow is $\mathrm{Ca}/\hat{K}_B = \eta\dot{\epsilon}a^3/K_B$: smaller $\hat{K}_B$ indicates that the sheet is more flexible. In this study, we explore two types of sheets: "stiff" sheets ($\hat{K}_B = \infty$) with in-plane deformability, which strongly resist bending deformations and always stay flat, and "flexible" sheets with both in-plane and out-of plane deformability, which can wrinkle. We consider the stiff sheet case primarily as an idealized base case for comparison with the more realistic flexible case.

Additionally, we do not include thermal fluctuations, as we estimate them to be negligible under the conditions studied here. For example, for a polyethylene glycol (PEG) hydrogel [48] sheet with radius of 100 μm and thickness of 100 nm suspended in water, its estimated shear strain energy ($\sim 10^9 k_BT$) and bending energy ($\sim 3 \times 10^5 k_BT$) are much larger than thermal energy.

Numerical methods

The numerical method for the elasticity problem is adapted from Charrier *et al.* [21, 128]. We simulate the sheet by keeping track of nodes that move as material points on the sheet surface. From the above two energies, we obtain the summed nodal elastic force ($\mathbf{F}_{e,i} = \mathbf{F}_{s,i} + \mathbf{F}_{b,i}$) exerted on each node from the first variation of the total energy with respect to the nodal displacements. Each discretized element of the sheet is assumed to have homogenous deformation, so the element edges always remain linear. The deformed element is compared to its equilibrium shape under a local coordinate transformation via a rigid body rotation, and the displacement for any point inside the element is obtained by linear interpolation from the nodal positions. The detailed implementation can be found in references [42, 43, 79]. The total nodal force $\mathbf{F}_{e,i}$ is evaluated by summing the elastic force $(\mathbf{F}_{e,i})_j$ due to deformation of each surrounding element j shared by the node i: $\mathbf{F}_{e,i} = \sum_j (\mathbf{F}_{e,i})_j$, where the sum is over all elements meeting at the node. For the results shown, we discretize the disk with 1600 elements and 841 nodes. We have verified that changes in mesh resolution lead to only small quantitative changes in the results and no qualitative changes.

In the present work, we consider a small, thin sheet and assume that the particle Reynolds number $\mathrm{Re} = \rho\dot{\epsilon}a^2/\eta$ is negligible. Under these assumptions, inertia of the sheet and fluid are negligible, so the forces on each point on the sheet sum to zero and the fluid is governed by the Stokes equation. For each node on the sheet surface, the elastic force $\mathbf{F}_{e,i}$ exerted by the sheet on the fluid is balanced with hydrodynamic force $\mathbf{F}_{h,i}$ from the fluid:

$$\mathbf{F}_{e,i} + \mathbf{F}_{h,i} = \mathbf{0}. \tag{4.6}$$

To account for the fact that the forces are not completely localized to the nodal positions, we use the method of regularized Stokeslets to solve for the fluid motion [28]: the force $\mathbf{F}_i = -\mathbf{F}_{h,i}$ exerted by node i on the fluid corresponds to a regularized force density $\mathbf{f}_i^\kappa = \mathbf{F}_i\delta_\kappa(\mathbf{x} - \mathbf{X}_i)$, where $\mathbf{X}_i$ is the position of node i and $\delta_\kappa(\mathbf{x})$ is a regularized delta function with regularization parameter κ. Thus, the governing equations are the Stokes equation with regularized nodal forces and the continuity equation:

$$\begin{gathered} -\nabla p + \eta\nabla^2\mathbf{v} + \textstyle\sum_i \mathbf{F}_i\delta_\kappa(\mathbf{x} - \mathbf{X}_i) = \mathbf{0} \\ \nabla \cdot \mathbf{v} = 0. \end{gathered} \tag{4.7}$$

The velocity field generated due to a regularized point force $\mathbf{f} = \mathbf{F}\delta_\kappa(\mathbf{x} - \mathbf{X}_i)$ can be represented using a regularized Stokeslet $\mathbf{G}_\kappa$:

$$\mathbf{v}_\kappa(\mathbf{x}) = \mathbf{G}_\kappa(\mathbf{x} - \mathbf{X}_i) \cdot \mathbf{F}. \tag{4.8}$$

As $1/\kappa \to 0$, $\mathbf{G}_\kappa$ reduces to the usual Stokeslet operator $\mathbf{G}(\mathbf{x} - \mathbf{X}_i) = 1/8\pi\eta r(\mathbf{I} + (\mathbf{x} - \mathbf{X}_i)(\mathbf{x} - \mathbf{X}_i)/r^2)$, where $r = ||\mathbf{x} - \mathbf{X}_i||$. There are many ways to regularize a delta function $\delta_\kappa(\mathbf{x})$; we choose a regularization function for which the difference between $\mathbf{G}$ and $\mathbf{G}_\kappa$ decays exponentially as $\kappa r \to \infty$ [50, 59, 122]:

$$\delta_\kappa(\mathbf{x}-\mathbf{X}_i) = \frac{\kappa^3}{\sqrt{\pi}^3}\exp(-\kappa^2 r^2)\left[\frac{5}{2}-\kappa^2 r^2\right]. \tag{4.9}$$

With this choice,

$$\mathbf{G}_\kappa(\mathbf{x}-\mathbf{X}_i) = \frac{\mathrm{erf}(\kappa r)}{8\pi\eta r}\left(\mathbf{I}+\frac{(\mathbf{x}-\mathbf{X}_i)(\mathbf{x}-\mathbf{X}_i)}{r^2}\right)+\frac{\kappa e^{-\kappa^2 r^2}}{4\pi^{3/2}\eta}\left(\mathbf{I}-\frac{(\mathbf{x}-\mathbf{X}_i)(\mathbf{x}-\mathbf{X}_i)}{r^2}\right). \tag{4.10}$$

In the simulations, κ must be chosen to scale with the minimum node-to-node distance $l_{\min}$. We take $\kappa l_{\min} = 2.1842$, which is obtained from a validation case of a disk in biaxial extensional flow discussed in [195]. We represent the total velocity at a point $\mathbf{x}$ as

$$\mathbf{v}(\mathbf{x}) = \mathbf{v}_\infty(\mathbf{x}) + \mathbf{v}_p(\mathbf{x}) = \mathbf{v}_\infty(\mathbf{x}) + \sum_i \mathbf{G}_\kappa(\mathbf{x}-\mathbf{X}_i)\cdot\mathbf{F}_i. \tag{4.11}$$

At each time step, after updating the force balance, we update the nodal positions by applying the condition that they move with the local fluid velocity in Eq. 6.23, thereby satisfying the no-slip and no-penetration conditions:

$$\frac{d\mathbf{X}_i}{dt} = \mathbf{v}(\mathbf{X}_i). \tag{4.12}$$

This equation is solved with a fourth-order Runge-Kutta method. For numerical stability, the time step applied follows $\Delta t = 0.1\mathrm{Ca}l_{\min}$. If Ca is large, we apply an upper limit of 5×10^{-4} strain unit per time step.

4.3 Results

4.3.1 Dynamics of stiff sheets

We begin the discussion of dynamics in uniaxial extensional flow by introducing the dynamics of a stiff sheet that has extremely large bending stiffness ($\hat{K}_B = \infty$) and always stays flat.

The dynamics of a stiff sheet serve as a base case to understand the more complicated flexible sheets discussed in later sections. For simplicity, we impose the infinite stiffness criterion by directly preventing any out-of-plane deflection in the numerical simulation. Our primary quantity for characterizing the conformation of a sheet will be its half-length l in the z-direction, which at rest reduces to its radius a.

One important observation of a sheet in uniaxial flow is that the only stable orientation of the sheet aligns with the flow direction. This observation agrees with Park *et al.* [129] for orientation of nanocomposites in uniaxial extension. Therefore, we only focus on the initial condition where the sheet aligns with flow direction: the sheet always lies in the $x-z$ plane.

Figure 4.1(a) - (c) presents bifurcation diagrams for the steady state value l_s vs. Ca with different choices of parameter c, with the definition of l shown in Fig. 4.1(d). For a simple neo-Hookean model ($c = 0$), shown in Fig. 4.1(a), the conformation stretches without bound once a critical capillary number $\mathrm{Ca}_c = 0.39$ is exceeded, yielding a singularity. (This is analogous to the unbounded stretching of a bead-spring dumbbell of a polymer in solution when the spring is Hookean [50].) For a nonlinear Yeoh model with small but finite c (Fig. 4.1(b)), beyond Ca_c, the compact state loses existence, and the sheets evolve to a stretched state – the singularity in the Hookean case at Ca_c is replaced by a saddle-node bifurcation at which the compact branch loses existence. Quasistatically decreasing Ca shows that the stretched steady state branch persists down to another critical (saddle-node bifurcation) value Ca_s, below which all initial conditions relax back to the compact state. That is, when $\mathrm{Ca}_s < \mathrm{Ca} < \mathrm{Ca}_c$, this case displays bistability between a weakly stretched compact branch and a fully stretched branch. Figure 4.1(d) shows examples of compact and stretched conformations for $\mathrm{Ca} = 0.37$ from Fig. 4.1(b). This bifurcation behavior is qualitatively similar to what has been previously predicted for sheets in planar and biaxial extension [195].

We compare two examples from Fig. 4.1(b) to show the difference in dynamics for sheets with and without bistability: Figure 4.1(e) shows the transient length evolution of sheets for

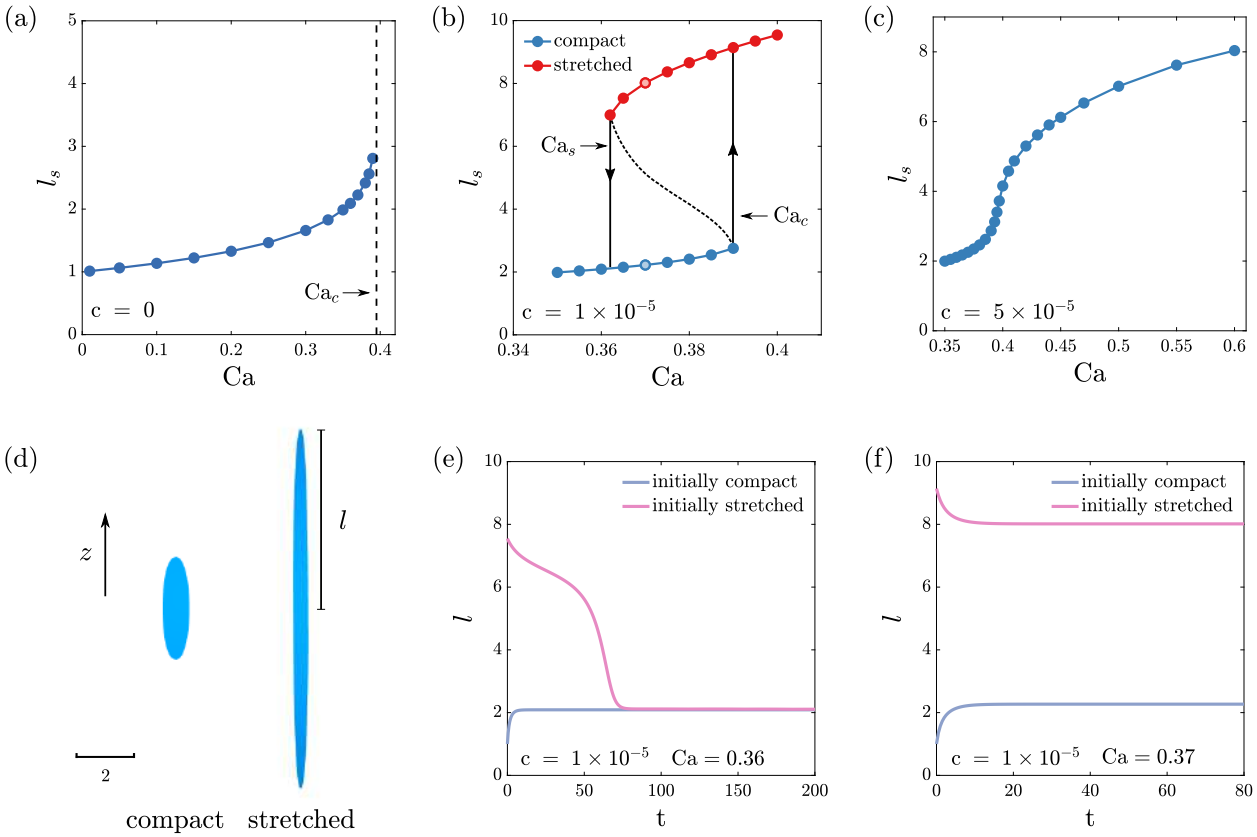


Figure 4.1: (a) Steady state half-length l_s vs. Ca for a stiff disk with $c = 0$ (neo-Hookean) in uniaxial extensional flow, indicating a singularity in l_s. (b) l_s vs. Ca for a stiff disk with $c = 1 \times 10^{-5}$ in uniaxial extensional flow. Blue symbols represent a compact final conformation and red symbols represent a stretched final conformation. Ca_c and Ca_s are the two critical Ca marked beside the arrows. (c) l_s vs. Ca for a stiff disk with $c = 5 \times 10^{-5}$ in uniaxial extensional flow, with a smooth transition observed. (d) Examples of bistable sheets for $\mathrm{Ca} = 0.37$ with $c = 1 \times 10^{-5}$, corresponding to light symbols in Fig. 4.1(b). The figure shows the front view of compact and stretched states with half-length labeled l_s. (e) Examples of transient length evolution for stiff sheets with $\mathrm{Ca} = 0.36$ and $c = 1 \times 10^{-5}$, below the bistability regime. (f) Examples of transient length evolution for stiff sheets with $\mathrm{Ca} = 0.37$ and $c = 1 \times 10^{-5}$, in the bistable regime.

a value of Ca below the bistable regime, as either a compact or stretched initial condition both result in a compact final conformation as the only stable steady state; Figure 4.1(f) indicates that if Ca is inside the bistable regime, the sheet either becomes compact or remains stretched based on its initial condition, with both states being stable.

The bistability regime depends on the value of c. Smaller c indicates larger extensibility, with $c = 0$ the special case of neo-Hookean elasticity. The bistability arises only when c is small. Figure 4.1(c) shows an example where c is sufficiently large that l_s increases smoothly

with increasing Ca. (As c increases, Ca_s approach one another, eventually merging and disappearing.) Recalling that c can be viewed as inversely related to the extensibility of the polymer subchains in the sheet, we suspect that the reason that bistability was not observed in the DNA networks of [164] is the relatively low molecular weight of the DNA that they used, leading effectively to a value of c above the bistability regime. In addition, we note that changing c has negligible influence on the stretching dynamics of the compact branch, because the strain is relatively small for compact conformations. The current study focuses on the compact-stretched transition, so below we only discuss the influence of deformation on the transition with choices of c that show bistability ($c = 1 \times 10^{-5}$).

4.3.2 Dynamics of flexible sheets in the compact (low Ca) regime

In this section, we probe into the compact branch shown in Fig. 4.1(b). Here, we remove the infinite stiffness constraint to make the sheet flexible, so the dynamics depend on bending stiffness $\hat{K}_B$. When the sheet is compact, the dynamics are not sensitive to c, as the penalty from cubic energy term is small. Therefore, we present the following results with a simple neo-Hookean model ($c = 0$), where a singularity appears beyond $\mathrm{Ca}_c = 0.39$.

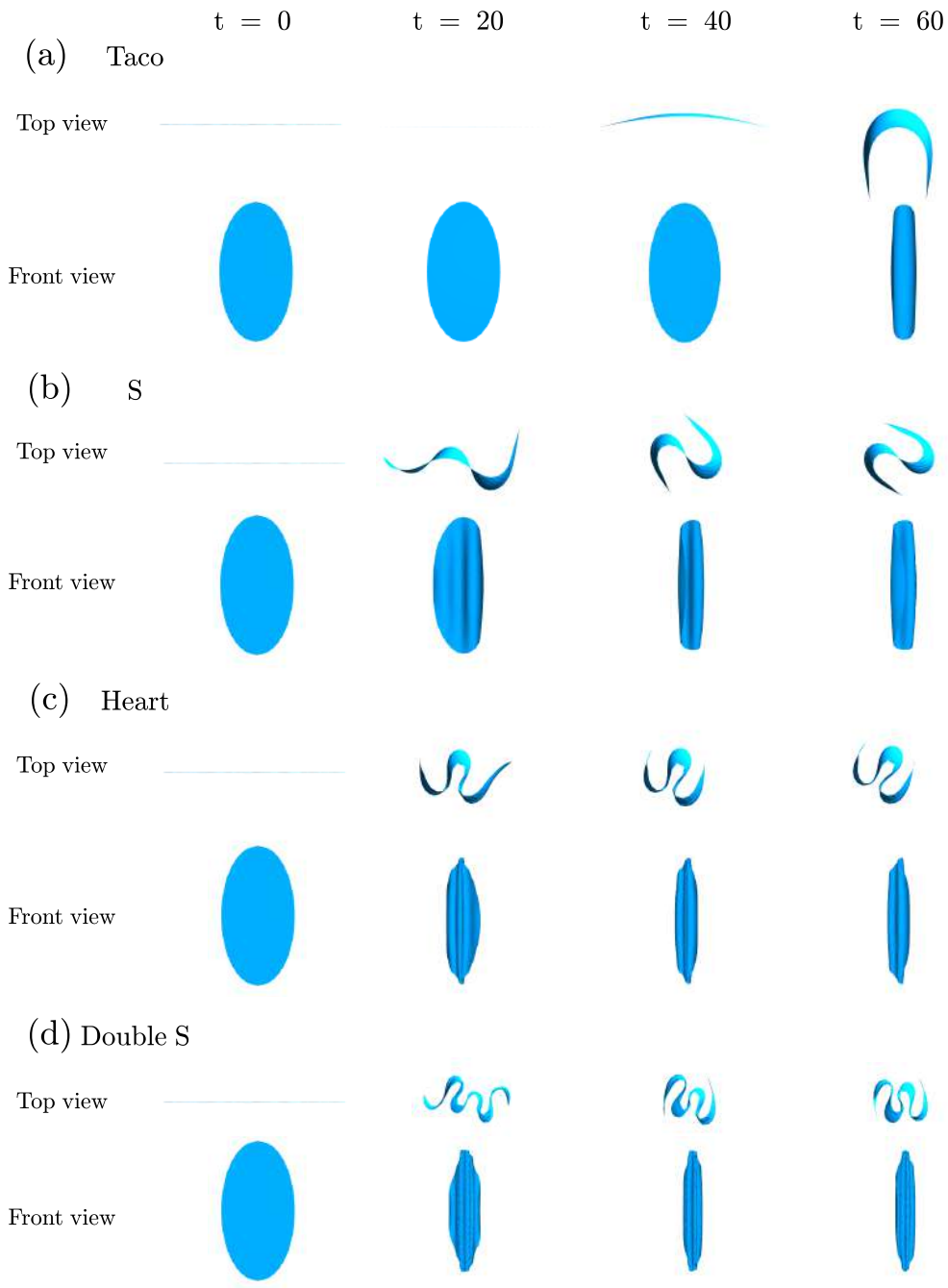


Figure 4.2: Top view ($x-y$ plane) and front view ($x-z$ plane) of shape evolutions for a deformable sheet with Ca $= 0.25$ and decreasing $\hat{K}_B$: (a) Taco ($\hat{K}_B = 5 \times 10^{-3}$), (b) S shape ($\hat{K}_B = 1 \times 10^{-3}$), (c) Heart ($\hat{K}_B = 3 \times 10^{-4}$), (d) Double S ($\hat{K}_B = 1 \times 10^{-4}$).

The dynamics of flexible sheets in uniaxial flow are complicated due to flow-induced out-of-plane deformation and are highly dependent on Ca and $\hat{K}_B$. We perform numerical simulations by applying a small and random out-of-plane perturbation to the flat steady

states shown in Fig. 4.1(b). We found that, depending on $\hat{K}_B$, the sheet either resists perturbation and stays flat, or develops into different wrinkled conformations.

Figure 4.2 shows a transition of final conformation, for a sheet with fixed Ca and decreasing $\hat{K}_B$, from a flat stable steady state to more complicated geometries. With decreasing stiffness, the first non-flat conformation appeared is a C shape, or a "taco" shape (Fig. 4.2(a)) as the circular sheet folds onto itself. The next conformation observed is an S shape, as shown in Fig. 4.2(b). This shape and some of the other wrinkled shapes slowly rotate around the z axis during flow, due to the asymmetry of the conformation. For even smaller $\hat{K}_B$, the sheet develops into more complicated structures, such as "heart" and "double S", as shown in Fig. 4.2(c) and Fig. 4.2(d), respectively. A full parameter sweep of results for a range of Ca and $\hat{K}_B$ will be given below, after we illustrate the various types of conformations that we observe.

Since the sheets with different $\hat{K}_B$ develop into various conformations, we here illustrate how different conformations affect the stretching dynamics from two perspectives: the stretched length of the sheet and the force dipole exerted by the sheet on the flow. Figure 4.4(a) shows the transient stretched length l for the cases presented in Fig. 4.2. All sheets begin with the same flat steady state (fixed Ca) and a small random perturbation. Interestingly, we observe that as the sheet begins to wrinkle, the induced out-of-plane deformation leads to a decrease in stretched size. The decrease in l can be easily observed in Fig. 4.2. From Fig. 4.4(a), sheets with smaller $\hat{K}_B$ display a more significant decrease in stretched length, and the decrease in the stretched length is associated with the type of conformation observed. For instance, as the taco folds onto itself, it "embraces" and traps fluid inside the taco, screening it from the fluid motion outside of the taco.

To visualize the effect of this hydrodynamic screening of the interior of the taco from the imposed flow, we examine the velocity on a symmetry plane cutting vertically through the taco shape. Figure 4.3b shows this plane and the velocity magnitude $||\mathbf{v}||$ on it. We show a slice through the flat steady state in Fig. 4.3a as a reference, where the velocity field is

similar to the bulk extensional flow. By comparing with the flat case, we observe that the velocity inside the taco is smaller than outside, indicating hydrodynamic screening of the interior. In Fig 4.3c, we also present results for an S conformation. Here the decrease in velocity of the fluid inside the wrinkles is even more apparent than in the taco case. Because of this effect, the sheet is less exposed to the extensional flow, leading to the decrease in length. This hydrodynamic screening applies as well for the other conformations: for the heart or double S shapes, fluid is trapped in the wrinkles. Those conformations have different stretched lengths because of the different extents of hydrodynamic screening.

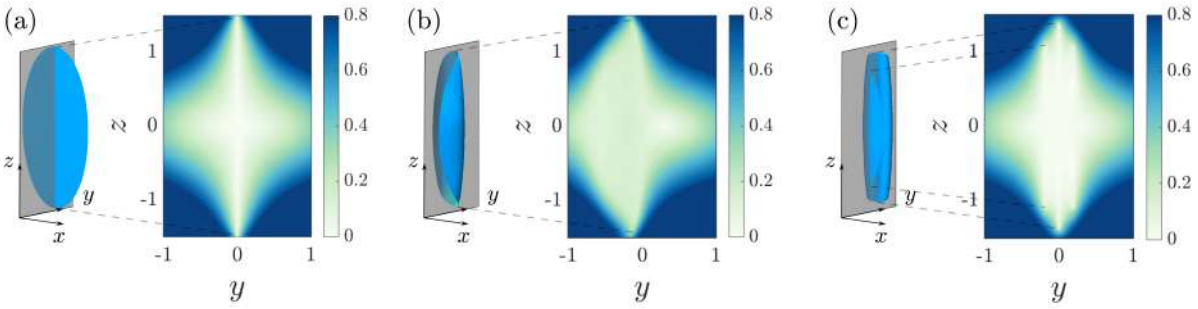


Figure 4.3: Velocity norm $||\mathbf{v}||$ on a slice (plane $x = 0$) through the steady states at Ca = 0.25: (a) A flat sheet as at t = 0 in Fig. 4.2. (b) The taco shape in Fig. 4.2(a). (c) The S shape in Fig. 4.2(b).

The deformation of the sheets is closely related to the stress that they exert on the fluid, so it is also of interest to examine the force dipole associated with the deforming sheets. (The total stress associated with the sheets is simply the force dipole per sheet times the number density in suspension.) The force dipole is given by:

$$\mathbf{D} = -\sum_i \mathbf{F}_i \mathbf{x}_i, \tag{4.13}$$

where $\mathbf{F}_i$ is the force exerted on the fluid by node i on the sheet. The eigenvalues σ_i of $\mathbf{D}$ reveal the strength of the dipole along the three principal directions. Here, the first eigenvalue σ_1 indicates the dipole acting along the z axis (flow direction). The second and third eigenvalues correspond to two orthogonal dipoles on the $x - y$ plane.

In Fig. 4.4(b), we plot evolution of σ_1 for same cases from conformations from Fig. 4.4(a).

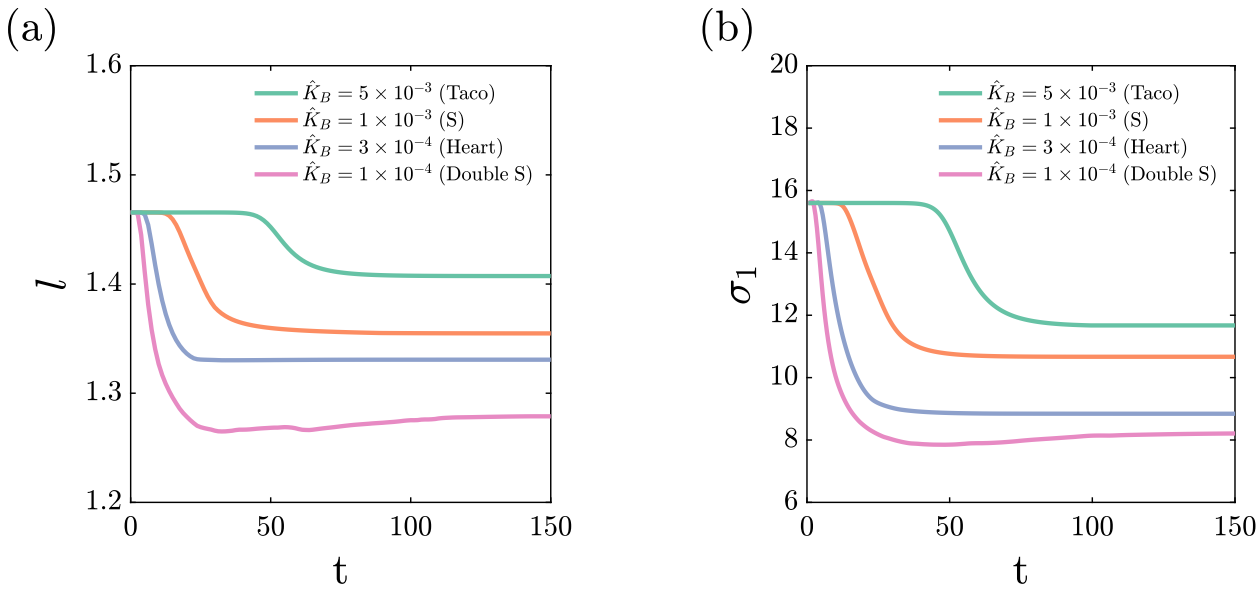


Figure 4.4: (a) Transient stretched length evolution of different conformations in Figure 4.2 with fixed Ca = 0.25. (b) Largest eigenvalue σ_1 evolution of the cases in Figure 4.4(a).

Here, we focus on σ_1, as the two in-plane eigenvalues are negative and small in magnitude. The evolution of σ_1 follows that of stretched length. The magnitude of σ_1 relates to the stretched length of the sheet because more stretched sheets exert stronger force dipole along the flow direction.

4.3.3 Linear stability analysis for compact sheets

We aim to probe into the buckling instability and find the dependence of sheet elasticity on different deformations via a linear stability analysis. For a steady state, if the system experiences small and random perturbations, the analysis can evaluate the linear stability of each perturbation pattern and find unstable deformations, or unstable modes that make the steady-state unstable.

Here, we briefly introduce the key steps of the linear stability analysis. For a dynamical system, where the system observation can be described by a state $\mathbf{x}$, the time evolution of the system can be described by some unknown function f.

$$\dot{\mathbf{x}} = f(\mathbf{x}) \tag{4.14}$$

If the system exists a steady state $\mathbf{x}_s$, it indicates the time evolution of a steady state is zero, or $f(\mathbf{x_s}) = 0$. If we add a random perturbation to the steady state with a small magnitude $\varepsilon \ll 1$, such that the induced deformation remains in the linear regime. The perturbed system can be described as:

$$\mathbf{x} = \mathbf{x}_s + \varepsilon\hat{\mathbf{x}}, \tag{4.15}$$

where $\hat{\mathbf{x}}$ is a random deformation pattern acting on the steady state. Since the perturbation is small, we Taylor-expand the system around the steady state $\mathbf{x}_s$:

$$\begin{aligned} \dot{\mathbf{x}} &= f(\mathbf{x}_s + \varepsilon\hat{\mathbf{x}}) = \dot{\mathbf{x}}_s + \varepsilon\dot{\hat{\mathbf{x}}} \\ &= f(\mathbf{x}_s) + \varepsilon\mathbf{L}\hat{\mathbf{x}} + O(\varepsilon^2), \end{aligned} \tag{4.16}$$

where $\mathbf{L}$ is the Jacobian. We can ignore the steady state evolution as well as the higher-order terms in ε (as ε is a small magnitude), thereby linearizing the system:

$$\dot{\hat{\mathbf{x}}} = d\hat{\mathbf{x}}/dt = \mathbf{L}\hat{\mathbf{x}}. \tag{4.17}$$

We solve the integral and obtain the relation between the time evolution of the perturbation patterns $\hat{\mathbf{x}}(t)$ and the initial perturbation pattern $\hat{\mathbf{x}}0$:

$$\hat{\mathbf{x}}(t) = e^{\mathbf{L}t}\hat{\mathbf{x}}_0 = \mathbf{A}\hat{\mathbf{x}}_0. \tag{4.18}$$

More generally, we can assume that at any time t, the evolution of the system in small time τ ahead (τ should be small enough to make the system stay in the linear regime with a small deviation from the steady state) can be approximated by:

$$\hat{\mathbf{x}}(t+\tau) = e^{\mathbf{L}\tau}\hat{\mathbf{x}}_t = \mathbf{A}\hat{\mathbf{x}}_t. \tag{4.19}$$

That is, in the linear regime, we obtain an operator $\mathbf{A} = e^{\mathbf{L}\tau}$, as a linear mapping from

the initial condition to τ units afterward. In this linearized system, we can examine the stability via the eigenvalues of $\mathbf{A}$ or $\mathbf{L}$. Assume the eigenvalues (λ) are complex, we have the following stability criteria:

$$\begin{cases} \mathrm{Re}(\lambda_{\mathbf{L}}) > 0, & \text{unstable} \\ \mathrm{Re}(\lambda_{\mathbf{L}}) \leq 0, & \text{stable} \end{cases} \quad \text{or} \quad \begin{cases} ||\mathrm{Re}(\lambda_{\mathbf{A}})|| > 1, & \text{unstable} \\ ||\mathrm{Re}(\lambda_{\mathbf{A}})|| \leq 1, & \text{stable.} \end{cases} \tag{4.20}$$

In the following, we will elaborate based on the standard of $\mathbf{L}$. Note that eigenvalues $\lambda_{\mathbf{L}}$ of matrix $\mathbf{L}$ are related to those of $\mathbf{A}$ by $\lambda_{\mathbf{A}} = e^{\lambda_{\mathbf{L}}\tau}$, and two matrices share the same eigenvectors, which are the perturbation modes. If a mode has an eigenvalue with a positive real part $\mathrm{Re}(\lambda_{\mathbf{L}}) > 0$, the mode is unstable and its amplitude as a component of the initial condition will grow exponentially until nonlinear effects become important. In contrast, a mode with an eigenvalue that has a negative real part $\mathrm{Re}(\lambda_{\mathbf{L}}) < 0$ will decay exponentially. In summary, the goal of linear stability analysis is to filter out those unstable modes that can destabilize the steady state.

Under some special circumstances, the operator $\mathbf{A}$ may remain unknown. We develop a method that can extract dominant eigenvectors and eigenvalues. The method has two concurrent steps: generate a vector space that contains the information of $\mathbf{A}$ and extract information from the vector space. The idea is based on a concept called Krylov subspace, which allows us to obtain eigenvalues and eigenvectors of an unknown linear operation by iteratively operating on an initial condition to generate a vector space. For a linear transformation of a vector $\mathbf{b}$ through an unknown linear operator $\mathbf{A}$: $\mathbf{Ax} = \mathbf{b}$, we can generate a series of vectors by repetitively operating $\mathbf{A}$ on $\mathbf{b}$ and form a vector space $\mathcal{K}_r(A, b)$, where r is the numbers of operations.

$$\mathcal{K}_r(\mathbf{A}, \mathbf{b}) = \mathrm{span}\left\{\mathbf{b}, \mathbf{Ab}, \mathbf{A}^2\mathbf{b}, \ldots, \mathbf{A}^{r-1}\mathbf{b}\right\} \tag{4.21}$$

The vector space formed is called a Krylov subspace, and each vector in the space is a collec-

tion of different powers of $\mathbf{A}$ acting on $\mathbf{b}$, starting from $\mathbf{A}^0\mathbf{b} = \mathbf{b}$. Each vector in $\mathcal{K}_r(\mathbf{A}, \mathbf{b})$ is linearly independent with $r < n$, where n is the maximum dimension of the Krylov subspace. We can obtain the eigenvectors of this vector space thereby understanding the information of the unknown operator $\mathbf{A}$. Ideally, the dominant eigenvalues and eigenvectors extracted should converge with enough vectors spanning the Krylov subspace.

To obtain information from the Krylov subspace, we apply a method called Arnoldi iteration, which is an iterative method that gives an approximation of eigenvalues and eigenvectors [170]. Basically, for each iteration (each operation of $\mathbf{A}$ acting on the previous vector), we expand the dimension of Krylov subspace thereby extracting more information about the unknown operator, as a Gram-Schmidt approach.

Though $\mathbf{A}$ remains unknown, we gradually reconstruct $\mathbf{A}$ using the basis obtained from the Krylov subspace. Once we collect enough information, the reconstructed operator can indirectly tell us the information of $\mathbf{A}$. From the linear stability analysis, we want to construct an eigenbasis $\mathbf{Q}$ and a matrix $\mathbf{H}$, such that:

$$\mathbf{AQ} = \mathbf{QH}. \tag{4.22}$$

For each iteration (each operation of $\mathbf{A}$ acting on the previous vector), we can extract a basis vector to fill in $\mathbf{Q}$, and add information to matrix $\mathbf{H}$. In this study, we intentionally keep the basis in $\mathbf{Q}$ orthonormal via a Gram-Schmidt alogrithm, such that we can make the following transformation simply by taking the transpose of the basis matrix:

$$\mathbf{A} = \mathbf{QHQ}^T. \tag{4.23}$$

It is evident that the known matrix $\mathbf{H}$ is the unknown operator $\mathbf{A}$ in a different basis $\mathbf{Q}$. Moreover, we take the eigen decomposition to both $\mathbf{A}$ and $\mathbf{H}$:

$$\mathbf{S_A}\mathbf{\Lambda_A}\mathbf{S_A}^{-1} = \mathbf{QS_H}\mathbf{\Lambda_H}\mathbf{S_H}^{-1}\mathbf{Q}^T. \tag{4.24}$$

Since they share the same eigenvalues $\mathbf{\Lambda_A} = \mathbf{\Lambda_H}$, we obtain the transformation between eigenvectors:

$$\mathbf{S}_A = \mathbf{Q}\mathbf{S}_H. \tag{4.25}$$

In summary, after enough iterations, we can reconstruct the eigenvalues and eigenvectors of the unknown operator $\mathbf{A}$ based on $\mathbf{Q}$ and $\mathbf{H}$. The eigenvalues of $\mathbf{H}$ reveal the stability of $\mathbf{A}$ and eigenvectors are the deformation patterns that can be calculated based on a change of basis.

Now we illustrate how to implement the linear stability analysis on the sheet. In uniaxial extensional flow, we found a steady state when a flat sheet aligns with the flow (z) direction. Typically, the steady state is a slightly stretched sheet (based on specific Ca) with infinitely large bending stiffness ($\mathrm{E_V} \to 0$). We stack all the nodal positions on the sheet and shape them as a position vector $\mathbf{x}$ and $\mathbf{x}_s$ is the position vector at the steady state.

The analysis aims to get the knowledge of the operator $\mathbf{A}$ to extract stability information, which is unknown in the sheet case. Instead, we make full use of our nonlinear simulations and determine $\mathbf{A}\hat{\mathbf{x}}_t$ by performing our full nonlinear in the case where ε and τ are very small as the dynamics are approximately linear. To determine the dominant eigenvalues and eigenvectors, we use a modified Arnoldi iteration method. Figure 4.6 shows some typical

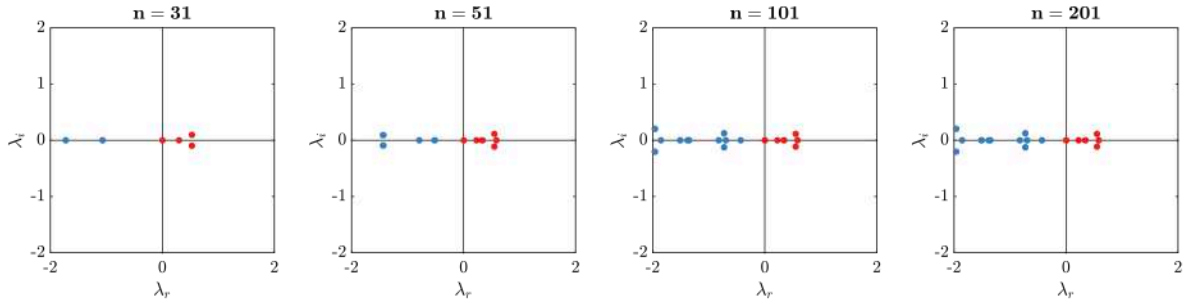


Figure 4.5: Convergence of unstable modes with numbers of iterations (n).

modes arising in our analysis and the names we have given them based on their shapes. One important mode (leftmost in Fig. 4.6) is the rotational invariance mode, which always has a zero eigenvalue ($\lambda_L = 0$). It arises because the shape dynamics are independent of

orientation around the z axis.



Figure 4.6: Top view of examples of deformation modes (added to the flat steady state) obtained from linear stability analysis.

We now apply the linear stability analysis to help understand the numerical simulation results by performing a parameter sweep of Ca and $\hat{K}_B$. Figure 4.7 consists of two parts: the shaded area with different colors are results from linear stability analysis, showing numbers of unstable modes found for sheets with different Ca and $\hat{K}_B$; the markers represent final conformations from numerical simulation. For nonlinear simulations, the initial condition chosen is a flat (compact) steady state at the corresponding Ca (the steady state obtained from a stiff sheet) subjected to a small random perturbation. If no compact steady state is available (the special cases above Ca_c), we start from a sheet at equilibrium with randomly perturbed surface.

The results in Fig. 4.7 are divided into three parts based on the number of unstable modes found. The green area shows the regime where no unstable modes are found, so linear stability analysis predicts that the sheet relaxes to the flat steady state under infinitesimal perturbation. For those sheets with no unstable modes, their final conformation with finite random initial conditions from numerical simulation also stays flat. We only introduce perturbations at $t = 0$, so if a sheet evolves to the flat state it will stay there forever.

In the blue regime, the stability analysis gives one unstable mode, the taco mode. The numerical simulation agrees with what we understand from linear stability analysis: if the taco is the only unstable mode, it is the only unstable deformation that the sheet evolves into, as the sheet is stable under all other types of perturbation. Therefore, the taco is the only stable conformation in the long-term. The linear stability analysis also can predict the final conformation in this regime when only one unstable mode emerges.

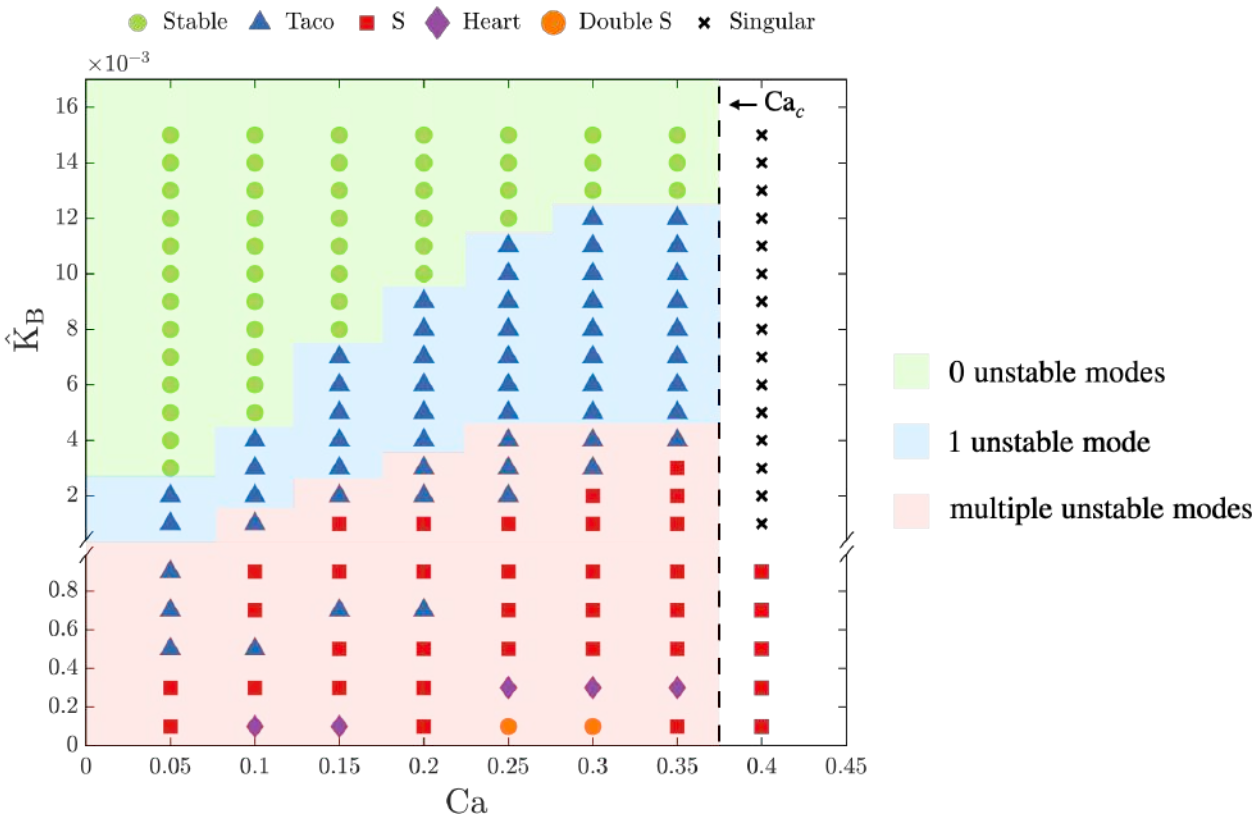


Figure 4.7: Simulation results and linear stability analysis for a disk with neo-Hookean model ($c = 0$). The symbols represent the final conformation from numerical simulation, where the initial condition is a compact and flat sheet under random perturbation, except for the sheets above Ca_c. The color of the shaded region indicates the number of unstable modes obtained from linear stability analysis.

When it comes to the red area, the presence of multiple unstable modes implies that various potential deformations can be obtained, depending on the initial condition. Here, the numerical simulation also suggests many complicated conformations. From the phase diagram, the simulation shows a transition from taco to more complicated S, heart and double S with decreasing $\hat{K}_B$. In order to understand these complicated scenarios, we present two examples in this regime to help illustrate the relation between unstable modes and final conformation. Figure 4.8 shows the shape evolution of the unstable modes fed as the initial condition in two cases. The first case ($\mathrm{Ca} = 0.2$, $\hat{K}_B = 3 \times 10^{-3}$) only has two unstable modes, and is located at the border of red and blue area. The second case ($\mathrm{Ca} = 0.2$, $\hat{K}_B = 1 \times 10^{-3}$) has more than two unstable modes, and we only show two of them.

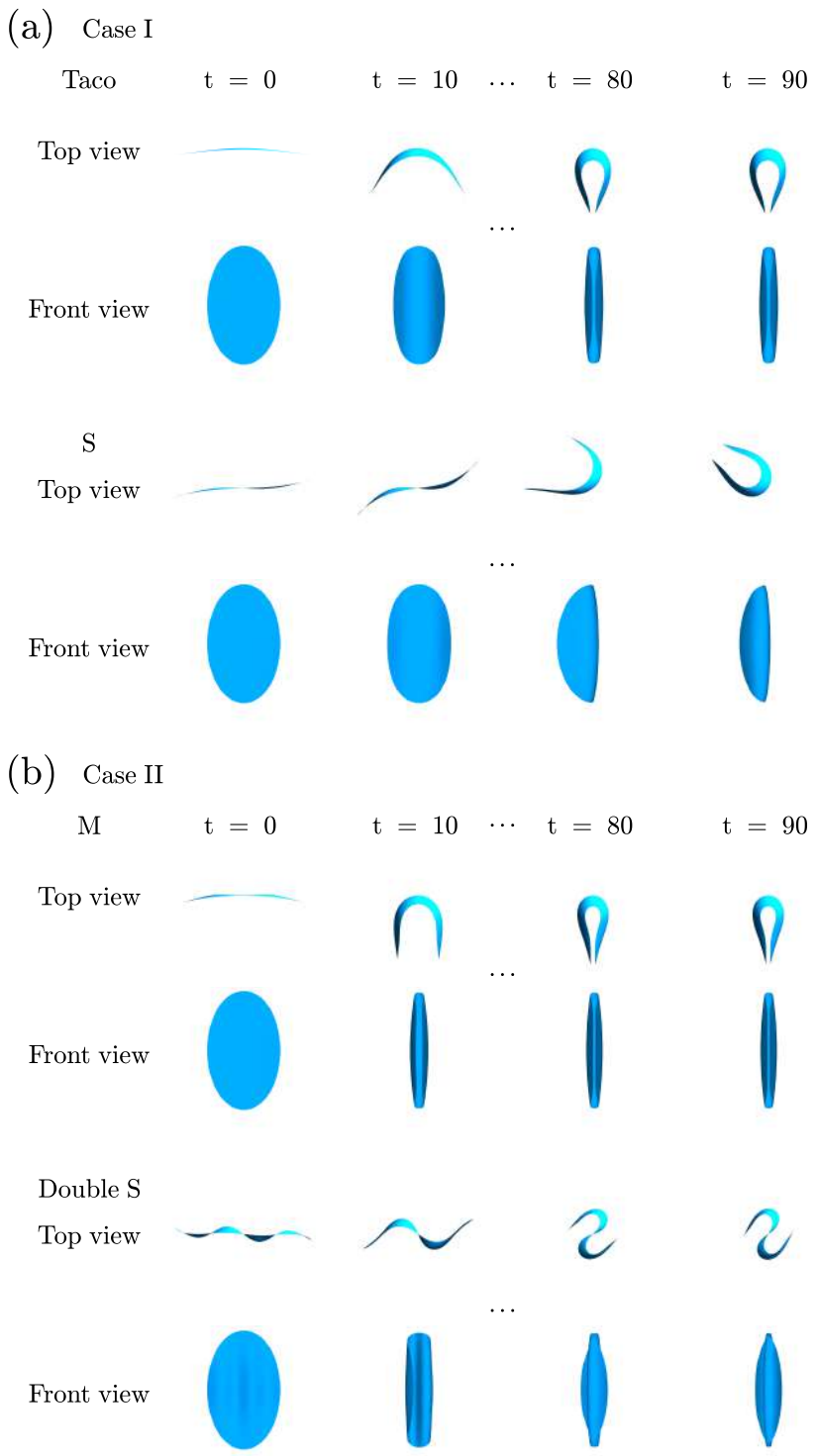


Figure 4.8: Top view and front view of evolutions of modes when they become unstable, with their short-term and long-term dynamics. (a) Taco and S with Ca = 0.2, $\hat{K}_B = 3 \times 10^{-3}$. (b) M and double S with Ca = 0.2, $\hat{K}_B = 1 \times 10^{-3}$.

Based on the evolution in Fig. 4.8(a), the first case, the long time dynamics from either taco or S initial conditions evolve into a taco. This observation shows the limit of the linear analysis that it is unable to precisely determine the long term dynamics of a nonlinear simulation. The second case, Fig. 4.8(b), is more complex, with multiple unstable modes that show different unstable wrinkling patterns. The mirror symmetrical mode M and rotationally symmetric mode double S keep their symmetry for both the short-term and long-term dynamics. Therefore, the mode evolution also implies that the long-time sheet conformations in the red area may vary based on the initial condition, especially for cases with small $\hat{K}_B$.

We observed above that the wrinkling instability leads to a decrease in the steady-state length. We conclude this section with an interesting extreme example of this phenomenon. If Ca exceeds Ca_c, there is no steady state at all for the flat neo-Hookean sheet: the sheet stretches indefinitely. Nevertheless, if the bending stiffness is sufficiently small that the sheet wrinkles, the wrinkled sheet will reach a finite-length steady state. This observation is indicated previously in Fig. 4.7 for $\mathrm{Ca} = 0.4$. Figure 4.9(a) shows the length evolution for a case where this happens, and Fig. 4.9(b) shows the corresponding shape evolution. The

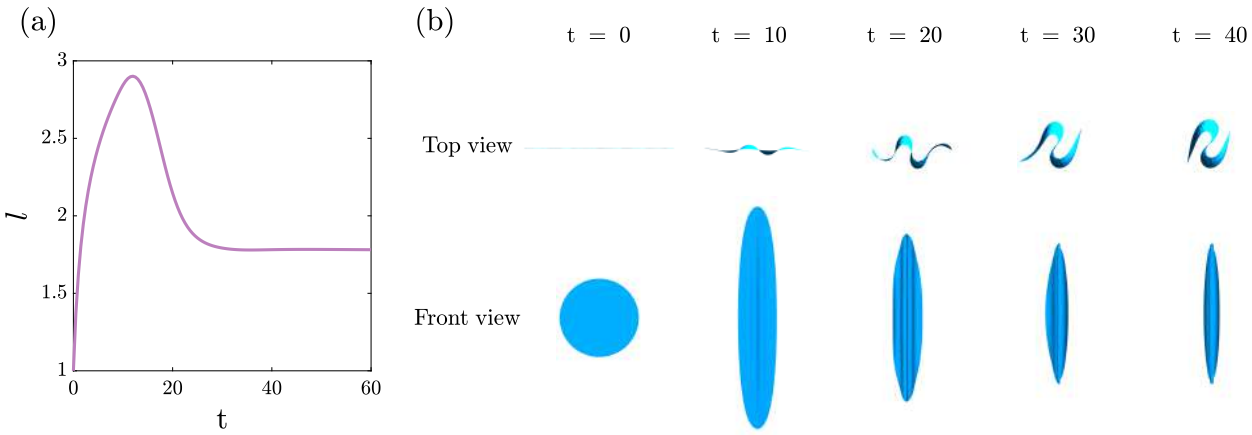


Figure 4.9: Dynamics of a flexible sheet for $\mathrm{Ca} > \mathrm{Ca}_c$ for the neo-Hookean model ($c = 0$): $\mathrm{Ca} = 0.4$, $\hat{K}_B = 5 \times 10^{-4}$. (a) Evolution of length. (b) Snapshots of evolution.

sheet is at rest at $t = 0$ when flow begins. Initially, the length increases, but once the sheet begins to wrinkle, l decreases and then reaches a steady state value. The wrinkling leads to the hydrodynamic screening of the sheet surface in the folds, reducing the local drag on

the sheet and causing it to reach a finite steady state value of l. These results imply that the actual Ca_c might vary with $\hat{K}_B$ in the compact-stretched transition, as we discuss in the next section.

4.3.4 Dynamics of flexible sheets in the stretched (high Ca)

In this section, we first continue the discussion of wrinkling with a focus on the stretched branch in Fig. 4.1(b). Then, we address the influence of wrinkling on the compact-stretched transition and bistability.

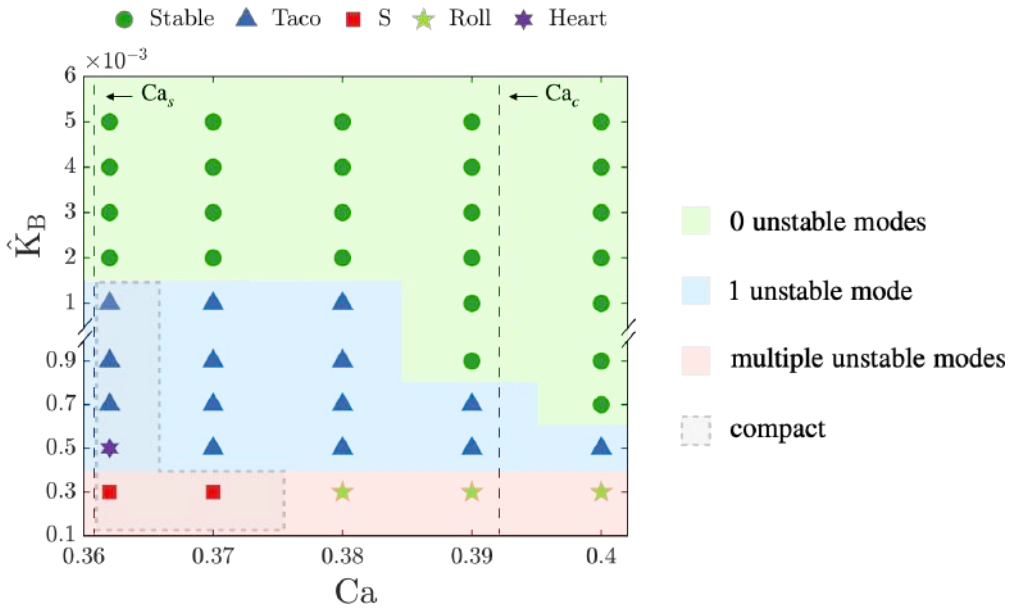


Figure 4.10: Simulation results and linear stability analysis for a disk for parameters encompassing the bistable regime for the flat sheet ($c = 1 \times 10^{-5}$). The symbols represent the final conformation from numerical simulation, where the initial condition is a stretched and flat sheet under random perturbation. The boxed region indicated where an initially stretch state reverts to a compact state upon wrinkling. The color of the shaded region indicates the number of unstable modes obtained from linear stability analysis.

When a sheet is highly stretched, it experiences strong shear stresses due to its increased length and surface area, which further affects the conformation. We performed a parameter sweep focusing on the stretched Ca regime in Fig. 4.1(b) and combined the linear stability analysis to examine the influence of $\hat{K}_B$, and thus the wrinkling instability, on the conformation. Figure 4.10 illustrates the final conformation of the sheet with different $\hat{K}_B$, as well

as the number of unstable modes obtained from linear stability analysis. Compared with Fig. 4.7 for compact sheets, Fig. 4.10 indicates that stretched sheets are more resistant than compact sheets at same parameter values to out-of-plane deformation when $\hat{K}_B$ is relatively large: a compact sheet wrinkles while a stretched sheet with same parameters stays flat. Interestingly, in contrast to the compact regime, where sheets with larger Ca deform first, stretched sheets with smaller Ca first evolve into non-flat conformations while stretched sheets with larger Ca stay flat.

We observed that upon decreasing $\hat{K}_B$, the stretched sheets close to Ca_s may snap to the compact branch after wrinkling, exhibiting a significant decrease in stretched length. Due to hydrodynamic screening (reduced drag) arising from wrinkling, a fully stretched shape can no longer be maintained. We indicate those cases in Fig. 4.10 as a boxed area. This observation implies an increase in Ca_s for smaller $\hat{K}_B$.

We also performed linear stability analysis on the stretched steady states and split Fig. 4.10 into three parts based on the number of unstable modes. The stability analysis results agree with simulation in identifying the regime where sheets stay flat and where sheets become taco-shaped. For sheets with multiple unstable modes, the final conformation again depends on the initial conditions – multiple stable final wrinkled states are possible. Figure 4.10 shows that initially flat sheets with small $\hat{K}_B$ can form asymmetric shapes like the roll that is shown in Fig. 4.11. These shapes slowly rotate due to their asymmetry, and the final conformations deviate significantly from the shape of the unstable modes from linear analysis.

To summarize the influence of wrinkling on the bistability, we present in Fig. 4.11 the bifurcation diagrams of stretch vs. Ca for four different values of $\hat{K}_B$, showing results for flat sheets and sheets allowed to wrinkle. Figure 4.11(a) shows the bifurcation diagram for a relatively stiff sheet ($\hat{K}_B = 5 \times 10^{-3}$): all cases on the stretched branch stay flat, while the compact branch wrinkles, displaying a taco shape. Figure 4.11(e) presents a snapshot of the taco shape that is found at the point labeled 'e' on Fig. 4.11(a). At this stage, both Ca_c

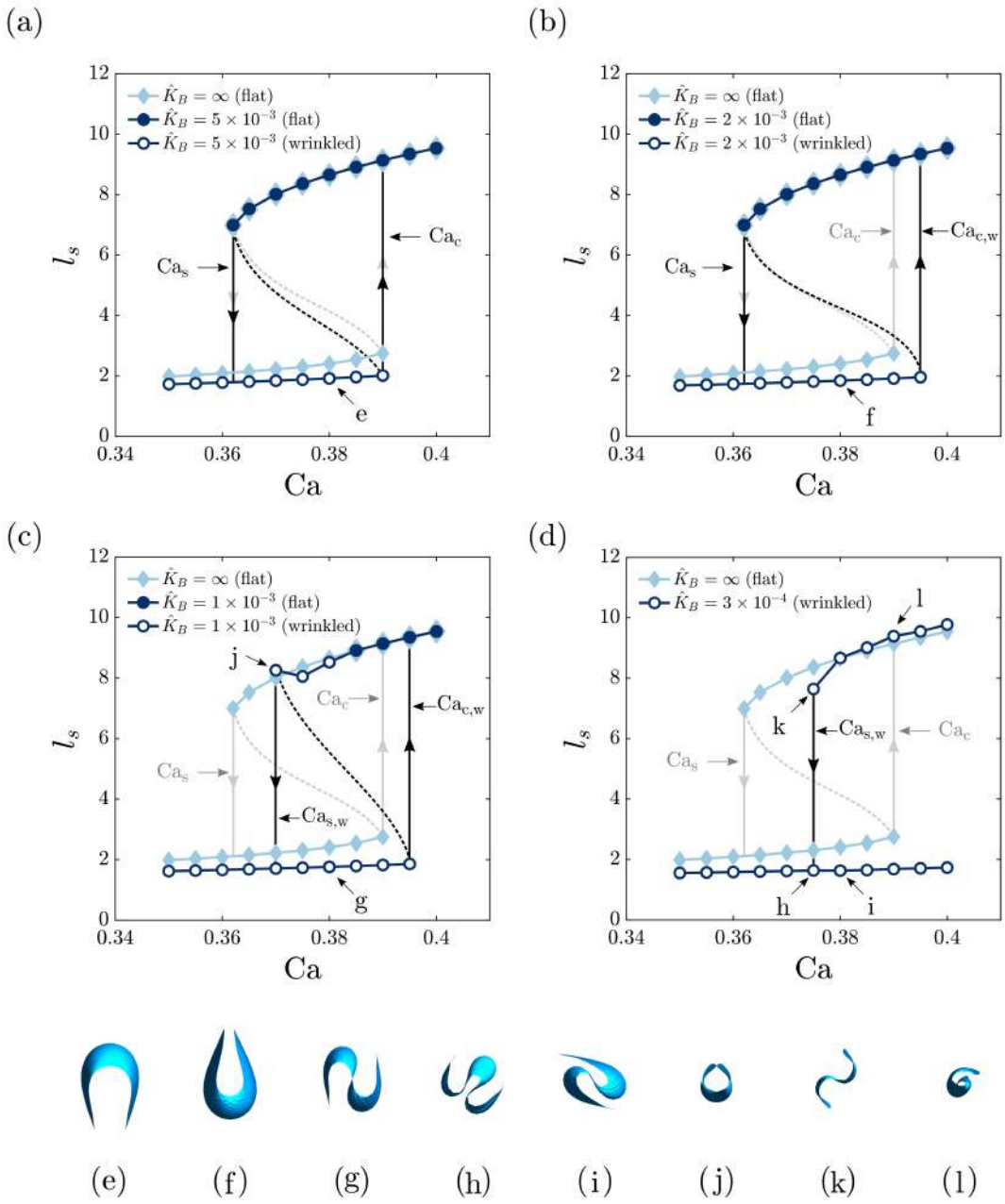


Figure 4.11: (a)-(d): Bifurcation diagram for a flexible disk ($c = 1 \times 10^{-5}$). For reference, the light blue data indicate results for a flat stiff sheet. The hollow data points show a wrinkled sheet and the filled points represent a flat state. (a) $\hat{K}_B = 5 \times 10^{-3}$. (b) $\hat{K}_B = 2 \times 10^{-3}$. (c) $\hat{K}_B = 1 \times 10^{-3}$. (d) $\hat{K}_B = 3 \times 10^{-4}$. Labels $\mathrm{Ca}_{c,w}$ or $\mathrm{Ca}_{s,w}$ denote critical capillary numbers for the wrinkled case. (e)-(l): Conformations at the points labeled e - l on the bifurcation diagrams.

and Ca_s are close to the values found for the flat case.

If we decrease $\hat{K}_B$ to 2×10^{-3} (Fig. 4.11(b)), the Ca_c for the compact branch begins

to shift to higher Ca due to wrinkling, and we denote the new critical capillary number $\mathrm{Ca}_{c,w}$. The interval between Ca_c and $\mathrm{Ca}_{c,w}$ is similar to the case we described above for the neo-Hookean model, in which cases above the singularity can maintain a compact state due to wrinkling-induced hydrodynamic screening. For this parameter set, the steady shapes on the compact branch are tacos (Fig. 4.11(f)) and the stretched branch remains flat.

When $\hat{K}_B = 1 \times 10^{-3}$ (Fig. 4.11(c)), we observe that some stretched sheets also wrinkle, which induces a transition back to a compact state, resulting in a shift of the upper saddle-node bifurcation to a larger value of Ca that we denote $\mathrm{Ca}_{s,w}$. Here the conformations on that compact branch all become a rotating S, as shown in Fig. 4.11(g). For the stretched branch, the deformed sheets form a taco (Fig. 4.11(j)).

Finally, Fig. 4.11(d) shows a case, $\hat{K}_B = 3 \times 10^{-4}$, where both the upper and lower critical capillary numbers strongly deviate from the stiff case. Here, we did not determine the new Ca_c specifically as it is above the parameter range we have considered. The compact branch exhibits two different conformations: heart (Fig. 4.11(h)) for $\mathrm{Ca} < 0.38$ and S (Fig. 4.11(i)) otherwise. On the stretched branch, all cases evolve into two non-flat conformations. Except the case $\mathrm{Ca} = 0.375$, which becomes a S (Fig. 4.11(k)), all other cases become a slowly rotating roll shape (Fig. 4.11(l)). In summary, based on what we have observed, decreasing $\hat{K}_B$ strongly modifies the compact-stretched transition by shifting saddle-node bifurcations to higher Ca.

4.4 Summary

We have applied numerical simulation and linear stability analysis to systematically explore the compact-stretched transition of soft elastic sheets in uniaxial extensional flow.

For stiff sheets ($\hat{K}_B = \infty$) modeled with the neo-Hookean model, we observe a singularity in conformation at a critical capillary number Ca_c. Sheets modeled with the Yeoh model and small values of the nonlinearity parameter c exhibit a discontinuous transition to a highly

stretched state beyond Ca_c – a *compact-stretched* transition. The discontinuity in size marks a bistable regime (defined by Ca_s and Ca_c), where both compact and stretched states can exist based on deformation history.

For flexible sheets, wrinkling instability strongly modifies the compact-stretched transition and bistability. In the compact regime, we observe various wrinkled conformations with different sizes, due to different extents of hydrodynamic screening: the sheet traps the fluid inside wrinkles, leading to a decrease in stretched length. With sufficiently small $\hat{K}_B$, cases above Ca_c can stay in a compact conformation without becoming fully stretched, resulting in a larger Ca_c for wrinkled sheets. We develop a simple linear stability analysis that can predict some of the conformations.

In the stretched regime, the linear stability analysis can also predict the final conformation of stretched sheets with limited unstable modes. Compared with the compact sheets at the same parameter values, the stretched sheets are more resistant to out-of-plane deformation. Highly stretched flat sheets with small $\hat{K}_B$ may become wrinkle and snap to compact conformations, yielding a larger Ca_s. Therefore, we find the decrease in $\hat{K}_B$ shifts the bistable regime to higher Ca.

This study deepens our fundamental understanding of the dynamics of soft sheet-like particles in uniaxial extensional flow and displays important interactions between the compact-stretched transition and wrinkling instabilities. The broad parameter range considered here covers sheets with different in-plane deformability and out-of-plane flexibility, ranging from flexible nanosheets to extensible polymer films. We believe the current work will help guide the design of processes for flow-controlled assembly and synthesis of sheet-like particles.

5

Complex dynamics of elastic sheets in shear flow

We study the dynamics of a thin elastic sheet freely suspended in shear flow at low Reynolds numbers. The sheet with rest shape of a disk or a rectangle is initially placed inside the flow-gradient (shear) plane. For a disk sheet, we identified a stable wiggling motion, corresponding to a dynamic S-shape buckling instability that can be predicted by a simple linear stability analysis. The analysis yields a number of dynamic buckling modes that contribute to the understanding of nonlinear long-term dynamics. On the other hand, we also found unique flapping dynamics: sheets buckle up and down relative to the shear plane with alternating directions. The periodic flapping arises from limited extensibility and the interplay between shear flow and sheet elasticity, which exists in a wide range of dimensionless flow strength and is confirmed by experimental observations made by our collaborator. For a rectangle sheet, apart from the aforementioned flapping, we observed interesting swirling and kayaking motions. Here, the dynamics are strongly determined by the aspect ratio. We observed a nonmonotonic evolution of the buckling threshold with an increasing sheet aspect ratio. The complex dynamics observed shed light on applications involving the suspension of sheet-like particles like thin polymeric films and graphene.

5.1 Introduction

Dynamics and deformations of elastic objects in flow is a classical problem of fluid-structure interaction. At zero Reynolds number, rigid particles like spheroids in shear flow are known to undergo Jeffery orbits, with dynamics only determined by initial orientations [64]. For deformable particles, strong fluid-structure interactions coupled with particle elasticity may induce nonlinear deformations, leading to complex dynamics. Deformable particles such as flexible filaments [37, 56, 93, 161], vesicles [8, 10, 71, 109], and capsules [1, 38, 159] have been extensively studied in shear flow, with many interesting dynamics reported that deviate from Jeffery's predictions. Among the observed morphologies of elastic bodies in Stokes flow, oscillating deformations are of recent interest. Slender filament tumbles in shear flow. Flexible filaments experience periodic deformation combined with tumbling due to straining components from the shear, which gives rise to buckling instability. With increasing flexibility, filaments show a transition from tumbling to a snaking motion, and very flexible filaments may coil during rotation [37, 56, 93, 161]. Other examples of oscillatory motions include the vacillating-breathing in vesicles [8, 10, 109] and swinging in red blood cell capsules [1, 38, 159], where the main axis of the particle oscillates around the flow direction and the body undergoes a breathing motion.

While filaments, vesicles, cells, and other soft particles have been extensively studied in shear, relatively little attention has been paid to the dynamics of thin elastic sheets. Aside from fundamental interest, there is a strong need for such studies due to the increasing prevalence of fluid-suspended thin elastic sheets in various materials processing operations. The processing of two-dimensional (2D) sheets in shear flow is common in nanosheet synthesis like graphene, where in shear flow flexible sheets show complex instability in response to shear-induced deformation [4, 24, 141]. Specifically, the thin structure nature offers 2D sheets less resistance to out-of-plane buckling compared to in-plane deformation, making it easy to develop a 3D shape from a flat state. Some recent works have explored the dynamics of thin sheets in shear flow [39, 67, 89, 133, 150, 156, 157, 186, 187] by addressing the importance

of initial orientation, interfacial effects, and deformability. Thin elastic sheets behave similarly to fibers as they evidence buckling, crumbling, stretching. In extensional flows, highly stretchable sheets show a coil-stretch-like transition with bistable conformations, while sufficiently flexible sheets in uniaxial extensional flow also show complex wrinkling instability due to compressive stress [195, 196]. In a shear flow it has been shown that during the tumbling dynamics due to the rotational component of the shear flow, a thin sheet can buckle due to the compressional hydrodynamic force [133]. A recent simulation study demonstrates that non-Brownian flexible sheets can reach a global steady state in shear flow where the sheet rests within the flow-vorticity plane, as a flow-aligned state [156]. However, so far no oscillatory trajectories have been observed for elastic sheets in shear, which are reported in this study.

The present work describes computational and experimental observations of a non-Brownian thin, nearly-inextensible elastic disk in shear flow. A dimensionless parameter determining the relative strengths of flow and bending stiffness is varied over a wide range, and when flow is strong relative to stiffness, complex “flapping" dynamics of the sheet, with alternating flapping directions along the vorticity axis, are observed. In simulations, stable wiggling dynamics besides flapping can arise from a flat rolling sheet under small and random perturbation. A linear stability analysis is developed that can precisely determine the buckling threshold when a flat disk becomes unstable as well as the wiggling motion.

5.2 Methods

We apply numerical simulations to model an incompressible sheet in two categories of rest shapes shown in Fig 5.1: a disk with a radius of a and a rectangle-like sheet with a fixed long edge $2a$ and a short edge $2a\omega$, where ω varies from 0.2 to 1 indicating sheets with different aspect ratios (e.g. $\omega = 0.5$ represents a rectangle with an aspect ratio of 2, and $\omega = 1$ represents a square sheet with an aspect ratio of 1). The sheet is freely suspended in

a Newtonian fluid with viscosity η and experiences a simple shear flow with the shear rate $\dot{\gamma}$. The sheet is initially placed in the shear (flow-gradient) plane with its normal aligned with the vorticity axis, shown in Fig 5.1(c).

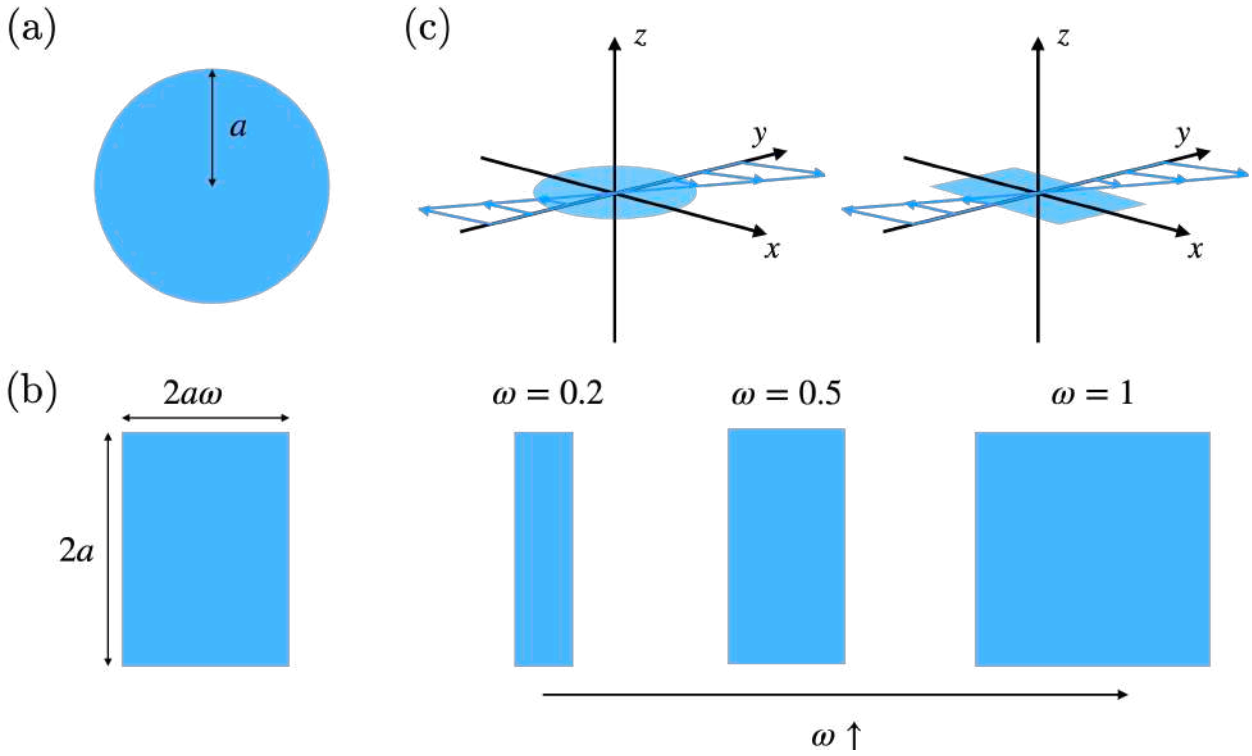


Figure 5.1: Rest shape of interest: (a) A disk with a radius of a. (b) Rectangle-like sheets with long edge sized $2a$ and short edge sized $2a\omega$, with examples including a slender ribbon ($\omega = 0.2$), a rectangle ($\omega = 0.5$) and a square ($\omega = 1$) with increasing ω. (c) Illustration of the initial condition for a disk and a rectangle: the sheet lies inside the shear (flow-gradient) plane.

The elastic responses of the sheet include in-plane stretching and out-of-plane bending[21, 42, 195, 196]. The in-plane deformation is modeled as a neo-Hookean solid with strain energy density W:

$$W = \frac{G}{2}(I - 3), \tag{5.1}$$

where G is a 2D shear modulus and I is the first invariant of the Cauchy deformation tensor. The bending energy is evaluated by adding a penalty to deflection angle $\theta_{\alpha\beta}$ between neighboring elements:

$$E_b = \sum_{\text{adj } \alpha,\beta} k_b \left[1 - \cos(\theta_{\alpha\beta} - \theta_0)\right], \tag{5.2}$$

where k_b is the bending constant calculated from bending stiffness K_B, by comparing Eq 5.2 with the energy of a disk buckled into part of a cylinder with known curvature. The angle θ_0 is zero as we assume a flat equilibrium state. The total elastic force exerted by the sheet on fluid at a random material point $\mathbf{X}_i$ is obtained by taking the derivative of energy: $\mathbf{F}_i = -\partial E/\partial \mathbf{X}_i$.

To nondimensionalize the system, we scale length with sheet radius a, and time with shear rate $\dot{\gamma}$. For mechanical responses, the capillary number $\mathrm{Ca} = \eta\dot{\gamma}a/G$ compares flow strength to in-plane deformation. Smaller Ca indicates a less extensible sheet – in the present work we consider nearly inextensible sheets, with $\mathrm{Ca} = 0.01$. We have confirmed that a further decrease in Ca has no qualitative change in sheet dynamics but rather a decrease in the flapping amplitude (See the following section). The bending flexibility of the disk compared to viscous shear strength is measured by an elastoviscous number: $\mathrm{E_V} = \eta\dot{\gamma}a^3/K_B$. Smaller $\mathrm{E_V}$ implies a sheet that resists out-of-plane deformation.

We assume that the inertia of the fluid is negligible so that the fluid motion is governed by Stokes equation. In this Chapter, we consider two scenarios: fluid motion in free space and under a free surface.

Modeling of fluids in free space

The fluid velocity in free space is resolved with the method of regularized Stokeslet, as introduced in the previous section. As a summary, the perturbation velocity field at location $\mathbf{x}$ generated due to a regularized point force $\mathbf{f} = \mathbf{F}\delta_\kappa(\mathbf{x} - \mathbf{X}_i)$ at $\mathbf{X}_i$ can be represented using a regularized Stokeslet $\mathbf{G}_\kappa$: $\mathbf{v}_p(\mathbf{x}) = \mathbf{G}_\kappa(\mathbf{x} - \mathbf{X}_i) \cdot \mathbf{F}$, where $\mathbf{G}_\kappa$ is the regularized Green's function:

$$\mathbf{G}_\kappa(\mathbf{x} - \mathbf{X}_i) = \frac{\mathrm{erf}(\kappa r)}{8\pi\eta r}\left(\mathbf{I} + \frac{(\mathbf{x} - \mathbf{X}_i)(\mathbf{x} - \mathbf{X}_i)}{r^2}\right) + \frac{\kappa e^{-\kappa^2 r^2}}{4\pi^{3/2}\eta}\left(\mathbf{I} - \frac{(\mathbf{x} - \mathbf{X}_i)(\mathbf{x} - \mathbf{X}_i)}{r^2}\right), \quad (5.3)$$

where $r = ||\mathbf{x} - \mathbf{X}_i||$ and κr scales regularization distance. As $\kappa r \to \infty$, $\mathbf{G}_\kappa$ reduces to Stokeslet solution $\mathbf{G}(\mathbf{x} - \mathbf{X}_i) = 1/8\pi\eta r(\mathbf{I} + (\mathbf{x} - \mathbf{X}_i)(\mathbf{x} - \mathbf{X}_i)/r^2)$ [50].

Modeling of fluids under a free surface

In this case, the boundary conditions of fluids are changed due to the presence of a free surface. We aim to solve the Stokes equation subject to no-penetration and no-shear stress conditions. More specifically, for an arbitrary position $\mathbf{x}$ located at the free surface, the fluid satisfies:

$$\begin{aligned} v_z(\mathbf{x}) &= 0, \\ (\mathbf{I} - \mathbf{nn}) \cdot (\mathbf{n} \cdot \sigma) &= \mathbf{0}, \end{aligned} \tag{5.4}$$

where v_z is velocity component along z (vorticity) direction, $\mathbf{n}$ is the vector normal to the free surface, and σ is Cauchy-stress tensor. The above two boundary conditions make the free surface stress-free, as $\partial v_x/\partial z = \partial v_y/\partial z = 0$.

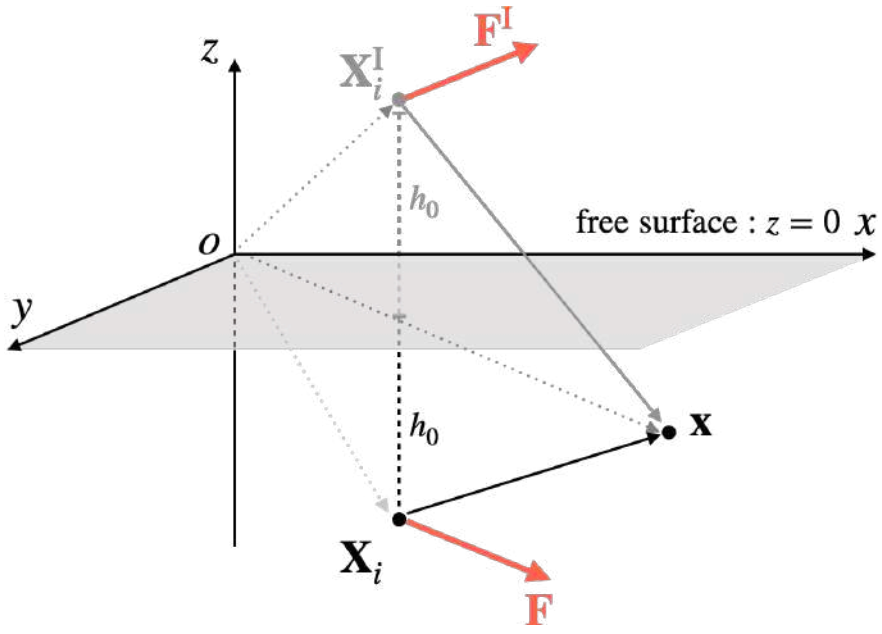


Figure 5.2: The image Stokeslet to solve a force density below a free surface. The free surface locates at the plane $z = 0$. A point force with strength $\mathbf{F}$ is located below the surface at $\mathbf{X}_i$. Its image force is located at $\mathbf{X}_i^{\mathrm{I}}$ above the surface.

To numerically account for the presence of free surface, we add an image Stokeslet system across the surface plane $z = 0$, which is the air-solution interface. Such treatment allows fluid particles locate on the surface to satisfy no penetration and no shear stress boundary

conditions. Therefore, for a given regularized point force $\mathbf{f} = \mathbf{F}\delta_\kappa(\mathbf{x} - \mathbf{X}_i)$ (with strength $\mathbf{F} = [F_x, F_y, F_z]^{\mathrm{T}}$) located at position $\mathbf{X}_i$ with distance h_0 below the free surface, its image Stokeslet with strength $\mathbf{F}^{\mathrm{I}} = [F_x, F_y, -F_z]^{\mathrm{T}}$ is located at position $\mathbf{X}_i^{\mathrm{I}}$ with distance h_0 above the surface. The perturbation velocity field $\mathbf{v}_p(\mathbf{x})$ due to the sheet at any position $\mathbf{x}$ below the free surface:

$$\begin{aligned}\mathbf{v}_p(\mathbf{x}) &= \mathbf{G}_\kappa\left(\mathbf{x} - \mathbf{X}_i\right)\cdot\mathbf{F} + \mathbf{G}\left(\mathbf{x} - \mathbf{X}_i^{\mathrm{I}}\right)\cdot\left(\mathbf{I} - 2\boldsymbol{e}_z\boldsymbol{e}_z\right)\cdot\mathbf{F}^I \\ &= \left[\mathbf{G}_\kappa\left(\mathbf{x} - \mathbf{X}_i\right) + \mathbf{G}\left(\mathbf{x} - \mathbf{X}_i^{\mathrm{I}}\right)\cdot\left(\mathbf{I} - 2\boldsymbol{e}_z\boldsymbol{e}_z\right)\right]\cdot\mathbf{F}\end{aligned} \tag{5.5}$$

Compared with the free space case, the perturbation velocity field also decays as $1/r$ but is significantly larger because the diffused momentum is not absorbed by the free surface but instead gets reflected back into the domain.

Characterization of deformations

We characterize the deformation on the sheet by measuring the deformation amplitude Δz along the vorticity (z) direction based on a local coordinate centered by the disk center. Fig 5.3 shows a disk stays flat and aligns along the vorticity direction. We define the maximum z position above the disk center $z_{\max}$, and the minimum z position below the disk center $z_{\min}$, such that the disk owns a deformation amplitude $\Delta z = |z_{\max}| + |z_{\min}|$ along the vorticity axis. The example in Fig 5.3 shows the case where $z_{\max} = 1$ and $z_{\min} = -1$ and deformation amplitude $\Delta z = 2$.

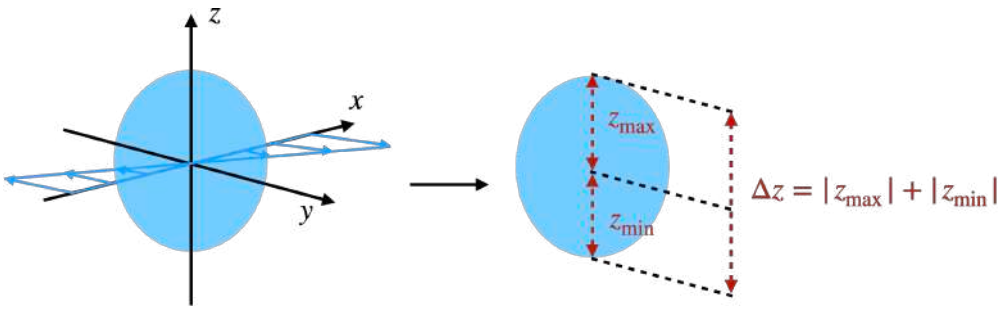


Figure 5.3: Illustration of deformation measurement based on a local coordinate centered by the disk center. The maximum and minimum z nodal positions are marked as $z_{\max}$ and $z_{\min}$, with a deformation amplitude defined as$\Delta z = |z_{\max}| + |z_{\min}|$.

Ca dependence

In this study, we assume an almost inextensible sheet by enforcing a small Ca = 0.01. Here, we examine this assumption with test cases to confirm that a further decrease in Ca gives no qualitative change in dynamics. We focus on two sheets with different dynamics: $E_V = 22$ (flapping) and $E_V = 38$ (wiggling). The detailed characterization of dynamics can be found in the following section. Fig 5.4 compares the deformation amplitude for two sheets with decreasing Ca. The results indicate that the decrease in Ca leads to a decrease in the deformation amplitude without a qualitative change in dynamics. Therefore, it is reasonable to assume that Ca = 0.01 rules out the influence of in-plane deformability.

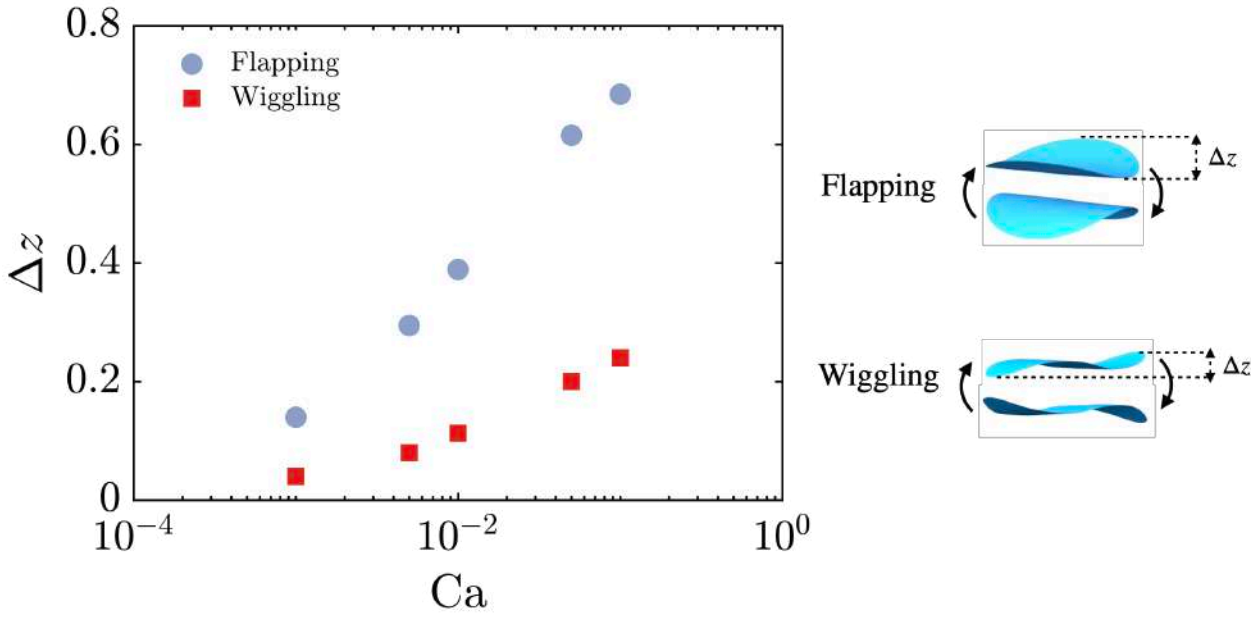


Figure 5.4: Deformation amplitude Δz as a function of Ca for two sheets that show flapping and wiggling, separately. The decrease in Ca leads to a decrease in deformation amplitude while the dynamics converge qualitatively.

5.3 Dynamics of a disk in simple shear flow

To illustrate the disk dynamics in shear flow, we first focus on a basic case where the disk is freely suspended in an unbounded simple shear flow. We begin with the introduction of

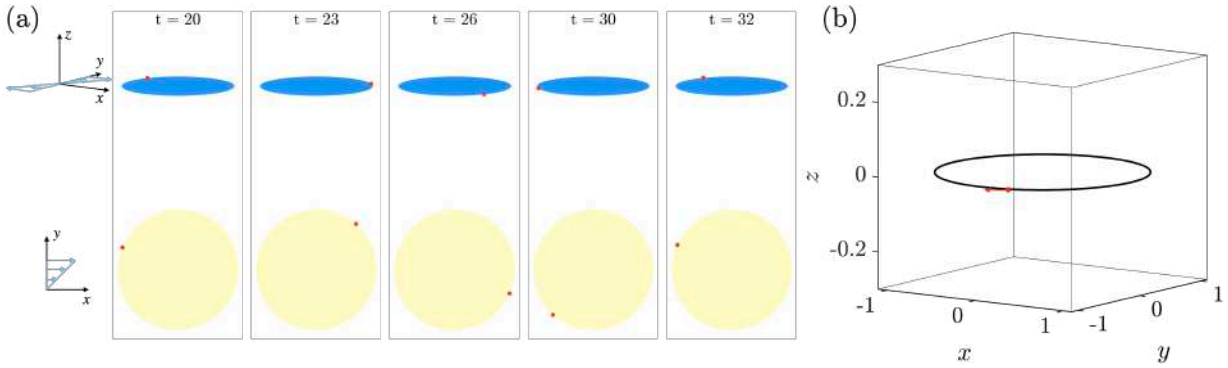


Figure 5.5: (a) Snapshots of a sheet with $E_V = 5$ undergoing periodic 2D rolling motion. A red marker is placed on the edge to track the dynamics. (b) Steady-state trajectory of the marker.

characteristic dynamics observed in the simulation. This is followed by a discussion of the dependence of dynamics on E_V. Finally, we compare the simulation results with experiments done by our collaborator.

5.3.1 Characteristic dynamics

Rolling

Rolling is a 2D periodic motion where the sheet rotates inside the flow-gradient plane. When the sheet is stiff with small E_V, the sheet is stable to small perturbation, and out-of-plane deformation is observed (i.e. below the buckling threshold). As shown in Fig 5.5, the marker on the sheet rotates in the flow while the outer shape of the sheet remains unchanged, which is analogous to the tank-treading motion in capsules and vesicles. The trajectory of the marker chases out to be a circle.

Flapping

The flapping dynamics are observed when a slightly folded C-shape is used as the initial condition. Snapshots of free space simulation in Fig 5.6(a) for the case $E_V = 47$ illustrate one cycle of a flapping motion in three different views, with a reference flat sheet at equilibrium ($\dot{\gamma}t = 0$). Similar to the dynamics observed in experiments, the rotating sheet experiences continuous folding followed by relaxation, while folded direction alternates along the vorticity (z) direction.

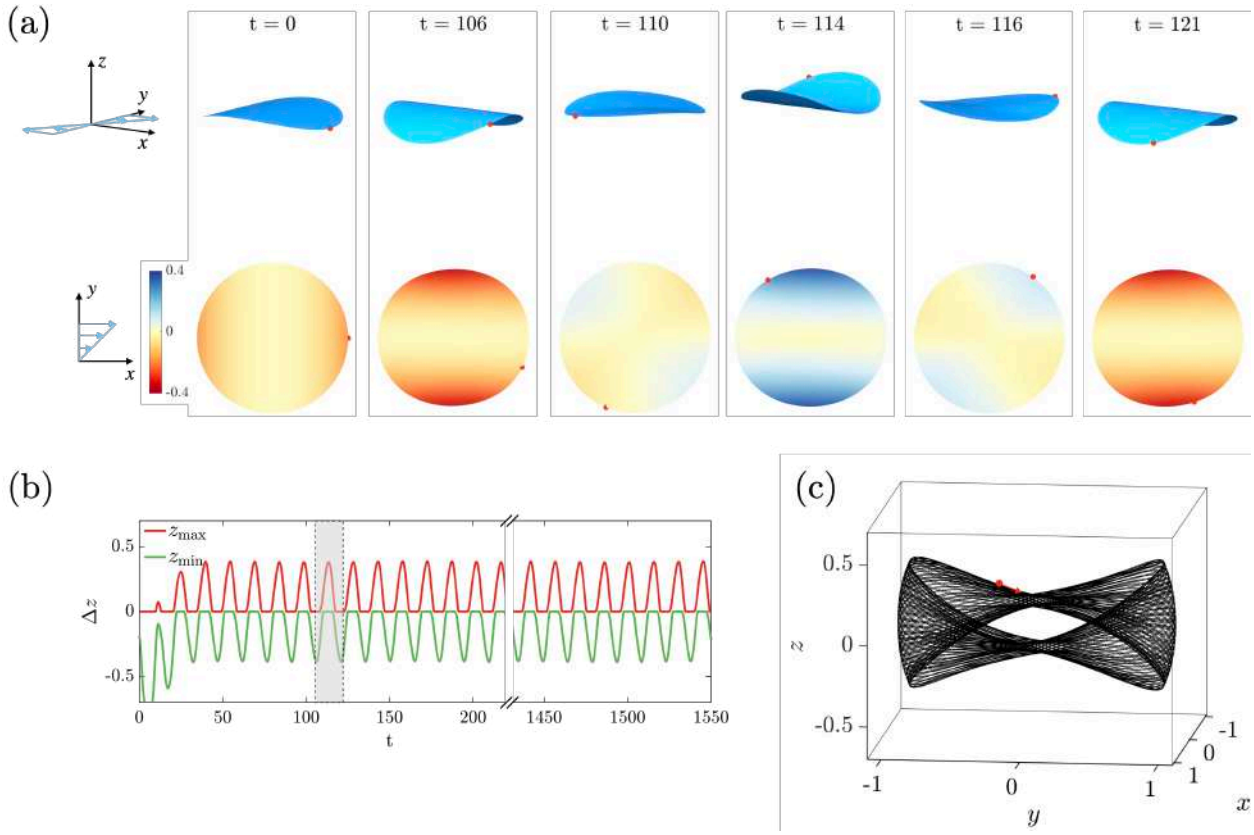


Figure 5.6: (a) Snapshots of a disk with $E_V = 38$ undergoing periodic flapping motion. A red marker is placed on the edge to track the dynamics. (b) Evolution of max (z_{max}) and min (z_{min}) deformation amplitude relative to the sheet center. The shaded area represents the dynamics from the snapshots. (c) Lagrangian trajectory of the marker focused by the sheet center during periodic flapping.

Snapshots ($\Delta\dot{\gamma}t = 10$ and $\Delta\dot{\gamma}t = 18$) show two distinct C-shapes buckling toward opposite vorticity axis, with the folded edges roughly aligned with the gradient axis due to rotation. In addition, we observed two non-flat relaxed shapes ($\Delta\dot{\gamma}t = 14$ and $\Delta\dot{\gamma}t = 22$) as transition states. For example, in $\Delta\dot{\gamma}t = 14$, the upward folding along the major extension axis vanishes and the downward folding along the major compression axis amplifies to trigger opposite flapping. A complete flapping period involves two symmetric flapping motions, thereby resulting in zero net displacements along the vorticity direction. It is important to highlight that the non-flat transition states exhibit nonzero Gaussian curvatures, whereas a perfectly inextensible sheet maintains a constant zero Gaussian curvature. Consequently, the alternating flapping may not be observed in the case of a completely inextensible disk.

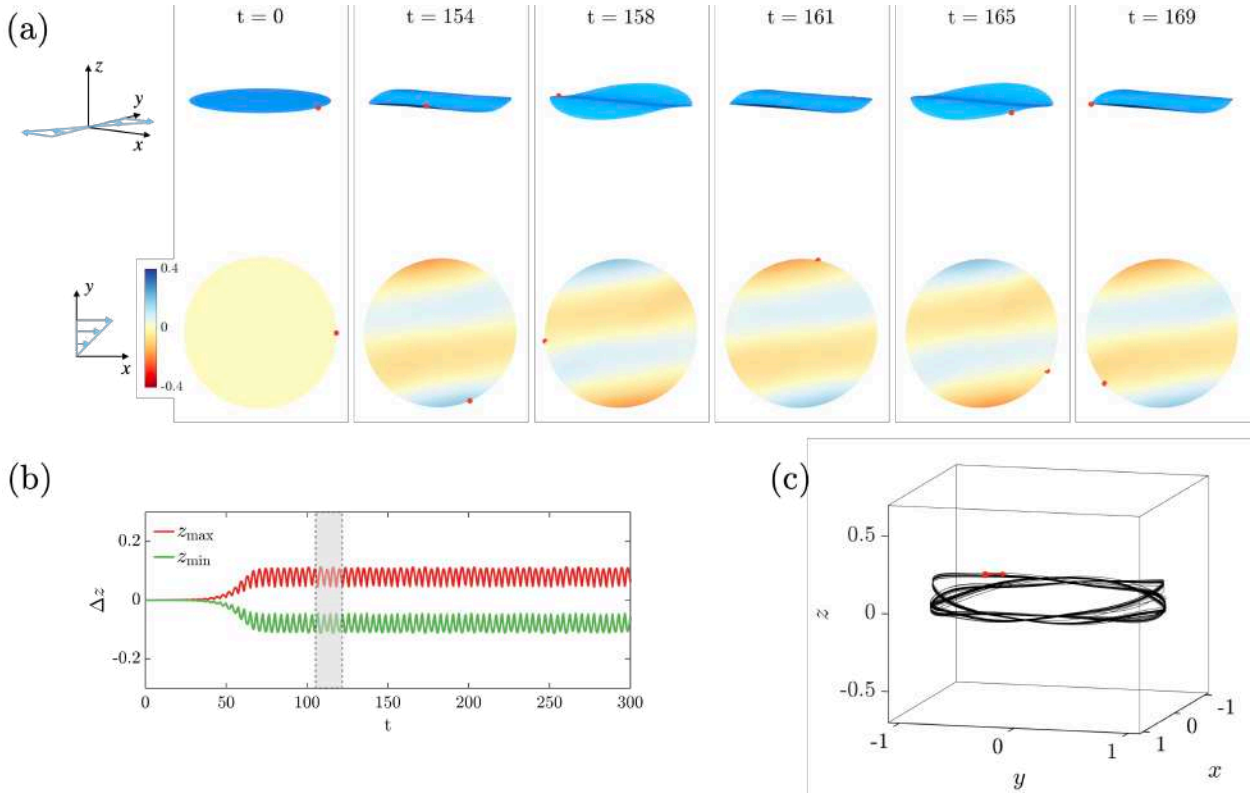


Figure 5.7: (a) Snapshots of a disk with $E_V = 38$ undergoing symmetric wiggling motion. A red marker is placed on the edge to track the dynamics. (b) Evolution of max (z_{max}) and min (z_{min}) deformation amplitude relative to the sheet center. The shaded area represents the dynamics from the snapshots. (c) Lagrangian trajectory of the marker focused by the sheet center during periodic wiggling.

One counterintuitive but robust observation is that the period of the flapping motion does not coincide with the time period of the rotation of the disk, as can be seen from the simulation result in Figure 5.6(a) by following the red marker on the boundary of the disk. This fact also leads to the trajectory of the marker spans the flapping regime in Figure 5.6(c). More generally, while the shape evolution is time-periodic, the motion of the material elements of the disk is quasi-periodic. The periodic nature of flapping motion is also observed in the evolution of deformation amplitude. Fig 5.6 (b) shows the evolution of the maximum and minimum z position of the sheet relative to the sheet center, which indicates the periodicity of flapping. The C-shape deformation can be observed as the alternate peak of z_{max} and z_{min}.

Wiggling

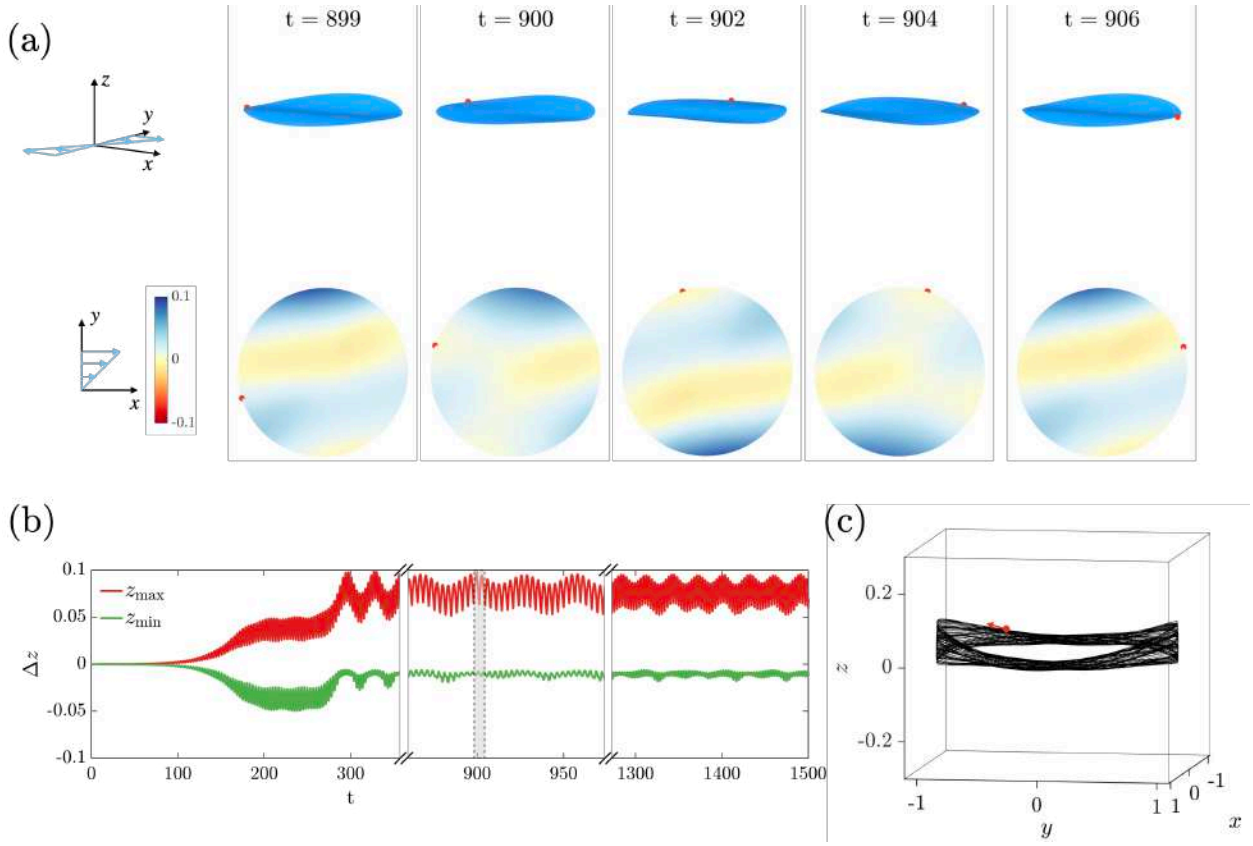


Figure 5.8: (a) Snapshots of a disk with $E_V = 25$ undergoing asymmetric wiggling motion. A red marker is placed on the edge to track the dynamics. (b) Evolution of max (z_{max}) and min (z_{min}) deformation amplitude relative to the sheet center. The shaded area represents the dynamics from the snapshots. (c) Lagrangian trajectory of the marker focused by the sheet center during wiggling.

Wiggling describes the motion where the disk undergoes a periodic and dynamic S shape transition. It can be obtained by perturbing a rolling disk and is the first 3D motion that arises from an initially flat disk above the buckling threshold. The dynamics can be complex because wiggling can be either symmetric or asymmetric, determined by E_V. We first show a symmetric wiggling motion in Fig 5.7. As the rolling disk becomes unstable, the sheet buckles due to compressive stresses and form an S shape wrinkling. The sheet experiences periodic compression and extension, making the S shape relax and buckle. Fig 5.7(a) demonstrates two wiggling periods and it is evident that $t = 154$ and $t = 158$ indicate two S shapes with opposite deformations. Similar to the flapping motion, the motion of material elements is quasi-periodic, such that the trajectory of the marker spans the wiggling domain.

Symmetric wiggling is commonly observed at the beginning stage of deformation for several hundreds of strain units. Later on, the sheet shows a transition from symmetric wiggling to asymmetric wiggling, where S-shape deformation persists and becomes asymmetric relative to the sheet center. Fig 5.8 shows the evolution of a sheet near the buckling threshold. It stays symmetric wiggling for about 100 strain units, then the dynamics become asymmetric wiggling. The trajectory of the marker shows the S shape deformation deforms along the positive vorticity axis.

Flow-aligned

Flexible sheets with large E_V are sensitive to small perturbations. Interactions between many unstable evolution directions lead to complex transient dynamics. Interestingly, almost all flexible sheets finally reach a stable flat state in the flow-vorticity plane, where it experiences the least shear stress. We denote it as a flow-aligned state. It is worth noting that, flow-aligned sheets are stable because in the simulation the sheet takes zero thickness. Therefore, as it approaches the flow-vorticity plane, there is no hydrodynamic torque caused by the zero thickness, and the sheet is trapped in this flat state forever. A particle with finite thickness will tumble.

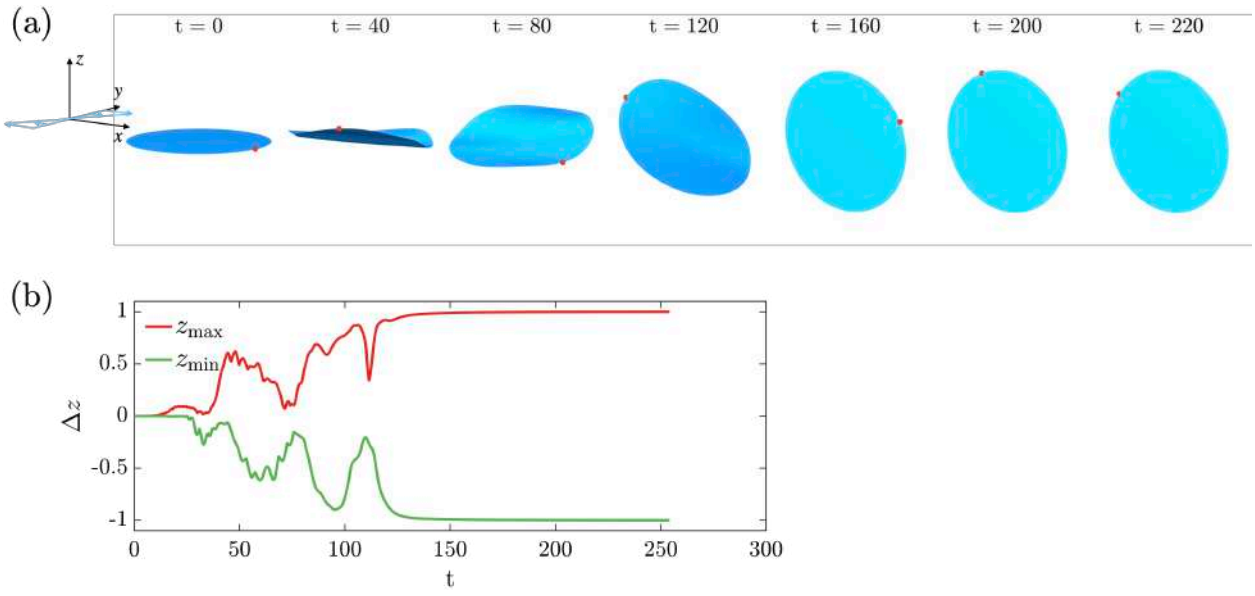


Figure 5.9: (a) Snapshots of a disk with $E_V = 96$ reaching the flow-aligned state. (b) Evolution of max (z_{max}) and min (z_{min}) deformation amplitude relative to the sheet center.

5.3.2 Bifurcation diagram and linear stability analysis

To more fully investigate the evolution of the dynamics with E_V, we performed time-integration of the computational model over a broad range of E_V, as well as examined the linear stability of the rolling state. We tested two types of initial perturbations away from the rolling flat sheet state: (1) small random shape perturbations and (2) perturbations with a "C-shape" similar to the observed flapping shape described above. The long-term dynamics (over 800 strain units) are characterized based on a deformation amplitude $\Delta z = \max_{\text{nodes}} z - \min_{\text{nodes}} z$ as shown in Fig 5.10(a).

Under small random perturbations, initially flat sheets are stable, returning to the in-plane rolling motion when $E_V < 22$. At $E_V = 22$, the in-plane motion becomes linearly unstable (as confirmed by the linear stability analysis below), exhibits a supercritical linear buckling instability: the sheet evolves with an out-of-plane S-shaped deformation that we call "wiggling", and the S shape oscillates by switching folding direction dynamically as the sheet rotates. With increasing E_V, the wiggling shows a larger deformation amplitude. Finally, for $E_V > 38$, wiggling becomes unstable and sheets evolve to a "flow-aligned" state: a flat conformation in the $x - z$ plane. Due to the assumption of zero thickness, a flow-aligned sheet will remain flow-aligned forever.

When subjected to a finite-amplitude C-shaped perturbation, sheets with $E_V < 14$ evolve back to the 2D rolling motion. At $E_V = 14$, a sufficiently large initial perturbation will amplify and the sheet evolves into stable periodic flapping. More generally, with increasing E_V, we identified two out-of-plane solution branches arising from $E_V = 14$, indicated in Fig 5.10(a), corresponding to a saddle-node bifurcation. The first branch is the stable flapping solution just described, whose flapping amplitude Δz increases with E_V. Additionally, we found an unstable branch that represents a critical Δz required to obtain stable flapping. Below the unstable branch, the symmetric deformation decays and the dynamics are governed by the linear buckling instability: the sheet either stays flat ($E_V < 22$) or evolves to the wiggling branch ($E_V > 22$).

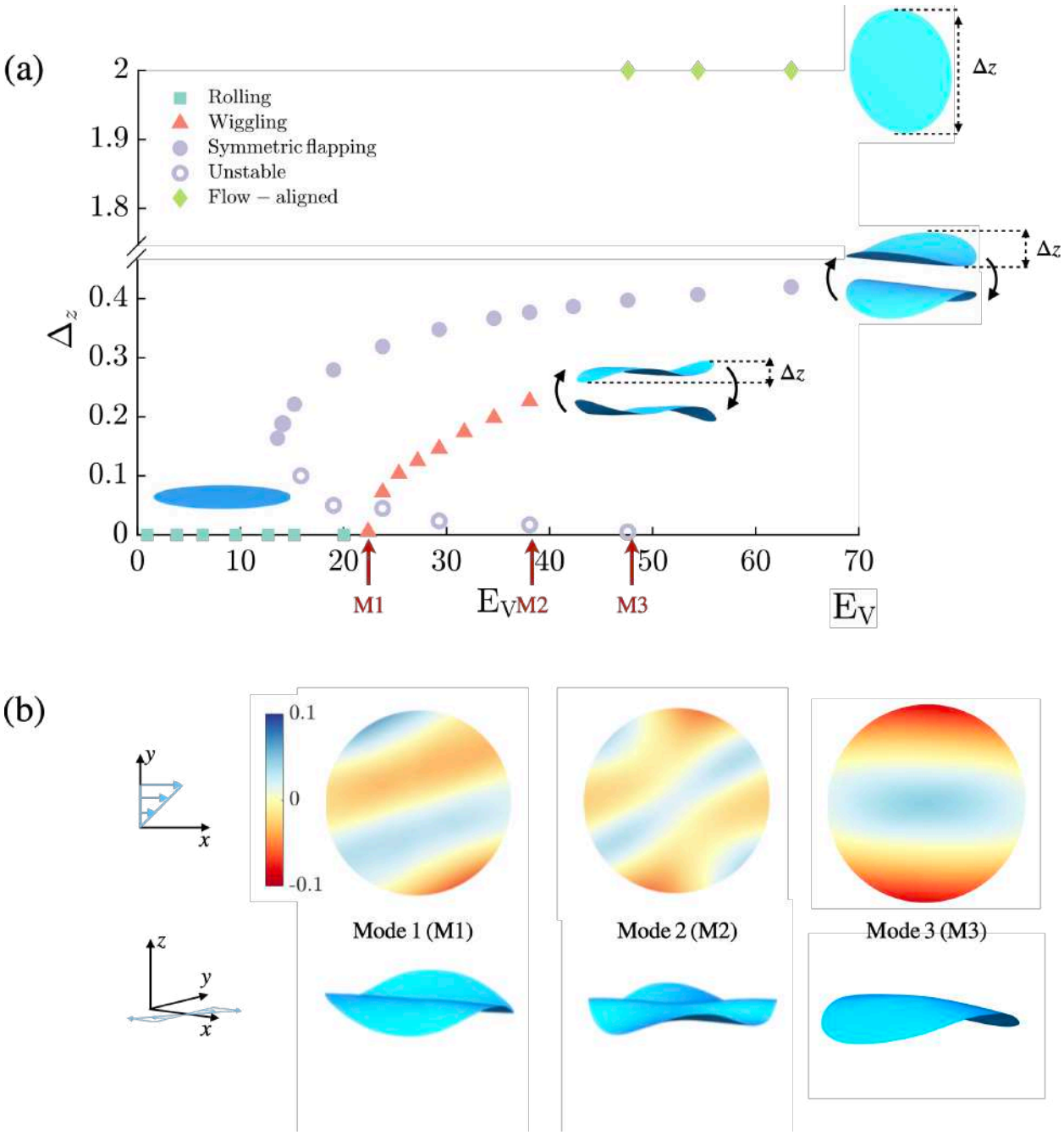


Figure 5.10: (a) Bifurcation diagram of deformation amplitude out of shear plane $\Delta z = z_{\max} - z_{\min}$ vs. E_V from simulation. Snapshots indicate the final dynamics within the observation window. (b) Examples of unstable deformation modes (M1-M3) obtained from stability analysis. Modes are plotted with a random magnitude. Modes become unstable at $E_V = 22$ for mode 1, $E_V = 38$ for mode 2, and $E_V = 48$ for mode 3, with all E_V labeled in the bifurcation diagram.

The buckling instability of the flat state described above can be analyzed in further detail by a linear stability analysis; this also provides insight into further modes of instability and

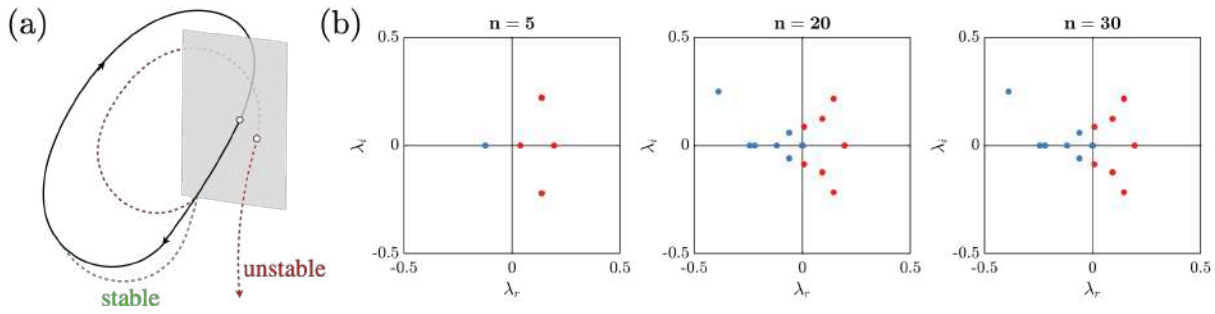


Figure 5.11: (a) Illustration of Floquet analysis. The black trajectory represents the periodic solution. Red and green trajectories represent an unstable and a stable perturbation, separately. (b) Convergence of eigenvalues (λ^L) with numbers of iterations (n). 30 Arnoldi iterations are sufficient for eigenvalues to converge.

their impact on long-term behavior. Because the motions of material points in the rotating flat sheet are time-periodic, this analysis makes use of Floquet theory: i.e. we investigate the response of the periodic rotating solution with a period T ($\mathbf{X}(t) = \mathbf{X}(t+T)$) to infinitesimal perturbation. The detailed implementation to obtain eigenmodes can be found in Sec 4.3.3 from the previous Chapter in extensional flow. The major difference is that the shear flow requires a whole period while the extensional flow owns a steady state. By linearizing the system, we obtain eigenvalues λ^L and eigenmodes that show the linear stability of the system. That is, we can find unstable perturbation patterns with a positive growth rate ($\mathrm{Re}(\lambda^L) > 0$) that make dynamics diverge from a 2D rolling disk.

In Fig 5.10(b), we show the first three non-flat unstable modes. The first unstable mode (M1) has a rotation symmetric S shape and emerges around $\mathrm{E_V} = 22$, showing a linear buckling instability. It is worth noting that the S mode arises exactly at the buckling threshold $\mathrm{E_V}$ in nonlinear simulations, indicating the linear analysis precisely predicts the $\mathrm{E_V}$ where the 2D rolling becomes unstable in Fig 5.10(a). The second unstable mode (M2) appears at $\mathrm{E_V} = 38$ with an M shape deformation and the third mode (M3) arises at $\mathrm{E_V} = 48$ with a C shape.

Though linear analysis is incapable of predicting nonlinear dynamics, it helps explain the long-term evolution based on the evolution of unstable modes. For instance, the evolution of the S mode directly shows wiggling, which predicts the existence of the wiggling solution.

In the nonlinear simulation, the sheet experiences small and random perturbations. The parameter regime where only the S mode arises ($22 < E_V < 38$) reaches stable wiggling as it is the only unstable direction to evolve. The evolution of M mode ($38 < E_V < 48$) in the linear regime stays a dynamic M-shape flapping. However, due to the interaction with the dominant S mode, the long-term evolution of the M mode depends on E_V from becoming wiggling to flapping. This shows the limit of the linear study as it cannot precisely capture the nonlinear dynamics with multiple unstable modes. When the third unstable mode arises ($E_V > 48$), the nonlinear interaction between unstable modes destabilizes periodic deformations and triggers the sheet to become flow-aligned.

5.3.3 Experimental observations

We collaborate with Dr. Hugo Perrin and Dr. Lorenzo Botto to explore a disk in simple shear flow. The following experiments are performed by Dr. Hugo Perrin.

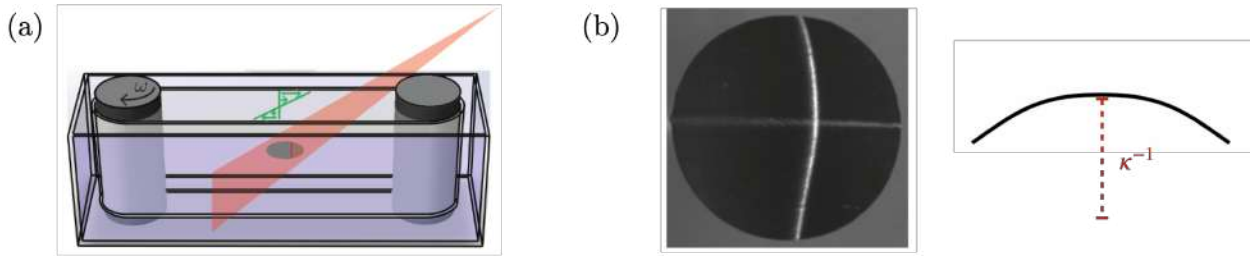


Figure 5.12: (a) Experiment setup: the shear cell generates quasi 2D-shear flow. The inclined laser sheet shines on the disk. The intersection of the laser sheet with the disk measures the local height of the disk with a view from the top (z vorticity direction) and out-of-shear-plane deformation can be extracted. (b) An example of curvature measurement extracted from the laser line on the sheet.

Experiment setup

Thin films of silicon elastomer (Young's modulus $E \simeq 4$ GPa) and different thicknesses ranging in $h \simeq 100 - 200$ μm were cut in a disk shape of radius $a = 1.6$ cm. The shear cell is composed of a belt-driven device by two co-rotating cylinders of diameter 6 cm – see Fig5.12(a). A motor, connected to one of the cylinders, imposes a controlled shear rate in the range $\dot{\gamma} = 0.4 - 10$ s^{-1}. The sheets were placed in glycerol (the viscosity is $\eta \simeq 1$ Pa.s

and the density is $\rho \simeq 1.2 \times 10^3$ kg.m^{-3}). The maximum Reynolds number Re is in the order of 1 at the maximum shear rate. With the use of tweezers, the disk was set with its normal vector along the vorticity direction. Optical measurements with a camera were carried out from the top, i.e. along the vorticity direction of the undisturbed shear flow. An incline laser line is projected on the disk. The deformation of the disk is measured by the distortion of the laser line. We extracted from the images the curvature $\kappa(t)$ by fitting a parabola to the laser line – see Fig 5.12(b). Measurements were performed with a time resolution of 0.01 s and with a spatial resolution of 25 μm/pixel. Even though the maximum Re is of order 1, in analyzing the results we will consider a low Reynolds approximation (Stokes flow). As it will appear later, this approximation gives a reasonable agreement between the simulations and the experimental data.

Comparison

When a flexible disk is placed in a shear flow with the normal vector along the direction of vorticity, the disk rotates and for a strong shear flow, the disk additionally exhibits periodic flapping. More quantitatively, Fig 5.13(a) shows experimental images of the disk (in black) as seen from above (along the z axis) at different times for $\mathrm{E_V} \simeq 47$. The white line on the disk is the intersection line of the disk with the incline laser sheet. The line periodically changes its curvature. From the curvature of the laser line, we extracted the curvature κ of the sheet along the axis y. The measured curvature, see Fig 5.13(b), shows a periodic oscillation between positive and negative curvature. The amplitude of the beat is quite noticeable since it is of the order of $\kappa a \simeq 1$.

We provide a direct comparison between experiments and simulation with the center curvature κ evolution in Fig 5.13(b), which measures the curvature along the slice in $y - z$ plane shown in Fig 5.13(a). We choose roughly two flapping cycles for $\mathrm{E_V} = 47$ and overlap their κ evolution in Fig 5.13(b). Simulation and experiment show good agreement in κ evolution and share a similar flapping period around $\dot{\gamma}T = 15$.

The flapping dynamics exist in a wide range of $\mathrm{E_V}$ in both experiments and simula-

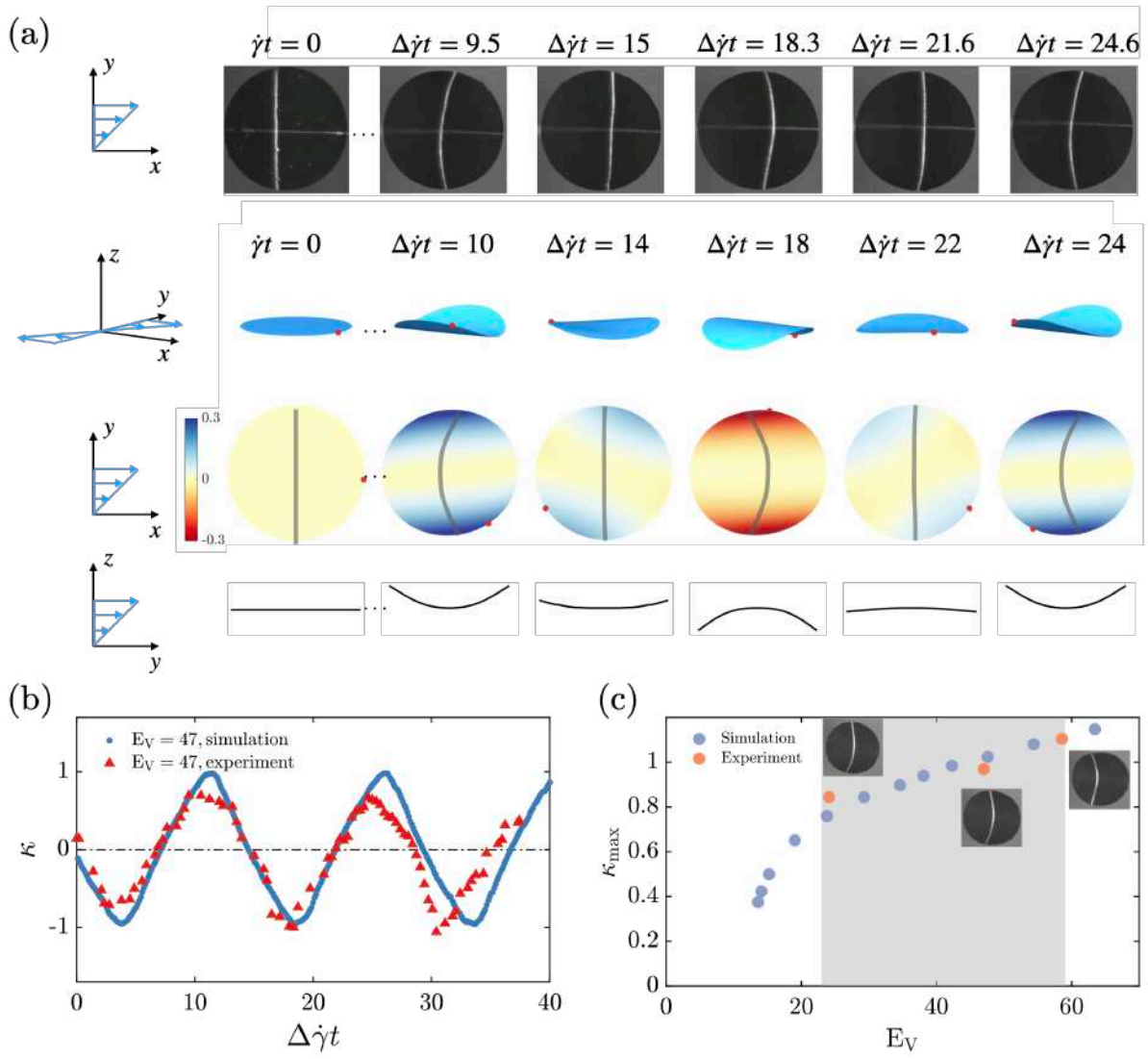


Figure 5.13: (a) Experiment and simulation snapshots for $E_V = 47$ show flapping. The laser line indicates the height of the sheet along the vorticity z direction and the curvature κ along the laser slice can be extracted from the curvature of the laser line. $\dot{\gamma}t = 0$ is the disk at equilibrium. Simulation snapshots for $E_V = 47$ show flapping with three views. The 3D view provides a direct view of flapping dynamics. The flow-gradient (xy) plane view shows a heat plot measuring the deformation amplitude out of the shear plane at the sheet center with an interface with an inclined plane (gray line) to mimic the laser sheet in the experiment. The gradient-vorticity (yz) plane view illustrates the sheet deformation along the slice defined by the laser line. (b) Comparison of curvature κ evolution on the sheet between experiment and simulation from (Fig 5.13(a)). The alternating sign of κ indicates the sheet flaps up and down away from the shear plane. (c) Evolution of κ_{max} vs. E_V showing flapping regime in experiment: $E_V = 24 - 59$, and in simulation: $E_V = 14 - 64$. Snapshots show flapping sheets observed in experiments.

tions. Experimentally, flapping dynamics were observed for E_V in the range from 24 to 59. Below $E_V \simeq 24$ the disk doesn't deform, rotate and leave the initial shear plane. Above

$E_V \simeq 59$ the disk deforms in higher modes and leaves the shear plane. We present the flapping regimes in Fig 5.13(c) and compare the maximum center curvature during flapping κ_{max} between experiments and simulations. Overall, the simulation shows a wider range of flapping regimes.

One important observation is the noticeable asymmetry of flapping motion in experiments. In contrast to symmetric flapping in free space simulation, the sheet in experiments prefers flapping downward (along $-z$ axis), resulting in a more negative evolution in κ. The asymmetry observed in experiments can be attributed to the presence of a free surface, which plays a crucial role in shaping the sheet's dynamics. We have conducted simulations of a flat sheet under a free surface and observed a similar asymmetric flapping motion, which will be elaborated on in the following section. Moreover, we found that the free surface can induce a C-shape deformation on an initially flat sheet, thereby facilitating the evolution toward flapping.

5.4 Dynamics of a disk in shear flow under a free surface

The free surface is an interface where the liquid is in contact with the open air and fluid particles near the free surface experience zero shear stress. In experiments, the polymeric sheet is freely suspended in glycerol under the air-glycerol surface, or simply a free surface. Simulations have suggested that the dynamics arising from an initially flat sheet subject to small and random perturbations are wiggling, a dynamic S-shaped deformation. However, experimental observations have revealed that flapping naturally arises from an initially flat disk. Since the major difference in operating conditions here is the presence of a free surface, we are motivated to investigate its influence on the shear flow dynamics.

As mentioned in the methods, the free surface is located at the plane $z = 0$. The disk is oriented with an initial distance z_0 below the free surface, while the sheet itself lies inside

the flow-gradient plane. In the following, we set $z_0 = -0.5$ to make the disk initially close to the free surface to better examine this effect. We have verified that, though dynamics are determined by the distance away from the free surface, they are not sensitive to the deformation history based on the parameter regime interested. That is, when a disk with $z_0 = -0.5$ migrates away from the surface and arrives at $z = -1$, the dynamics agree with the disk released at $z_0 = -1$, except for those sheets become unstable and flow-aligned.

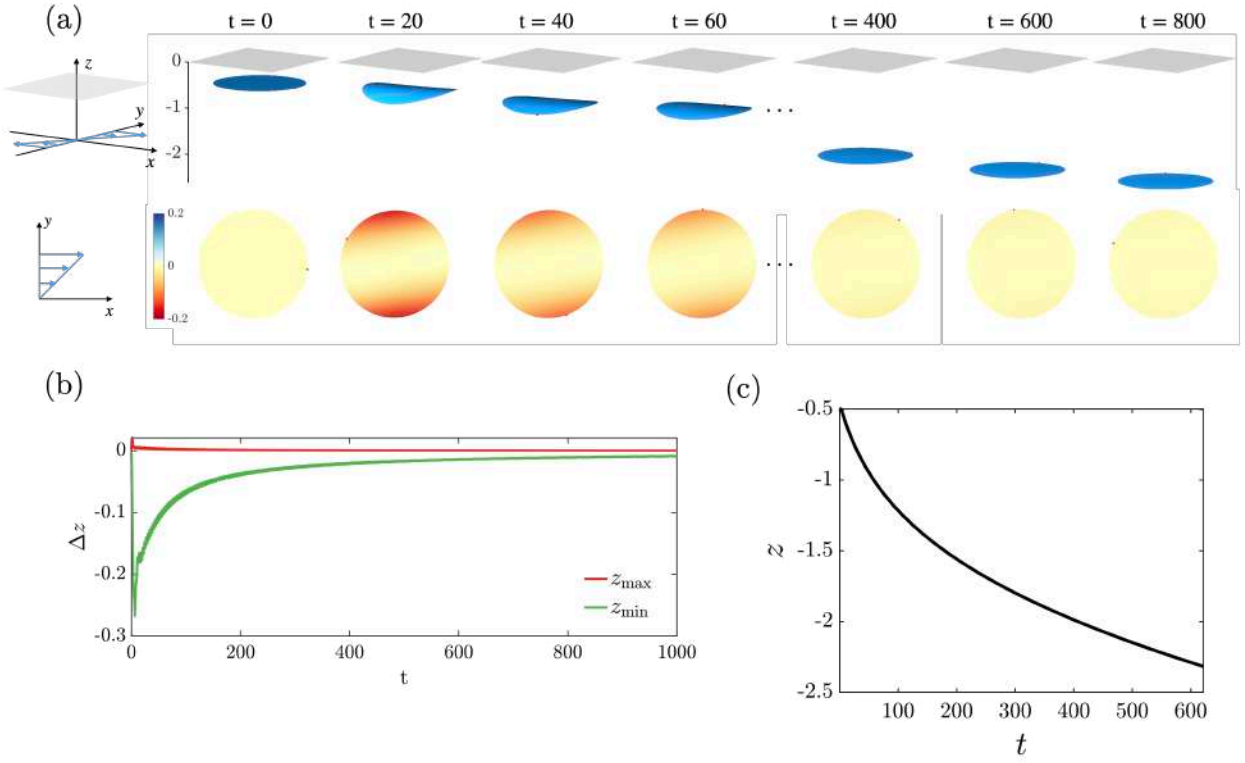


Figure 5.14: Snapshots of a disk ($E_V = 4$) initially inside the shear plane at $z_0 = -0.5$ below the free surface, with colored plots indicating z position of the sheet relative to the sheet center. The grey layer represents the free surface located at $z = 0$. The disk forms a stable taco shape migrating away from the free surface. (b) Evolution of max (z_{max}) and min (z_{min}) deformation amplitude relative to the sheet center. The shaded area represents the dynamics from the snapshots. (c) Evolution of distance away from the free surface z.

In the following, we introduce two transient evolutions to illustrate the free surface effect. Fig 5.14 shows a disk with $E_V = 4$, which is stiffer compared to the buckling threshold $E_V^C = 22$ examined in the free space. Notably, the sheet quickly deforms into a taco shape facing away from the free surface as indicated at $t = 0$, while the material points on the disk undergo tank-treading-like motion. Due to the free surface breaking spatial symmetry,

the deformed taco sheet migrates away from the free surface and the deformation gradually vanishes. This is indicated in the evolution of deformation amplitude. Finally, when the sheet arrives around $d = 2$, the deformation on the sheet vanishes, and the sheet rolls in the flow-gradient plane, which agrees with what we find in free space.

Based on the observations, we can make several comments.

- Free surface effect influences the dynamics within a certain range. When the sheet is away from the free surface, the dynamics assemble free space.

- The buckling threshold near the free surface is significantly lower than that in free space.

- The deformation induced by the free surface on an initially flat sheet is symmetric, whereas in free space C-shape deformation only arises from symmetric perturbations.

Perhaps we can gain more understanding of the free surface with a more flexible sheet. In the case $\mathrm{E_V} = 50$ in Fig 5.15, the disk flaps when close to the free surface. However, the flapping is strongly biased as it only flaps away from the free surface along with the migration of the sheet. During migration, the sheet starts showing upward flapping, and the upward flapping amplitude gradually increases, which indicates the fact that as the sheet migrates away, the free surface effect gradually vanishes.

The above observations can are related to two facts. Though the induced velocity field under a free surface scales as $1/r$, the velocity magnitude is significantly larger than that in free space. This happens because the free surface reflects the momentum back to the fluid domain and amplifies the velocity [50]. Therefore, under the same force, the sheet under a free surface is easier to deform, decreasing the buckling threshold. We can also treat the free surface effect as placing a second sheet on the top of the free surface, as the image Stokeslet in the free surface formulation, such that the influence of the second sheet increases hydrodynamic interactions that lead to deformation.

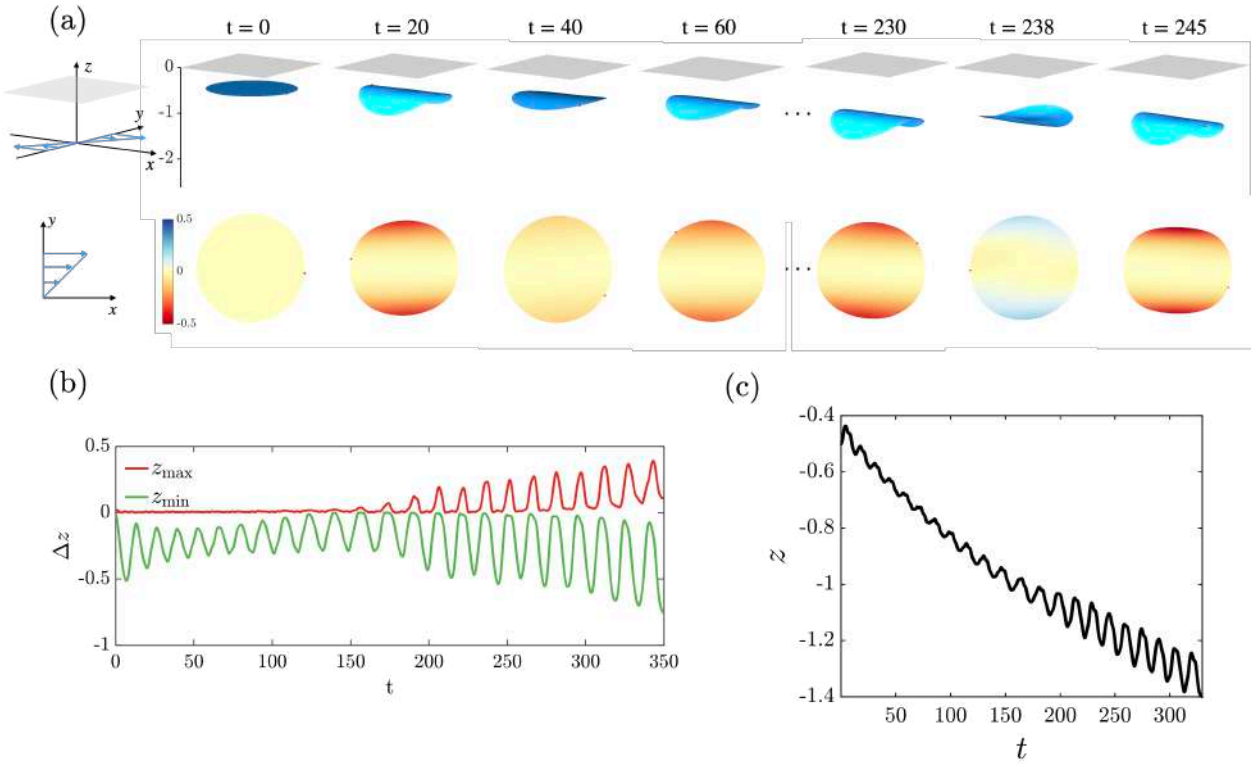


Figure 5.15: (a) Snapshots of a disk ($E_V = 50$) initially inside the shear plane at $z_0 = -0.5$ below the free surface, with colored plots indicating z position of the sheet relative to the sheet center. The grey layer represents the free surface located at $z = 0$. (b) Evolution of max (z_{max}) and min (z_{min}) deformation amplitude relative to the sheet center. The shaded area represents the dynamics from the snapshots. (c) Evolution of distance away from the free surface z.

The two examples above indicate that the free surface triggers symmetric deformations on the sheet. To explain the origin of the symmetric deformation, we did the linear stability analysis for a rolling disk under a free surface at $z = -1$. Unlike the free space results where an S-shaped mode is the first out-of-plane unstable mode, we obtained a dominant C-shape mode (Fig 5.16(a)) in all test cases, which confirms the fact that free surface induces symmetric deformation that leads to flapping.

To give a more detailed comparison with experiments, we include the free surface effect and compare deformation amplitude at $E_V = 47$. The data were taken when the sheet is around $z = -1$. Fig 5.16(b) shows that the curvature evolution from the free surface case is biased as the free surface hinders upward flapping. This observation qualitatively agrees with the experiment.

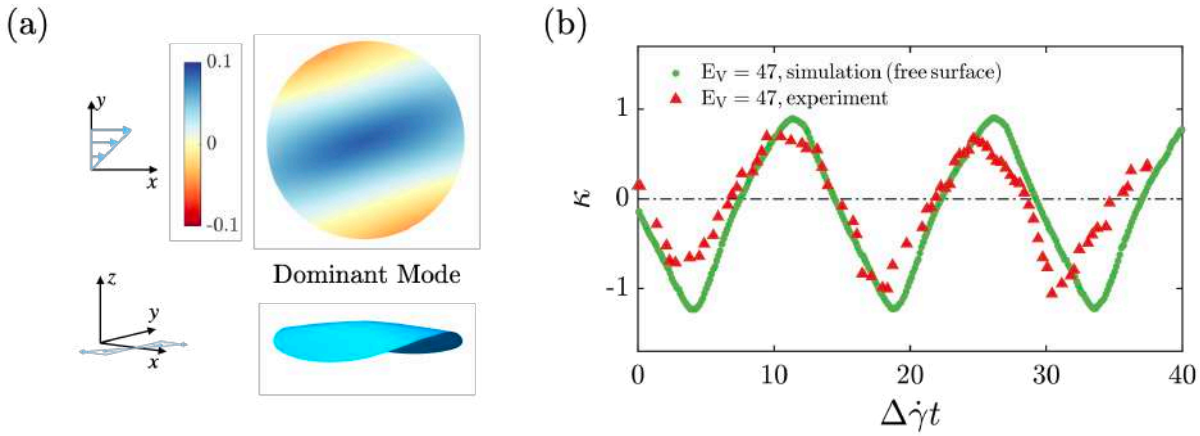


Figure 5.16: (a) The dominant unstable mode obtained from linear stability analysis for a flat sheet rolling at the plane $z = -1$ under a free surface at $z = 0$. (b) Comparison of curvature κ evolution on the sheet between experiment (Fig 5.13(a)) and free surface simulation for $E_V = 47$. The alternating sign of κ indicates the sheet flaps up and down away from the shear plane.

Finally, we summarized the free surface dynamics by recording the dynamics with different E_V with $z_0 = -0.5$ in Fig 5.17. For all cases, the free surface effect induces migration and sheets drift along the $-z$ direction.

Here, we consider a sheet to be flat when the deformation amplitude $\Delta z < 0.05$ and we count the taco case in Fig 5.14 as a special case in one-side flapping. The phase diagram gives an overview of dynamical regimes. We have verified that the dynamics are not determined by the initial distance z_0 except for the markers that show flow-aligned. For example, if the sheet initially locates at the regime of two-side flapping, the dynamics will soon become flapping and start migrating. For the flow-aligned regime, we found an initially flat sheet undergoes two-side flapping and eventually becomes flow aligned.

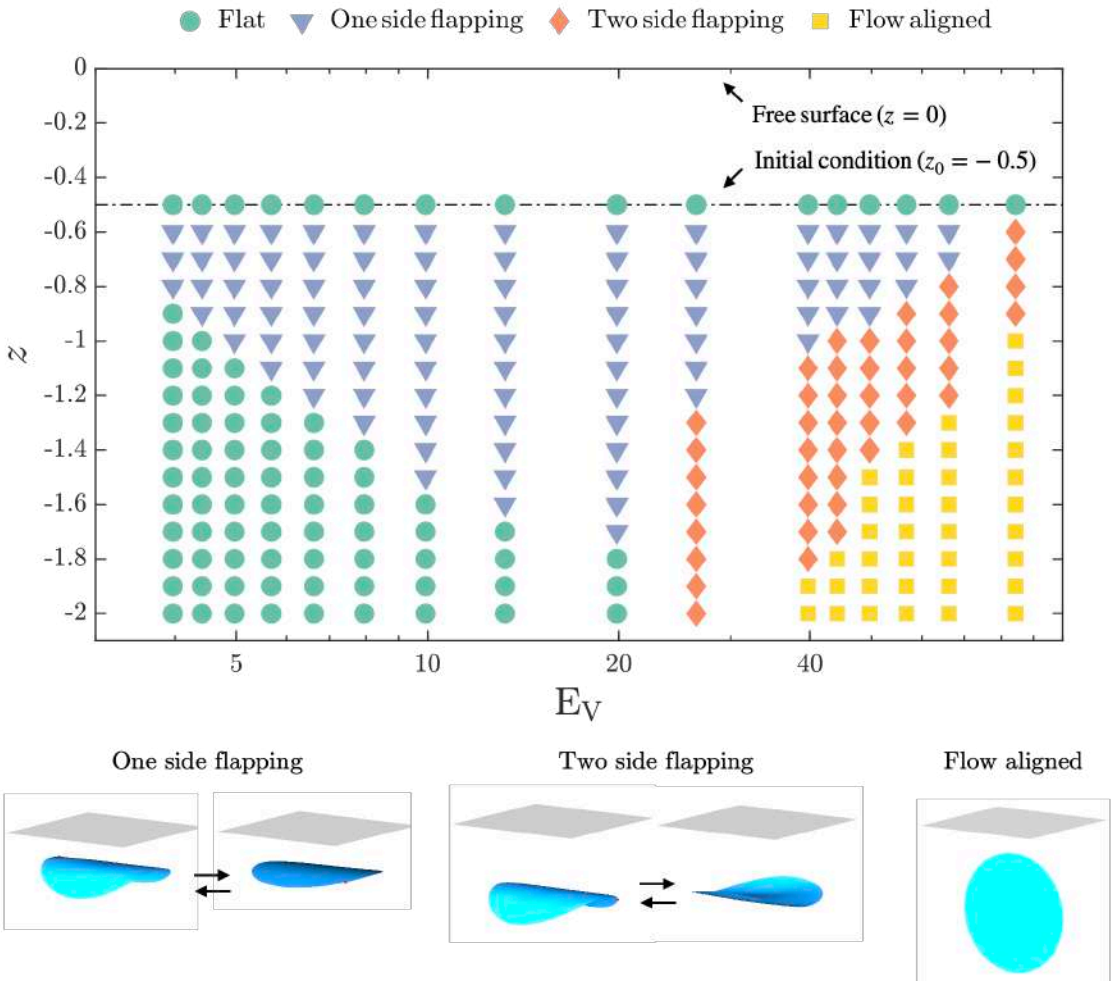


Figure 5.17: Phase diagram of dynamics at different height (z) below the free surface ($z = 0$). All sheets are initially located at the plane $z_0 = -0.5$. The markers represent the dynamics of the sheet at the corresponding z.

5.5 Dynamics of a rectangle sheet in simple shear flow

In the previous section, we gave a detailed analysis of a disk in unbounded shear flow. Now we switch the gear to discuss a family of different rest shapes as rectangles.

5.5.1 Tumbling sheets

We revisited the model validation case presented in Chapter 2 with a more detailed illustration. A flat rectangle sheet with $\omega = 0.5$ is initially placed near the flow-vorticity plane

with the normal vector of the sheet arranged 10° relative to the gradient direction inside the flow-gradient plane (see Fig 5.18).

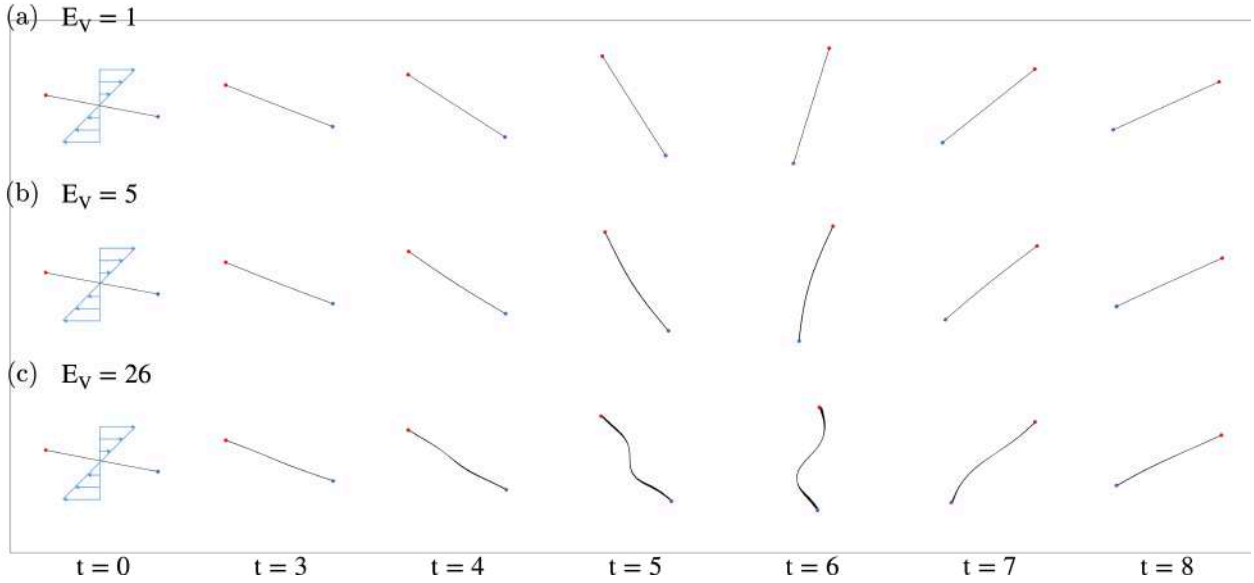


Figure 5.18: Snapshots of a rectangle tumbling in shear flow with increasing E_V. The long edge of the rectangle aligns with $x - y$ plane and is initially oriented 10° from the flow direction. (a) A stiff sheet shows no buckling with $E_V = 1$. (b) A flexible sheet shows C-shape buckling with $E_V = 5$. (c) A flexible sheet shows S-shape buckling with $E_V = 25$.

Once the sheet starts tumbling, sufficiently flexible sheets show different buckling deformation responses while passing through the major compressive axis of the shear flow. The buckling soon vanishes as tumbling continues and all sheets complete about half of a tumbling cycle by gradually approaching the flow-vorticity plane, as an "aligned" state. It is worth noting that the aligned state is meta-stable. Strong perturbation may induce tumbling followed by a repeated long aligned process. Due to the limitation of the methods, the sheet will finally be trapped in the aligned state as there is no hydrodynamic torque generated for a zero-thickness sheet to undergo a Jeffery-like tumbling. We may fix this by adding an artificial hydrodynamic torque based on the actual thickness of the sheet. However, the thin-structured nature makes the thickness effect negligible for the dynamics before the alignment process and we choose to leave the sheet with zero-thickness.

Figure 5.18 presents the time evolution of three different responses observed during tumbling. With increasing flexibility, the sheet shows a transition from a stiff sheet below the

buckling threshold to flexible sheets with C-shape and S-shape wrinkling patterns. We then plot the temporal buckling state B of the above cases in Fig 5.19(a). All three cases show a local peak around $t = 5.5$, as the most buckled state right after the sheet passes through the major compressive axis of shear flow. This indicates that tumbling delays the deformation triggered by compressive stress. The most buckled state (markers in Fig 5.19(a)) are listed.

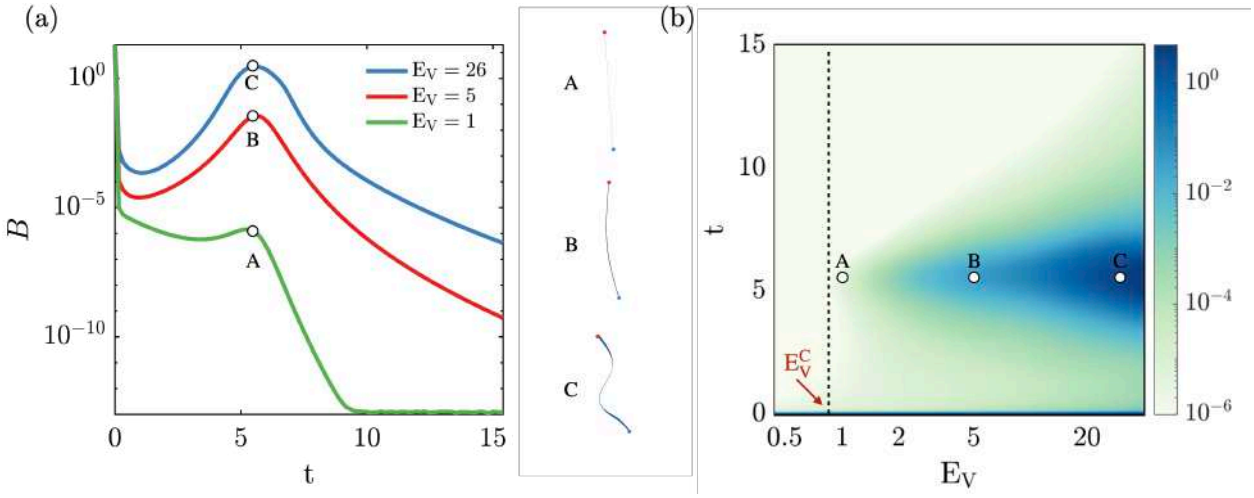


Figure 5.19: (a) Evolution of wrinkling parameter B on the sheet for three cases from Fig 5.18. A-C are snapshots of the most wrinkled states at $t = 5.5$. (b) Evolution of buckling state for sheets with different $\mathrm{E_V}$. The color scales the extent of buckling $E_b^\star$ and the markers indicate the snapshots A-C. The buckling threshold is estimated to be $\mathrm{E_V^C} \sim 1$.

We summarize the buckling evolution of sheets covering a range of flexibility in Fig 5.19(b). Here, we determined the buckling threshold as $\mathrm{E_V^C}$ 1. Since the deformation remains 2D, we assume the change in shapes has negligible influence on the buckling dynamics. In experimental observations made by Perrin *et al.* [133], the buckling threshold estimated is larger due to the limit of resolution for curvature measurement. When applying the curvature measurement to the simulation, we obtain an almost identical buckling threshold.

5.5.2 Characteristic dynamics

We now shift the gear to explore a different rest shape: rectangle sheets, with the tuning parameter ω that varies the sheet from a slender ribbon to a square. Unlike the tumbling case where the dynamics remain 2D and are not sensitive to the change in the rest shape,

the dynamics for a sheet initially inside the shear plane are determined by both ω and E_V.

To begin with, we introduce several characteristic dynamics that have been highlighted in the simulation. The order is roughly based on sheets with increasing flexibility, but some dynamics are also determined by the aspect ratio.

2D rotating

When the sheet is stiff, it is stable to perturbations and returns to rotate inside the shear plane, similar to the 2D rolling observed for the disk.

Stiff kayaking

We report a Jeffery-like kayaking motion observed for stiff sheets with small ω (slender sheets) in Fig 5.20. During kayaking, the sheet stays flat and gradually rotates out of the initial shear plane. The out-of-plane motion is triggered by the initial random perturbation. Though the sheet resists small perturbation, it becomes tilted and is slightly off the shear plane. As a result, the sheet tumbles while gradually leaving the shear plane. This effect is more evident for more slender sheets.

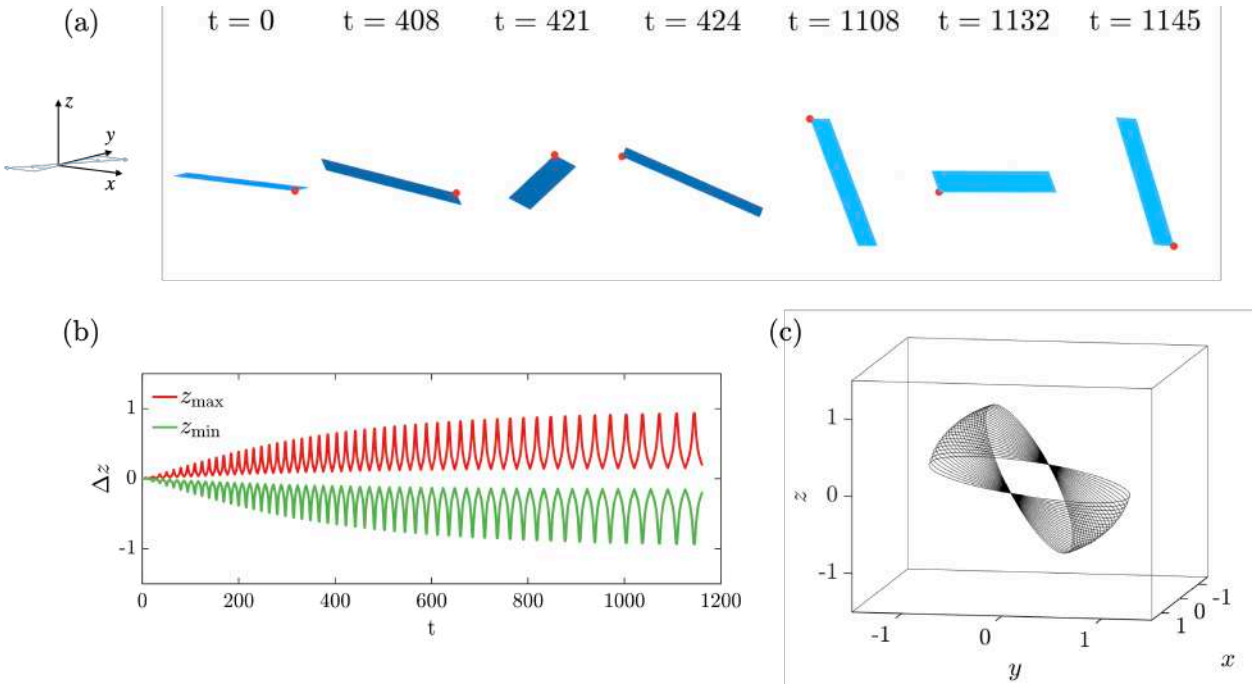


Figure 5.20: (a) Snapshots of transient evolution of a sheet with $\omega = 0.2$ and$E_V = 13$. (b) Evolution of max (z_{max}) and min (z_{min}) deformation amplitude relative to the sheet center. (c) The transient Lagrangian trajectory of the marker.

Flapping

In the disk case, we reported unique flapping dynamics with the sheet buckles up and down relative to the shear plane. For rectangle sheets, we observed similar flapping motions in a wide range of ω. Compared with the disk, rectangle-like sheets show two major differences. First, while the flapping in the disk arises only from a symmetric perturbation, the flapping in rectangle sheets arises from random perturbations. Second, the disk shows periodic flapping motion with a quasi-periodic motion of material points on the disk. In contrast, the flapping in a rectangle sheet is periodic. Fig 5.21 shows a complete flapping cycle. The trajectory of the marker traces out a closed orbit.

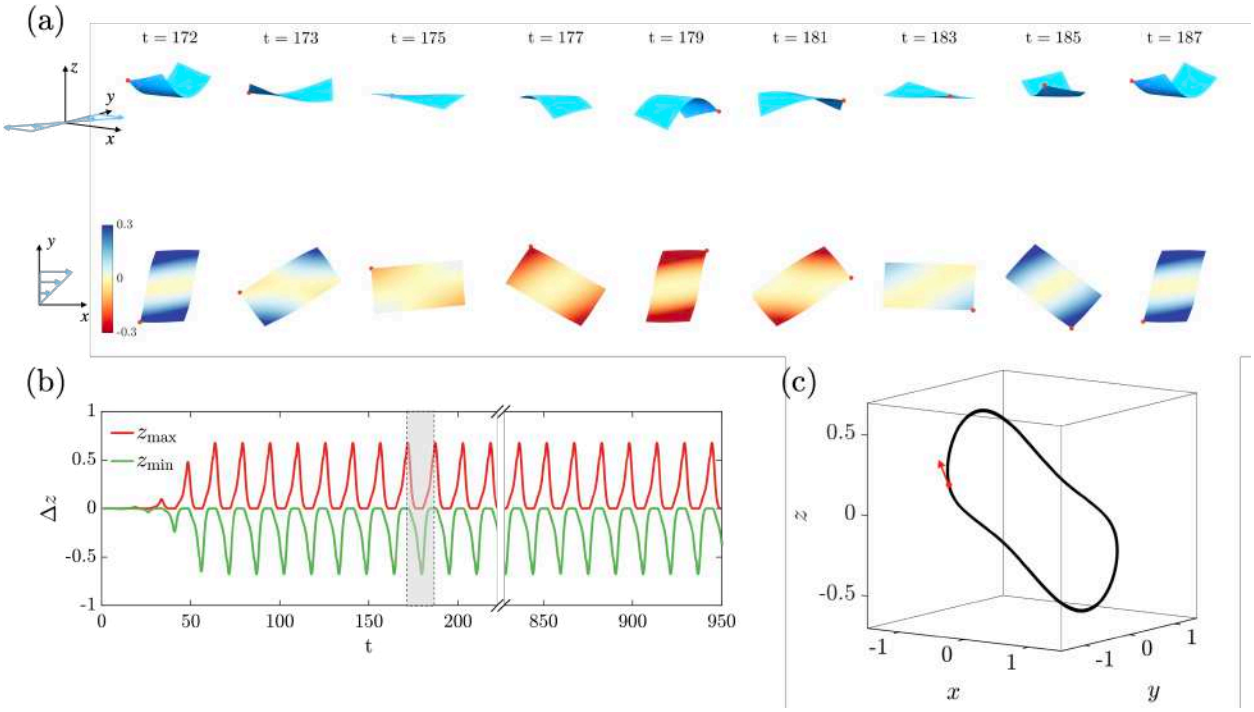


Figure 5.21: (a) Snapshots of periodic flapping motion for $\omega = 0.5$ and $E_V = 8$. (b) Evolution of deformation amplitude z_{max} and z_{min} relative to the center of the sheet. The shaded area indicates the snapshot in (a). (c) The Lagrangian trajectory (based on the sheet center) of the marker after reaching the steady state.

Swirling

For sheets with ω close to one (more square-like), we observed an interesting motion named swirling, where four corners of the sheet folded toward the same direction during rotation. We identified two types of swirling: symmetric and asymmetric. When the sheet is

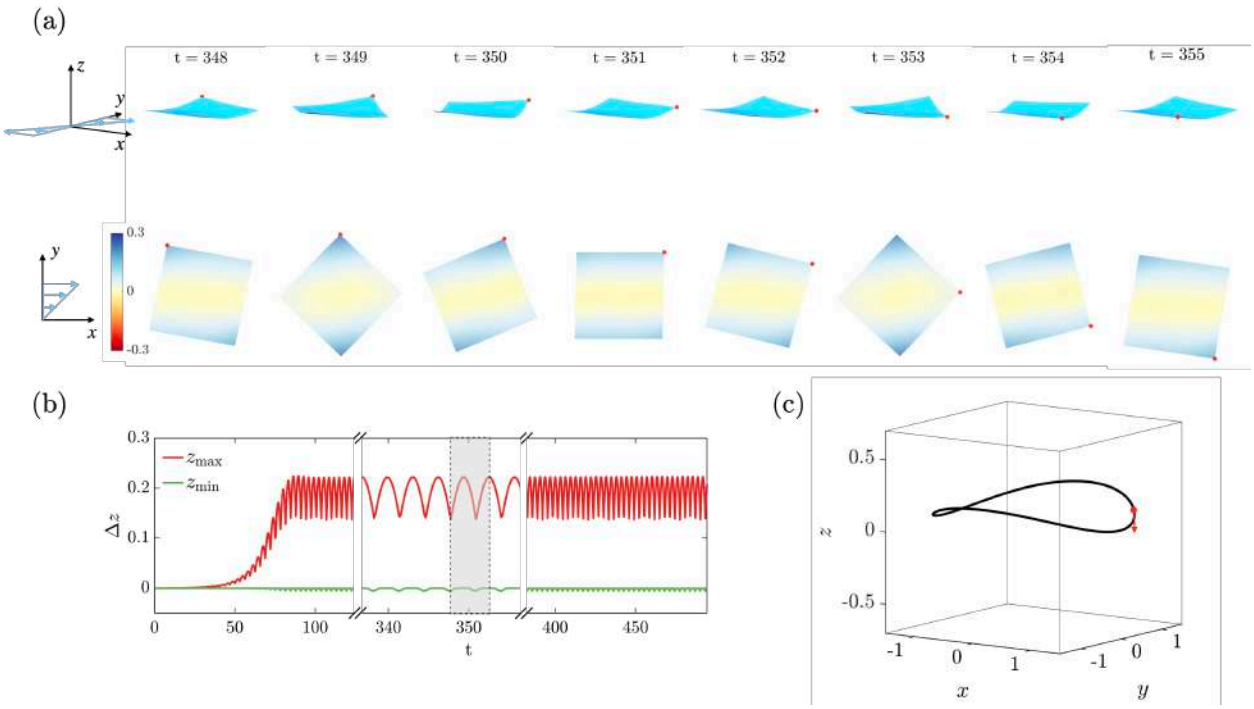


Figure 5.22: (a) Snapshots of symmetric swirling motion for $\omega = 1$ and $E_V = 7$. (b) Evolution of deformation amplitude z_{max} and z_{min} relative to the center of the sheet. The shaded area indicates the snapshot in (a). (c) The Lagrangian trajectory (based on the sheet center) of the marker after reaching the steady state.

flexible enough to deform out of the 2D rotating, the buckling instability triggers a symmetric swirling motion out of the shear plane shown in Fig 5.22. In this case, all corners are facing the positive vorticity axis, and the deformations are symmetric across the diagonal. When the sheet is oriented as in $t = 348$, two corners aligned with the major compressive are compressed, and two aligned with the tensile axis are relaxed. The most bucked state, due to rotation, is when the sheet roughly aligns with the gradient direction ($t = 349$). Fig 5.22(a) indicates two periods of asymmetric swirling. The motion is periodic and the period of the rotation of the sheet is four times longer than the period of the swirling (it takes four swirling cycles for the marker to translate one cycle).

When the sheet becomes more flexible, the appearance of higher deformation modes makes swirling more complicated. The deformation on the sheet is asymmetric as the folding of one corner guides the rotation of the sheet. In Fig 5.23, this can be observed by the snapshots $t = 343$.

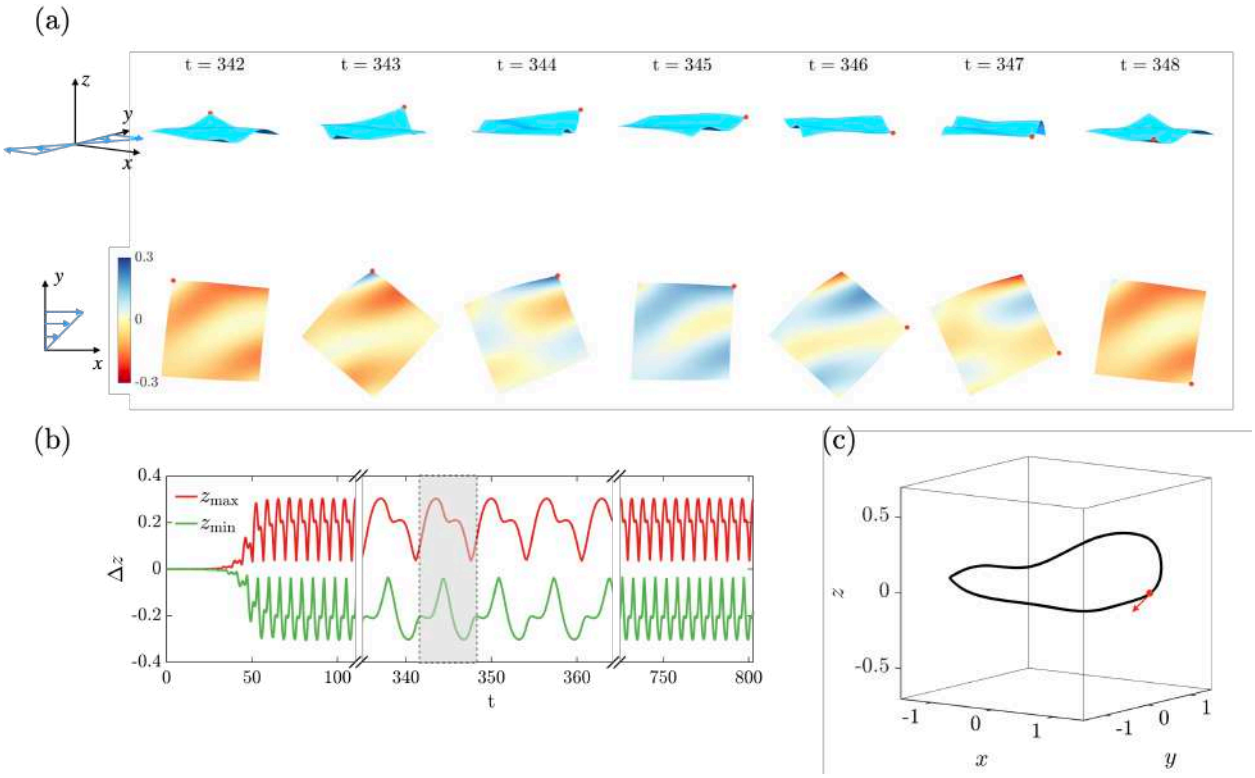


Figure 5.23: (a) Snapshots of asymmetric swirling motion for $\omega = 1$ and $E_V = 13$. (b) Evolution of deformation amplitude z_{max} and z_{min} relative to the center of the sheet. The shaded area indicates the snapshot in (a). (c) The Lagrangian trajectory (based on the sheet center) of the marker after reaching the steady state.

The swirling motion breaks spatial symmetry and shows a net drift along the vorticity direction.

Flow aligned

Similar to the disk case, very flexible sheets undergo complex transient dynamics and gradually approach the flow-vorticity plane.

5.5.3 Bifurcation and phase diagram

To summarize the free space dynamics for rectangles, we show the bifurcation diagrams of dynamics evolution with increasing E_V. We select two cases: a rectangle with $\omega = 0.5$ and a square with $\omega = 1$.

For both cases, we observed a transition for rotating sheets becoming unstable and de-

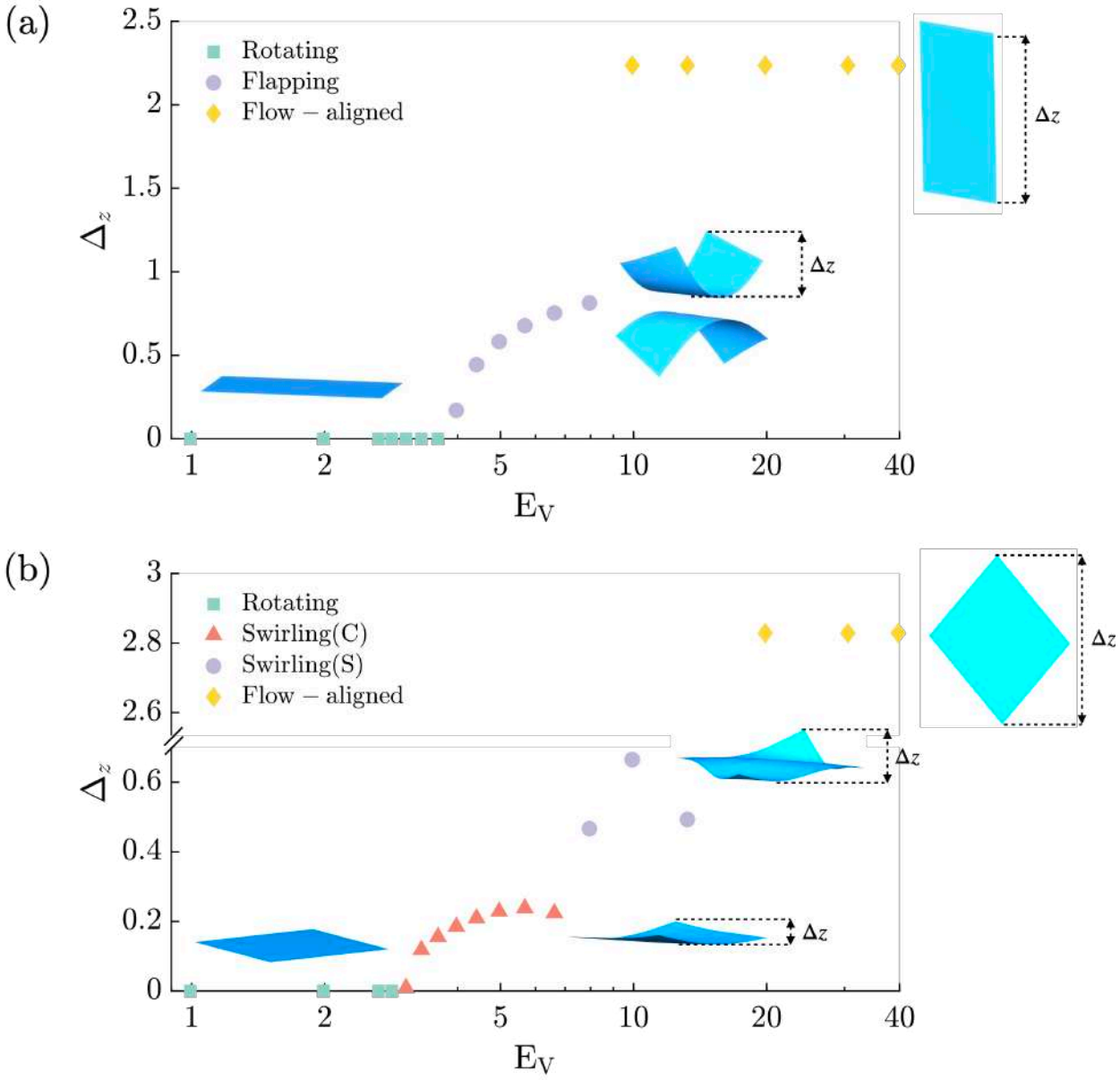


Figure 5.24: Phase diagram for a rectangle sheet with different ω and stiffness E_V in free space: (a) Rectangle with $\omega = 0.5$. (b) Square with $\omega = 1$. Markers represent the steady state dynamics.

forming out of the shear plane. The rectangle shows a larger buckling threshold compared to the square, because of the fact that it is harder to deform along a shorter edge. Therefore, the periodic compressive stresses acting on the square sheet with two long edges make it easier to trigger buckling instability. Another major difference here is that symmetric flapping only arises for the rectangle while asymmetric swirling arises for the square. It is intriguing

that a flat steady state can trigger both symmetric and asymmetric dynamics. Finally, it is not a surprise that very flexible sheets all end up aligning with the flow-vorticity plane.

To include a comprehensive understanding of rectangles in shear flow, we present a phase diagram by exploring the parameter space of ω and E_V for a sheet initially lying inside the shear plane in Fig 5.25.

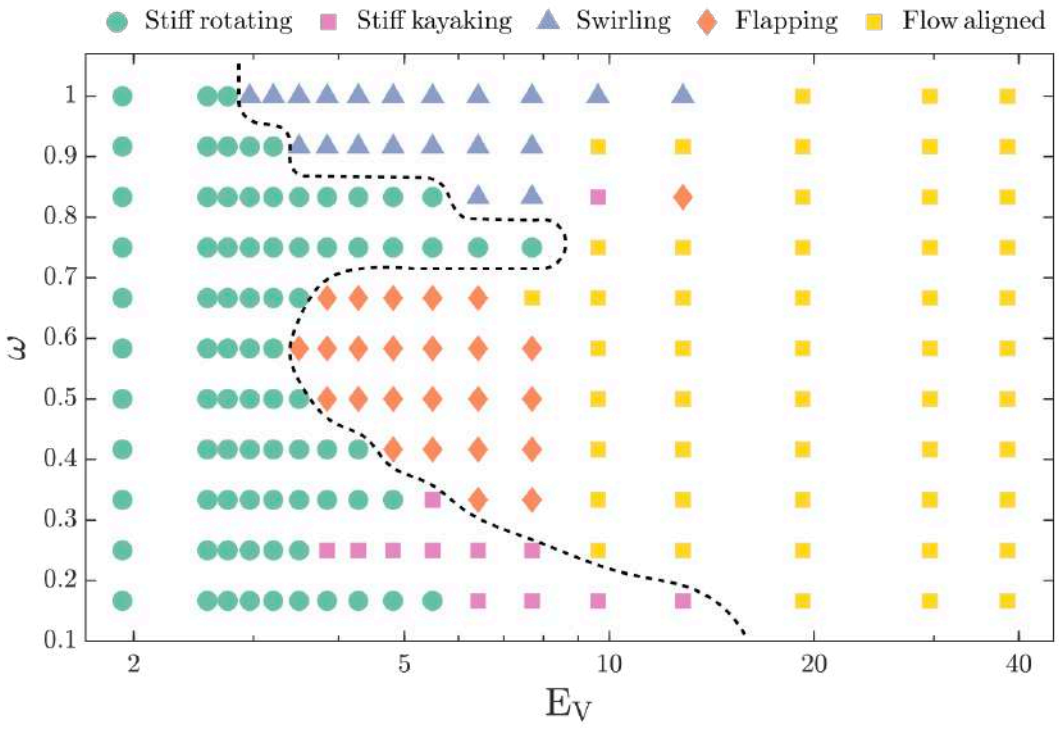


Figure 5.25: Phase diagram for a rectangle sheet with different ω and stiffness E_V in free space. Markers represent the steady state dynamics.

For sheets with small E_V, all rest shapes are stable to perturbation and remain inside the shear plane showing stiff rotating. For slender sheets with $\omega < 0.3$, the initial perturbation may trigger the kayaking motion, where the sheet leaves the shear plane without buckling. For intermediate E_V, sheets show out-of-plane deformation and the dynamics vary with sheet geometry. Flexible sheets with $\omega < 0.75$ show periodic flapping and square-like sheets arrest periodic swirling motion. For large E_V, flexible sheets end up with the aligned state. Typically, very flexible sheets are easier to be disturbed by the shear flow and evolve to the

aligned state more quickly.

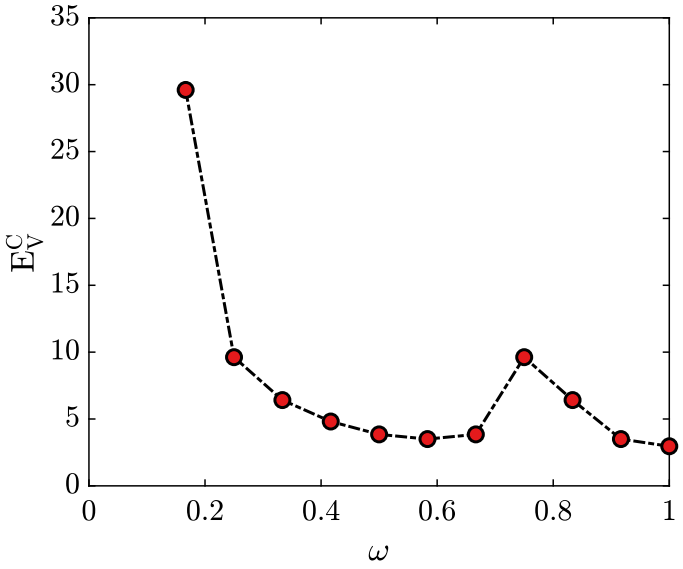


Figure 5.26: Buckling threshold E_V^C as a function of sheet size ω for a rectangle sheet initially inside the shear plane.

One interesting observation from the phase diagram is the relation between the buckling threshold E_V^C and the sheet size ω shown in Fig 5.26. We denote that sheets undergoing rotating and kayaking show no wrinkling observed on the sheet as below the buckling threshold. Surprisingly, the buckling threshold of the sheet shows a non-monotonic relation with the size of the sheet. For $\omega < 0.66$ (slender sheets), the buckling threshold decreases with ω, indicating a longer side edge eases the buckling. This is followed by an increase of buckling threshold with ω. Typically, For $\omega > 0.75$, the similar buckling threshold decreases with ω again. Generally, sheets with small ω show a larger E_V^C due to the smaller width that is more resistant to buckling compared to a larger width. However, we noticed a small regime in $0.67 < \omega < 0.83$ that shows a non-monotonic trend, and the sheet becomes more resistant to buckling. Interestingly, for $\omega = 0.75$, the sheet does not show buckling till the flow strength is strong enough to make the sheet flow-aligned. Moreover, it also separates the dynamic from flapping to swirling once the rotating becomes unstable. Future investigations are needed to probe into this size-dependent stiffening observation.

5.6 Summary

In this Chapter, we showed a detailed and systematic analysis of the dynamics of a thin elastic sheet in shear flow in the Stokes regime. Sheets with the rest shapes of a disk or a rectangle are considered and we are interested in the initial condition where the sheet is placed in the shear plane subject to perturbations.

Under small and random perturbation, a sufficiently flexible disk “rolling" in the shear plane shows a supercritical linear instability with increasing E_V from a flat state to a periodic wiggling motion, corresponding to a dynamic S-shape buckling instability. With further increase in E_V, sheets beyond the wiggling regime show complex dynamics that lead to the alignment of the sheet in the flow-vorticity plane. We developed a linear stability analysis and obtained a family of unstable modes that help understand the simulation results. The presence of the first unstable S-shape mode successfully predicts the buckling instability leading to wiggling, and the appearance of the second M-shape mode demonstrates the onset where the sheets become flow-aligned due to nonlinear interactions between unstable modes.

Under finite C-shaped perturbation, the disk shows stable flapping dynamics in a wide regime of E_V, where the sheet shows periodic C-shaped deformation with alternating buckled directions along the vorticity axis. The flapping is a result of periodic compressive and tensile stresses from shear flow and arises from the limited extensibility of the sheet. We identified a stable flapping branch with increasing E_V and an unstable branch that originates subcritically from a linear C-shape perturbation at large E_V. The flapping dynamics are confirmed experimentally from our collaborator’s results, and the evolution of curvature measured at the disk center as well as the flapping regime in E_V all show quantitative agreement with our simulation.

The fact that wiggling was not reported in experiments motivated us to study the disk under a free surface. With a combination of numerical simulation and linear stability analysis, we found the presence of a free surface induces symmetric buckling on the disk thereby

facilitating the formation of flapping observed in experiments. In addition, we developed a phase diagram illustrating the evolution of dynamics under the free surface.

Beyond a disk sheet, we also investigated a rectangle sheet with different aspect ratios (controlled by a parameter ω) in simple shear flow, varied from a slender ribbon (small ω) to a square (large ω). The results indicate slight changes in rest shape can lead to qualitatively different dynamics. For all sheets with small E_V below buckling threshold, sheets resist perturbation and rotate inside the shear plane. One exception is for ribbons, due to their slenderness, can be perturbed out of the shear plane without buckling. Above the buckling threshold, we identified a regime of E_V with periodic motions determined by ω, such as periodic flapping for intermediate ω (rectangle-like sheets) and periodic swirling for large ω (square-like sheets). Very flexible sheets for all shapes show complex dynamics that finally lead to alignment of sheets in flow-vorticity plane. Typically, we found a non-monontonic decrease of buckling threshold with ω.

The rich dynamics observed from elastic sheets contribute to the understanding of shear-induced morphologies of soft particles processed in shear flow. The knowledge serves as fundamental to investigating more complex systems, such as the suspension of graphene and polymer films, and the influence of sheet morphologies on macroscopic rheological properties.

6

Free-space and near-wall dynamics of a flexible sheet sedimenting in Stokes flow

We present a numerical study of a thin elastic sheet with small extensibility freely sedimenting in a viscous fluid. Two scenarios are investigated: sedimentation in free space and near an infinite wall, where the wall can be tilted. Elastic sheets with a rest shape of a square are modeled with a finite-element-based continuum model that accounts for in-plane stretching and out-of-plane bending. The fluid motion is computed by the method of regularized Stokeslets in the free space and regularized Blaketlets near a wall. During sedimentation, the interplay between gravity and the elastic response of sheets gives rise to complex deformation and reorientation dynamics, measured by a dimensionless elasto-gravitational number (E_G). In free space, sheets attain a stable orientation by aligning perpendicular to gravity. Sheets with larger deformability adopt more compact conformations and experience smaller hydrodynamic drag, thereby sedimenting faster. A sheet with a random initial orientation evolves reorients to align perpendicular to gravity, accompanied by lateral drift in free space. We identified two reorientation mechanisms with increasing flexibility: rotating and bending. When the sheet is placed near an infinite wall, sedimentation is hindered compared

to that in free space due to wall-induced hydrodynamic drag. Near a vertical wall, sheets exhibit asymmetric conformations that cause the sheet to migrate away, with the migration dynamics determined by E_G. The difference in flexibility leads to a non-monotonic trend in the evolution of wall-normal distance. Near a tilted wall, sheets either deposit or slide along the wall with a fixed wall-normal distance.

6.1 Introduction

The sedimentation dynamics of particles in a viscous fluid under gravitational or centrifugal forces have been receiving significant interest for their ubiquity in many applications and biological systems [6, 12, 32, 52, 58, 112, 146, 175, 178, 179, 185, 197, 200]. So far, extensive research has been done to explore sedimentation dynamics for various particle configurations, such as filaments [17, 31, 65, 81, 91, 144, 154], rings [52, 53], cylinders [19, 102], and spheroids [104, 110, 132]. However, one universal geometry has rarely been investigated: thin elastic sheets. Sedimentation of elastic sheets is prevailing in the synthesis of polymer films, nanosheets, and quantum dots [6, 32, 58, 179, 185, 197, 200]. For example, graphene flakes obtained by liquid-phase exfoliation are separated via centrifugation [6, 58, 185, 197]. Therefore, the knowledge of sheet-like particle sedimentation is crucial to predict sheet conformations obtained from centrifugation but is lacking. In this paper, we fill this gap by providing a fundamental understanding of thin sheets sedimenting in a viscous fluid. Besides particle configuration, sedimentation dynamics are affected by many factors, including particle stiffness [31, 91], aspect ratio [65], fluid properties [9, 158]. In this work, we focus on two typical aspects: particle elasticity and wall effects. Below, we review some related works of other particle configurations to provide insights for understanding elastic sheets.

It is known that rigid particles, like rigid spheroids and rods, sedimenting in an unbounded environment maintain their initial orientation due to Stokes flow reversibility [50]. A tilted initial orientation can induce continuous drift of the particle in the lateral direction

thereby the particle sediments with a fixed angle determined by initial orientation. In contrast, deformability allows particles to adjust their orientation and introduce more complex sedimenting dynamics. For instance, sedimenting flexible slender fibers and filaments form varied shapes in free space and have a unique and stable orientation as the end-to-end vector is perpendicular to gravity, as a result of nonlocal hydrodynamic interactions [81]. From a numerical and analytical study, Li *et al.* found that a weakly flexible filament with random initial conditions reorients to a unique orientation and conformation, where the reorientation trajectories are restricted to a cloud with envelope size determined by flexibility [91]. In a recent work of non-Brownian simulations, Cunha *et al.* studied sedimenting flexible filaments modeled with a bead-spring system and characterized the final shapes of filaments varying from almost horizontal to horseshoe-like based on flexibility [31]. Moreover, they identified three different reorientation dynamics: rotating, bending, and snaking with decreasing resistance to gravity-induced deformation. Gruziel and coworkers examined a knotted deformable closed chain with a rest shape of ring sedimenting in a viscous fluid. In both experiments and simulations, they observed the knots often attained a toroidal structure with oscillating intertwined loops during sedimentation [52]. In a later study, Gruziel *et al.* also gave a detailed investigation of loop flexibility and found rich sedimentation dynamics [53]. For more complex geometries, Peltomaki and Gompper did a numerical study of deformable red blood cells sedimentation using multi-particle collision dynamics and triangulated membranes. They characterized and presented a phase diagram of three gravity-induced shapes depending on elasticity: parachutes, teardrops, and fin-tailed spheres [132]. Matsunaga *et al.* extended the study by considering red blood cells with different ratios of internal and external fluid viscosity to investigate the reorientation dynamics during sedimentation [104]. The studies of single-particle sedimenting in free space benefit the understanding of more complex scenarios. When multiple particles sediment together, the deformation and collective sedimentation dynamics of particles are affected by inter-particle hydrodynamic interactions. Recent experiments and simulations have reported interesting hydrodynamic repulsion and

attraction, as well as shape deformations [17, 19, 144, 154]. We will not elaborate on this topic as the present work focuses on single-particle dynamics.

In contrast to sedimenting in free space, the sedimenting dynamics can be strongly modified with the presence of boundaries. It is known that particles next to the wall sediment slower compared to free space because the wall-induced drag hinders sedimentation. Rigid particles like a tilted rod close to a wall no longer maintain the orientation. Instead, rigid particles rotate and migrate away from the wall. Russel *et al.* first reported characteristic glancing or reversing dynamics of a rod sedimenting near a vertical wall, determined by the initial angle of the rod approaching the wall [143]. Mitchell and Spagnolie later extended the study to a rigid spheroidal particle with an arbitrary aspect ratio next to a tilted wall [110] at zero Reynolds number. They developed analytical solutions based on the method of images for randomly oriented prolate and oblate spheroids and found 3D dynamics like glancing, reversing, and wobbling based on the symmetry of initial orientations. In addition, they identified a stable sliding trajectory when the wall is slightly tilted. In more complex scenarios, Salez and Mahadevan numerically studied a sedimenting cylinder near a thin compressible elastic, and tilted wall. They observed that under specific conditions, the cylinder show a sliding motion: the cylinder sediments along the tilted wall while keeping a fixed distance away from the boundary. They also found that the competition between drag and wall deformation results in spontaneous oscillation of cylinder with lift during sedimentation [148]. Subsequent experiments and simulations probed into the effect of wall elasticity on the sliding and rotation dynamics of the cylinder [138, 147].

The aforementioned studies provide good insights into flexible particle sedimentation and the similarity between elastic sheets and elastic filaments imply that rich dynamics can be found for a sedimenting 2D sheet in a viscous fluid. In this work, we present a numerical study to systematically investigate the sedimentation dynamics of an almost inextensible elastic sheet by addressing the influence of sheet elasticity and wall effects. The structure of this work is as follows. In Section 6.2, we present the model and numerical methods to

simulate an almost inextensible sheet. We introduce two different flow solvers to account for the sedimentation in free space and near-wall sedimentation, separately. In Section 6.3, we introduce simulation results by first discussing the free space sedimentation, which is purely determined by the effect of sheet flexibility. Next, we place an elastic sheet next to an infinite solid wall to examine the wall effects, where the wall can be tilted. We conclude in Section 6.4.

6.2 Methods

6.2.1 Model setup

We consider an elastic thin sheet with a square rest shape that sediments in a stationary viscous fluid. The fluid is Newtonian with viscosity η and density ρ_f. The square sheet has edge $2a$ and thickness h such that $h \ll a$. Thus, the sheet has a traction-free edge, along which fluid exerts no forces. The weight of the sheet can be described as $4\rho_s g a^2 h$, where ρ_s is density and g is the gravitational constant. The gravity acts along the positive x axis with y and z marked as lateral directions. In this work, we investigate two scenarios: the sheet sediments 1) in an unbounded fluid, and 2) next to an infinite and solid wall, where the wall can be adjusted to be tilted. The initial condition of the sheet is described by an orientation angle ϕ, which is defined as the angle between the normal vector $\mathbf{n}$ of the sheet and the positive y axis. (i.e. $\phi = 90^\circ$ indicates the sheet sediments perpendicular to gravity and $\phi = 0^\circ$ when the sheet sediments parallel to gravity.) In the near-wall scenario, the wall can be tilted with an angle α. If the wall remains vertical ($\alpha = 0^\circ$), it aligns with the plane $y = 0$, such that y becomes the wall-normal direction. The initial distance between the center of mass of the sheet and the wall surface is measured by the wall-normal distance d_0. Figure 6.1 illustrates the setup by placing a sheet with $\phi = 90^\circ$ next to a wall tilted by $\alpha = 30^\circ$.

We model the sheet as a continuum with a no-slip surface, where material points on

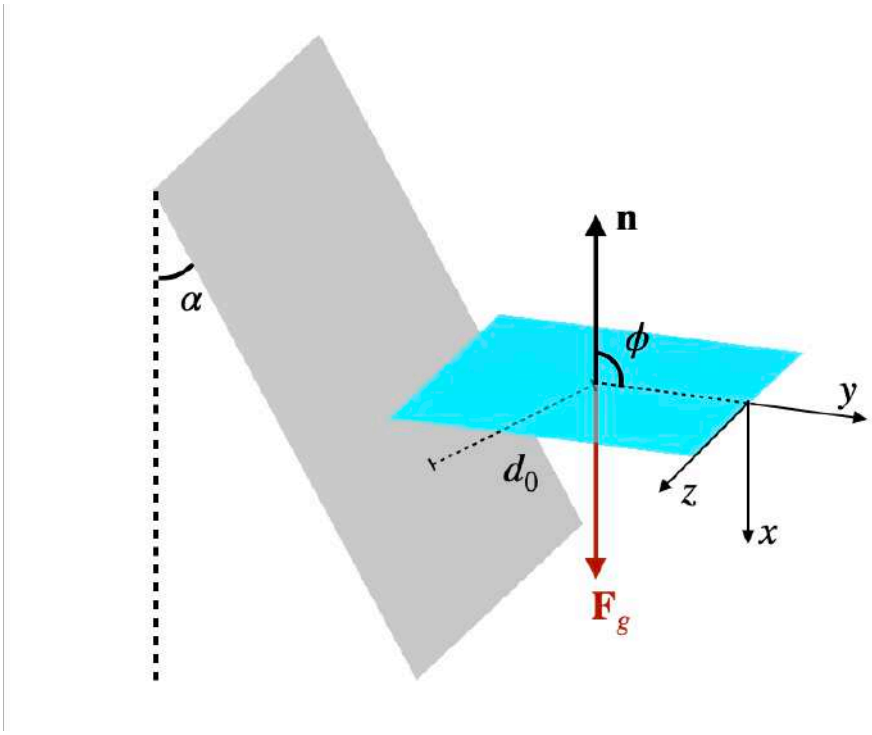


Figure 6.1: Illustration of a square sheet sedimenting next to a tilted wall. The case shows the sheet with initial wall-normal distance $d_0 = 1.5$ is oriented $\phi = 90°$ and the titled wall angle is $\alpha = 30°$.

the surface move with the same velocity as the local fluid. The no-slip boundary condition also implies that the sheet is impermeable – if the sheet moves with the local fluid velocity, then no fluid is passing through the sheet. The sheet surface is discretized into triangular elements with a node at each corner. Detailed numerical methods will be introduced in the following section.

The total strain energy of the elastic sheet can be written as the sum of in-plane strain energy E_s and out-of-plane bending energy E_b:

$$E = E_s + E_b. \tag{6.1}$$

Here, the in-plane strain energy is evaluated by integrating the strain energy density W over the sheet surface. We choose a nonlinear neo-Hookean model (NH), as it is often used to model rubber-like polymer structures, with the form:

$$W_{\mathrm{NH}} = \frac{G}{2}\left(I_1 - 3\right). \tag{6.2}$$

The two-dimensional shear modulus G scales with the equilibrium thickness h. The term I_1 is the first invariant of the right Cauchy-Green deformation tensor, and depends on the local principal stretch ratios λ_i along the tangential direction of the sheet surface:

$$I_1 = \lambda_1^2 + \lambda_2^2 + \frac{1}{\lambda_1^2\lambda_2^2}. \tag{6.3}$$

The last term denotes λ_3, as the stretch ratio along the thickness direction, is obtained by incompressibility of the material ($\lambda_1\lambda_2\lambda_3 = 1$).

For the bending energy E_b, we apply a simple bending model that sums the energy due to dihedral angles $\theta_{\alpha\beta}$ between neighboring elements [42, 43]:

$$E_b = \sum_{\mathrm{adj}\ \alpha,\beta} k_b\left(1 - cos(\theta_{\alpha\beta} - \theta_0)\right), \tag{6.4}$$

where k_b is the bending constant calculated from bending stiffness K_B, by comparing E_b with the energy of a square bending into part of a cylinder with known curvature: $k_b = 1.03K_B$. The angle θ_0 is zero as we assume a flat equilibrium state. We also denote the sum of deflection on the sheet as a wrinkling parameter $B = \sum_{\mathrm{adj}\ \alpha,\beta}\left(1 - cos(\theta_{\alpha\beta} - \theta_0)\right)$, which simply represents the extent of wrinkling on the sheet surface and is related to the total bending energy by the bending constant: $E_b = k_b B$.

For a sedimenting particle, the body force due to gravity acting on the sheet is described by a potential U.

$$U = \Delta\rho g a h_0 \Delta x \tag{6.5}$$

We also include a truncated Lennard-Jones(LJ) repulsive potential to prevent the sheet from self-intersecting. Numerically, the potential acts between all the nodes, except for the nodes that are located within 3-ring neighbors of the targeted node at the equilibrium state. The

potential has the form:

$$E_{LJ} = \begin{cases} 4\varphi_0 \left[\left(\frac{\sigma}{r}\right)^{12} - \left(\frac{\sigma}{r}\right)^{6} \right], & \text{if } r < \sigma \\ 0, & \text{otherwise} \end{cases} \tag{6.6}$$

where r is the instant distance between nonadjacent nodes, σ scales the range of the potential, and φ_0 measures is the strength of the potential. Here, we choose $\sigma = 0.06a$ and $\varphi_0 = 4\times10^{-6}$ such that the potential has no influence on the dynamics for sheets without intersection. We find that the only case where the repulsive force is active is when the sheet edge would otherwise cut through the surface, which only occurs for sheets with very small bending stiffness. In addition, we also apply a similar truncated LJ potential between the sheet and the wall. Basically, we apply a strong repulsive potential to prevent sheets from entering a distance d_{lim} from the wall, and the potential only acts along the wall-normal direction in the range $d < d_{\text{lim}}$. It is worth noting that, this interaction only acts when the sheet fully deposits on the wall and has no other effect on near-wall dynamics.

We introduce two nondimensional parameters to describe the aforementioned mechanical properties. The capillary number $\text{Ca} = \Delta\rho g a h_0/G$ compares the viscous stresses exerted by the fluid on the sheet to the in-plane elastic response of the sheet. Larger Ca indicates that the sheet is more deformable. In this study, we mainly focus on an almost inextensible sheet, such that the in-plane deformation is strongly constrained with a small capillary number $\text{Ca} = 0.01$. We have verified that a further decrease in Ca (by 10 times) results in no qualitative change in sedimentation conformations. The comparison between bending and gravity is measured by elasto-gravitational number $\text{E}_\text{G} = \Delta\rho g a^3 h_0/K_B$: larger E_G indicates that the sheet is more flexible. In this study, we mainly focus on the influence of E_G.

6.2.2 Numerical methods

The numerical method for the elasticity problem is adapted from Charrier *et al.* [21]. We simulate the sheet by keeping track of nodes that move as material points on the sheet surface. From the elastic energies, we obtain the summed nodal elastic force ($\mathbf{F}_{e,i} = \mathbf{F}_{s,i} + \mathbf{F}_{b,i}$) exerted on each node from the first variation of the total energy with respect to the nodal displacements. Each discretized element of the sheet is assumed to have homogenous deformation, so the element edges always remain linear. The deformed element is compared to its equilibrium shape under a local coordinate transformation via a rigid body rotation, and the displacement for any point inside the element is obtained by linear interpolation from the nodal positions. The detailed implementation can be found in references [42, 43, 195, 196]. The total nodal force $\mathbf{F}_{e,i}$ is evaluated by summing the elastic force $(\mathbf{F}_{e,i})_j$ due to the deformation of each surrounding element j shared by the node i: $\mathbf{F}_{e,i} = \sum_j (\mathbf{F}_{e,i})_j$, where the sum is over all elements meeting at the node.

Besides the elastic force, we also need to consider the external body force $\mathbf{F}_g$. The body force acting on the sheet has been assigned to each node based on the Voronoi area around the node at the equilibrium state. Due to the conservation of mass, the nodal body force $\mathbf{F}_{g,i}$ remains constant in the simulation.

$$\mathbf{F}_{g,i} = A_{\text{Voronoi},i} \Delta\rho h_0 g. \tag{6.7}$$

For the results shown, we discretize the square sheet with 1152 elements and 625 nodes. We have verified that changes in mesh resolution lead to only small quantitative changes in the results and no qualitative changes.

6.2.3 Fluid solver

In the present work, we consider a small, thin square sedimenting at low Reynolds number. Under these assumptions, the inertia of the fluid at the particle scale is negligible, and the

fluid is governed by the Stokes equation. For each node on the sheet surface, the elastic force $\mathbf{F}_{e,i}$ exerted by the sheet on the fluid, the external body force $\mathbf{F}_{g,i}$ acting on the sheet are balanced with hydrodynamic force $\mathbf{F}_{h,i}$ from the fluid:

$$\mathbf{F}_{e,i} + \mathbf{F}_{g,i} + \mathbf{F}_{h,i} = \mathbf{0}. \tag{6.8}$$

To account for the fact that the forces are not completely localized to the nodal positions, we use the method of regularized Stokeslets to solve for the fluid motion [28]: the force $\mathbf{F}_i = -\mathbf{F}_{h,i}$ exerted by node i on the fluid corresponds to a regularized force density $\mathbf{f}_i^\kappa = \mathbf{F}_i\delta_\kappa(\mathbf{x} - \mathbf{X}_i)$, where $\mathbf{X}_i$ is the position of node i and $\delta_\kappa(\mathbf{x})$ is a regularized delta function with regularization parameter κ. Thus, the governing equations are the Stokes equation with regularized nodal forces and the continuity equation:

$$\begin{gathered} -\nabla p + \eta\nabla^2\mathbf{v} + \textstyle\sum_i \mathbf{F}_i\delta_\kappa(\mathbf{x} - \mathbf{X}_i) = \mathbf{0} \\ \nabla \cdot \mathbf{v} = 0. \end{gathered} \tag{6.9}$$

Free-space sedimentation

In an unbounded fluid, the velocity field generated due to a regularized point force $\mathbf{f} = \mathbf{F}\delta_\kappa(\mathbf{x} - \mathbf{X}_i)$ can be represented using a regularized Stokeslet $\mathbf{G}_\kappa$ [50, 195, 196],:

$$\mathbf{v}_\kappa(\mathbf{x}) = \mathbf{G}_\kappa(\mathbf{x} - \mathbf{X}_i) \cdot \mathbf{F}. \tag{6.10}$$

As $1/\kappa \to 0$, $\mathbf{G}_\kappa$ reduces to the usual Stokeslet operator $\mathbf{G}(\mathbf{x} - \mathbf{X}_i) = 1/8\pi\eta r(\mathbf{I} + (\mathbf{x} - \mathbf{X}_i)(\mathbf{x} - \mathbf{X}_i)/r^2)$, where $r = ||\mathbf{x} - \mathbf{X}_i||$. There are many ways to regularize a delta function $\delta_\kappa(\mathbf{x})$; we choose a regularization function for which the difference between $\mathbf{G}$ and $\mathbf{G}_\kappa$ decays exponentially as $\kappa r \to \infty$ [50]:

$$\delta_\kappa(r) = \frac{\kappa^3}{\sqrt{\pi}^3}\exp(-\kappa^2 r^2)\left[\frac{5}{2} - \kappa^2 r^2\right]. \tag{6.11}$$

With this choice,

$$\mathbf{G}_\kappa(\mathbf{x}-\mathbf{X}_i) = \frac{\mathrm{erf}(\kappa r)}{8\pi\eta r}\left(\mathbf{I} + \frac{(\mathbf{x}-\mathbf{X}_i)(\mathbf{x}-\mathbf{X}_i)}{r^2}\right) + \frac{\kappa e^{-\kappa^2 r^2}}{4\pi^{3/2}\eta}\left(\mathbf{I} - \frac{(\mathbf{x}-\mathbf{X}_i)(\mathbf{x}-\mathbf{X}_i)}{r^2}\right). \quad (6.12)$$

In the simulations, κ must be chosen to scale with the minimum node-to-node distance $l_{\min}$. We take $\kappa l_{\min} = 2.1842$, which is obtained from a validation case of a disc in biaxial extensional flow discussed in [195]. We represent the total velocity at a point $\mathbf{x}$ as

$$\mathbf{v}(\mathbf{x}) = \mathbf{v}_\infty(\mathbf{x}) + \mathbf{v}_p(\mathbf{x}) = \mathbf{v}_\infty(\mathbf{x}) + \sum_i \mathbf{G}_\kappa(\mathbf{x}-\mathbf{X}_i)\cdot\mathbf{F}_i. \quad (6.13)$$

Near-wall sedimentation

The presence of an infinite wall complicates the problem as we require an extra boundary condition for the fluid: the velocity needs to vanish on the no-slip wall ($\mathbf{v}(y=0)=0$, assume a vertical wall with $\alpha = 0°$) [13]. Therefore, the velocity field generated to a regularized point force is now accounted for by the regularized Blakelet to satisfy this boundary condition [2, 29]. The regularized Blakelet consists of a regularized Stokeslet and an image system across the wall which contains a combination of multipolar expansion terms from the Stokes equation that together cancel the induced velocity on the wall to enforce no-slip condition. Compared to singular solution derived by Blake, we need two extra rotlets to account for residual terms due to regularization. Following Ainley *et al.* [2], we apply two types of regularized delta functions: $\delta_\kappa(\mathbf{x})$ and $\delta^d_\kappa(\mathbf{x})$ to regularized different terms in the image system. Here, $\delta_\kappa(r)$ is from Eq. 6.11, and $\delta^d_\kappa(r)$ has the form:

$$\delta^d_\kappa(\mathbf{x}) = \frac{\kappa^3}{\sqrt{\pi}^3}\exp(-\kappa^2 r^2). \quad (6.14)$$

Two functions satisfy the relation:

$$\delta_\kappa(\mathbf{x}) = \frac{1}{2}\left(r\frac{\partial\delta^d_\kappa(\mathbf{x})}{\partial r} + 5\delta^d_\kappa(\mathbf{x})\right). \quad (6.15)$$

We define $\mathbf{r} = \mathbf{x} - \mathbf{X}_i$ and $\mathbf{R} = \mathbf{x} - \mathbf{X}_i^I$, where $\mathbf{X}_i$ is the the position of the node i and $\mathbf{X}_i^I$ is the corresponding image point. Therefore, the regularized Blakelet $\mathbf{B}_\kappa$, in indicial notation form, can be expressed as:

$$\begin{aligned} B_{\kappa,ij}(\mathbf{r}) &= G_{\kappa,ij}(\mathbf{r}) - G_{\kappa,ij}(\mathbf{R}) \\ &\quad - 2y_0\left(\delta_{jl} - 2\delta_{j2}\delta_{2l}\right)\left(D_{\kappa,i2l}(\mathbf{R}) - \frac{y_0}{2\eta}P^d_{\kappa,il}(\mathbf{R})\right) \\ &\quad + 2y_0\left(R_{\kappa,il}(\mathbf{R}) - R^d_{\kappa,il}(\mathbf{R})\right)\epsilon_{jl2}. \end{aligned} \tag{6.16}$$

where the regularized Stokeslet $\mathbf{G}_\kappa(\mathbf{r})$, the image regularized Stokeslet $\mathbf{G}_\kappa(\mathbf{R})$, the regularized Stokes doublet $\mathbf{D}_\kappa(\mathbf{R})$ and the rotlet $\mathbf{R}_\kappa(\mathbf{R})$ are regularized by function $\delta_\kappa(\mathbf{x})$. The regularized potential dipole $\mathbf{P}_\kappa(\mathbf{R})$ and the second rotlet $\mathbf{R}^d_\kappa(\mathbf{R})$ are regularized by the alternative function $\delta^d_\kappa(\mathbf{x})$. Note that if $1/\kappa \to 0$, the solution recovers the singular Blakelet as two rotlets cancel each other [2, 29]. Here,

$$G_{\kappa,ij}(\mathbf{r}) = \frac{1}{8\pi\eta}\left[\left(\frac{\operatorname{erf}(\kappa r)}{r} + \frac{2\kappa \mathrm{e}^{-\kappa^2 r}}{\sqrt{\pi}}\right)\delta_{ij} + \left(\frac{\operatorname{erf}(\kappa r)}{r} - \frac{2\kappa \mathrm{e}^{-\kappa^2 r}}{\sqrt{\pi}}\right)\frac{r_i r_j}{r^2}\right], \tag{6.17}$$

$$G_{\kappa,ij}(\mathbf{R}) = \frac{1}{8\pi\eta}\left[\left(\frac{\operatorname{erf}(\kappa R)}{R} + \frac{2\kappa \mathrm{e}^{-\kappa^2 R}}{\sqrt{\pi}}\right)\delta_{ij} + \left(\frac{\operatorname{erf}(\kappa R)}{R} - \frac{2\kappa \mathrm{e}^{-\kappa^2 R}}{\sqrt{\pi}}\right)\frac{R_i R_j}{R^2}\right], \tag{6.18}$$

$$\begin{aligned} D_{\kappa,i2l}(\mathbf{R}) = \frac{1}{8\pi\eta}\Bigg[&\frac{1}{R^2}\left(\frac{\operatorname{erf}(\kappa R)}{R} - \frac{2\kappa \mathrm{e}^{-\kappa^2 R^2}}{\sqrt{\pi}}\right)\left(\delta_{2l}R_i - \delta_{i2}R_l + R_2\left(\delta_{il} - 3\frac{R_i R_l}{R^2}\right)\right) \\ &-2\kappa^2\frac{2\kappa \mathrm{e}^{-\kappa^2 R^2}}{\sqrt{\pi}}\left(\delta_{i2}R_l - R_2\frac{R_i R_l}{R^2}\right)\Bigg], \end{aligned} \tag{6.19}$$

$$P^d_{\kappa,il}(\mathbf{R}) = -\frac{1}{4\pi}\left[\frac{1}{R^2}\left(\frac{\operatorname{erf}(\kappa R)}{R} - \frac{2\kappa(2\kappa^2R^2+1)\mathrm{e}^{-\kappa^2R^2}}{\sqrt{\pi}}\right)\left(\delta_{il} - \frac{3R_iR_l}{R^2}\right) + \frac{4\kappa\mathrm{e}^{-k^2R^2}}{\sqrt{\pi}R^2}\frac{R_iR_l}{R^2}\right], \tag{6.20}$$

$$R_{\kappa,il}(\mathbf{R}) = \left(\frac{\operatorname{erf}(\kappa R)}{4\pi R^3} + \frac{\kappa\left(\kappa^2R^2-1\right)\mathrm{e}^{-\kappa^2R^2}}{2\pi^{\frac{3}{2}}R^2}\right)\epsilon_{ilm}R_m, \tag{6.21}$$

$$R^d_{\kappa,il}(\mathbf{R}) = \left(\frac{\operatorname{erf}(\kappa R)}{4\pi R^3} - \frac{\kappa\mathrm{e}^{-\kappa^2R^2}}{2\pi^{\frac{3}{2}}R^2}\right)\epsilon_{ilm}R_m. \tag{6.22}$$

Therefore, the total velocity at a point $\mathbf{x}$ as

$$\mathbf{v}(\mathbf{x}) = \mathbf{v}_\infty(\mathbf{x}) + \mathbf{v}_p(\mathbf{x}) = \mathbf{v}_\infty(\mathbf{x}) + \sum_i \mathbf{B}_\kappa(\mathbf{x}-\mathbf{X}_i)\cdot\mathbf{F}_i. \tag{6.23}$$

At each time step for either the free space or the near wall case, after updating the force balance, we update the nodal positions by applying the condition that they move with the local fluid velocity in Eq. 6.23, thereby satisfying the no-slip and no-penetration conditions:

$$\frac{d\mathbf{X}_i}{dt} = \mathbf{v}(\mathbf{X}_i). \tag{6.24}$$

This equation is solved with a forward-Euler method. We have verified the solution with other numerical methods such as the fourth-order Runge-Kutta method, and find that the higher-order method shows negligible effects on the results based on the timestep used. For numerical stability, the timestep applied follows $\Delta t = 0.1\mathrm{Ca}l_{\min}$, and we enforce an upper limit of 5×10^{-4} strain unit per time step.

6.3 Results

6.3.1 Sedimentation in free space

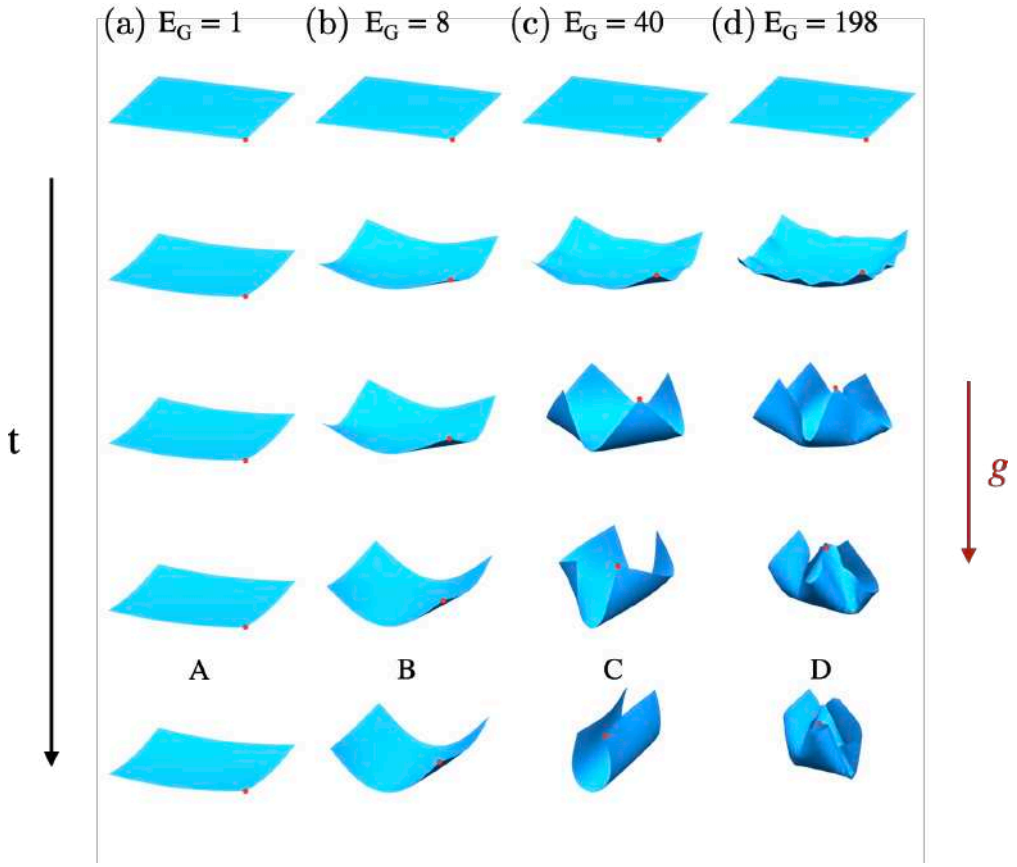


Figure 6.2: Snapshots of a square sheet sedimenting in free space with $\phi = 90°$. (a) Flat ($E_G = 1$). (b) Convex taco ($E_G = 8$). (c) Concave taco ($E_G = 40$). (d) Complex ($E_G = 198$). A-D represent the final steady conformation. Snapshots only show the conformation evolution without actual sedimenting distance.

We first consider an almost inextensible sheet sedimenting in free space. The initial orientation of the sheet aligns perpendicular to gravity as $\phi = 90°$, which is a stable orientation and will be discussed in detail later. In Figure 6.2, we show four distinct examples of sheets with increasing E_G to address the effect of sheet flexibility on gravity-induced deformation. For stiff sheets shown in Fig 6.2(a), sheet elasticity dominates over gravity. The sheet settles with an almost flat conformation, with negligible deformation observed on the surface. With increasing E_G, gravity is comparable to sheet elasticity. Due to hydrodynamic interactions

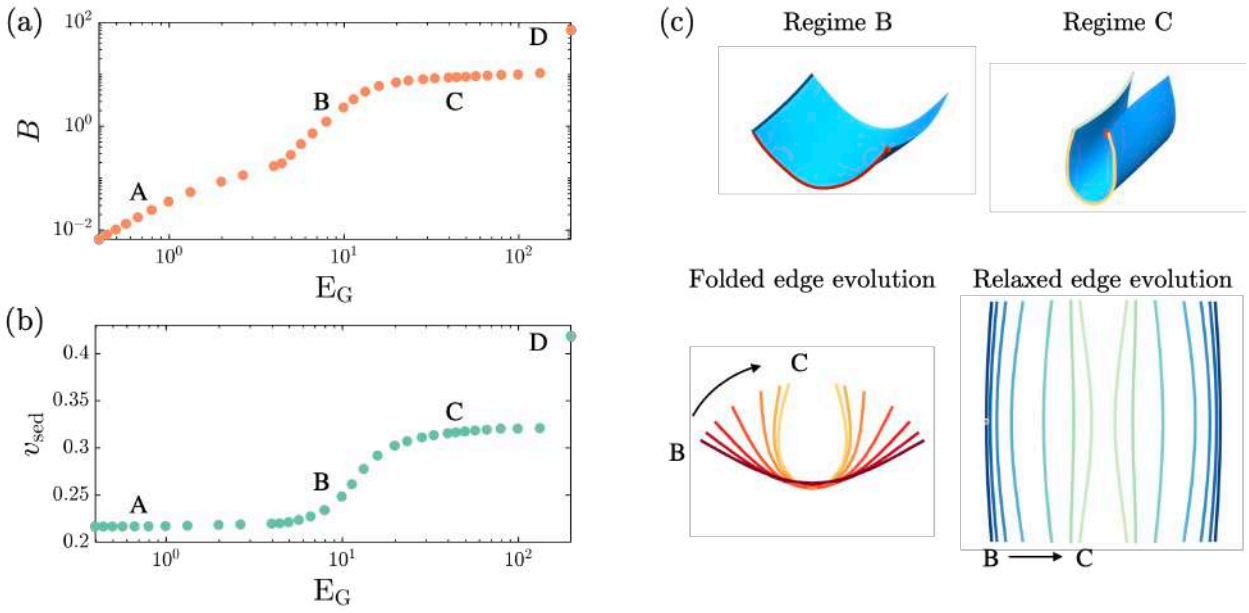


Figure 6.3: Characterization of sedimentation dynamics. A-D are steady conformations shown in Fig 6.2 representing four distinct regimes. (a) Evolution of wrinkling parameter B on the sheet vs. E_G. (b) Terminal velocity v_{sed} vs. E_G. (c) The transition of conformations between regime B and regime C is shown as the evolution of folded and relaxed edges.

between different parts of the sheet surface, the center part of the sheet initially sediments faster, which drives the four corners to symmetrically lift upward. This metastable state soon becomes unstable and two edges fold inward as folded edges while the other two edges relax as relaxed edges together to form a taco shape. Based on E_G, we observed two types of tacos. A less flexible sheet (Fig 6.2(b)) indicates a convex taco. The folded edges form a V shape, and the relaxed edges are convex. A more flexible sheet (Fig 6.2(c)) ends up with a concave taco. The folded edges become a U shape, and the relaxed edges are concave. For very flexible sheets as Fig 6.2(d), small resistance to buckling leads to a complex geometry that is not considered in this study.

We characterize the sedimentation dynamics by examining the folding on the sheet and sedimentation velocity of the final steady conformations. We measure the extent of folding by calculating the wrinkling parameter B defined earlier (the sum of deflection between all neighboring elements) for a group of sheets spanning parameter space of E_G in Fig 6.3(a). With increasing E_G, sheets are more wrinkled and become more compact. We quantify the

sedimenting dynamics by measuring a terminal velocity v_{sed} when the sheet reaches a steady conformation, shown in Fig 6.3(b). The results indicate that more flexible sheets sediment faster. Here, we observe four different regimes, corresponding to the four examples (A-D) given in Fig 6.2. With increasing E_G, sheets show stronger buckling and the conformation becomes more compact. The more compact conformation experiences smaller drag and makes the sheet sediments faster in free space. Typically, the transition of shape conformations assembles flexible filament sedimentation with increasing flexibility. For instance, the evolution of relaxed edges in Fig 6.3(c) demonstrates a smooth transition from a V-shape (regime B) to a U-shape (regime C). Elastic sheet conformations are more complex than fiber. With the transition of buckled edges, sheets also show a transition of the relaxed edges from convex to concave, in order to accommodate a less wrinkled state.

As mentioned at the beginning of the section, the sheet has a preferred sedimenting orientation perpendicular to gravity. This argument is robust to initial conditions as we examine case B in Figure 6.2 ($\text{E}_\text{G} = 8$) with different initial orientations. The evolution of deformation on the sheet is tracked by the wrinkling parameter B in Fig 6.4(a), which demonstrates that all ϕ reach the same conformation shown in Figure 6.2, as the only stable conformation. Though arriving at the same conformation, the difference in initial conditions shows a significant change in the transient reorientation dynamics, which is shown as the evolution of lateral drift distance d in Fig 6.4(b). There is no drift observed in the case $\phi = 90°$, which implies a stable orientation. The drift distance d increases with decreasing of ϕ and the maximum drift happens when the sheet is initially parallel to the gravity ($\phi = 0°$). Therefore, by the symmetry of free space, all possible sedimenting trajectories of the sheet are restricted to a cloud. This observation agrees with observations in flexible filament [91]. We denote the maximum lateral drift distance (when $\phi = 0°$) as d_{max}.

We summarize d_{max} for a group of sheets spanning parameter space of E_G in Fig 6.4(c). The drift due to reorientation is strongly influenced by E_G as more flexible sheets show smaller d_{max}. After carefully examining the dynamics, we introduce two categories of different

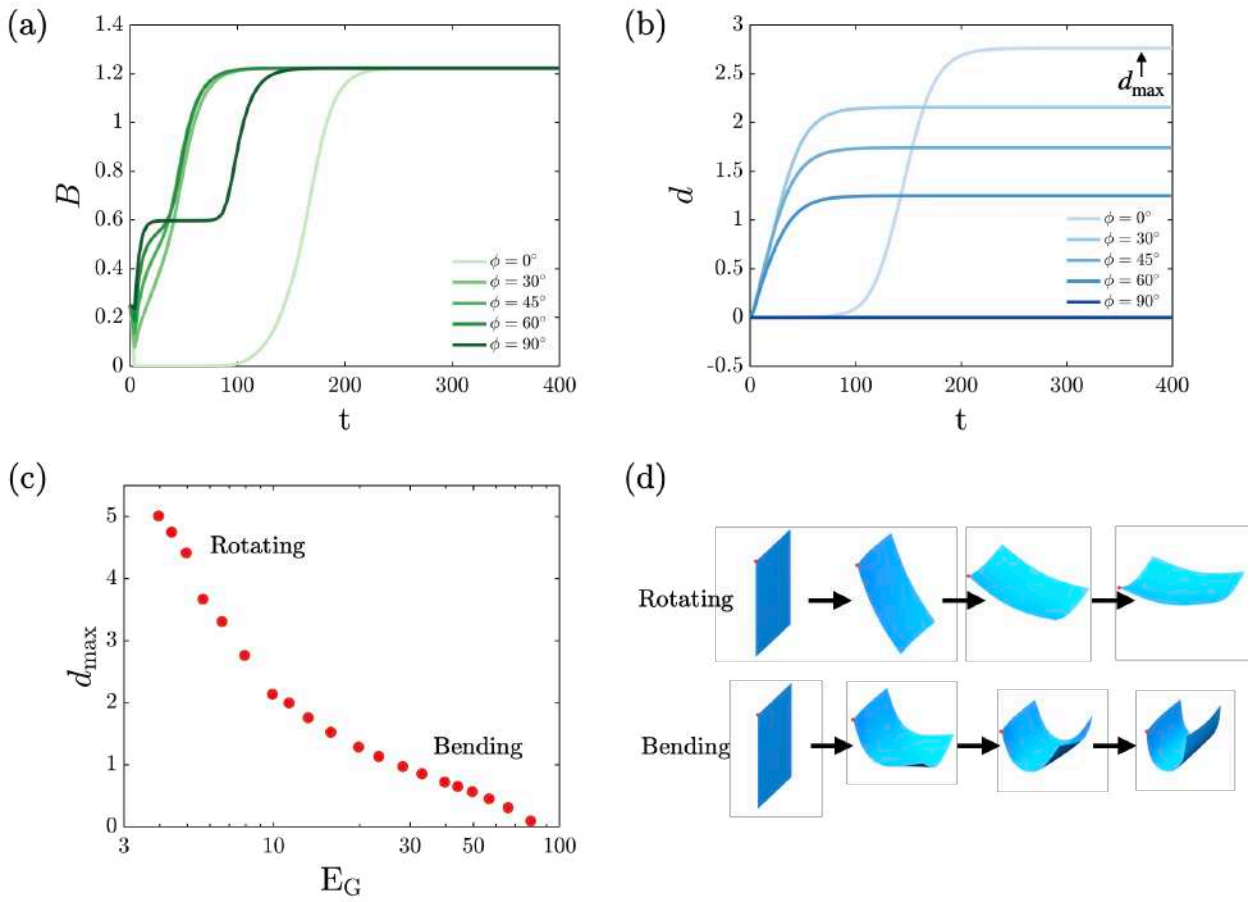


Figure 6.4: Influence of initial orientation ϕ and E_G on the sheet reorientation dynamics: (a) Transient evolution of buckling on the sheet for $E_G = 8$ with different initial orientation ϕ. (b) Transient evolution of lateral drift distance d on the sheet for $E_G = 8$ with different initial orientation ϕ. The maximum drift distance is denoted d_{max}. (c) Maximum lateral distance d_{max} for sheets with different E_G. (d) Illustration of two types of reorientation dynamics: rotating ($E_G = 4$) and bending ($E_G = 13$) from selected cases in Fig 6.4c. The sheet is initially oriented as $\phi = 0°$ subject to small and random perturbations.

reorientation dynamics: rotating and bending, with examples illustrated in Fig 6.4(d). Here, all sheets initially stay parallel to gravity subject to small and random perturbations. For stiff sheets, perturbation induces small deformation on the sheet while the sheet stays almost flat. However, the small deformation makes the current orientation unstable and the sheet reorients to align perpendicular to gravity. During the reorientation, the sheet rotates around the sheet center while the asymmetric and tilted conformation induces the drift along the lateral direction resulting in evident translation.

Unlike the stiff sheet, the flexible sheet bends during reorientation. Interestingly, the

upper and lower part of the sheet shows relatively independent deformation: the upper part bends slightly, and the lower part of the sheet folds and rotates relatively to the sheet center to form a taco shape. We denote this type of reorientation as bending and bending sheets introduce smaller lateral drift compared to rotating. For larger E_G, the flexibility ensures a quick folding reorientation and the drift becomes negligible. We summarized the evolution of maximum drift distance $d_{\max}$ with E_G in Fig 6.4(c), where the two different reorientation types can be recognized. Similar orientation dynamics were also reported in reorientation dynamics of flexible filaments [81, 91].

6.3.2 Sedimentation next to a wall

In this section, we place the sheet next to an infinite wall, which can be adjusted with an angle α. We first illustrate the dynamics next to a vertical wall ($\alpha = 0°$) and apply the initial orientation $\phi = 90°$, which is the stable orientation in free space. The sheet is initially a distance $d_0 = 1.5$ away from the wall. In addition, we also examined an initial distance $d_0 = 3$ far away from the wall to assess the dependence of dynamics on the initial distance.

The presence of the wall breaks spatial symmetry, resulting in an asymmetric sheet conformation in contrast to a symmetric sheet in free space. The asymmetric sheet, due to anisotropic drag, exhibits drift of the sheet along the wall-normal (lateral) direction while sedimenting. Eventually, the sheet migrates away from the wall and we denote that the sheet escapes from the wall. In Fig 6.5 (a), we show the migration dynamics of three cases with increasing E_G, where free space evolutions of the sheets are symmetric tacos. Due to the wall-induced asymmetry, conformations in all cases are tilted at the early stage of sedimentation: the side edge facing the wall is slightly above the edge away from the wall.

The migration dynamics of the sheet are strongly determined by E_G. In the short term, the relatively stiff sheet (case A $E_G = 8$ in Fig 6.5(a)) directly migrates away from the wall. In contrast, the other two flexible sheets initially migrate toward the wall. The noticeable difference in dynamics arises from the sheet conformations. In case A, small E_G leads to a

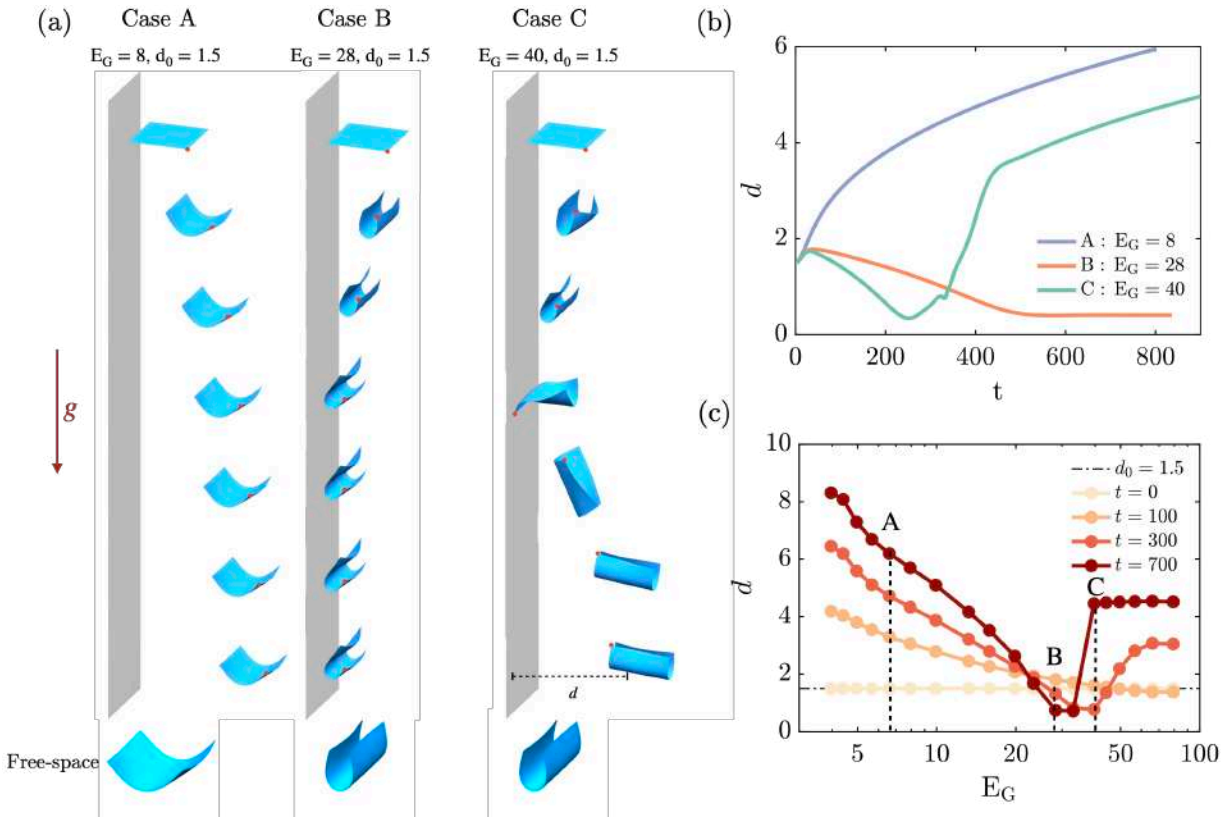


Figure 6.5: (a) Snapshots of dynamics near a vertical wall with initial orientation $\phi = 90°$ and $d_0 = 1.5$. Case A, $E_G = 8$: the sheet directly migrates away from the wall. Case B, $E_G = 28$: the sheet first migrates toward the wall and becomes trapped. Case C, $E_G = 40$: the sheet first migrates toward the wall and then reorient to escape. The transient migration distance away from the wall is denoted d. Each case has its steady free space conformation for comparison. (b) Transient evolution of migration distance d for three sheets in Fig 6.5(a). (c) Temporal evolution of migration distance d for sheets with different E_G, with labels indicating cases shown in Fig 6.5(a).

slightly folded sheet where elasticity dominates and the overall orientation of the asymmetric taco tilts away from the wall due to the unbalanced side edges. The resultant shape fosters the sheet to drift away from the boundary. In cases B and C, the sheet becomes more flexible and the conformations are more compact with two side edges getting close to each other. The change in conformation makes the overall orientation of the sheet now determined by both the side edges and the center of the sheet, such that the overall orientation is tilted toward the wall, leading to the drift toward the boundary.

In the long term, the stiff sheet in case A continues migrating away, while flexible sheets reorient near the wall and take on a shape that eases migration. That is, the stronger wall-

induced asymmetry near the wall triggers the outer side edge of the flexible sheet to turn inside out with a flip. Here, a sufficiently flexible sheet (case C) forms a taco with an overall orientation now tilting away from the wall, and the new orientation causes the sheet to drift away, as indicated in Fig 6.5(a). For a small regime of intermediate E_G like case B, the sheet becomes trapped near the wall. More specifically, the buckled sheet sediments next to the wall with an almost constant wall-normal distance, while the conformation shows weak oscillations as the conformation manages to reorient. Since the sheet is not flexible enough, the wall hinders the flipping of the sheet resulting in a sustained oscillation in sheet conformation. The oscillation in conformation is small and is almost negligible in Fig 6.5(a). Overall, the sheet is "sliding" next to the wall with a fixed distance. It is worth noting that the sliding sheet is a result of both initial orientation and E_G. If the sheet is initially oriented away from the wall, it immediately triggers the migration and the sheet escapes away from the wall.

The above examples illustrate three distinct responses of a sheet next to a vertical wall, determined by E_G. To characterize the migration, we plot the evolution of wall-normal distance d in Fig 6.5(b). The flexible sheet (case C) migrates slower compared to the stiffer sheet (case A) as it first drifts toward the wall and reorients to migrate away, indicating a non-monotonic increase in the wall-normal distance. The intermediate E_G (case B) becomes trapped around the wall. One important observation is the migration velocity, indicated by the slope, decreases with the wall-normal distance. The wall effect is a nonlocal interaction and migration is a long-range effect. However, if the sheet is placed sufficiently far away from the wall, it will recover the symmetric free space dynamics.

To elaborate on the migration dynamics, we examine the evolution of d in the parameter space of E_G in Fig 6.5(c). At short times ($t < 100$), migration distance decreases with E_G and very flexible sheets begin to drift toward the wall. When $t = 300$, flexible sheets reorient near the wall and migrate away, while sheets with intermediate E_G become trapped around the wall, resulting in a non-monotonic trend in d. Here, we identified two transition regimes

of E_G: $E_G \sim 23$ shows the threshold when the sheet immediately migrates away from the wall, and $23 < E_G < 28$ marks the onset where the sheet can successfully reorient around the wall and escape away. In addition, we examined the influence of initial distance by placing the sheet away from the wall with $d_0 = 3$ and the results are in qualitative agreement with the near wall condition. Since the wall effect is long-range, flexible sheets initially drift toward the wall such as case B and C in Fig 6.5(a) follows the same dynamics even when the sheet is initially away. However, we suspect that once d_0 is large enough where wall effects are negligible, the dynamics will change.

Finally, we can dig into the migration dynamic with a simple scaling analysis. A rigid particle that sediments next to a vertical wall does not migrate due to the Stokes reversibility [50], i.e. there is no wall-normal velocity generated by a Stokeslet next to a wall as the Blakelet solution completely cancels the wall-normal component. Therefore, the migration observed in simulations is due to a dipolar field arising from the next term in multipole expansion, such that the migration velocity decays as $1/d^2$: $\mathrm{v} = \mathrm{d}d/\mathrm{d}t \sim 1/d^2$ when the sheet is relatively away from the wall. By integrating the equation and taking the initial condition $d(t = 0) = d_0$, we obtain a simple scaling between the wall-normal distance d and t:

$$d = (3kt + {d_0}^3)^{1/3}. \tag{6.25}$$

To test the scaling, we take case A in Fig 6.5(a) and use the evolution of d to fit Eq 6.25. Surprisingly, the comparison in Fig 6.6 shows that the simple scaling gives a good power-law fit when the sheet is relatively far away from the wall. The deviation from the fitting curve for $t < 100$ has two contributions. The first is near-wall hydrodynamics, which includes all terms in the multipole expansion (the dipole term becomes dominant only when the sheet is far away from the wall). The other factor is the change in conformation as the sheet deforms from a flat state to adopt a taco conformation for $t < 100$.

Compared to the vertical wall, the tilted wall with $\alpha > 0^\circ$ introduces more complex sedimenting dynamics. By taking $\alpha = 30^\circ$, we introduce three dynamics observed in simulations:

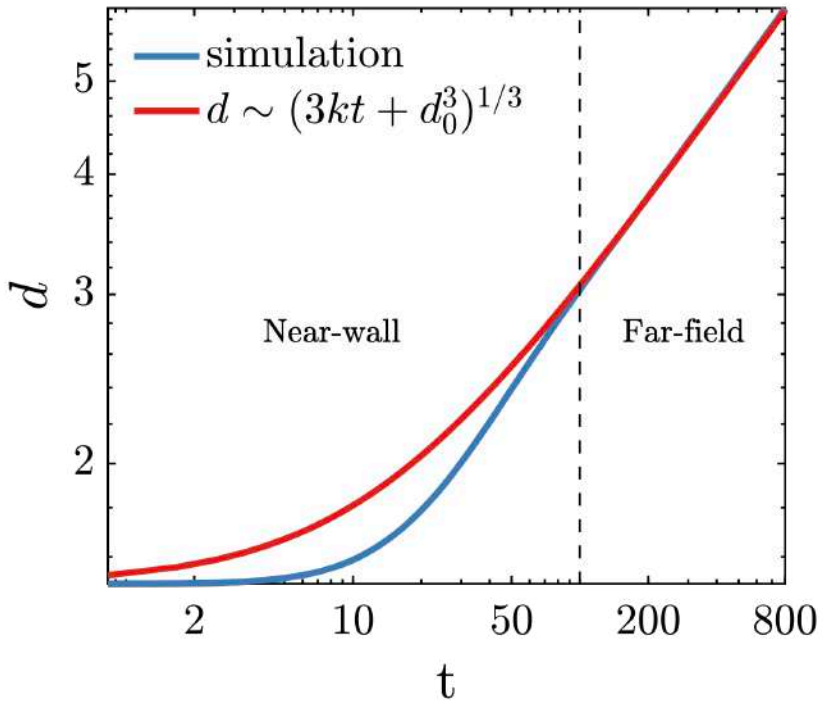


Figure 6.6: Comparison of wall-normal distance evolution for case A ($E_G = 8$) in Fig 6.5(a) by a fitting equation $d = (3kt + {d_0}^3)^{1/3}$ with $k = 0.085$ and $d_0 = 1.5$. We consider the dynamics for $t < 100$ to be governed by near-wall effects.

depositing (case A), sliding (case B), and rolling (case C) in Fig 6.7(a). When the wall is tilted, gravity pulls the sheet toward the wall. For relatively stiff sheets ($E_G = 1$ in Case A), the increased hydrodynamic drag due to wall effects causes the slightly folded sheets to be incapable of maintaining deformation. Therefore, the sheet relaxes as it approaches the boundary and finally deposits on the wall. In simulations, we apply a repulsive potential to prevent direct contact between the sheet and wall surface, such that the relaxed sheet becomes flat and sediments with a small fixed distance matching with the repulsive potential range. This is indicated in the evolution of the wall-normal distance d in Fig 6.7(c) for case A.

For intermediate E_G, flexible sheets remain folded as they approach the tilted wall. There are two competing effects. The wall-induced asymmetric conformation drives the sheet to migrate away from the boundary as in the vertical wall case. Meanwhile, gravity pulls the

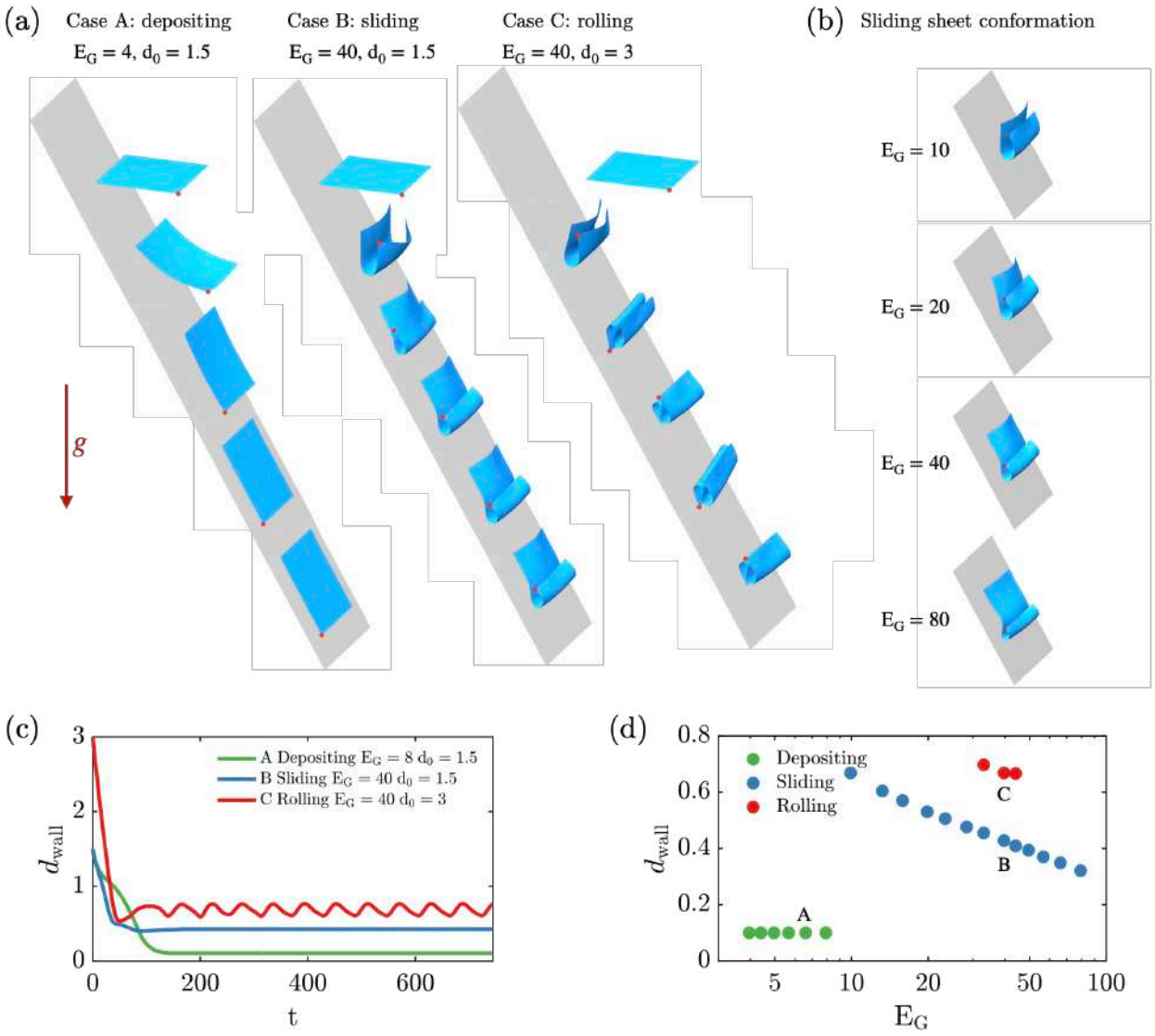


Figure 6.7: (a) Snapshots of dynamics near a tilted wall ($\alpha = 30°$) with initial orientation $\phi = 90°$: Case A. $E_G = 1$: the sheet deposits on the wall. Case B. $E_G = 40$: the sheet initially close to the wall ($d_0 = 1.5$) reaches a steady conformation and slides along the wall. Case C. $E_G = 40$: the sheet initially far from the wall ($d_0 = 3$) folds and rolls along the wall. (b) Shape evolution of steady sliding sheets with increasing E_G. (c) Transient evolution of wall-normal distance d for cases shown in Fig 6.7(a). (d) Steady wall-normal distance d_s for sheets next to a tilted wall with $\alpha = 30°$.

sheet toward the wall. When these two effects are balanced, sufficiently flexible sheets may reach a steady conformation while sedimenting at a fixed distance away from the tilted wall, as a sliding motion. The evolution of wall-normal distance reaches a fixed distance in Fig 6.7(c). We want to address the difference between sliding and depositing. Depositing is a

result of added repulsive potential as we do not account for the contact between wall and sheets. In reality, the sheet will deposit on the wall without sedimenting. The sliding sheets, however, result from pure near-wall hydrodynamics due to the interplay between gravity, sheet elasticity, and wall angle. The removal of repulsive potential does not affect sliding sheets. The sliding is analogous to the sliding for a rigid spheroid particle near a tilted wall observed by Michell *et al.* [110], where the spheroid sediments next to a tilted wall with a fixed orientation angle and keeps a fixed wall-normal distance. The sliding sheet conformation is determined by $\mathrm{E_G}$. We illustrate several sliding conformations with increasing $\mathrm{E_G}$ in Fig 6.7(b). To accommodate different hydrodynamic stress, the equilibrium sliding sheets adopt different conformations and wall-normal distances based on $\mathrm{E_G}$. In general, stiffer sheets show less asymmetric conformation and stay a relatively large distance away from the wall. Flexible sheets show an inverse "J" shape, with folding mainly located around the lower part of the sheet and staying relatively close to the wall.

In certain parameter regimes, sliding dynamics may be influenced by the initial distance from the wall. When $\alpha = 30^\circ$, we identified a small regime of $\mathrm{E_G}$ where sheets show an interesting rolling motion when initially far from the wall. Case C in Fig 6.7(a) with $\mathrm{E_G} = 40$ reveals an interesting rolling motion. The far wall initial distance ($d_0 = 3$) allows the sheet to buckle while approaching the wall and fully fold as a compact S shape near the wall. The folded sheet then tumbles next to the wall and results in an oscillatory trajectory in Fig 6.7(c). In contrast, a near-wall initial condition ($d_0 = 1.5$) lacks space to fully fold on itself and ends up sliding, which indicates the sliding here is a result of hindered transient reorientation dynamics.

We summarize the different dynamics observed for $\alpha = 30^\circ$ by plotting the steady wall-normal distance d_s for the equilibrium dynamics in Fig 6.7(d). When $\mathrm{E_G} < 8$, sheets deposit on the wall as maintaining a small distance within the repulsive potential range. Sheets with $\mathrm{E_G} > 8$ reach a steady conformation and slide along the wall, while the steady wall-normal distance d_s decreases with $\mathrm{E_G}$. Rolling only occurs in a small parameter regime when the

sheet is initially away from the wall.

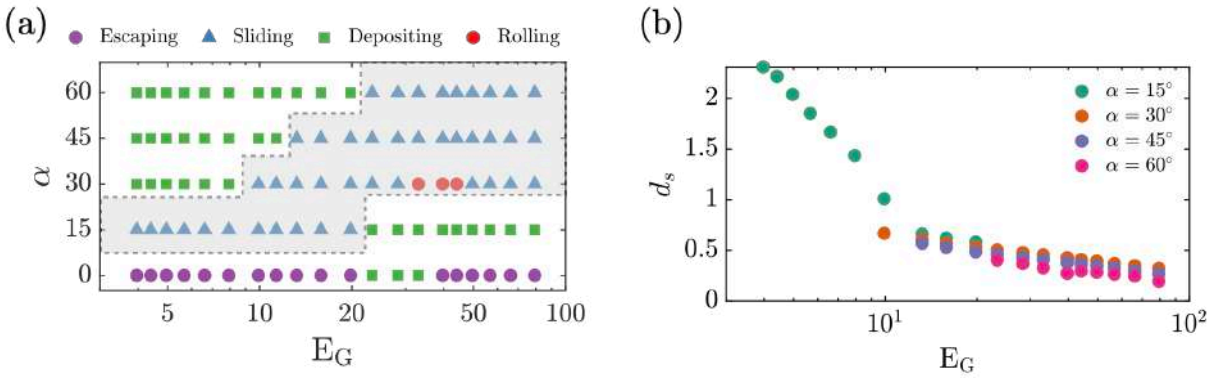


Figure 6.8: (a) Phase diagram for E_G vs. α. Symbols represent the sheet dynamics. (b)Steady wall-normal distance d_s for sliding sheets (boxed region in Fig 6.8(a)) with different E_G and α.

To systematically explore the influence of flexibility E_G and wall angle α, we did a parameter sweep with the long-term dynamics summarized in Fig 6.8(a). For every case, we tested two different d_0 to rule out dynamics due to the transient state. Typically, when the wall is vertical ($\alpha = 0°$), sheets escape the wall except for a small parameter regime that sheets are trapped due to reorientation. Once the wall is tilted, sheets either become trapped near the wall region or deposited on the boundary. For each α, we determined a transition E_G to distinguish between sheets deposited on the wall and sheets trapped near the wall (marked as the boundary between sliding and depositing). One observation is that the threshold E_G to deposit increases with α. Interestingly, under a small wall angle ($\alpha = 15°$), the sheet deposits at large E_G. In addition, we plot the steady wall-normal distance d_s for the sliding sheets for different E_G and α in Fig 6.8(b). For all α, d_s decreases with E_G. We notice that most of the cases explored fall onto a universal curve. The phase diagram provides a potential strategy to separate sheet-like particles. For example, to separate particles with different E_G, we may choose a wall angle such that the transition E_G of specific α lies in between E_G of particles. Consequently, stiffer particles deposit on the wall while more flexible particles slide and can be collected downstream.

6.4 Summary

In this work, we perform numerical simulations to systematically explore the sedimentation of an almost inextensible but flexible square sheet in a viscous fluid. An elasto-gravitational number E_G is used to measure the ratio between gravity and bending elasticity. We addressed two scenarios: sedimenting in free space or beside an infinite planar wall, where the wall can be tilted.

In free space, the sheet takes on a stable orientation perpendicular to gravity, with a unique steady conformation that is independent of initial orientations. Sheets adopt more compact shapes with increasing E_G, varying from almost flat to taco-like buckled shapes, and more folded shapes sediment faster as they experience smaller hydrodynamic drag. The randomly oriented sheets reorient toward the stable orientation, which induces lateral drift. The maximum drift happens when the sheet is initially aligned with gravity. We identified two different reorientation dynamics, and the drift distance due to reorientation increases with E_G.

The presence of a wall introduces asymmetry to the sheet conformation, and the sedimentation dynamics are determined by both E_G and the wall-tilted angle α. When next to a vertical wall, asymmetry in sheet conformation leads to the migration of the sheet away from the wall. We found three different drifting dynamics determined by E_G, and observed a non-monotonic trend of migration distance evolution due to the different responses in complex buckled shapes. When the wall is tilted, wall-induced migration competes with gravity-induced deformation, leading to the observation of three novel types of dynamics: depositing, sliding, and rolling. We developed a phase diagram to show the dependence of dynamics on α and E_G, and determined the transition E_G between depositing and sliding for different α.

This study deepens our understanding of the sedimentation dynamics of sheet-like particles and provides several strategies for particle separation. Based on E_G, we may separate particles via different settling velocities, or different migration distances if next to a vertical

wall. Typically, a more robust separation method is to adjust the wall tilted angle. Since we know the transition E_G, an appropriate wall angle can make the relatively stiff sheets deposit on the wall while the more flexible particles keep sliding.

7

Conclusions and future work

7.1 General summary

In this thesis, we developed a systematic framework to understand the dynamics of soft elastic sheets in several flow conditions. Motivated by the paucity in fundamental knowledge for elastic sheets, we explored the dynamics from freely suspended sheets in extensional and shear flow to a sedimenting sheet in a viscous fluid.

We visited the extensional flow in Chapter 3 and Chapter 4. In Chapter 3, we studied the conformational hysteresis for a highly stretchable polymeric sheet in planar and biaxial extensional flows. The nature of two extensional flows that enforces a flat steady state allows us to purely focus on the in-plane deformation. With a nonlinear hyperelastic model, we captured a coil-stretch-like transition in sheet conformation from a compact state to a fully stretched state, along with a bistable regime in flow strength where both steady states can exist. We applied an artificial Brinkman model to screen the hydrodynamic interactions and proved the existence of bistability requires hydrodynamic interactions between different parts of the sheet surface. Next, we continued the discussion of conformational bistability in Chapter 4 with a uniaxial extensional flow, where the radially compressive stresses lead to buckling instability. We showed the wrinkled sheets arrest a smaller stretched size due to the hydrodynamic screening of trapped fluids in the wrinkling, and highlighted the influence of

wrinkling on bistable dynamics. We also developed an Arnoldi-based linear stability analysis that can predict the buckling threshold as well as nonlinear dynamics in certain regimes of flexibility.

In Chapter 5, we explored the dynamics of elastic sheets with different rest shapes in a simple shear flow. For all the rest shapes, we identified characteristic motions and observed a transition from 2D rotating inside the shear plane to complex shear-induced 3D deformations with increasing flexibility. For the disk, we identified two stable solutions based on assigned perturbations: a dynamic S-shape buckling instability as a wiggling motion and a periodic C-shaped flapping motion. A linear stability analysis was developed that yields a number of deformation modes and can predict linear dynamics such as buckling instability. Notably, the flapping motion found in simulations has been confirmed by experiments done by our collaborator, and the results show quantitative agreement with simulations. For rectangles, we address the influence of aspect ratio and observed a non-monotonic relation between aspect ratio and buckling threshold.

Beyond freely suspended sheets, we explore the sedimentation dynamics of a square in Chapter 6. In free space, we systematically examined the influence of dimensionless flexibility on the equilibrium conformations as well as the reorientation dynamics. The free space sedimentation dynamics observed are comparable to that in a flexible filament. Sheets with larger deformability adopt more compact conformations and experience smaller hydrodynamic drag, thereby sedimenting faster. Moreover, we extended the study by placing the sheet next to an infinite wall. When the wall remains vertical, migration of sheets is expected due to the breaking of spatial symmetry and is strongly determined by sheet flexibility. We observed a non-monotonic which reveals qualitatively different dynamics. When the wall is titled, the sheet may slide along the near-wall or deposit on the wall as a result of the interplay between sheet flexibility and wall effects.

In the following sections, we present several potential directions for future research, including some improvements to the current model and interesting areas to explore.

7.2 Model development

7.2.1 Elastic sheet with a finite thickness

In the current formulation, the sheet is taken to have zero thickness hydrodynamically because it is modeled as a single layer of nodes. This assumption is based on the fact that thin sheets usually have a thickness negligible compared to their lateral dimensions. For example, graphene flakes obtained from liquid-phase exfoliation have a lateral size of micrometers while the thickness is in nanometers, which can be a thousand times different.

In extensional flow, the sheet thickness does not play a role as the buckling occurs along the lateral direction of the sheet. In shear flow, however, we find sufficiently flexible sheets become flow-aligned: the sheet approaches the flow-vorticity plane and stays there. This is analogous to a fiber with an infinite aspect ratio. For the sheet with a finite thickness, the shear stress acting on the top and bottom sides of the sheet induces a bending moment to trigger the tumbling of the sheet. If the sheet has zero thickness, the bending moment is zero and the sheet is trapped in the flow-aligned state. On the other hand, Jeffery's solution also shows the tumbling period of a rigid disk $T \sim (AR + AR^{-1})$. A disk with zero thickness has $AR \to \infty$ thereby resulting in an infinite T to tumble. To better capture the shear flow dynamics and add physics to the model, we propose to model an elastic sheet with a finite thickness h, where h is much less than the lateral length scale a.

There are two potential solutions to implement the finite thickness. Based on the fact that thickness only matters when the sheet approaches the flow-vorticity plane, one solution is to keep the current formulation and assign the sheet an artificial hydrodynamic torque based on h. We assume the layer of nodes is located on the mid-surface of the sheet and artificial torque is assigned on the node based on the bending arm $\frac{h}{2}$ along the direction normal to the mid-surface. and the surface traction $\mathbf{s}$ for both sides, where the traction can be evaluated based on an interpolation of the velocity on the surface.

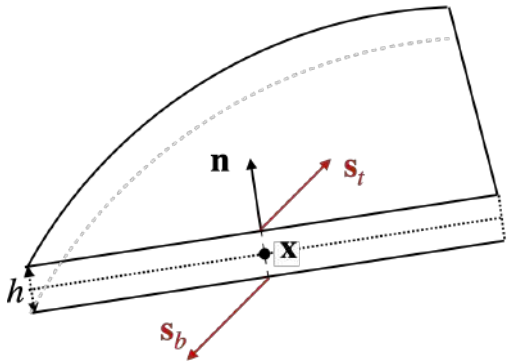


Figure 7.1: Implementation of artificial torque to account for finite thickness h: $\mathbf{n}$ is normal to the upper surface and $\mathbf{s}$ is the surface traction. Index t indicates top surface and b for the bottom. $\mathbf{t}$ is a directional vector along the traction.

$$\mathbf{T} = \int_{\Gamma} \frac{h}{2}\mathbf{n} \times \mathbf{s}_t - \frac{h}{2}\mathbf{n} \times \mathbf{s}_b dS. \tag{7.1}$$

Therefore, once the sheet approaches the flow-vorticity plane, the small hydrodynamic torque would help flip the sheet to complete a tumbling cycle. The formulation above requires an estimation of h, which determines the aspect ratio of the sheet. The aspect ratio of the current sheet is zero, making the corresponding Jeffery orbit period infinite. This could be another test case to validate the model with Jeffery's orbit.

The second potential solution is to model the sheet with actual thickness. The 3D fiber modeled with a bead-spring system by [20, 82] inspires us to come up with a 3D model for a thin elastic sheet. Instead of modeling the mid-surface, we track the material points located on both sides of the sheet. That is, we use Hookean springs with a stiffness constant k to interconnect the nodes on the other side of the sheet. FIG shows an example of a square sheet with thickness h. Fig 7.2 shows two potential implementations. Fig 7.2(a) is a simple toy version with every node only connecting to one corresponding node on the other sheet. The system in Fig 7.2(b) is more complicated as every node connects to the corresponding node as well as the surrounding nodes in its one-ring neighborhood. We show a simple test case in Fig 7.2(c) using the simple connection in Fig 7.2(a). Though the sheet shows periodic tumbling, the top and bottom surfaces are sheared with a relatively unrealistic gap. This toy

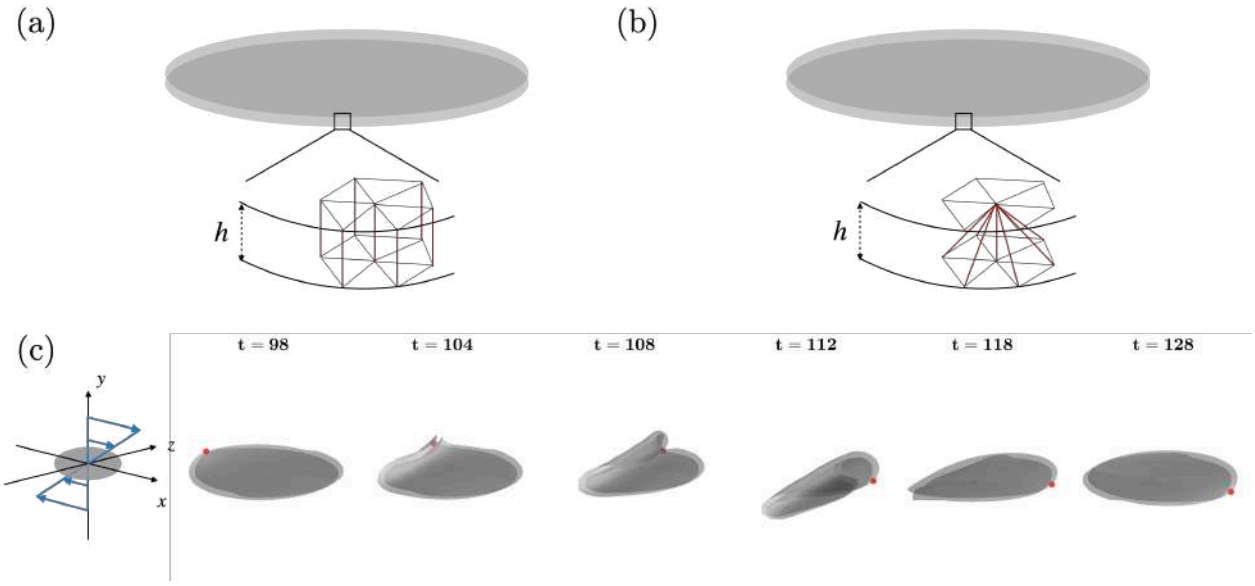


Figure 7.2: (a) Simplified spring system with every node connected directly to the node on the other surface. (b) Improved spring system with every node connected to the corresponding node and its one-ring neighbor nodes on the other surface. (c)Example of tumbling flexible sheets with the top surface and bottom surface connected by the simple spring system in (a).

model suggests that a finer connected network such as Fig 7.2(b) may resolve this problem.

7.2.2 Nonlinear bending method

The current formulation applies a linear bending model where the assigned energy penalty is linearly proportional to the deflection angle θ and is valid only when θ remains small. This approximation is easy to implement and is widely used in the modeling of capsules, vesicles as well as elastic sheets. However, it is challenged when the sheet shows a large deflection angle between elements, which requires a finer mesh discretization to keep θ small. On the other hand, the method only captures linear bending dynamics. Therefore, it is necessary to introduce a nonlinear bending to account for more realistic dynamics.

The nonlinear bending formulation from capsule and vesicle studies provides a possible solution [54]. The method applies the principle of virtual work to the Canham-Helfrich energy:

$$E_b = \frac{K_B}{2}\int_\Gamma (2\kappa_H + c_0)^2 dS + \overline{K_B}\int_\Gamma \kappa_G dS. \tag{7.2}$$

Assume the local bending force density $\mathbf{f}_b$ associated with the response of energy δE_b to the infinitesimal deformation $\delta\mathbf{R}$ on the sheet surface Γ:

$$\delta E_b = \int_\Gamma \mathbf{f}_b \cdot \delta\mathbf{R} dS. \tag{7.3}$$

The deformation $\delta\mathbf{R}$ is split into normal and tangential components. A well-established normal bending formulation was developed by Zhong-can *et al.* [203] to study deformation in vesicles. The tangential component is omitted in the vesicle study because it is included the enforcement of constant area. Capovilla *et al.* [18] introduced the tangential bending stresses formulation when considering membrane can be stretched with local area change by transforming the deformation a Lie derivative, which is the directional derivative relative to the surface curvilinear coordinates. The detailed numerical methods for nonlinear bending are well-documented in [159]. While the method can be adapted to account for nonlinear bending in sheets, there are several challenges that remained. The second term in the Helfrich energy denotes the contribution due to Gaussian curvature. For a closed surface like capsules and vesicles, this term is a topological invariant ensured by the Gauss-Bonnet theorem: $\int_\Gamma \kappa_G dS$ is constant and vanishes after taking variations. For a sheet with open edges, this term is associated with the geodesic curvature k_g integrated along the boundary, which requires extra treatment to the formulation. Moreover, the boundary conditions are changed due to the presence of free edges. The case discussed here is similar to a membrane with open edges, which has been investigated by some researchers [11, 54, 124, 172]. Though the membrane model considers a line tension along the open edge, potential modifications can be made to adapt the nonlinear bending formulation to elastic sheets.

7.3 Multiple sheets interaction

In Chapter 1, we reviewed many applications involving the suspension of thin sheets. The highly nonlinear deformation and dynamics of the sheet are sensitive to particle-particle

interactions, which further influence the rheological properties. For example, the suspension of graphene oxide in a circular Couette flow shows shear-thinning properties when the shear rate is large which causes the graphene to stack and align with the flow direction [107, 108, 135]. Salussolia *et al.* studied the interacting elastic sheets in shear flow and characterized interesting hydrodynamic-induced dynamics such as parallel sliding, bending, and reattachment [150]. Their study provides insights into the flow-induced morphologies and particle-particle interactions but the simulation is based on a 2D formulation. Another motivation comes from a recent experimental study by Perrin and coworkers [133]. They investigated the buckling of a pair of rectangle sheets in a shear cell and found that a pair of sheets show buckling below the critical buckling shear rate of a single sheet. This study indicates the morphology of sheets in suspension may deviate from the dilute limit due to particle interactions. From our shear flow results, we learned that deformable sheets show complex 3D dynamics in shear flow. Therefore, we aim to get a comprehensive understanding of particle-particle interactions in the dilute limit before moving on to the suspension.

Here, we first use our model to reproduce Perrin *et al.*'s observation on the reduced buckling threshold due to the presence of a second sheet [133]. Their experiments are based on two rectangles tumbling in shear flow. Though our model here is based on the disk, we determined the buckling threshold $\mathrm{E_V^C} \sim 4$ for a disk, which is close to $\mathrm{E_V^C} \sim 1$ we got for a rectangle. This fact suggests that the tumbling dynamics are not purely in 2D and are influenced by the lateral dimensions.

Figure 7.3 shows two cases $\mathrm{E_V} = 8$ (Fig 7.3(b)) and $\mathrm{E_V} = 4$ (Fig7.3(c)) that are close to the buckling threshold of a single disk. Similar to what Perrin *et al.* observed in experiments (Fig 7.3(a)), sheets show deformation even about ten times stiffer than the buckling threshold. The two cases show buckling instability: two sheets first bend away from each other when align with the major compression axis of the flow ($t = 0.9$). As tumbling continues, the deformation decrease ($t = 5$). A slight increase in buckling appears after sheets pass the major extension axis, where the sheets buckle toward each other ($t = 7$). As discussed

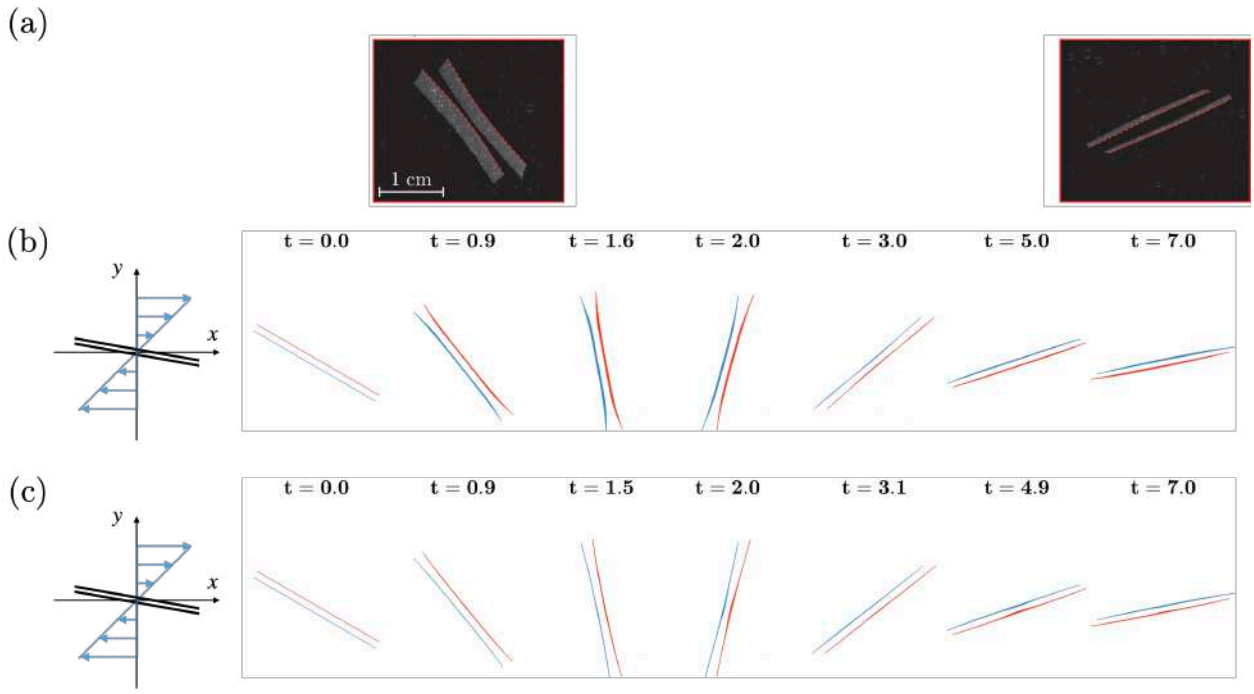


Figure 7.3: (a) Snapshots of two tumbling sheets with $E_V \sim 30$ (estimated) showing deformation from experiments in [133]. (b) Snapshots of two tumbling disks with $E_V = 8$. (c) Snapshots of two tumbling disks with $E_V = 4$.

in [133], the deformation on the sheet is mainly caused by the dipolar perturbation field generated by the second sheet.

7.4 Exfoliation

Liquid-phase exfoliation is a robust method to achieve massive production of 2D materials. Previously, several works have examined the exfoliation with either a continuum model [14, 88, 144, 173] or molecular dynamic simulations [51]. The simulation of exfoliation requires extra considerations. For example, the small size of 2D materials like graphene makes thermal fluctuation important, which makes it necessary to include Brownian motion. On the other hand, the no-slip condition no longer holds for sheets with atomic thickness.

In this case, we simplify the problem by taking advantage of the current model and extend the study of multiple sheets interaction to tackle the exfoliation. Since the main interaction

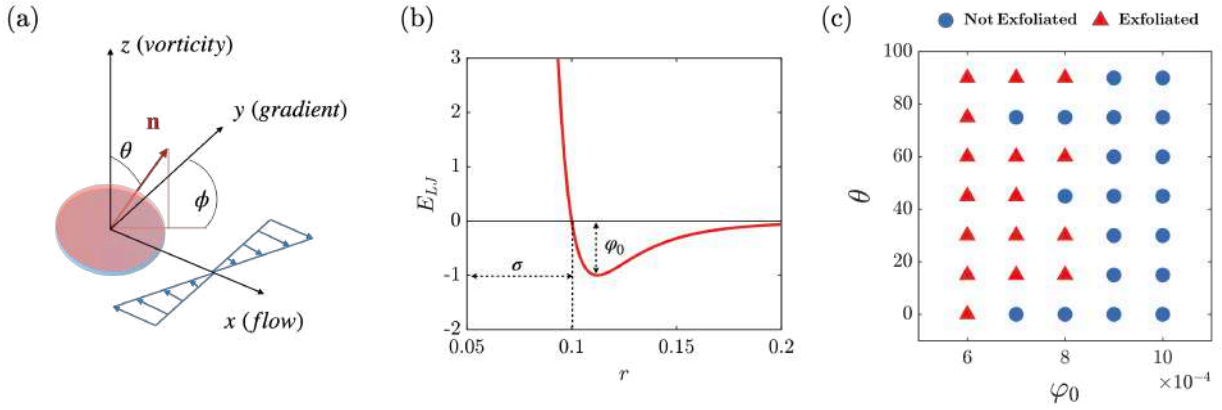


Figure 7.4: (a) Comparison of swimming distance Δ based on actuation frequency ω. Larger ω results in faster swimming. (b) Comparison of swimming distance Δ based on sheet flexibility. More flexible sheet results in faster swimming.

between layers of sheets is the van der Waals interaction, we include the full Lennard Jones potential and focus on the exfoliation between multiple sheets.

$$E_{LJ} = 4\varphi_0 \left[\left(\frac{\sigma}{r}\right)^{12} - \left(\frac{\sigma}{r}\right)^{6} \right], \tag{7.4}$$

where r is the distance between nonadjacent nodes at equilibrium state, σ is the range of the potential, and φ_0 measures is the strength of the potential. We sheets are initially placed parallel to each other with an inter-layer distance d_0 with initial conditions defined by two angles θ and ϕ indicated in Fig 7.4.

Here, we use a couple of examples to briefly show the idea of modeling exfoliation. We consider the interaction potential strength φ_0 and the initial orientation θ of the layered sheet in shear flow. The long-term dynamics are considered based on whether the sheet is exfoliated. Fig 7.5 presents two cases with the same mechanical properties. The first example shows exfoliated sheets with relatively weak interaction. The evolution of an averaged gap between sheets $< d >$ Fig 7.5(c) marks the exfoliation. In the second case, sheets are not exfoliated. Instead, they become flow-aligned as introduced in the shear flow case. Since sheets are attracted due to potential, they can be treated as a thick plate with a thickness

of the gap size. Therefore, we observed continuous tumbling.

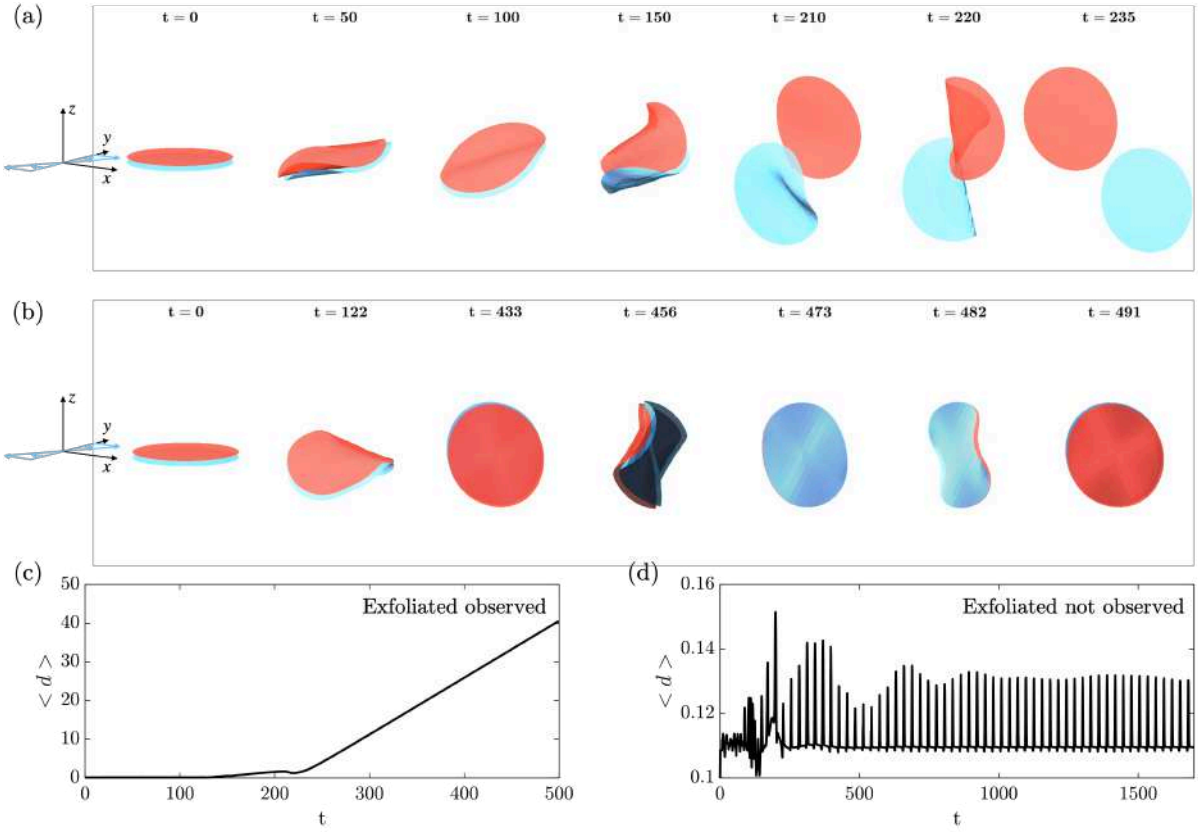


Figure 7.5: Examples of two sheets with van der Waals interactions: (a) Two sheets successfully exfoliate. (b) Two sheets fail to exfoliate. (c) Evolution of the averaged inter-layer distance $< d >$ for the exfoliated case in Fig 7.5(a). (d) Evolution of the averaged inter-layer distance $< d >$ for the unexfoliated case in Fig 7.5(b).

We summarize the exfoliation dynamics in Fig 7.4(c) and found that beyond a specific φ_0, sheets with random orientations all result in exfoliation. In the preliminary results, we only visited the dependence on the initial orientation θ and interaction strength φ_0, while previous work found the exfoliation relates to the shear rate, number of layers of sheets, and the size of the sheet.

7.5 Biohybrid sheets

Locomotion at low Re can be challenging because the swimmer needs to overcome irreversibility in Stokes flow. In Chapter 1, we briefly introduced the Stokes flow reversibility with an example of the scallop theorem: for rigid particles such as two rods connected by an active hinge, the cyclic motion in time leads to no net motion in Stokes flow. In the example of the self-propelled biohybrid filament [181], the filament overcomes the reversibility by the flexibility of the filament. Every time the cell contracts that deforms the filament, the elasticity allows the restoration of the filament back to its equilibrium shape thereby breaking the symmetry. However, this fact also contributes to the low efficiency of swimming as the net displacement for one cycle is small compared to its body length. On the other hand, very flexible filament is also undesired, because the flexible nature of the filament prescribes the contraction in a local regime where the deformation cannot be propagated along the body. On the other hand, the swimming muscular thin polymer film developed by Feinberg *et al.* [45] indicates the importance of cell distribution. The sheet with anisotropic distribution of cells can swim while the sheet with isotropic distribution fails to swim.

Here, we present a toy model for a swimming sheet. Unlike the prescribed wave method applied in [111], we aim to develop a swimming strategy based on the actuation from the hybrid biological tissue on the sheet. We assume cardiomyocytes are used as a power source and are distributed along a line on a square sheet. The sheet is freely suspended in a stationary viscous fluid. and satisfies the zero-net-force and zero-net-torque conditions [50, 84]. As indicated in Fig 7.6(a), the sheet has a limited thickness h, and contractile forces generated by cardiomyocytes are concentrated on the node where the cell is numerically seeded. Adapted from a model of biohybrid flagellar [121], the contractile force magnitude is given as:

$$F = A[\cos(\omega t - k) + 1], \tag{7.5}$$

where A is the amplitude to be determined, ω is the actuation frequency, k is a phase,

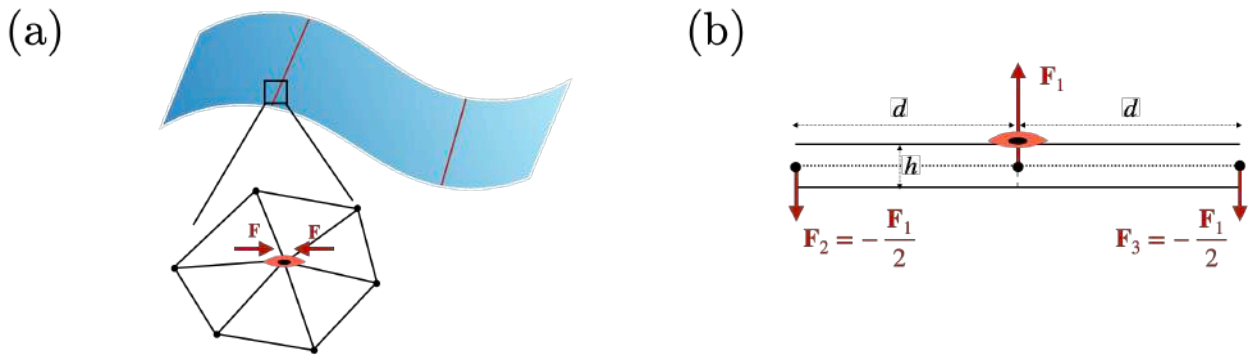


Figure 7.6: (a) The schematic of a self-propelled sheet with a surrounded patch. Red color is the alignment of cells. θ is the angle between node-to-node displacement and contraction force. (b) The schematic of induced moments generated by cell contraction. d is the node-to-node distance.

and the constant 1 ensures a positive magnitude. The contraction of the cardiomyocytes creates torques with a bending arm of $h/2$. The induced moments result as forces on the nodes. Different from the synthetic flagellar swimmer described in [121], the contraction force influences the surrounding region, instead of two filaments, and the mesh may not align with the force direction. We propose that the induced moment at node i is related to the angle θ with respect to the force direction and the node-to-node distance d. It remains unclear how the contractile force will interact with each other. Further details need to be refined based on the proposed model.

We use the aforementioned toy model to examine the swimming dynamics based on three aspects: cell alignment, cell actuation, and substrate flexibility. Fig 7.7 compares two sheets with different alignments of cells based on their swimming distance Δ. To swim at low Re, the particle needs to overcome the Stokes reversibility. The sheet with cells distributed along the center has almost zero net displacements, while the sheet with cells distributed close to the edge swims in the fluid. Typically, the center-aligned sheet is similar to the scenario described in the scallop theorem where the upward motion is canceled by the downward motion due to Stokes reversibility. Though the flexibility of the sheet allows the sheet to break the symmetry due to the relaxation of the sheet from the deformation, this effect is not evident and results in almost zero swimming distance. In contrast, the asymmetric

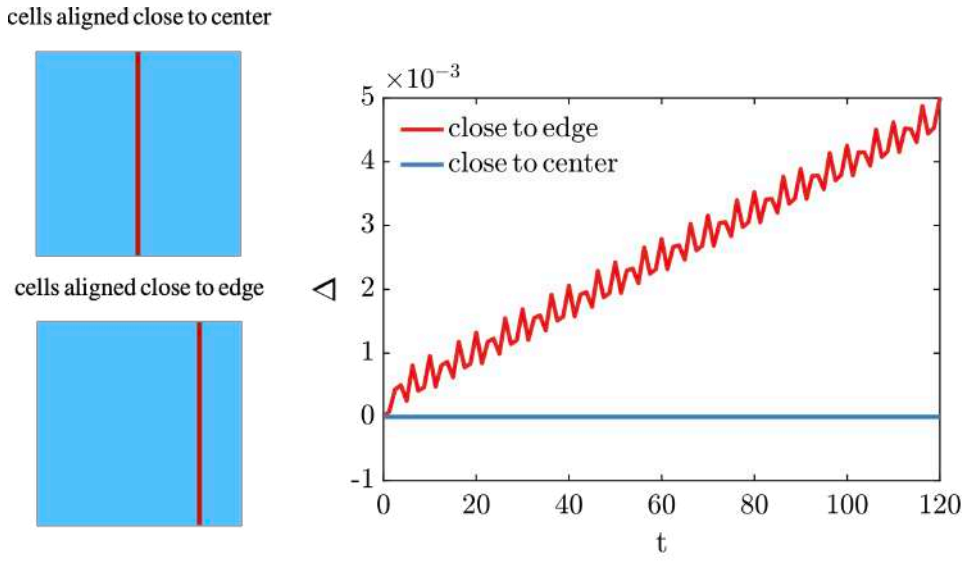


Figure 7.7: Comparison of swimming distance Δ based on alignments of cardiomyocytes: alignment along the centerline and alignment close to the edge.

alignment close to the edge show evident swimming, and the swimming distance in space increase almost linearly with time. However, swimming efficiency is poor as the displacement traveled by each cycle is negligible.

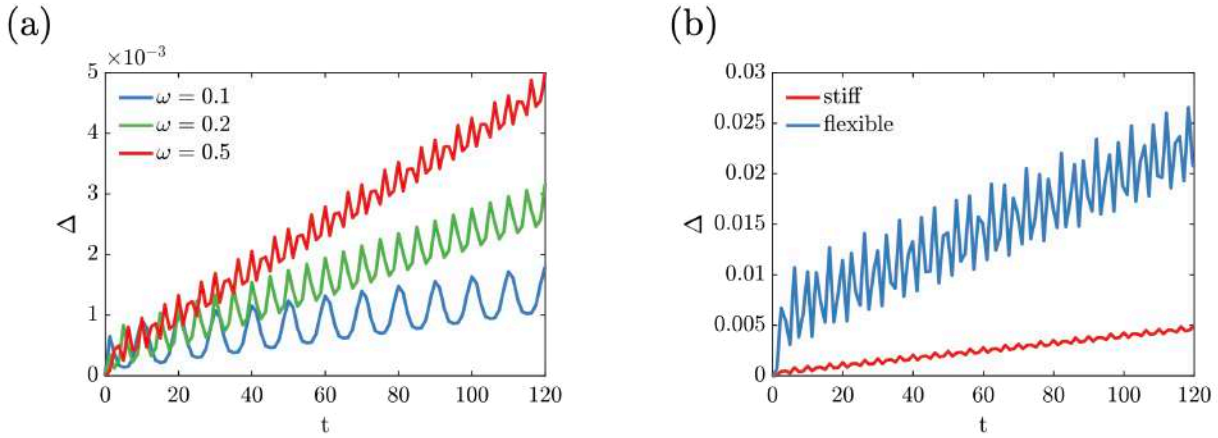


Figure 7.8: (a) Comparison of swimming distance Δ based on actuation frequency ω. Larger ω results in faster swimming. (b) Comparison of swimming distance Δ based on sheet flexibility. More flexible sheet results in faster swimming.

Furthermore, we examined the influence of the actuation frequency ω and substrate flexibility. Fig 7.8(a) demonstrated more frequent actuation leads to faster swimming, which

is expected. Fig 7.8(b) shows a flexible sheet swims faster than a less flexible sheet. One possible explanation is the flexible sheet facilitates the deformation due to the contraction of cells, resulting in a larger bending amplitude. However, when the sheet becomes too flexible, it is possible that the deformation due to actuation will be localized around where the cells are distributed and fail to propagate through the sheet.

7.6 Flexible filaments in simple shear flow

This proposed work is an extension of a class project.

Fiber model

We applied the model developed in [20, 82] to model a flexible fiber based on a bead-spring system. Fig 7.9(a) shows the setup of the fiber: the intrinsically straight fiber is modeled as a cylinder with an equilibrium length L and a diameter D, and the cylinder surface is discretized by stacking layers of cross-sections along the filament centerline. Each cross-section is described by $N_c = 8$ nodes along the edge and the fiber contains N_f cross-sections. The distance between sections is set as approximately the spacing between adjacent nodes on the individual section, such that the total number of nodes on the fiber surface is $N_c \times N_f$. The nodes are interconnected by linear Hookean springs. More specifically, a single node is connected with all the nodes in the same cross-section and all the nodes on the two neighboring cross-sections. As indicated in Fig 7.9(a), the node (from a section in the middle) is connected with $7(\text{same section}) + 2 \times 8(\text{two neighboring sections}) = 23$ nodes.

The total elastic energy in the fiber is contributed by all the elastic springs inside the filament:

$$E = \frac{1}{2} \sum_j k_j l_j^2 \left(\frac{\|\mathbf{x}_{j_1} - \mathbf{x}_{j_2}\|}{l_j} - 1 \right)^2, \tag{7.6}$$

where k_j is the stiffness of a spring with the rest length l_j that connects the node $\mathbf{x}_{j_1}$ and $\mathbf{x}_{j_2}$. The force at each nodal position is obtained by taking the derivative of the energy with

respect to the position and sum over all springs meeting at the node.

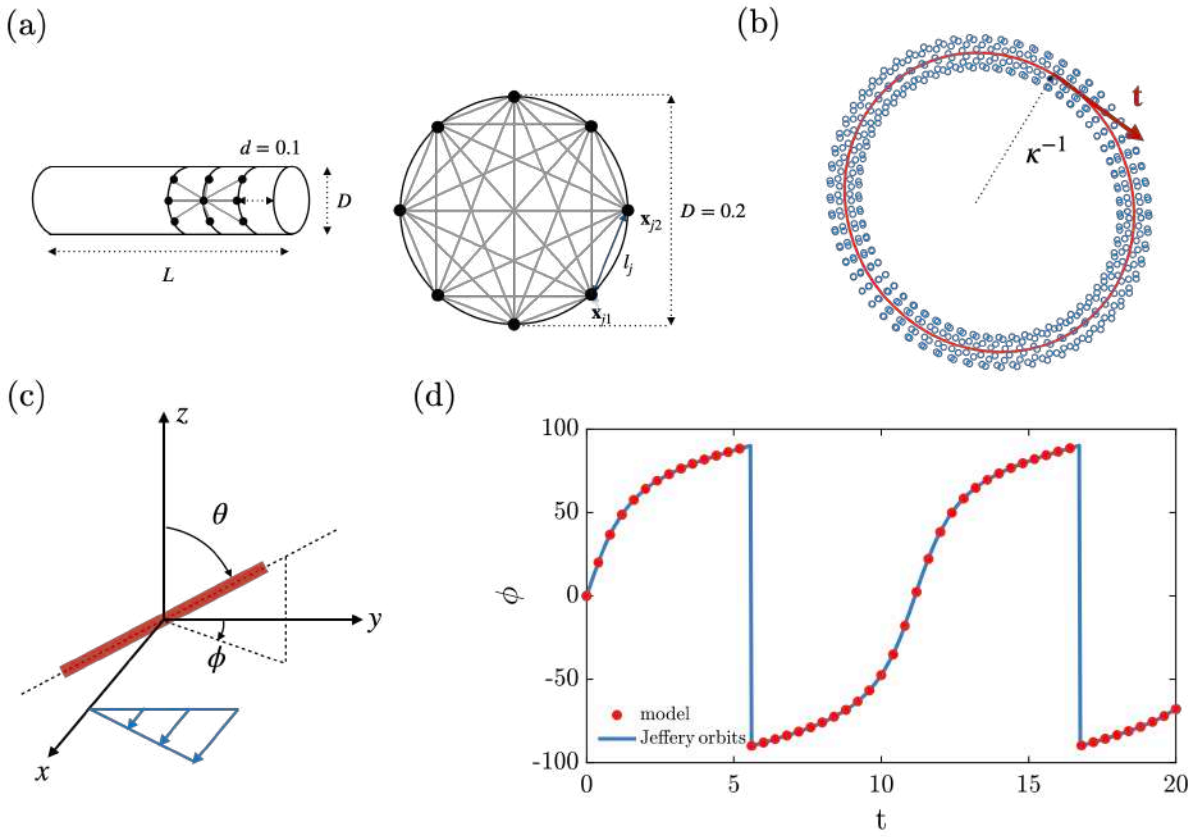


Figure 7.9: (a) Illustration of fiber conformation. (b) Measurement of bending stiffness K_B by bending a fiber with a fixed curvature κ. (c) Illustration of fiber orientations in shear flow. (d) Comparison of angle ϕ for a tumbling rigid fiber with analytical Jeffery orbit solutions.

In this model, the special treatment of the bead-spring network accounts for both the tensile stress and bending rigidity. Since all springs share the same stiffness constant k_j, the material is considered to be homogenous and isotropic. Moreover, the bending rigidity K_B now is determined by the spring constant k_j and the topology of the filament. By assuming a straight filament at equilibrium, the bending energy is estimated based on the Euler-Bernoulli beam theory. Given the centerline position $\mathbf{X}(s)$ and filament length L, the bending energy E_b is:

$$E_b = \frac{1}{2} K_B \int_0^L (\frac{d\mathbf{t}}{ds})^2 ds, \tag{7.7}$$

where $\mathbf{t}$ is the local unit tangential vector that directly gives the estimate of local curvature

$\kappa = d\mathbf{t}/ds$. For a filament bent into a circle with prescribed known curvature κ (Fig 7.9(b)), the bending energy becomes:

$$E_b = \frac{1}{2} K_B \kappa^2, \tag{7.8}$$

and the bending rigidity K_B can be obtained as:

$$K_B = \frac{2E_b}{\kappa^2 L}. \tag{7.9}$$

Following other fiber literature, we define a dimensionless elasto-viscous number $\mathrm{E_V} = 8\pi\eta\dot{\gamma}L^4/cK_B$. It is worth noting that $\mathrm{E_V}$ also considers the filament aspect ratio. Larger $\mathrm{E_V}$ represents a more flexible fiber. The governing equation is the Stokes equation and is solved by the method of regularized Stokeslet.

Model validation

We validate the fiber model by comparing the evolution of orientation of an almost rigid filament (small $\mathrm{E_V}$) in shear flow with analytical Jeffery's solutions from Chapter 1. The centerline of the filament initially lives inside the flow-gradient plane and tumbles.

$$\tan\theta = \frac{CAR_e}{\sqrt{AR_e^2\cos^2\phi + \sin^2\phi}}, \quad \tan\phi = AR_e \tan(\frac{2\pi t}{T} + k). \tag{7.10}$$

Here, the equivalent aspect ratio AR_e of the filament is converted by a prefactor 0.72 from the actual aspect ratio AR: $\mathrm{AR}_e = 0.72\mathrm{AR}$. In addition, the tumbling filament inside the shear plane has a fixed $\theta = \pi/4$ thereby an infinitely large orbit constant $C \to \infty$ and we track the dynamics with angle ϕ. In Fig 7.9(d), the model's evolution of angle ϕ agrees well with that of analytical solutions.

Dynamics of a single filament

Here, we study the dynamics of a fiber with different initial conditions. We explore the parameter space of initial angle θ while keeping $\phi = 90^\circ$ for fibers with different aspect ratios ($AR = 5$ and $AR = 7$) and flexibility. The evolution of θ is plotted in Fig 7.10. The angle

θ is varied from 5° to 85°. As a reference from Jeffery orbit, fiber with $\theta = 0°$ undergoes a rolling motion, and $\theta = 90°$ leads to a tumbling motion.

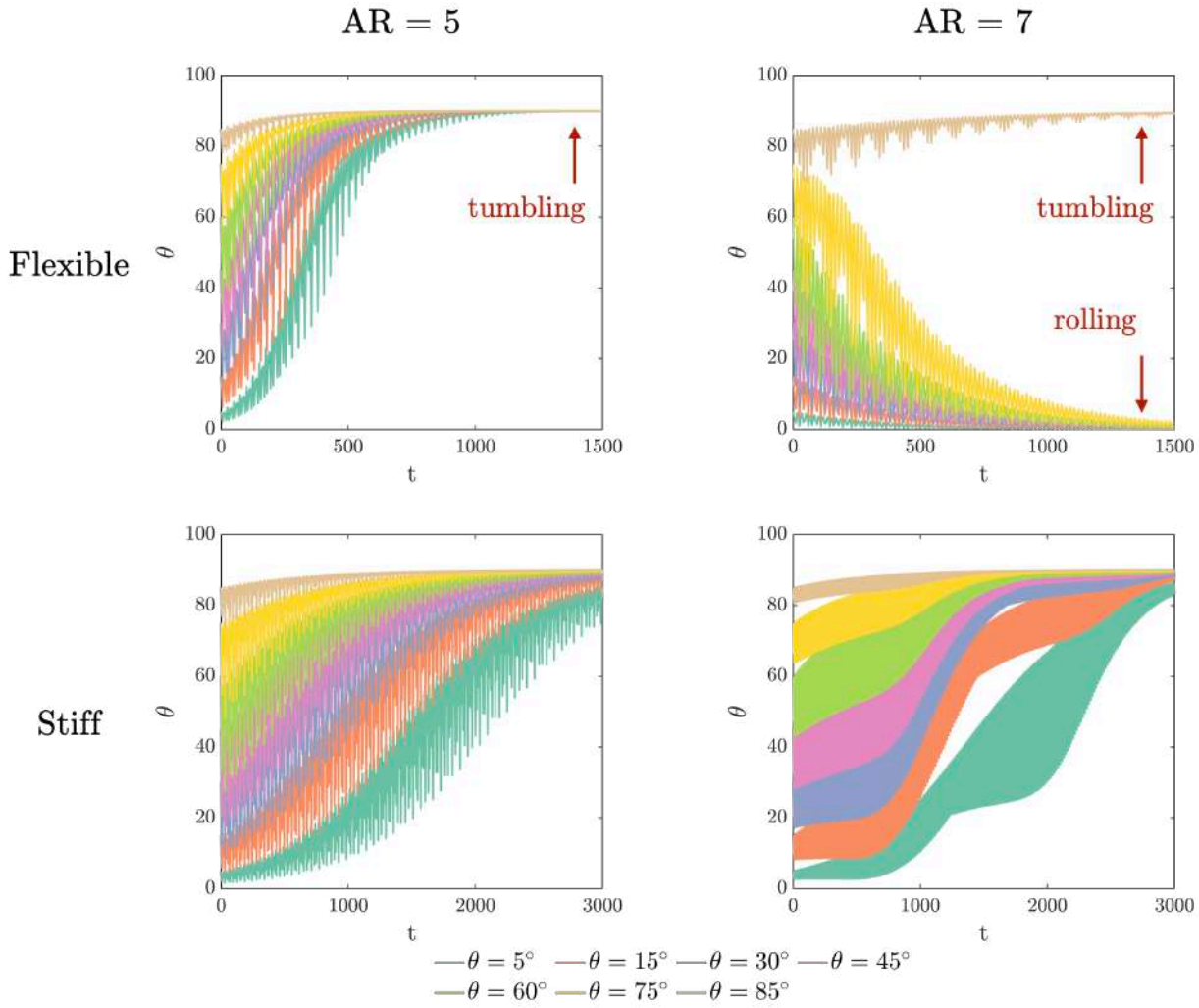


Figure 7.10: Evolution of angle θ for a fiber with different aspect ratios and flexibility tested with various initial orientations.

For flexible fiber, a small aspect ratio ($AR = 5$) shows a global attractor as $\theta = 90°$, which indicates all fibers end up tumbling. Interestingly, fiber with a relatively larger aspect ratio leads to a multiplicity in steady state dynamics. Only the initial condition $\theta = 85°$ becomes tumbling while all other conditions lead to rolling. For relatively stiff fibers, fibers with different initial orientations all become tumbling. Further investigation can be conducted to probe into this multiplicity arising from initial orientation.

8

Code

8.1 Code overview

We gave an overview of the base code for a sheet with an arbitrary rest shape placed in an arbitrary flow field. The source code is available from the Graham Group website, or you can contact the author and the author's thesis advisor. The C++ code applies **Armadillo** C++ library for linear algebra calculation and **HDF5** library for the output file. CMake is used to generate the makefile. Please check the availability of required libraries before compiling.

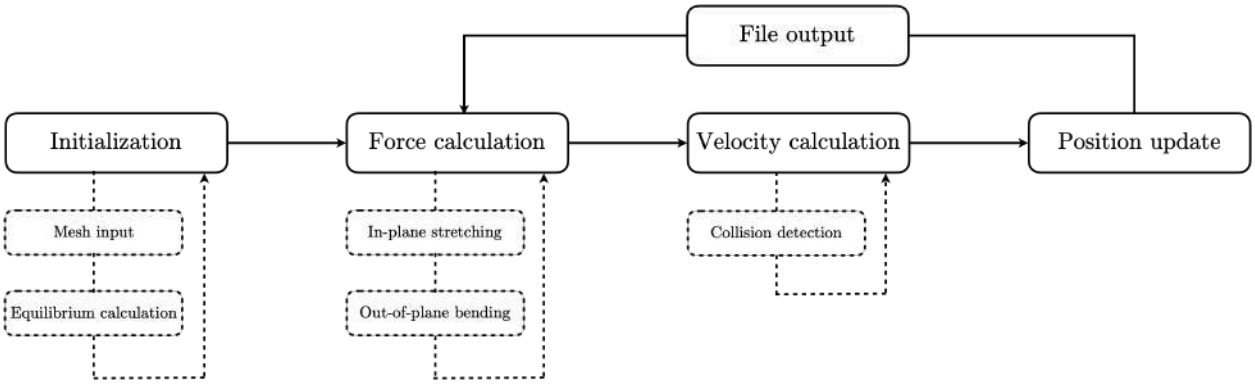


Figure 8.1: Overview of code structure.

The structure of the code follows the method described in Chapter 2 with two parts. The initialization part reads input files and calculates equilibrium statistics. The iterative

part follows the order of force evaluation based on current deformation, velocity calculation due to forces exerted on the fluids, position update, and file output. The code contains files listed in Table 8.1.

File	Functions
`sheet.h`	head file
`main.cpp`	main functions
`generate_initial`	functions to tune initial condition and generate equilibrium data
`cal_stretching.cpp`	functions to calculate in-plane stretching nodal forces
`cal_bending.cpp`	functions to calculate out-of-plane bending nodal forces
`cal_vel.cpp`	functions to calculate velocity with regularized Stokeslet method
`input.txt`	input file with lists of set parameters
`ref.h5`	input file with mesh position and triangulation information
`CMakeLists.txt`	CMake file for code compiling

Table 8.1: List of files and their functions.

After generating the makefile via CMake and compiling, the executable file `sheet` can be copied to a new folder. The folder to run a job requires to contain the following files:

- executable file `sheet`
- input file `input.txt`
- position and triangulation reference file `ref.h5`

The simulation begins by inputting the text file: `./sheet < input.txt` in terminal and the file `ref.h5` will be read automatically.

8.2 Code excerpt

8.2.1 Initialization

The code requires an input text file along with a reference file containing equilibrium position and triangulation. The rest shape can be arbitrary but with some restrictions:

- The mesh is required to base on triangular discretization.
- The solver regulates a maximum of 8 triangular elements meeting at one node.

The flow chart of initialization is visualized in Fig 8.2.

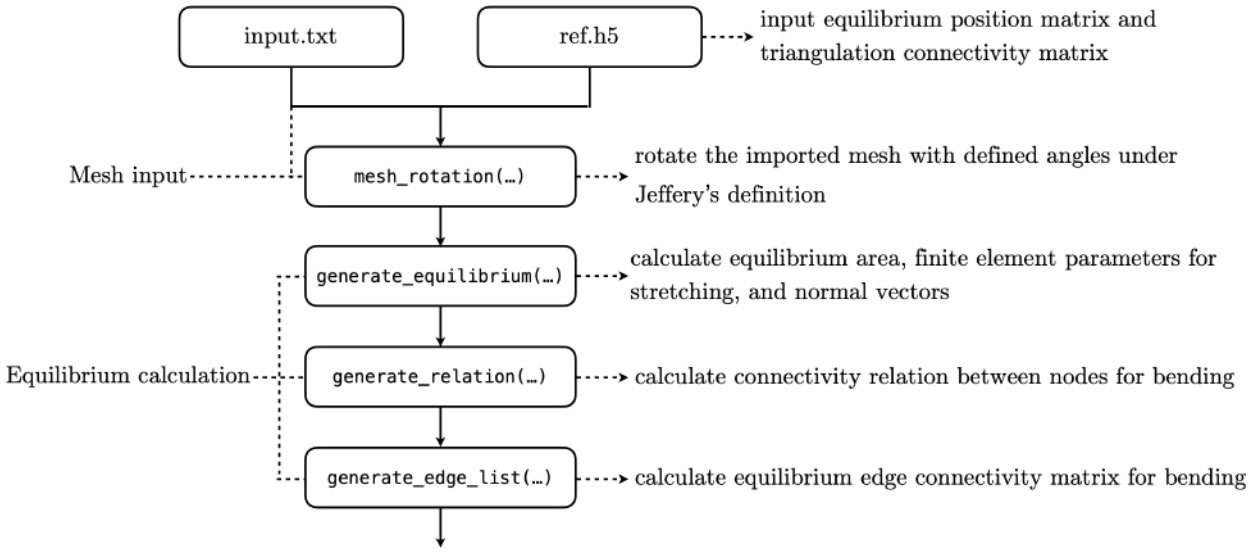


Figure 8.2: Code structure for initialization.

To start the simulation, we need to prepare two input files: `input.txt` and `ref.h5`. The former contains 16 parameters that describe the initial conditions, mechanical parameters, and time integration settings of the sheet. You need to make sure all the parameters are within a reasonable range. For example, a smaller time step is required for stiffer sheets otherwise the code will break. The latter file contains equilibrium mesh information that can be prepared by self-generation or mesh-generation software. The text file `input.txt` should have 16 rows, with each row defining a parameter. The code extracts the information into a vector and the parameters are assigned to the code as follows.

```
// read parameters from the input file (input.txt) into a vector var
vec var = read_input();

// read parameters from var
int restart = (int)var(0); // 1: continue a simulation; 0: start a new
    simulation
int file = (int)var(1); // the last file number to write output (e.g. if
    the last file is cap_000500.h5, put 500 to continue)

//initial orientation of sheet normal following Jeffery's definition
const double theta = PI*(var(2)/180.0); // rotation around x in degrees
const double phi = PI*(var(3)/180.0); // rotation around z in degrees
const double gamma = PI*(var(4)/180.0); // rotation around y in degrees
const double mag = var(5); // magnitude of initial random perturbation, 0
    means no perturbation

// mechanical properties
const double Ca = var(6); // Capillary number (dimensionless flow strength
    ), smaller Ca more rigid sheet
const double Ev = var(7); // Elastoviscous number (dimensionless bending
    modulus), smaller Ev stiffer sheet

const int membrane_type = var(8); // 0: neo-Hookean, 1: Yeoh
const double yeoh_c = var(9); // nonlinear parameter in hyperelastic model
    , larger means more strain-hardening, 0 means neo-Hookean

// flow condition
const int flow = (int)var(10); // -1: no flow, 0: biaxial, 1: uniaxial, 2:
     planar, 3: shear

// repulsive potential: only turn it on if you notice an intersection or
    edge cutting through the sheet surface
const int F_lj_control = (int)var(11); // 0: no repulsive potential, 1:
    with repulsive potential acting on a node with other nodes outside of
    its 3-ring neighborhood

// simulation setting
int step = (int)var(12); // total steps to run
const int save_step = (int)var(13); // save after save_step steps
const double max_dt = var(14); // maximum timestep possible
const int time_integral = var(15); // time integration method 0: forward
    Euler 1: RK4 2: RK2

int nnodes = pos.n_rows; // # of nodes
int ntris = tri.n_rows; // # of triangular elements
```

On the other hand, `ref.h5` file should include two matrices: a position matrix `pos` and a triangulation connectivity matrix `tri`, showing a sheet with *nnodes* nodes and *ntris* triangular elements. The position matrix `pos` has the dimension *nnodes* $\times$ 3, with each row representing the position of a node. The triangulation matrix `tri` owns the dimension

ntris $\times$ 3, with each row representing three node numbers of a specific triangular element.

The parameter `restart` and `file` allows simulations to continue based on previous results if `restart == 1`. If a continued simulation, it will reload the position matrix from the latest output file defined by `file`. Otherwise, it will begin a new simulation if `restart == 0`.

```
// check if restart, otherwise, read from last written file
if (restart == 1){
  sprintf(name, "cap_%06d.h5", file);
  status = pos.load(hdf5_name(name, "pos"));
  status = tri.load(hdf5_name(name, "tri"));
  status = t.load(hdf5_name(name, "t"));
  cout << "Reloading complete!" << endl;
}else{
  file = 0;

  // add perturbation to the sheet surface along the surface normal of
   each node. Only when you first run it!
  if (mag > 0){
    pos = add_perturb(mag, pos, normal.row(0), nnodes);
  }

  cout << "Initialization complete!" << endl;
}
```

8.2.2 Iterative calculation

The iterative calculation evolves the time forward based on the initial condition of the sheet. The related functions of the loop are shown below. For each iteration, the force evaluation is split into two parts: *in-plane stretching* force matrix `F_s` (*nnodes* $\times$ 3) and *out-of-plane bending* force matrix `F_b` (*nnodes* $\times$ 3), implemented via two functions below.

```
// evaluate nodal force
F_s = cal_stretching(pos, tri, eq_pos, area_eq, membrane_type, yeoh_c, Ca,
    A, B, nnodes, ntris);
F_b = cal_bending_simple(pos, tri, c_0, edge, Ev, nnodes, ntris);
F = F_s + F_b; // sum two forces together
```

We obtain a force matrix $\mathbf{F}$ with dimension *nnodes* $\times$ 3 that represents the force exerted by the sheet on the fluid. Based on this, we evaluate the perturbation velocity at the position of nodes due to those forces and combine the free velocity field to obtain the velocity on each node. The code below list gives three different velocity fields, which can be further modified to account for more complex scenarios.

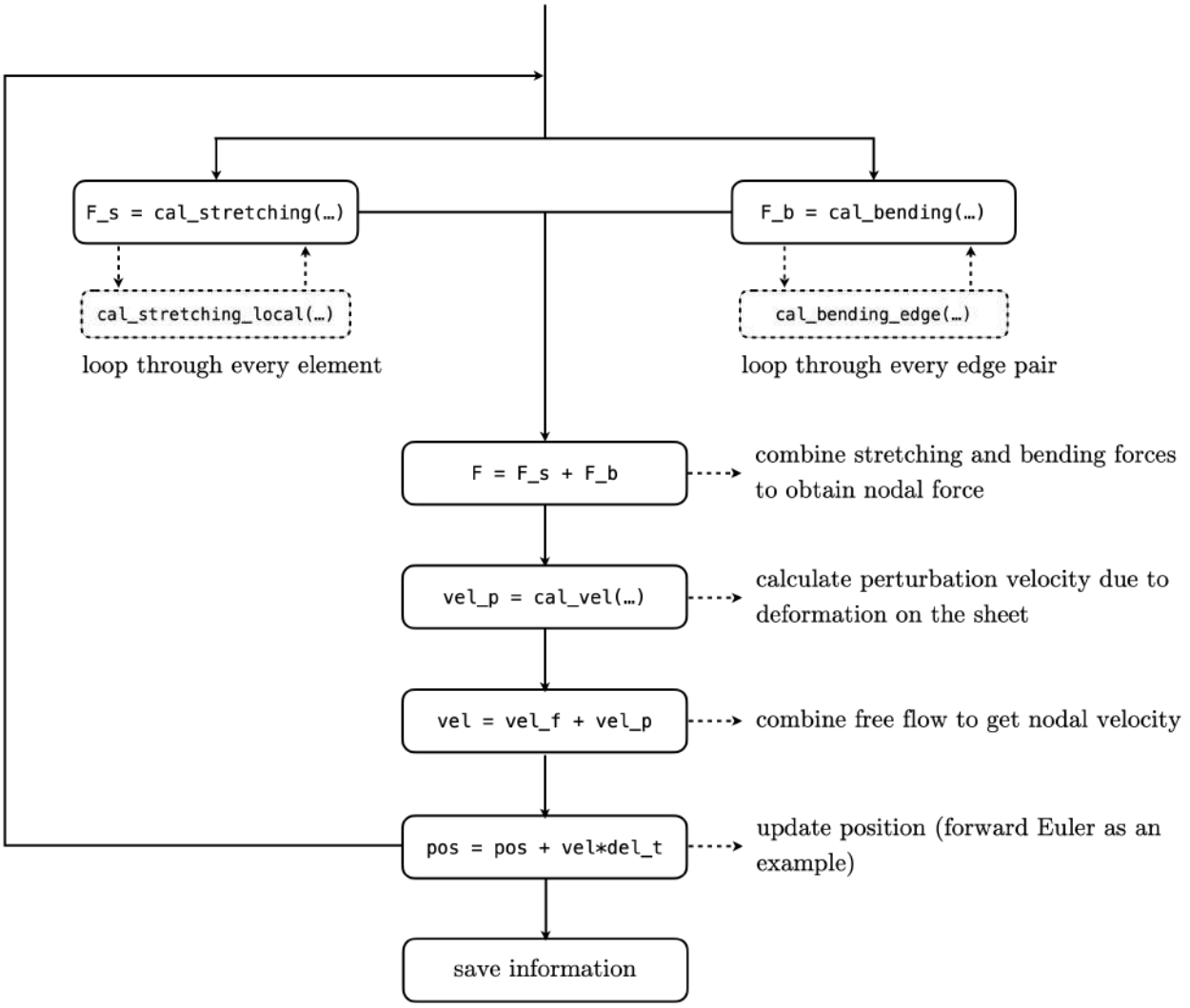


Figure 8.3: Code structure for the iterative process.

```
// evaluate perturbation velocity vel_p
vel_p = cal_vel(min, F, pos, nnn, nnodes, kappa, F_lj_control);

// set free flow velocity vel_f
if (flow == 0){ // biaxial extensional flow in x-y-z plane (0.5x,0.5y,-z)
  vel_f.col(0) = 0.5*pos.col(0);
  vel_f.col(1) = 0.5*pos.col(1);
  vel_f.col(2) = -pos.col(2);
} else if (flow == 1){ // uniaxial extensional flow in x-y-z plane (-0.5x
   ,-0.5y,z)
  vel_f.col(0) = -0.5*pos.col(0);
  vel_f.col(1) = -0.5*pos.col(1);
  vel_f.col(2) = pos.col(2);
} else if (flow == 2){ // planar extensional flow in x-y-z plane (x,0,-z)
  vel_f.col(0) = pos.col(0);
  vel_f.col(2) = -pos.col(2);
} else if (flow == 3){ // simple shear (y,0,0)
```

```
  vel_f.col(0) = pos.col(1);
} else { // static flow
  // doing nothing
}

// update velocity of nodes
vel = vel_f + vel_p;
```

We update the position of nodes either forward Euler or fourth-order Runge-Kutta method. The information can be saved occasionally depending on settings.

```
bool status;
// save data based on set save_step
if (remainder(step, save_step) == 0){
  sprintf(name, "cap_%06d.h5", file);
  status = pos.save(hdf5_name(name, "pos"));
  status = tri.save(hdf5_name(name, "tri", hdf5_opts::append));
  status = t.save(hdf5_name(name, "t", hdf5_opts::append));
  status = Fsave.save(hdf5_name(name, "Fsave", hdf5_opts::append));

  cout << "save to " << name << endl;
  if (status != 1){
    cout << "Problems with saving data!" << endl;
  }
  file++;
}
step--;
```

For post-processing, the information stored in output files (`cap_000000.h5` for example) can be extracted using MATLAB.

```
pos = h5read('cap_000000.h5','//pos');
tri = h5read('cap_000000.h5','//tri');
t = h5read('cap_000000.h5','//t');
F = h5read('cap_000000.h5','//Fsave');
```

References

[1] M. Abkarian, M. Faivre, and A. Viallat. Swinging of red blood cells under shear flow. *Physical Review Letters*, 98(18):188302, 2007.

[2] J. Ainley, S. Durkin, R. Embid, P. Boindala, and R. Cortez. The method of images for regularized Stokeslets. *Journal of Computational Physics*, 227(9):4600–4616, 2008.

[3] M. AlAmer, A. R. Lim, and Y. L. Joo. Continuous synthesis of structurally uniform graphene oxide materials in a model taylor–couette flow reactor. *Industrial & Engineering Chemistry Research*, 58(3):1167–1176, 2018.

[4] M. AlAmer, S. Zamani, K. Fok, A. Satish, A. R. Lim, and Y. L. Joo. Facile production of graphenic microsheets and their assembly via water-based, surfactant-aided mechanical deformations. *ACS Applied Materials & Interfaces*, 12(7):8944–8951, 2020.

[5] S. Alben and M. J. Shelley. Flapping states of a flag in an inviscid fluid: bistability and the transition to chaos. *Physical Review Letters*, 100(7):074301, 2008.

[6] C. Backes, D. Hanlon, B. M. Szydlowska, A. Harvey, R. J. Smith, T. M. Higgins, and J. N. Coleman. Preparation of liquid-exfoliated transition metal dichalcogenide nanosheets with controlled size and thickness: a state of the art protocol. *JoVE (Journal of Visualized Experiments)*, (118):e54806, 2016.

[7] K. Baek, G. Yun, Y. Kim, D. Kim, R. Hota, I. Hwang, D. Xu, Y. H. Ko, G. H. Gu, J. H. Suh, et al. Free-standing, single-monomer-thick two-dimensional polymers through covalent self-assembly in solution. *Journal of the American Chemical Society*, 135(17):6523–6528, 2013.

[8] P. Bagchi and R. M. Kalluri. Dynamics of nonspherical capsules in shear flow. *Physical Review E*, 80(1):016307, 2009.

[9] L. Becker, G. McKinley, and H. Stone. Sedimentation of a sphere near a plane wall: weak non-Newtonian and inertial effects. *Journal of Non-Newtonian Fluid Mechanics*, 63(2-3):201–233, 1996.

[10] T. Biben, A. Farutin, and C. Misbah. Three-dimensional vesicles under shear flow: Numerical study of dynamics and phase diagram. *Physical Review E*, 83(3):031921, 2011.

[11] A. Biria, M. Maleki, and E. Fried. Continuum theory for the edge of an open lipid bilayer. *Advances in Applied Mechanics*, 46:1–68, 2013.

[12] M. Bjornmalm, M. Faria, X. Chen, J. Cui, and F. Caruso. Dynamic flow impacts cell–particle interactions: sedimentation and particle shape effects. *Langmuir*, 32(42):10995–11001, 2016.

[13] J. R. Blake. A note on the image system for a Stokeslet in a no-slip boundary. In *Mathematical Proceedings of the Cambridge Philosophical Society*, volume 70, pages 303–310. Cambridge University Press, 1971.

[14] L. Botto. Toward nanomechanical models of liquid-phase exfoliation of layered 2d nanomaterials: Analysis of a π- peel model. *Frontiers in Materials*, 6:302, 2019.

[15] F. P. Bretherton. The motion of rigid particles in a shear flow at low reynolds number. *Journal of Fluid Mechanics*, 14(2):284–304, 1962.

[16] C. A. Brisbois and M. O. De La Cruz. Locomotion of magnetoelastic membranes in viscous fluids. *Physical Review Research*, 4(2):023166, 2022.

[17] M. Bukowicki and M. L. Ekiel-Jeżewska. Sedimenting pairs of elastic microfilaments. *Soft Matter*, 15(46):9405–9417, 2019.

[18] R. Capovilla and J. Guven. Stresses in lipid membranes. *Journal of Physics A: Mathematical and General*, 35(30):6233, 2002.

[19] R. Chajwa, N. Menon, and S. Ramaswamy. Kepler orbits in pairs of disks settling in a viscous fluid. *Physical Review Letters*, 122(22):224501, 2019.

[20] B. Chakrabarti, Y. Liu, J. LaGrone, R. Cortez, L. Fauci, O. Du Roure, D. Saintillan, and A. Lindner. Flexible filaments buckle into helicoidal shapes in strong compressional flows. *Nature Physics*, 16(6):689–694, 2020.

[21] J. Charrier, S. Shrivastava, and R. Wu. Free and constrained inflation of elastic membranes in relation to thermoforming—non-axisymmetric problems. *The Journal of Strain Analysis for Engineering Design*, 24(2):55–74, 1989.

[22] T.-P. Chen, C.-W. Lin, S.-S. Li, Y.-H. Tsai, C.-Y. Wen, W. J. Lin, F.-M. Hsiao, Y.-P. Chiu, K. Tsukagoshi, M. Osada, et al. Self-assembly atomic stacking transport layer of 2d layered titania for perovskite solar cells with extended uv stability. *Advanced Energy Materials*, 8(2):1701722, 2018.

[23] K.-Y. Chun, S. H. Kim, M. K. Shin, Y. T. Kim, G. M. Spinks, A. E. Aliev, R. H. Baughman, and S. J. Kim. Free-standing nanocomposites with high conductivity and extensibility. *Nanotechnology*, 24(16):165401, 2013.

[24] A. Ciesielski and P. Samorì. Graphene via sonication assisted liquid-phase exfoliation. *Chemical Society Reviews*, 43(1):381–398, 2014.

[25] J. N. Coleman, M. Lotya, A. O'Neill, S. D. Bergin, P. J. King, U. Khan, K. Young, A. Gaucher, S. De, R. J. Smith, et al. Two-dimensional nanosheets produced by liquid exfoliation of layered materials. *Science*, 331(6017):568–571, 2011.

[26] G. Corsi, A. De Simone, C. Maurini, and S. Vidoli. A neutrally stable shell in a stokes flow: a rotational taylor's sheet. *Proceedings of the Royal Society A*, 475(2227):20190178, 2019.

[27] R. Cortez. The method of regularized Stokeslets. *SIAM Journal on Scientific Computing*, 23(4):1204–1225, 2001.

[28] R. Cortez, L. Fauci, and A. Medovikov. The method of regularized Stokeslets in three dimensions: analysis, validation, and application to helical swimming. *Physics of Fluids*, 17(3):031504, 2005.

[29] R. Cortez and D. Varela. A general system of images for regularized stokeslets and other elements near a plane wall. *Journal of Computational Physics*, 285:41–54, 2015.

[30] D. Crowdy. Flipping and scooping of curved 2d rigid fibers in simple shear: The jeffery equations. *Physics of Fluids*, 28(5):053105, 2016.

[31] L. H. Cunha, J. Zhao, F. C. MacKintosh, and S. L. Biswal. Settling dynamics of brownian chains in viscous fluids. *Physical Review Fluids*, 7(3):034303, 2022.

[32] R. Das, R. Bandyopadhyay, and P. Pramanik. Carbon quantum dots from natural resource: A review. *Materials Today Chemistry*, 8:96–109, 2018.

[33] A. Dato, V. Radmilovic, Z. Lee, J. Phillips, and M. Frenklach. Substrate-free gas-phase synthesis of graphene sheets. *Nano letters*, 8(7):2012–2016, 2008.

[34] D. Day, H. Hub, and H. Ringsdorf. Polymerization of mono-and bi-functional diacetylene derivatives in monolayers at the gas–water interface. *Israel Journal of Chemistry*, 18(3-4):325–329, 1979.

[35] P. De Gennes. Coil-stretch transition of dilute flexible polymers under ultrahigh velocity gradients. *The Journal of Chemical Physics*, 60(12):5030–5042, 1974.

[36] R. Dong, T. Zhang, and X. Feng. Interface-assisted synthesis of 2d materials: trend and challenges. *Chemical Reviews*, 118(13):6189–6235, 2018.

[37] O. Du Roure, A. Lindner, E. N. Nazockdast, and M. J. Shelley. Dynamics of flexible fibers in viscous flows and fluids. *Annual Review of Fluid Mechanics*, 51:539–572, 2019.

[38] J. Dupire, M. Socol, and A. Viallat. Full dynamics of a red blood cell in shear flow. *Proceedings of the National Academy of Sciences*, 109(51):20808–20813, 2012.

[39] S. Dutta and M. D. Graham. Dynamics of miura-patterned foldable sheets in shear flow. *Soft matter*, 13(14):2620–2633, 2017.

[40] S. Dutta and M. D. Graham. Dynamics of miura-patterned foldable sheets in shear flow. *Soft Matter*, 13(14):2620–2633, 2017.

[41] X.-J. Fan, R. B. Bird, and M. Renardy. Configuration-dependent friction coefficients and elastic dumbbell rheology. *Journal of Non-Newtonian Fluid Mechanics*, 18(3):255–272, 1985.

[42] D. A. Fedosov. *Multiscale modeling of blood flow and soft matter*. Citeseer, 2010.

[43] D. A. Fedosov, B. Caswell, and G. E. Karniadakis. Systematic coarse-graining of spectrin-level red blood cell models. *Computer Methods in Applied Mechanics and Engineering*, 199(29-32):1937–1948, 2010.

[44] L. Fei, B. P. Williams, S. H. Yoo, J. Kim, G. Shoorideh, and Y. L. Joo. Graphene folding in si rich carbon nanofibers for highly stable, high capacity li-ion battery anodes. *ACS Applied Materials & Interfaces*, 8(8):5243–5250, 2016.

[45] A. W. Feinberg, A. Feigel, S. S. Shevkoplyas, S. Sheehy, G. M. Whitesides, and K. K. Parker. Muscular thin films for building actuators and powering devices. *Science*, 317(5843):1366–1370, 2007.

[46] O. Forgacs and S. Mason. Particle motions in sheared suspensions: X. orbits of flexible threadlike particles. *Journal of Colloid Science*, 14(5):473–491, 1959.

[47] G. Fuller and L. Leal. The effects of conformation-dependent friction and internal viscosity on the dynamics of the nonlinear dumbbell model for a dilute polymer solution. *Journal of Non-Newtonian Fluid Mechanics*, 8(3-4):271–310, 1981.

[48] A. K. Gaharwar, S. A. Dammu, J. M. Canter, C.-J. Wu, and G. Schmidt. Highly extensible, tough, and elastomeric nanocomposite hydrogels from poly (ethylene glycol) and hydroxyapatite nanoparticles. *Biomacromolecules*, 12(5):1641–1650, 2011.

[49] H. Goldsmith, J. Marlow, and F. C. MacIntosh. Flow behaviour of erythrocytes-i. rotation and deformation in dilute suspensions. *Proceedings of the Royal Society of London. Series B. Biological Sciences*, 182(1068):351–384, 1972.

[50] M. D. Graham. *Microhydrodynamics, Brownian Motion, and Complex Fluids*, volume 58. Cambridge University Press, 2018.

[51] S. Gravelle, C. Kamal, and L. Botto. Liquid exfoliation of multilayer graphene in sheared solvents: A molecular dynamics investigation. *The Journal of Chemical Physics*, 152(10):104701, 2020.

[52] M. Gruziel, K. Thyagarajan, G. Dietler, A. Stasiak, M. L. Ekiel-Jeżewska, and P. Szymczak. Periodic motion of sedimenting flexible knots. *Physical Review Letters*, 121(12):127801, 2018.

[53] M. Gruziel-Słomka, P. Kondratiuk, P. Szymczak, and M. L. Ekiel-Jeżewska. Stokesian dynamics of sedimenting elastic rings. *Soft Matter*, 15(36):7262–7274, 2019.

[54] A. Guckenberger and S. Gekle. Theory and algorithms to compute helfrich bending forces: A review. *Journal of Physics: Condensed Matter*, 29(20):203001, 2017.

[55] J. Happel and H. Brenner. *Low Reynolds number hydrodynamics: with special applications to particulate media*, volume 1. Springer Science & Business Media, 1983.

[56] M. Harasim, B. Wunderlich, O. Peleg, M. Kröger, and A. R. Bausch. Direct observation of the dynamics of semiflexible polymers in shear flow. *Physical Review Letters*, 110(10):108302, 2013.

[57] P. He, A. J. Katan, L. Tubiana, C. Dekker, and D. Michieletto. Single-molecule structure and topology of kinetoplast dna networks. *Physical Review X*, 13(2):021010, 2023.

[58] Y. Hernandez, V. Nicolosi, M. Lotya, F. M. Blighe, Z. Sun, S. De, I. T. McGovern, B. Holland, M. Byrne, Y. K. Gun'Ko, et al. High-yield production of graphene by liquid-phase exfoliation of graphite. *Nature Nanotechnology*, 3(9):563–568, 2008.

[59] J. P. Hernández-Ortiz, J. J. de Pablo, and M. D. Graham. Fast computation of many-particle hydrodynamic and electrostatic interactions in a confined geometry. *Physical review letters*, 98(14):140602, 2007.

[60] E. Hinch. Mechanical models of dilute polymer solutions in strong flows. *The Physics of Fluids*, 20(10):S22–S30, 1977.

[61] X. Huang, Z. Huang, Q. Liu, A. Zhou, Y. Ma, J. Wang, H. Qiu, and H. Bai. Organic solvent-assisted lyophilization: A universal method of preparing two-dimensional material nanoscrolls. *ACS Omega*, 4(4):7420–7427, 2019.

[62] A. M. Hubbard, R. W. Mailen, M. A. Zikry, M. D. Dickey, and J. Genzer. Controllable curvature from planar polymer sheets in response to light. *Soft Matter*, 13(12):2299–2308, 2017.

[63] M. Jamal, A. M. Zarafshar, and D. H. Gracias. Differentially photo-crosslinked polymers enable self-assembling microfluidics. *Nature Communications*, 2(1):1–6, 2011.

[64] G. B. Jeffery. The motion of ellipsoidal particles immersed in a viscous fluid. *Proceedings of the Royal Society of London. Series A, Containing papers of a mathematical and physical character*, 102(715):161–179, 1922.

[65] L. Jianzhong, S. Xing, and Y. Zhenjiang. Effects of the aspect ratio on the sedimentation of a fiber in Newtonian fluids. *Journal of Aerosol Science*, 34(7):909–921, 2003.

[66] S. Jing, H. Jiang, Y. Hu, and C. Li. Graphene supported mesoporous single crystal silicon on cu foam as a stable lithium-ion battery anode. *Journal of Materials Chemistry A*, 2(39):16360–16364, 2014.

[67] C. Kamal, S. Gravelle, and L. Botto. Hydrodynamic slip can align thin nanoplatelets in shear flow. *Nature Communications*, 11(1):1–10, 2020.

[68] C. Kamal, S. Gravelle, and L. Botto. Alignment of a flexible platelike particle in shear flow: Effect of surface slip and edges. *Physical Review Fluids*, 6(8):084102, 2021.

[69] C. Kamal, S. Gravelle, and L. Botto. Effect of hydrodynamic slip on the rotational dynamics of a thin brownian platelet in shear flow. *Journal of Fluid Mechanics*, 919:A1, 2021.

[70] V. Kantsler, E. Segre, and V. Steinberg. Critical dynamics of vesicle stretching transition in elongational flow. *Physical review letters*, 101(4):048101, 2008.

[71] V. Kantsler and V. Steinberg. Orientation and dynamics of a vesicle in tank-treading motion in shear flow. *Physical Review Letters*, 95(25):258101, 2005.

[72] S. Keuleyan, M. Wang, F. R. Chung, J. Commons, and K. J. Koski. A silicon-based two-dimensional chalcogenide: growth of si2te3 nanoribbons and nanoplates. *Nano Letters*, 15(4):2285–2290, 2015.

[73] B. Kim, S. B. Lee, J. Lee, S. Cho, H. Park, S. Yeom, and S. H. Park. A comparison among neo-hookean model, mooney-rivlin model, and ogden model for chloroprene rubber. *International Journal of Precision Engineering and Manufacturing*, 13:759–764, 2012.

[74] S. Y. Kim, K. S. Yang, and B.-H. Kim. Improving the microstructure and electrochemical performance of carbon nanofibers containing graphene-wrapped silicon nanoparticles as a li-ion battery anode. *Journal of Power Sources*, 273:404–412, 2015.

[75] Y. S. Kim, K. W. Kim, D. Cho, N. S. Hansen, J. Lee, and Y. L. Joo. Silicon-rich carbon hybrid nanofibers from water-based spinning: The synergy between silicon and carbon for li-ion battery anode application. *ChemElectroChem*, 1(1):220–226, 2014.

[76] A. R. Klotz, B. W. Soh, and P. S. Doyle. Equilibrium structure and deformation response of 2d kinetoplast sheets. *Proceedings of the National Academy of Sciences*, 117(1):121–127, 2020.

[77] J. Kong, W. A. Yee, Y. Wei, L. Yang, J. M. Ang, S. L. Phua, S. Y. Wong, R. Zhou, Y. Dong, X. Li, et al. Silicon nanoparticles encapsulated in hollow graphitized carbon nanofibers for lithium ion battery anodes. *Nanoscale*, 5(7):2967–2973, 2013.

[78] M. J. Kory, M. Wörle, T. Weber, P. Payamyar, S. W. Van De Poll, J. Dshemuchadse, N. Trapp, and A. D. Schlüter. Gram-scale synthesis of two-dimensional polymer crystals and their structure analysis by x-ray diffraction. *Nature chemistry*, 6(9):779–784, 2014.

[79] A. Kumar and M. D. Graham. Accelerated boundary integral method for multiphase flow in non-periodic geometries. *Journal of Computational Physics*, 231(20):6682–6713, Aug. 2012.

[80] D. Kumar, C. M. Richter, and C. M. Schroeder. Conformational dynamics and phase behavior of lipid vesicles in a precisely controlled extensional flow. *Soft Matter*, 16(2):337–347, 2020.

[81] M. C. Lagomarsino, I. Pagonabarraga, and C. Lowe. Hydrodynamic induced deformation and orientation of a microscopic elastic filament. *Physical review letters*, 94(14):148104, 2005.

[82] J. LaGrone, R. Cortez, W. Yan, and L. Fauci. Complex dynamics of long, flexible fibers in shear. *Journal of Non-Newtonian Fluid Mechanics*, 269:73–81, 2019.

[83] Z. Lai, Y. Chen, C. Tan, X. Zhang, and H. Zhang. Self-assembly of two-dimensional nanosheets into one-dimensional nanostructures. *Chem*, 1(1):59–77, 2016.

[84] E. Lauga and T. R. Powers. The hydrodynamics of swimming microorganisms. *Reports on progress in physics*, 72(9):096601, 2009.

[85] P. LeDuc, C. Haber, G. Bao, and D. Wirtz. Dynamics of individual flexible polymers in a shear flow. *Nature*, 399(6736):564–566, 1999.

[86] B.-J. Lee, H.-Y. Yu, and G.-H. Jeong. Controlled synthesis of monolayer graphene toward transparent flexible conductive film application. *Nanoscale research letters*, 5:1768–1773, 2010.

[87] D. Y. Lee, J. T. Pham, J. Lawrence, C. H. Lee, C. Parkos, T. Emrick, and A. J. Crosby. Macroscopic nanoparticle ribbons and fabrics. *Advanced materials*, 25(9):1248–1253, 2013.

[88] O.-S. Lee and M. A. Carignano. Exfoliation of electrolyte-intercalated graphene: molecular dynamics simulation study. *The Journal of Physical Chemistry C*, 119(33):19415–19422, 2015.

[89] F. Y. Leong. Stability of solvated nanosheet in shear flow. *Applied Physics Letters*, 97(21):214102, 2010.

[90] T. G. Leong, B. R. Benson, E. K. Call, and D. H. Gracias. Thin film stress driven self-folding of microstructured containers. *Small*, 4(10):1605–1609, 2008.

[91] L. Li, H. Manikantan, D. Saintillan, and S. E. Spagnolie. The sedimentation of flexible filaments. *Journal of Fluid Mechanics*, 735:705–736, 2013.

[92] Y. Liang, Y. Li, H. Wang, and H. Dai. Strongly coupled inorganic/nanocarbon hybrid materials for advanced electrocatalysis. *Journal of the American Chemical Society*, 135(6):2013–2036, 2013.

[93] S. B. Lindström and T. Uesaka. Simulation of the motion of flexible fibers in viscous fluid flow. *Physics of Fluids*, 19(11):113307, 2007.

[94] J. Liu, C. Chen, C. He, J. Zhao, X. Yang, and H. Wang. Synthesis of graphene peroxide and its application in fabricating super extensible and highly resilient nanocomposite hydrogels. *ACS nano*, 6(9):8194–8202, 2012.

[95] J. Liu, W. Zan, K. Li, Y. Yang, F. Bu, and Y. Xu. Solution synthesis of semiconducting two-dimensional polymer via trimerization of carbonitrile. *Journal of the American Chemical Society*, 139(34):11666–11669, 2017.

[96] T. W. Liu. Flexible polymer chain dynamics and rheological properties in steady flows. *The Journal of chemical physics*, 90(10):5826–5842, 1989.

[97] X. Liu, T. H. Metcalf, J. T. Robinson, B. H. Houston, and F. Scarpa. Shear modulus of monolayer graphene prepared by chemical vapor deposition. *Nano Letters*, 12(2):1013–1017, 2012.

[98] Y. Liu, B. Chakrabarti, D. Saintillan, A. Lindner, and O. Du Roure. Morphological transitions of elastic filaments in shear flow. *Proceedings of the National Academy of Sciences*, 115(38):9438–9443, 2018.

[99] Y. Liu, J. Genzer, and M. D. Dickey. "2D or not 2D": Shape-programming polymer sheets. *Progress in Polymer Science*, 52:79–106, 2016.

[100] Y. Liu, Z. Xu, W. Gao, Z. Cheng, and C. Gao. Graphene and other 2d colloids: liquid crystals and macroscopic fibers. *Advanced Materials*, 29(14):1606794, 2017.

[101] J. Lukes, D. Lys Guilbride, J. Votypka, A. Zikova, R. Benne, and P. T. Englund. Kinetoplast dna network: evolution of an improbable structure. *Eukaryotic cell*, 1(4):495–502, 2002.

[102] M. Makino and M. Doi. Sedimentation of a particle with translation–rotation coupling. *Journal of the Physical Society of Japan*, 72(11):2699–2701, 2003.

[103] B. Marchetti, V. Raspa, A. Lindner, O. Du Roure, L. Bergougnoux, É. Guazzelli, and C. Duprat. Deformation of a flexible fiber settling in a quiescent viscous fluid. *Physical Review Fluids*, 3(10):104102, 2018.

[104] D. Matsunaga, Y. Imai, C. Wagner, and T. Ishikawa. Reorientation of a single red blood cell during sedimentation. *Journal of Fluid Mechanics*, 806:102–128, 2016.

[105] R. Matsuoka, R. Sakamoto, K. Hoshiko, S. Sasaki, H. Masunaga, K. Nagashio, and H. Nishihara. Crystalline graphdiyne nanosheets produced at a gas/liquid or liquid/liquid interface. *Journal of the American Chemical Society*, 139(8):3145–3152, 2017.

[106] S. M. Mehta, T. Jin, I. Stanciulescu, and K. J. Grande-Allen. Engineering biologically extensible hydrogels using photolithographic printing. *Acta Biomaterialia*, 75:52–62, 2018.

[107] Q. Meng and J. J. Higdon. Large scale dynamic simulation of plate-like particle suspensions. part i: Non-brownian simulation. *Journal of Rheology*, 52(1):1–36, 2008.

[108] Q. Meng and J. J. Higdon. Large scale dynamic simulation of plate-like particle suspensions. part ii: Brownian simulation. *Journal of Rheology*, 52(1):37–65, 2008.

[109] C. Misbah. Vacillating breathing and tumbling of vesicles under shear flow. *Physical Review Letters*, 96(2):028104, 2006.

[110] W. H. Mitchell and S. E. Spagnolie. Sedimentation of spheroidal bodies near walls in viscous fluids: glancing, reversing, tumbling and sliding. *Journal of Fluid Mechanics*, 772:600–629, 2015.

[111] T. D. Montenegro-Johnson, L. Koens, and E. Lauga. Microscale flow dynamics of ribbons and sheets. *Soft matter*, 13(3):546–553, 2017.

[112] B. Moths and T. Witten. Full alignment of colloidal objects by programmed forcing. *Physical Review Letters*, 110(2):028301, 2013.

[113] R. D. Mukhopadhyay, V. K. Praveen, A. Hazra, T. K. Maji, and A. Ajayaghosh. Light driven mesoscale assembly of a coordination polymeric gelator into flowers and stars with distinct properties. *Chemical Science*, 6(11):6583–6591, 2015.

[114] J.-H. Na, A. A. Evans, J. Bae, M. C. Chiappelli, C. D. Santangelo, R. J. Lang, T. C. Hull, and R. C. Hayward. Programming reversibly self-folding origami with micropatterned photo-crosslinkable polymer trilayers. *Advanced Materials*, 27(1):79–85, 2015.

[115] M. H. Nafar Sefiddashti, B. J. Edwards, and B. Khomami. Communication: A coil-stretch transition in planar elongational flow of an entangled polymeric melt. *The Journal of Chemical Physics*, 148(14):141103, 2018.

[116] M. H. Nafar Sefiddashti, B. J. Edwards, and B. Khomami. Communication: A coil-stretch transition in planar elongational flow of an entangled polymeric melt. *The Journal of chemical physics*, 148(14):141103, 2018.

[117] V. Narsimhan, A. P. Spann, and E. S. Shaqfeh. Pearling, wrinkling, and buckling of vesicles in elongational flows. *Journal of Fluid Mechanics*, 777:1–26, 2015.

[118] J. C. Nawroth, H. Lee, A. W. Feinberg, C. M. Ripplinger, M. L. McCain, A. Grosberg, J. O. Dabiri, and K. K. Parker. A tissue-engineered jellyfish with biomimetic propulsion. *Nature biotechnology*, 30(8):792–797, 2012.

[119] H. C.-H. Ng, A. Corker, E. García-Tuñón, and R. J. Poole. Go caber: Capillary breakup and steady-shear experiments on aqueous graphene oxide (go) suspensions. *Journal of Rheology*, 64(1):81–93, 2020.

[120] F. T. Nguyen and M. D. Graham. Buckling instabilities and complex trajectories in a simple model of uniflagellar bacteria. *Biophysical Journal*, 112(5):1010–1022, 2017.

[121] F. T. Nguyen and M. D. Graham. Impacts of multiflagellarity on stability and speed of bacterial locomotion. *Physical Review E*, 98(4):042419, 2018.

[122] H.-N. Nguyen and R. Cortez. Reduction of the regularization error of the method of regularized stokeslets for a rigid object immersed in a three-dimensional stokes flow. *Communications in Computational Physics*, 15(1):126–152, 2014.

[123] B. Ni, M. Huang, Z. Chen, Y. Chen, C.-H. Hsu, Y. Li, D. Pochan, W.-B. Zhang, S. Z. Cheng, and X.-H. Dong. Pathway toward large two-dimensional hexagonally patterned colloidal nanosheets in solution. *Journal of the American Chemical Society*, 137(4):1392–1395, 2015.

[124] D. Ni, H. Shi, and Y. Yin. Theoretical analysis of adhering lipid vesicles with free edges. *Colloids and Surfaces B: Biointerfaces*, 46(3):162–168, 2005.

[125] V. Nicolosi, M. Chhowalla, M. G. Kanatzidis, M. S. Strano, and J. N. Coleman. Liquid exfoliation of layered materials. *Science*, 340(6139):1226419, 2013.

[126] I. Nitsan, S. Drori, Y. E. Lewis, S. Cohen, and S. Tzlil. Mechanical communication in cardiac cell synchronized beating. *Nature Physics*, 12(5):472–477, 2016.

[127] K. S. Novoselov, A. K. Geim, S. V. Morozov, D.-e. Jiang, Y. Zhang, S. V. Dubonos, I. V. Grigorieva, and A. A. Firsov. Electric field effect in atomically thin carbon films. *science*, 306(5696):666–669, 2004.

[128] V. Pappu and P. Bagchi. 3D computational modeling and simulation of leukocyte rolling adhesion and deformation. *Comput Biol Med*, 38(6):738–753, Jan. 2008.

[129] J. U. Park, J. L. Kim, D. H. Kim, K. H. Ahn, S. J. Lee, and K. S. Cho. Rheological behavior of polymer/layered silicate nanocomposites under uniaxial extensional flow. *Macromolecular research*, 14(3):318–323, 2006.

[130] S.-J. Park, M. Gazzola, K. S. Park, S. Park, V. Di Santo, E. L. Blevins, J. U. Lind, P. H. Campbell, S. Dauth, A. K. Capulli, et al. Phototactic guidance of a tissue-engineered soft-robotic ray. *Science*, 353(6295):158–162, 2016.

[131] P. Payamyar, B. T. King, H. C. Öttinger, and A. D. Schlüter. Two-dimensional polymers: concepts and perspectives. *Chemical Communications*, 52(1):18–34, 2016.

[132] M. Peltomäki and G. Gompper. Sedimentation of single red blood cells. *Soft Matter*, 9(34):8346–8358, 2013.

[133] H. Perrin, H. Li, and L. Botto. Hydrodynamic interactions change the buckling threshold of parallel flexible sheets in shear flow. *arXiv preprint arXiv:2303.05282*, 2023.

[134] M. P. Petrich, D. L. Koch, and C. Cohen. An experimental determination of the stress–microstructure relationship in semi-concentrated fiber suspensions. *Journal of Non-Newtonian Fluid Mechanics*, 95(2-3):101–133, 2000.

[135] P. Poulin, R. Jalili, W. Neri, F. Nallet, T. Divoux, A. Colin, S. H. Aboutalebi, G. Wallace, and C. Zakri. Superflexibility of graphene oxide. *Proceedings of the National Academy of Sciences*, 113(40):11088–11093, 2016.

[136] M. Puig-de Morales-Marinkovic, K. T. Turner, J. P. Butler, J. J. Fredberg, and S. Suresh. Viscoelasticity of the human red blood cell. *American Journal of Physiology-Cell Physiology*, 293(2):C597–C605, 2007.

[137] C. Py, P. Reverdy, L. Doppler, J. Bico, B. Roman, and C. N. Baroud. Capillarity induced folding of elastic sheets. *The European Physical Journal Special Topics*, 166:67–71, 2009.

[138] B. Rallabandi, B. Saintyves, T. Jules, T. Salez, C. Schönecker, L. Mahadevan, and H. A. Stone. Rotation of an immersed cylinder sliding near a thin elastic coating. *Physical Review Fluids*, 2(7):074102, 2017.

[139] H. Rehage, E. Schnabel, and M. Veyssié. Rheological properties of two-dimensional model networks. *Die Makromolekulare Chemie: Macromolecular Chemistry and Physics*, 189(10):2395–2408, 1988.

[140] L. Ricotti, B. Trimmer, A. W. Feinberg, R. Raman, K. K. Parker, R. Bashir, M. Sitti, S. Martel, P. Dario, and A. Menciassi. Biohybrid actuators for robotics: A review of devices actuated by living cells. *Science robotics*, 2(12):eaaq0495, 2017.

[141] J. A. Rogers, M. G. Lagally, and R. G. Nuzzo. Synthesis, assembly and applications of semiconductor nanomembranes. *Nature*, 477(7362):45, 2011.

[142] J. Rotne and S. Prager. Variational treatment of hydrodynamic interaction in polymers. *The Journal of Chemical Physics*, 50(11):4831–4837, 1969.

[143] W. Russel, E. Hinch, L. G. Leal, and G. Tieffenbruck. Rods falling near a vertical wall. *Journal of Fluid Mechanics*, 83(2):273–287, 1977.

[144] G. Saggiorato, J. Elgeti, R. G. Winkler, and G. Gompper. Conformations, hydrodynamic interactions, and instabilities of sedimenting semiflexible filaments. *Soft matter*, 11(37):7337–7344, 2015.

[145] H. Sahabudeen, H. Qi, B. A. Glatz, D. Tranca, R. Dong, Y. Hou, T. Zhang, C. Kuttner, T. Lehnert, G. Seifert, et al. Wafer-sized multifunctional polyimine-based two-dimensional conjugated polymers with high mechanical stiffness. *Nature Communications*, 7(1):13461, 2016.

[146] D. Saintillan, E. Darve, and E. S. Shaqfeh. A smooth particle-mesh Ewald algorithm for stokes suspension simulations: The sedimentation of fibers. *Physics of Fluids*, 17(3), 2005.

[147] B. Saintyves, T. Jules, T. Salez, and L. Mahadevan. Self-sustained lift and low friction via soft lubrication. *Proceedings of the National Academy of Sciences*, 113(21):5847–5849, 2016.

[148] T. Salez and L. Mahadevan. Elastohydrodynamics of a sliding, spinning and sedimenting cylinder near a soft wall. *Journal of Fluid Mechanics*, 779:181–196, 2015.

[149] G. Salussolia, E. Barbieri, N. M. Pugno, and L. Botto. Micromechanics of liquid-phase exfoliation of a layered 2d material: A hydrodynamic peeling model. *Journal of the Mechanics and Physics of Solids*, 134:103764, 2020.

[150] G. Salussolia, C. Kamal, J. Stafford, N. Pugno, and L. Botto. Simulation of interacting elastic sheets in shear flow: Insights into buckling, sliding, and reassembly of graphene nanosheets in sheared liquids. *Physics of Fluids*, 34(5):053311, 2022.

[151] C. M. Schroeder, H. P. Babcock, E. S. Shaqfeh, and S. Chu. Observation of polymer conformation hysteresis in extensional flow. *Science*, 301(5639):1515–1519, 2003.

[152] C. M. Schroeder, R. E. Teixeira, E. S. Shaqfeh, and S. Chu. Characteristic periodic motion of polymers in shear flow. *Physical Review Letters*, 95(1):018301, 2005.

[153] T. A. Shapiro and P. T. Englund. The structure and replication of kinetoplast dna. *Annual Review of Microbiology*, 49(1):117–143, 1995.

[154] H. Shashank, Y. Melikhov, and M. L. Ekiel-Jeżewska. Dynamics of ball chains and highly elastic fibres settling under gravity in a viscous fluid. *Soft Matter*, 2023.

[155] M. J. Shelley and J. Zhang. Flapping and bending bodies interacting with fluid flows. *Annual Review of Fluid Mechanics*, 43:449–465, 2011.

[156] K. S. Silmore, M. S. Strano, and J. W. Swan. Buckling, crumpling, and tumbling of semiflexible sheets in simple shear flow. *Soft Matter*, 17(18):4707–4718, 2021.

[157] K. S. Silmore, M. S. Strano, and J. W. Swan. Thermally fluctuating, semiflexible sheets in simple shear flow. *Soft Matter*, 18(4):768–782, 2022.

[158] P. Singh and D. Joseph. Sedimentation of a sphere near a vertical wall in an Oldroyd-B fluid. *Journal of Non-Newtonian Fluid Mechanics*, 94(2-3):179–203, 2000.

[159] K. Sinha and M. D. Graham. Dynamics of a single red blood cell in simple shear flow. *Physical Review E*, 92(4):042710, 2015.

[160] R. Skalak, A. Tozeren, R. Zarda, and S. Chien. Strain energy function of red blood cell membranes. *Biophysical journal*, 13(3):245–264, 1973.

[161] A. M. Słowicka, H. A. Stone, and M. L. Ekiel-Jeżewska. Flexible fibers in shear flow approach attracting periodic solutions. *Physical Review E*, 101(2):023104, 2020.

[162] S. So and R. C. Hayward. Tunable upper critical solution temperature of poly (n-isopropylacrylamide) in ionic liquids for sequential and reversible self-folding. *ACS Applied Materials & Interfaces*, 9(18):15785–15790, 2017.

[163] S. So and R. C. Hayward. Tunable upper critical solution temperature of poly (n-isopropylacrylamide) in ionic liquids for sequential and reversible self-folding. *ACS Applied Materials & Interfaces*, 9(18):15785–15790, 2017.

[164] B. W. Soh and P. S. Doyle. Deformation response of catenated dna networks in a planar elongational field. *ACS Macro Letters*, 9(7):944–949, 2020.

[165] R. Stocker. Reverse and flick: Hybrid locomotion in bacteria. *Proceedings of the National Academy of Sciences*, 108(7):2635–2636, 2011.

[166] R. Tanner. Stresses in dilute solutions of bead-nonlinear-spring macromolecules. iii. friction coefficient varying with dumbbell extension. *Transactions of the Society of Rheology*, 19(4):557–582, 1975.

[167] G. I. Taylor. Viii. stability of a viscous liquid contained between two rotating cylinders. *Philosophical Transactions of the Royal Society of London. Series A, Containing Papers of a Mathematical or Physical Character*, 223(605-615):289–343, 1923.

[168] G. I. Taylor. Analysis of the swimming of microscopic organisms. *Proceedings of the Royal Society of London. Series A. Mathematical and Physical Sciences*, 209(1099):447–461, 1951.

[169] S. P. Timoshenko and S. Woinowsky-Krieger. *Theory of plates and shells*. McGraw-hill, 1959.

[170] L. N. Trefethen and D. Bau III. *Numerical linear algebra*, volume 50. Siam, 1997.

[171] M. Trushin and A. C. Neto. Stability of a rolled-up conformation state for two-dimensional materials in aqueous solutions. *Physical Review Letters*, 127(15):156101, 2021.

[172] Z. Tu and Z. Ou-Yang. Lipid membranes with free edges. *Physical Review E*, 68(6):061915, 2003.

[173] A. Venkatesh, V. Anand, and V. Narsimhan. Peeling of linearly elastic sheets using complex fluids at low reynolds numbers. *Journal of Non-Newtonian Fluid Mechanics*, 309:104916, 2022.

[174] L. M. Viculis, J. J. Mack, and R. B. Kaner. A chemical route to carbon nanoscrolls. *Science*, 299(5611):1361–1361, 2003.

[175] A. V. Vologodskii, N. J. Crisona, B. Laurie, P. Pieranski, V. Katritch, J. Dubochet, and A. Stasiak. Sedimentation and electrophoretic migration of DNA knots and catenanes, 1998.

[176] W. Wan, Z. Zhao, H. Hu, X. Hao, T. C. Hughes, H. Ma, L. Pan, and J. Qiu. Folding of graphene into elastic nanobelts. *Carbon*, 76:46–53, 2014.

[177] J. Wang, E. J. Tozzi, M. D. Graham, and D. J. Klingenberg. Flipping, scooping, and spinning: drift of rigid curved nonchiral fibers in simple shear flow. *Physics of Fluids*, 24(12):123304, 2012.

[178] C. Weber, M. Carlen, G. Dietler, E. J. Rawdon, and A. Stasiak. Sedimentation of macroscopic rigid knots and its relation to gel electrophoretic mobility of DNA knots. *Scientific Reports*, 3(1):1091, 2013.

[179] J. Wei, J. Qiu, L. Ren, K. Zhang, S. Wang, and B. Weeks. Size sorted multicolor fluorescence graphene oxide quantum dots obtained by differential velocity centrifugation. *Science of Advanced Materials*, 6(5):1052–1059, 2014.

[180] J. Wiest, L. Wedgewood, and R. B. Bird. On coil–stretch transitions in dilute polymer solutions. *The Journal of Chemical Physics*, 90(1):587–594, 1989.

[181] B. J. Williams, S. V. Anand, J. Rajagopalan, and M. T. A. Saif. A self-propelled biohybrid swimmer at low reynolds number. *Nature Communications*, 5(1):3081, 2014.

[182] Z. L. Wu, M. Moshe, J. Greener, H. Therien-Aubin, Z. Nie, E. Sharon, and E. Kumacheva. Three-dimensional shape transformations of hydrogel sheets induced by small-scale modulation of internal stresses. *Nature Communications*, 4(1):1586, 2013.

[183] Y. Xia, J. A. Rogers, K. E. Paul, and G. M. Whitesides. Unconventional methods for fabricating and patterning nanostructures. *Chemical Reviews*, 99(7):1823–1848, 1999.

[184] X. Xu and A. Nadim. Deformation and orientation of an elastic slender body sedimenting in a viscous liquid. *Physics of Fluids*, 6(9):2889–2893, 1994.

[185] Y. Xu, H. Cao, Y. Xue, B. Li, and W. Cai. Liquid-phase exfoliation of graphene: an overview on exfoliation media, techniques, and challenges. *Nanomaterials*, 8(11):942, 2018.

[186] Y. Xu and M. J. Green. Brownian dynamics simulations of nanosheet solutions under shear. *The Journal of Chemical Physics*, 141(2):024905, 2014.

[187] Y. Xu and M. J. Green. Brownian dynamics simulation of two-dimensional nanosheets under biaxial extensional flow. *Journal of Polymer Science Part B: Polymer Physics*, 53(17):1247–1253, 2015.

[188] Z.-L. Xu, B. Zhang, and J.-K. Kim. Electrospun carbon nanofiber anodes containing monodispersed si nanoparticles and graphene oxide with exceptional high rate capacities. *Nano Energy*, 6:27–35, 2014.

[189] J. Xue, T. Wu, Y. Dai, and Y. Xia. Electrospinning and electrospun nanofibers: Methods, materials, and applications. *Chemical Reviews*, 119(8):5298–5415, 2019.

[190] H. Yamakawa. Transport properties of polymer chains in dilute solution: hydrodynamic interaction. *The Journal of Chemical Physics*, 53(1):436–443, 1970.

[191] M. Yan, F. Wang, C. Han, X. Ma, X. Xu, Q. An, L. Xu, C. Niu, Y. Zhao, X. Tian, et al. Nanowire templated semihollow bicontinuous graphene scrolls: designed construction, mechanism, and enhanced energy storage performance. *Journal of the American Chemical Society*, 135(48):18176–18182, 2013.

[192] O. H. Yeoh. Some forms of the strain energy function for rubber. *Rubber Chemistry and Technology*, 66(5):754–771, 1993.

[193] R. Yi, F. Dai, M. L. Gordin, S. Chen, and D. Wang. Micro-sized si-c composite with interconnected nanoscale building blocks as high-performance anodes for practical application in lithium-ion batteries. *Advanced Energy Materials*, 3(3):295–300, 2013.

[194] J. Yoon, S. Jo, I. S. Chun, I. Jung, H.-S. Kim, M. Meitl, E. Menard, X. Li, J. J. Coleman, U. Paik, et al. Gaas photovoltaics and optoelectronics using releasable multilayer epitaxial assemblies. *Nature*, 465(7296):329, 2010.

[195] Y. Yu and M. D. Graham. Coil–stretch-like transition of elastic sheets in extensional flows. *Soft Matter*, 17(3):543–553, 2021.

[196] Y. Yu and M. D. Graham. Wrinkling and multiplicity in the dynamics of deformable sheets in uniaxial extensional flow. *Physical Review Fluids*, 7(2):023601, 2022.

[197] S. Zamani, J. S. Won, M. Salim, M. AlAmer, C.-w. Chang, P. Kumar, K. Amponsah, A. R. Lim, and Y. L. Joo. Ultralight graphene/graphite hybrid fibers via entirely water-based processes and their application to density-controlled, high performance composites. *Carbon*, 173:880–890, 2021.

[198] L. Zhang, J. J. Abbott, L. Dong, K. E. Peyer, B. E. Kratochvil, H. Zhang, C. Bergeles, and B. J. Nelson. Characterizing the swimming properties of artificial bacterial flagella. *Nano Letters*, 9(10):3663–3667, 2009.

[199] L. Zhang, Z. Wang, C. Xu, Y. Li, J. Gao, W. Wang, and Y. Liu. High strength graphene oxide/polyvinyl alcohol composite hydrogels. *Journal of Materials Chemistry*, 21(28):10399–10406, 2011.

[200] P. Zhang, B. Xu, G. Chen, C. Gao, and M. Gao. Large-scale synthesis of nitrogen doped mos2 quantum dots for efficient hydrogen evolution reaction. *Electrochimica Acta*, 270:256–263, 2018.

[201] H. Zhao and E. S. Shaqfeh. The shape stability of a lipid vesicle in a uniaxial extensional flow. *Journal of Fluid Mechanics*, 719:345, 2013.

[202] Y. Zhao, J. Guan, and S. J. Wu. Highly stretchable and tough physical silk fibroin–based double network hydrogels. *Macromolecular Rapid Communications*, 40(23):1900389, 2019.

[203] O.-Y. Zhong-Can and W. Helfrich. Bending energy of vesicle membranes: General expressions for the first, second, and third variation of the shape energy and applications to spheres and cylinders. *Physical Review A*, 39(10):5280, 1989.